Hartmann Wavefront Sensors for Advanced Gravitational Wave Interferometers

by

Aidan F. Brooks

Thesis submitted for the degree of
Doctor of Philosophy
in
The University of Adelaide
Department of Physics
School of Chemistry and Physics
July, 2007

For my parents

Contents

Abstract

The upgrade of gravitational wave interferometers from first- to second-generation will enable gravitational wave astronomy to become a reality, providing a new view of our Universe. One of the numerous upgrades in moving to the second-generation is the increased intra-cavity laser power in the interferometer optical cavities, which should reduce the shot-noise in the interferometer. Unfortunately, small, but finite, absorption of optical power in the intra-cavity optics will result in thermal gradients within the interferometer optics, which causes wavefront distortion of the cavity eigenmode. Numerical modelling, based on an analytic solution for the thermal gradient, has shown that the effect of the accumulated wavefront distortion on the cavity mode is to degrade the sensitivity of the interferometer, and it may cause instrument failure. The wavefront distortion must, therefore, be compensated and actuators for this purpose have been proposed but a suitable wavefront sensor is required.

In this thesis, I describe an interferometric validation of the analytic solution for the thermal gradient which, as discussed above, is central to numerical modelling of advanced GWI. The bulk of the thesis, however, concentrates on the development and testing of a wavefront sensor for wavefront compensation. I shall describe a Hartmann wavefront sensor that can measure wavefront changes, such as those due to substrate and coating absorption in GWI, with unprecedented precision and accuracy. It is simple to optimize and reliable, and appears very suitable for measuring wavefront distortion in advanced gravitational wave interferometers.

I shall also describe the deployment of the Hartmann wavefront sensor at the High Optical Power Test Facility in Western Australia to measure wavefront distortion in the optics of a high-optical-power cavity. Despite significantly increased environmental noise, the sensor measured the wavefront distortion in the optics with a precision necessary for deployment in an advanced gravitational wave interferometry. The Hartmann wavefront sensor measurements were verified using measurements of the intra-cavity mode size and intra-cavity power.

The potential use of the wavefront sensor for off-axis measurement of wavefront distortion in a gravitation wave interferometer prompted an investigation into reconstruction of the on-axis wavefront distortion. The proof-of-principle of the resulting single-view off-axis analysis is demonstrated using simulated and actual measurements.

Statement of Originality

This work contains no material which has been accepted for the award of any other degree or diploma in any university or other tertiary institution and, to the best of my knowledge and belief, contains no material previously published or written by another person, except where due reference has been made in the text.

I give consent to this copy of my thesis being made available in the University Library.

The author acknowledges that copyright of published works contained within this thesis (as listed below) resides with the copyright holder/s of those works.

SIGNED: .....

DATE: 7/11/07

Supervisors: Peter J. Veitch and Jesper Munch.

Acknowledgements

First and foremost I would like to thank my supervisors, Peter Veitch and Jesper Munch. I have really enjoyed working with you all these years. Your support and guidance has been invaluable and I am truly grateful for all your assistance.

To Thu-Lan Kelly: thank you so much for all your help on the Hartmann sensor over the years. You were always there for me when I needed those questions answered about your code.

To David Blair, David McClelland and everyone in ACIGA: your help and assistance at AIGO is most appreciated. I'd especially like to thank Chunnong Zhao and Yan Zewu: I couldn't have got my results without your help and all those late nights in the lab were so much more bearable with you guys around. Thanks also to Phil Willems for your assistance at AIGO. I'll miss discussing the Simpsons and Family Guy whilst simultaneously performing large scale Gaussian beam size measurements.

To Murray Hamilton; thanks for all your words of wisdom. I'll miss demonstrating the Photonics II experiments with you.

I'd like to thank Trevor Waterhouse and Bob Hurn for all your help over the years. If I ever needed a chat, you guys were always available.

To my fellow students in the Physics Department, thanks for all your support and cheer over the years. In particular, Brony, Skye and Catherine: thanks for always being up for a drink at the Unibar.

I'd like to acknowledge my colleagues in the Optics Group: Tom Rutten, Nick Chang, Miftar Ganija, Shu-Yen Lee, Keiron Boyd, Sean Manning,

Damien Mudge, Francois Jeanneret, David Ottaway and Alex Hemming. You guys made it fun to be at work. I'll miss those long afternoon discussions in the lunch room when we should have been working. In particular, I'd like to thank Blair Middlemiss for all the help in the workshop and for always being around when I needed a reality check.

To David Hosken and Matthew Heintze: quite simply, I wouldn't have made it without your help. I wish you all the best in the future and hope our paths will cross again soon.

To Peter and the crew at The Coffee Club: you kept me awake. Thanks for all the cheer and smiles over the last few years.

To my friends: Matthew, Sarah, Poh, Zoe, Andrew, Lily and Paul: I love you guys. You were always there for me, especially in those darkest hours. Thank you.

To my family: John, Megs, Lizzy, Peter and Jack: I can't believe how much we've all matured over the years. We've moved to different houses and cities, but have grown closer as a family. You will always be part of my world.

Lastly to Mum and Dad: your love and support over this time of trial has been beyond measure. Words cannot express how much it has meant to me and so I dedicate this thesis to you.

List of Symbols

Throughout this thesis, several symbols will be used repeatedly to represent specific quantities or parameters, the following is a list of these symbols and short descriptions for the readers convenience. This list is not exhaustive but every effort has been made to maintain conformity of symbols used here. Wherever possible standard symbols and notation have been used which appear in most laser texts.

$\mathrm{I}_{\mathrm{obj}}(x)$	...	Intensity profile of object beam
$\mathrm{I}_{\mathrm{ref}}(x)$	...	Intensity profile of reference beam
$\mathrm{I}_{\mathrm{int}}(x)$	...	Interference pattern between two beams
$\psi(x, t_i)$	...	Wavefront distortion at time t_i
L	...	Distance between Hartmann plate and CCD: lever arm
W	...	Wavefront
ΔW	...	Wavefront change (aberration)
S	...	Primary aberration defocus
k	...	Order of Parabolic function
h_{p}	...	Distance between holes on Hartmann plate
S_{thermal}	...	Apparent defocus due to thermal effects
N_p	...	Number of photons in a given time interval
p_s	...	Pixel size
x_c	...	x centroid

$C_{\Delta \mathrm{W}}$	...	Southwell noise coefficient (variance)
$\sigma_{\Delta W}$	...	RMS wavefront difference between adjacent holes
N_{ref}	...	Number of samples in reference centroid set average
N_{avg}	...	Number of images averaged over
z_0	...	nominal distance from fibre-couple output of SLD to Hartmann plate
Δz	...	displacement of fibre-couple output of SLD
$\mathbf{WD}^{(\mathbf{off})}$	...	2D off-axis wavefront distortion profile
$\mathrm{WD}_{\mathrm{SAPH}}^{(\mathrm{off})}$	...	vertical cross-section through $\mathbf{WD}^{(\mathbf{off})}$ corresponding to sapphire optic
$\mathrm{WD}_{\mathrm{FS}}^{(\mathrm{off})}$	...	vertical cross-section through $\mathbf{WD}^{(\mathbf{off})}$ corresponding to fused silica optic
$\mathrm{K}_{\mathrm{E1}}(t)$	...	coefficient describing the elongation of the sapphire distortion
$\mathrm{K}_{\mathrm{E2}}(t)$	...	coefficient describing the elongation of the fused-silica distortion
$\mathrm{K}_{\mathrm{C1}}(t)$	...	contribution of the fused-silica distortion to the sapphire distortion cross-section
$\mathrm{K}_{\mathrm{C2}}(t)$	...	contribution of the sapphire distortion to the fused-silica distortion cross-section
$\mathrm{WD}_{\mathrm{SAPH}}^{(\mathrm{on})}$	...	on-axis wavefront distortion due to sapphire
$\mathrm{WD}_{\mathrm{FS}}^{(\mathrm{on})}$	...	on-axis wavefront distortion due to fused-silica
$\mathrm{WD}_{\mathrm{cavity}}$	...	wavefront distortion experienced by cavity mode
$w_{\mathrm{ITM}}(S)$	...	cavity mode size at ITM as function of S
$w_{\mathrm{ETM}}(S)$	...	cavity mode size at ETM as function of S
$V_{ij}(r,z)$	...	ij-th annular volume element
$V_{ij}(r,z)$	...	ij-th annular volume element
$w_{ij}(x,y)$	...	path integral through $V_{ij}(r,z)$ projected onto plane $\mathrm{P}_{\mathrm{exit}}$

List of Figures

List of Tables

Chapter 1

The rewards and challenges of gravitational wave astronomy

1.1 The promise of new science and a better understanding of the Universe

1.1.1 Gravitational waves

Gravitational waves (GW) are ripples in spacetime, predicted by Einstein in 1918 [1] as a solution to the General Theory of Relativity. Although they have never been directly observed, there is excellent indirect evidence for their existence. The pulsar PSR B1913+16, discovered by Hulse and Taylor in 1974 [2], shows a decay in its orbital period that is consistent with loss of energy through the emission of gravitational waves as predicted by General Relativity [3]. This observation earned Hulse and Taylor a Nobel Prize in 1993.

The generation of GW is analogous to the generation of EM waves. EM waves are generated by the acceleration of charges and GW are generated by the acceleration of masses. Whilst EM waves are dipolar in nature, the lowest order GWs possible are quadrupolar in nature (monopolar GW and dipolar GW would violate conservation of mass-energy and conservation of

momentum, respectively [4]). Thus a passing quadrupolar GW exerts a tidal strain on space-time, stretching it along one axis and squeezing it along the perpendicular axis. This effect is characterized by the *tidal strain amplitude*, $h(t)$, such that a passing gravitational wave of amplitude $h(t)$ causes the distance, L_{test}, between two fiducial test masses to fluctuate by a time-varying differential amount, $\Delta L_{\text{test}}(t) = h(t)\, L_{\text{test}}$, [5]. The observable quantity $h(t)$ decays as $1/r$, where r is the distance between the source and the point of observation, a fact that becomes very important in the discussion of the measurement of GW.

The interaction between GW and matter is extremely weak and, therefore, the Universe is effectively transparent to GW and so the information they carry from their sources is uncontaminated [4]. Given that they may originate from areas, discussed in the following section, from which there is little to no direct EM radiation, GW illuminate the Universe in an entirely new and rich way.

1.1.2 Astrophysical sources of GW and the new science they may reveal

There are a variety of predicted astrophysical sources of GW. These sources each promise to reveal different types of new science in their GW radiation. The following is a short list of the main types of sources and the associated new science.

- Inspiral sources. Compact binary systems, such as PSR B1913+16, containing either, two neutron-stars (NS), a NS and a black-hole (BH), or two BHs radiate orbital energy as GWs with a characteristic 'chirp' signal [5]. When the first direct detection of GW occurs it will most probably be from the final decay and merger of the two objects in a compact binary system as these sources are very powerful, are predicted to occur frequently enough to be seen and as the time dependence of the GW signal emitted during the inspiral is believed to be

well-known. Detection of such a source would reveal new astrophysical information about the late inspiral and merger epochs of such an inspiral. Conversely, non-detection would say that the current models of GW generation are incorrect.

- Continuous sources, generally rotating asymmetric neutron stars (which may additionally be observable as pulsars), would reveal observations of extremely dense states of matter [4] and maybe reveal an information about free-quark matter [6].

- Burst sources. Detection of GW from the catastrophic core collapse of massive stars would help our understanding of these violent events, especially when combined with, for example, neutrino detections of the same event [4].

- Stochastic sources. Random source, for example, the gravitational-wave background from cosmological inflation [4], enabling testing of new unification physics.

The observation of GW holds great promise in terms of increasing our understanding of high energy astrophysical processes and non-linear General Relativity. Additionally, it holds the promise of potentially revealing evidence of new types of physics. As such grativational waves are a prominent topic in the scientific community and several large scale projects are underway to enable their direct detection and the development of observational gravitational wave astronomy.

1.2 The challenge of GW interferometry

1.2.1 First generation GW interferometry

The tidal strain effect of GWs on fiducial test masses can be observed by measuring the differential length change between a set of two test masses separated by a distance L_1 along one line and a second set of two test masses

separated by a similar distance L_2 along a perpendicular line. This measurement can be made using interferometry, hence the name gravitational wave interferometry (GWI).

A schematic of a GWI is shown in Figure 1.1. It is, essentially, an L-shaped Michelson interferometer formed from a laser, a beamsplitter, two arms of length L_1 and L_2 at right angles and a photo-diode measuring the output of the interferometer [7] [8]. The signal-to-noise is maximized by averaging for a dark fringe at the PD, and thus most of the power propagates back towards the power recycling mirror (PRM) which reflects it back into the interferometer. A GW, of correct polarization, passing through the device will compress one arm and distend the other. The change in the path length difference between the two arms, $\Delta L_{\rm arm}(t) = L_2(t) - L_1(t)$, is equal to the tidal strain amplitude, $h(t)$, multiplied by the average arm length, $L_{\rm arm}$. Hence, there is a time-varying phase change between the two arms and a time-varying change in the intensity on PD, both of which are proportional to the tidal strain amplitude.

The interferometer arms are kilometer-scale length (4 km in Initial LIGO) in order to increase the length of time that the light in the arms is exposed to a GW [7]. This has the effect of increasing the phase-delay between the two arms. The phase-delay is further increased by the addition of Fabry-Perot cavities.

Ignoring other noise sources (seismic and suspension thermal noise), the minimum strain, h_{min}, that can be measured is determined by photon shot noise at the beam splitter, which is inversely proportional to the square root of the number of photons, N_p, incident on the beam splitter in a given exposure time [7]. Therefore, h_{min}, is given by

$$h_{min} \approx \frac{\lambda}{B\, L_{\rm arm}} \frac{1}{\sqrt{N_p}} \tag{1.1}$$

where B is the mean number of times the light bounces back and forth in the Fabry-Perot cavities (proportional to the cavities' finesse) [7]. At

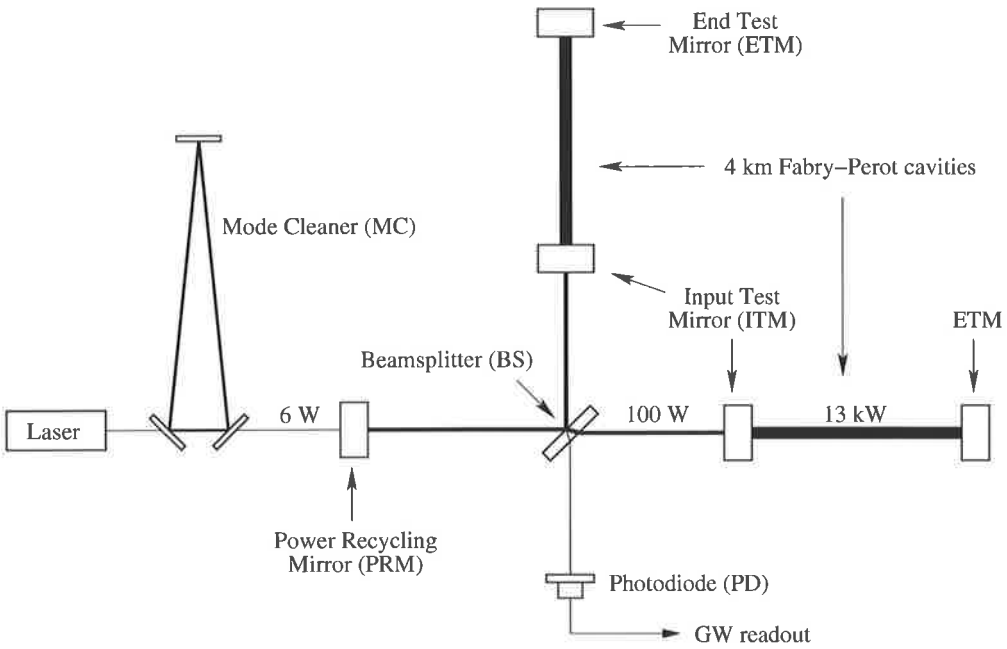

Figure 1.1: Schematic of a first generation GWI. A power-recycled Fabry-Perot long-baseline Michelson interferometer.

low frequencies, (< 200 Hz), the minimum detectable strain is degraded by seismic and suspension thermal noise. The minimum detectable strain at high frequencies, (> 200 Hz), can be decreased by increasing the number of photons incident on BS, accomplished by placing the PRM between the laser and BS to form a resonant cavity between PRM, ETM_1 and ETM_2.

The target strain sensitivity for Initial LIGO is approximately 3×10^{-22} @ 150 Hz [5]. The current sensitivity of Initial LIGO, expressed in units of $m/\sqrt{Hz}$, is shown in Figure 1.2. Converting to strain, by dividing by the 4 km length of the interferometer arms and multiplying by the square root of the frequency, shows that Initial LIGO has achieved its design stain sensitivity of approximately 3×10^{-22} @ 150 Hz. The strain sensitivity of Initial LIGO is such that there is a reasonable, though not certain, chance of detecting a GW in a year's worth of observations [8]. However, the aim of Initial LIGO is to demonstrate the up-scaling of laboratory interferometers to long-baselines with the projected improvement in sensitivity. In order to increase the probable rate of detection it necessary to move to improve the sensitivity of the interferometers, which requires the next-generation 'advanced' interferometers.

1.2.2 Advanced GWI enabling gravitational astronomy

The purpose of second-generation or 'advanced' interferometers is to increase the rate of detection of GWs to a point where GW astronomy becomes feasible. The justification for trying to accomplish this is related to the $1/r$ decay of $h(t)$. If a second-generation interferometer is N times more sensitive than first-generation one, it can detect a 'standard candle' N times further away. The beauty of this is that it operates in all three dimensions and the volume of space that is searched, and hence the event rate of GW, increases as N^3. Therefore, if an advanced interferometer can achieve a 10× increase in sensitivity, the number of detectable sources increases by a factor of 1000, and the estimated rate of detection of GWs will go from less than one detection every year to an average rate of one detection a day! [5]

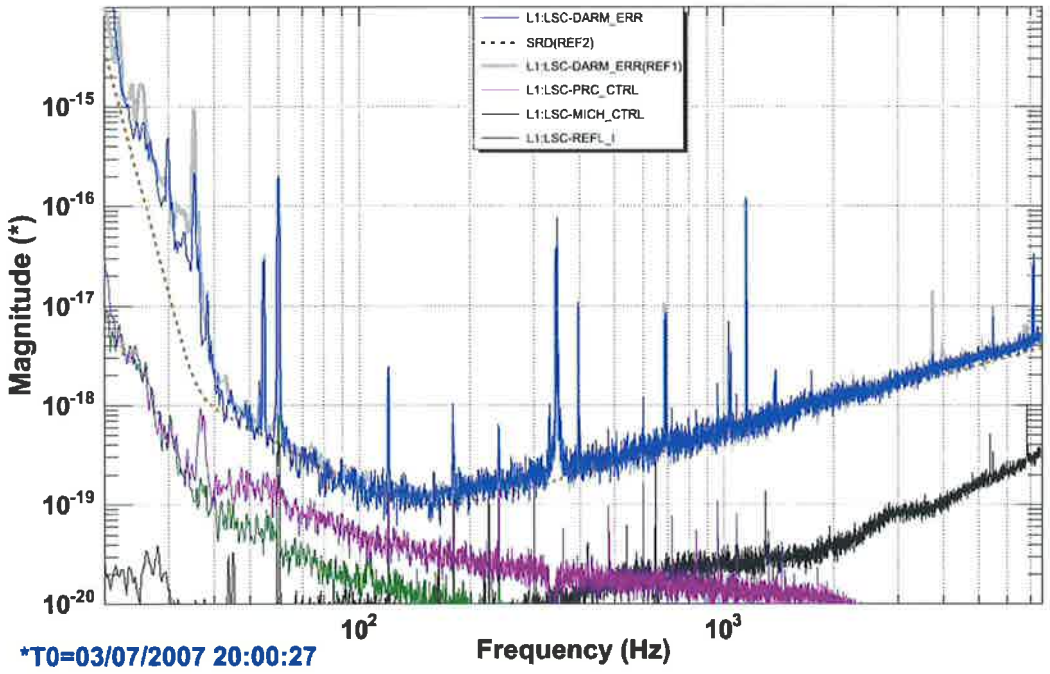

Figure 1.2: The blue curve, L1:LSC-DARR_ERR, shows the current sensitivity of Initial LIGO in units of $m/\sqrt{Hz}$, recorded 11th July 2007 at 04:56:07 UTC [9]. The sensitivity is limited by photon shot noise for frequencies > about 200 Hz.

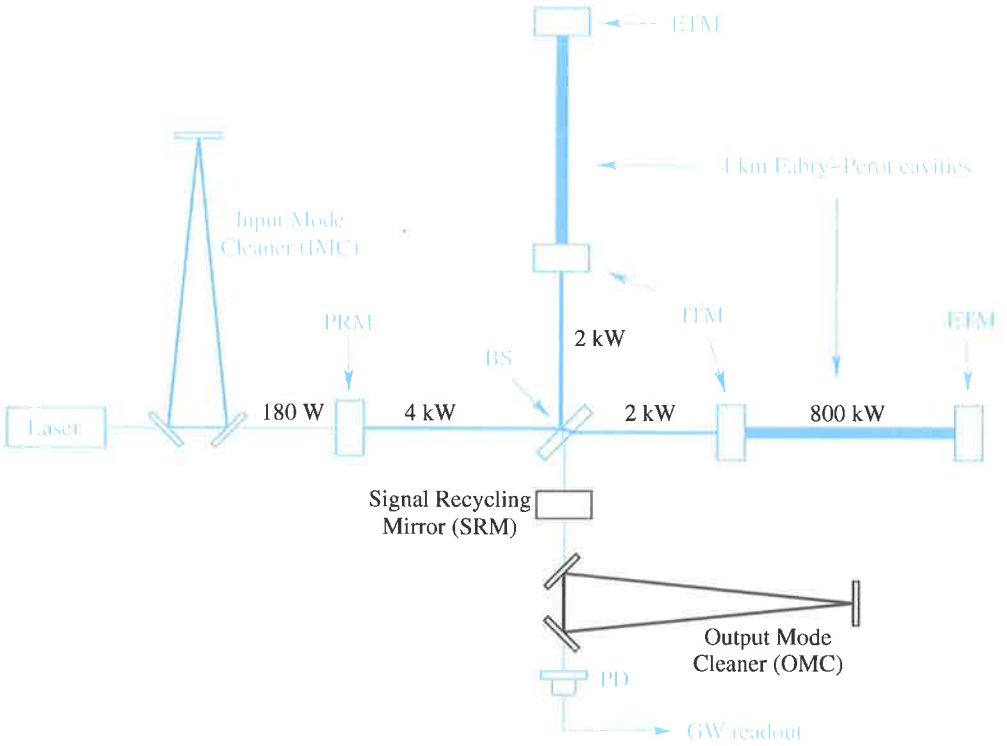

Figure 1.3: Schematic of a second generation GWI. A power-recycled signal-recycled Fabry-Perot long-baseline Michelson interferometer, including the approximate power levels expected in the input laser and interferometer cavities.

A schematic for an advanced GWI is shown in Figure 1.3. It largely resembles the first-generation GWI and the majority of the improvements to the device have been highlighted. The improvements targeted for Advanced LIGO are discussed below and divided into two groups, the first group are those associated with reducing noise sources not discussed in detail in this thesis, and the second group are those associated with increasing the number of photons at the BS and hence decreasing photon shot noise.

- The improvements associated with other noise sources are:
  - Better seismic isolation and suspension systems to reduce seismic motion coupling into the test masses

  - Heavier test masses made of higher quality material to decrease Brownian thermo-elastic noise and reduce radiation pressure noise.
  - An output mode cleaneradded to improve the spatial profile of any light incident on the PD.

- The improvements associated with decreasing shot noise:
  - Increasing the laser power from from 10 W to 180 W [5]
  - Increasing the power recycling factor from 30 to 80 [5] to increase the total stored power in the PRC from 100 W to $\approx$ 4 kW.
  - Adding a signal recycling mirror to enable resonant sideband extraction. In this system, the interferometer is turned into a tunable resonant cavity. This is useful for monitoring continuous sources at known frequencies [10].

As a result of the improvements Advanced LIGO is expected to be sensitive enough to measure strains as small as $\approx 3 \times 10^{-23}$ [11] in the range 60-300 Hz [5], resulting in an approximately 1000$\times$ increase in event rate for expected sources [11].

1.2.3 Higher stored power leads to wavefront distortion

The increase in optical power, while reducing the shot noise at the BS, also has some side-effects which adversely affect the interferometer. The high reflectivity (HR) coatings, anti-reflection (AR) coatings and optical substrates absorb a small but finite amount of the optical power in the PRC and the arm cavities, as illustrated in Figure 1.4. This is particularly significant for the substrates and the HR and AR coatings of the ITMs, the substrate and coating of the BS and the HR coating of the ETMs [12].

The absorbed power causes local heating of the optic and results in an internal temperature gradient. An analytic solution for the temperature

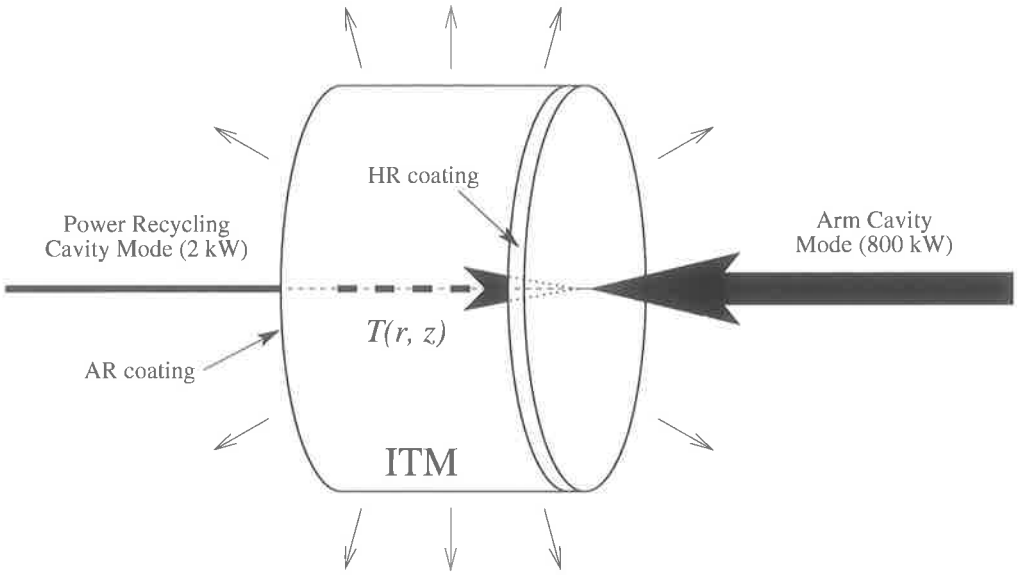

Figure 1.4: Absorption in ITM causes temperature distribution

distribution, $T(r, z)$, which has not been directly validated, was reported by Hello and Vinet [13]. The full form of this solution is outlined in Appendix A.1. The integral of $T(r, z)$ along the z-axis through the optic is also given there. As discussed by Lawrence [12], the distribution changes the optical properties in three ways:

1. Thermo-optic effect: the refractive index changes with temperature and, therefore, there is a change in the optical length along a path S through the material given by

$$\psi(r)_{\mathrm{TO}} = \frac{\mathrm{d}n}{\mathrm{d}T} \int_S T(r, z)\, \mathrm{d}s$$

   where $\mathrm{d}n/\mathrm{d}T$ is the thermo-optic coefficient. This effect is manifested within the substrate of the optic.

2. Elasto-optic effect: thermal expansion results in mechanical strain which results in local refractive index changes. The change in optical length

along a path S through the material is given by

$$\psi\left(r\right)_{\mathrm{EO}} \approx \alpha\, \mathrm{p}_{11} \int_S T(r,z)\, \mathrm{d}s$$

where α is the coefficient of thermal expansion and p_{11} is the component of the elasto-optic tensor along the probe beam polarization axis. This effect is also manifested within the substrate of the optic.

3. Thermo-elastic effect: The surfaces of the optic expand along the optical axis and the resulting change in optical path length is given by

$$\psi\left(r\right)_{\mathrm{TE}} \approx n_{\mathrm{optic}}\, \alpha \int_S T(r,z)\, \mathrm{d}s$$

where n_{optic} is the refractive index of the optic. It also changes the curvature of the surfaces, which affects reflection. Obviously, this effect is also manifested at the surfaces of the optic.

The resulting changes to the mirror properties adversely affect the performance of the interferometer, as discussed in the next section.

1.2.4 Advanced GWI: thermally-induced performance reduction

Essentially, the thermal distortion in the cavity optics scatters power from the fundamental spatial cavity mode into higher order spatial modes that are not resonant, as discussed by Strain *et al.* [14]. This has several effects on the behaviour of the interferometer.

1. Power scattered out of the carrier mode in the arm and power recycling cavities reduces the number of photons at the beam splitter.

2. Differential thermal lensing between the two arms of the interferometer increases the phase noise at the dark port [12] and results in a mismatch between the overlapping wavefronts at the beamsplitter [14].

3. Power is scattered out of the RF sidebands whose uses include, but are not limited to, measurement of the length of the PRC and also, in an AC readout scheme, readout of the GW signal itself [15].

These effects have been predicted in numerical models of high optical power cavities and advanced GWI (using the MELODY code [16]) and the thermal lensing has been shown to ultimately drive the advanced GW interferometer to failure [12]. It should be noted than these models are predicated on the assumption that the Hello-Vinet theory is correct.

The problem in a nutshell: *the ability to investigate new physics with advanced GWI is limited, in part, by thermal lensing in the optics of the GWI.*

1.3 Active compensation of absorption-induced wavefront distortion

1.3.1 Thermal compensation techniques

Compensation of wavefront distortion has been suggested as a solution to the problem of performance reduction of the interferometer and various techniques have been demonstrated. A brief summary of the suggested techniques is given below.

- Radiative heating from a shielded heating ring of the areas of a distorted optic not heated by the cavity mode, as illustrated in Figure 1.5. This was shown to be effective in reducing the overall distortion in a heated optic by Lawrence *et al.* [17].

- Conductive heating of the barrel of a compensation plate in a high power optical cavity was shown to produce a negative lens and compensate for wavefront distortion in the intracavity optics by Zhao *et al.* [18].

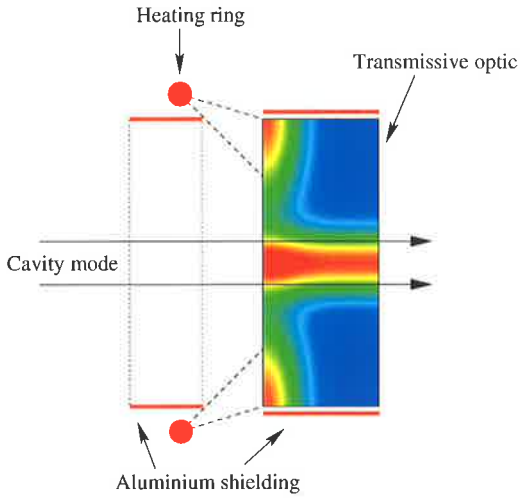

Figure 1.5: Cross-section showing radiative heating from a shielded heating ring

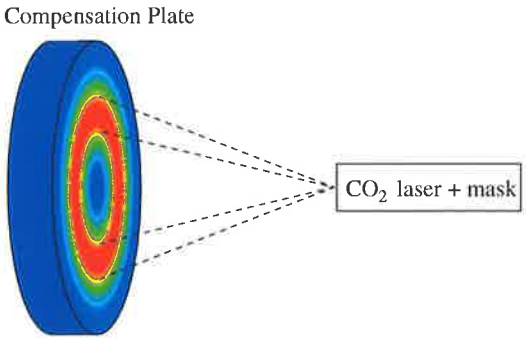

Figure 1.6: Staring heating of ITM

- A CO_2 laser beam with a specific intensity profile that 'stares' at a distorted optic, as illustrated in Figure 1.6, has been shown to be effective in compensating wavefront distortion in Initial LIGO [19].

- A scanning CO_2 raster pattern was proposed by Ryan Lawrence [12]. The initial design of Advanced LIGO does not include such an actuator within the Thermal Compensation System (TCS), but the design is left open to this installing this option [20].

All of the actuators listed above, however, require an accurate and sensitive wavefront sensor to measure the distortion and compensation, in order

to function as part of a closed-loop active thermal compensation system.

1.3.2 Wavefront sensor requirements for thermal compensation

The requirements for an accurate and sensitive wavefront sensor for Advanced LIGO have been investigated by Willems [21]. In Advanced LIGO, "the extraction efficiency of the GW sidebands through the signal recycling cavity (SRC) sets the most strigent requirement on TCS". The maximum acceptable phase error for the sidebands per round trip is 0.08 radians @ 1064 nm = 13.5 nm. This will ensure that no more than 0.1% of power is scattered out of the sidebands per round trip, or no more than 5% in total. The following requirements were therefore set for a wavefront sensor.

1. Sensor should have precision at least 10× better than this = 1.35 nm (or $\lambda/467$ @ 632.8 nm) [21]

2. The spatial resolution must be such as to not miss a feature from a point absorber [21]. This requires a 1 cm × 1 cm grid to cover a circular region 224 mm in diameter, approximately 23 × 23 sample points.

3. The sensor may need to be installed in an off-axis configuration [12].

The current TCS design for Advanced LIGO [20] requires an active thermal compensation system with dedicated wavefront sensors and actuators for each optic, as illustrated in Figure 1.7.

1.4 Wavefront sensors for TCS

Two types of potential wavefront sensors for TCS are interferometric and Hartmann-type sensors, the relative merits of which are presented in the following discussion.

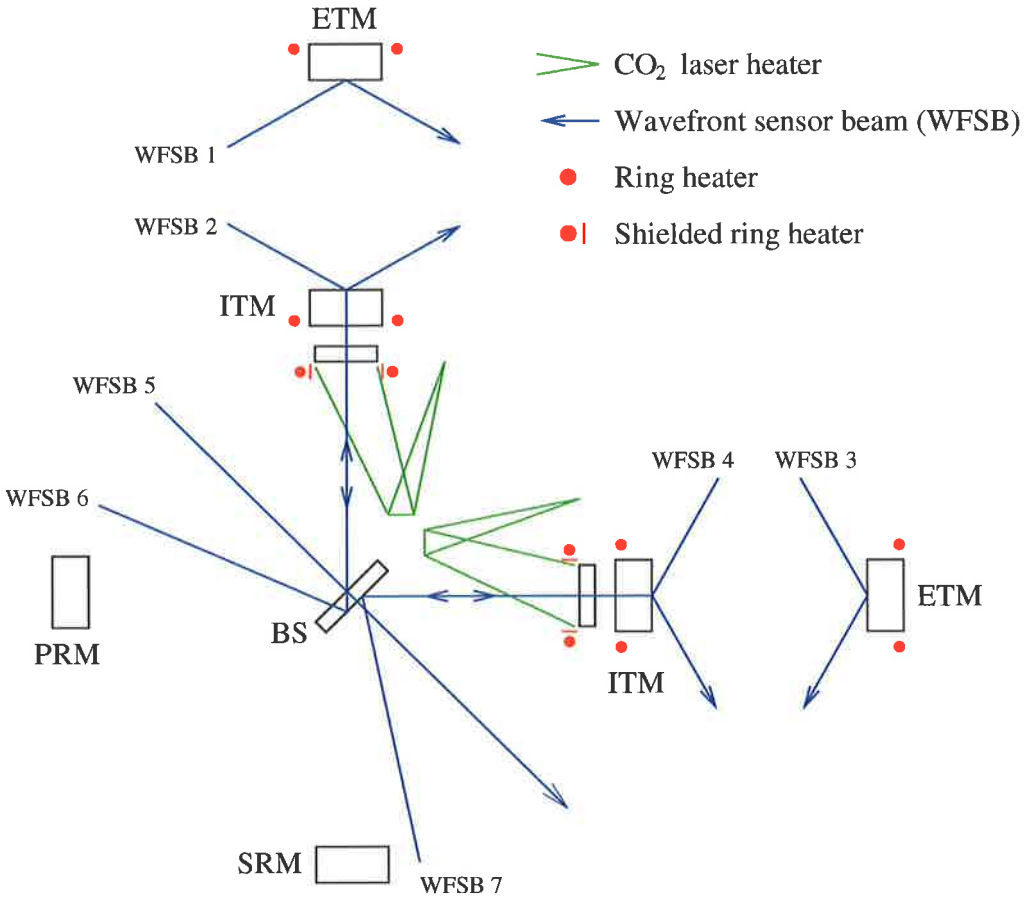

Figure 1.7: Schematic of initial design for wavefront sensors and TCS for Advanced LIGO [20]

An interferometer is capable of functioning as a wavefront sensor when its output is read by a CCD array. Phase shifting interferometry has achieved very high accuracy (1 nm) and precision (0.1 nm) [22]. This was accomplished by a attaching piezo-electric transducer (PZT) to a mirror in the reference arm of the interferometer, appyling a sinusoidally varying voltage to the PZT, and measuring the time-varying interference pattern on the CCD. The main drawback of an inteferometer is that it is highly intolerant of mechanical vibrations [23] and alignment issues. Additionally, the interferometric measurement of phase distortion induced by an object requires two separate path matched laser beam paths, increasing system complexity.

Hartmann-type sensors, discussed in detail in Chapter 3, can be summarized here as being based upon a geometrical technique that samples the gradient of the *wavefront* profile at a series of discrete points. Given that they only require a single path to measure wavefront distortion induced by an object, they are relatively insensitive to alignment (in comparison to an interferometer) and they offer a simpler alternative to interferometry. A Hartmann sensor has been reported with a precision of 2.1 nm ($\lambda/500$ @ 1064 nm) [24]. Additionally, commercially available variants called Shack-Hartmann sensors, also discussed further in Chapter 3, are quoted as having an accuracy of $\lambda/150$ @ 633 nm in an array of 25×19 lenslets [25].

The difference in the operation of the two sensors is summarised as follows: an interferometer measures the difference between two different paths recorded at the same time and a Hartmann-type sensor measures the difference between the same path recorded at two different times. Koch *et al.* [26] compared a SH sensor and a phase shifting interferometer (PSI) and determined that they had comparable performance. They also suggested PSIs could be replaced with SH sensors in order to reduce system complexity. Given the comparable performance of SH and Hartmann sensors, the conclusions of Koch *et al.* can be assumed to also apply to traditional Hartmamnn sensors.

Given the existing complexity of GWI design (see Figures 1.3 and 1.7),

the relative simplicity and promising performance of traditional Hartmann sensors make them an attractive choice for inclusion in an active thermal compensation system. As such, they were chosen for further study and development, described in this thesis, to determine their suitability for such a system.

1.5 This thesis

This thesis addresses several of the issues presented in the previous discussion. A verification of the theory of Hello and Vinet that underlies the numerical modelling of advanced GWI, described in Section 1.2.4, is presented in Chapter 2. This verification was performed in laboratory conditions using a Mach-Zehnder interferometer as the accuracy and sensitivity of the Hartmann sensor had not been established at the time of the test. The development of an ultra-sensitive and accurate Hartmann wavefront sensor, suitable for measurement of absorption-induced wavefront distortion in advanced GWI, is described in Chapters 3 and 4. The application of this sensor to the measurement of wavefront distortion in the input-coupling mirror of a Fabry-Perot cavity suspended in a vacuum system at the HOPTF is then presented in Chapter 5. This test was designed to produce a wavefront distortion similar to that expected in Advanced LIGO and is the first direct measurement of absorption-induced wavefront distortion in a GWI-like environment. Finally, the use of the HWS for single-view tomographic analysis of axially symmetric temperature distributions is described in Chapter 6. The overall effectiveness of the Hartmann wavefront sensor for measurement of thermal lensing in advanced GWI and potential future developments are summarised in Chapter 7.

Chapter 2

Interferometric test of Hello-Vinet model

2.1 Background

The analytical models for coating and substrate absorption-induced wavefront distortion (WD), published by Hello and Vinet [13], are used in the MELODY code which is used to model the behaviour of advanced gravitational wave interferometers. These time dependent models have not been validated however. Nevertheless, some aspects of WD theories have been investigated experimentally. Mansell *et al.* [27] measured absorption-induced wavefront distortion in a test sample, but compared the result to an simpler model proposed by Strain *et al.* [14] that does not include boundary conditions or any axial or temporal information. Lawrence *et al.* [17] verified the steady-state coating absorption analytic model by heating a cylindrical test optic with a CO_2 laser beam with a Gaussian profile. The temporal model of Hello and Vinet was indirectly validated by Zhao *et al.* [18] when they induced a thermal lens in one the mirrors of a Fabry-Perot optical cavity and observed its effect on the cavity mode. However, no direct validation with a wavefront measurement of either the coating or substrate temporal Hello-Vinet models, or the substrate steady-state Hello-Vinet model have

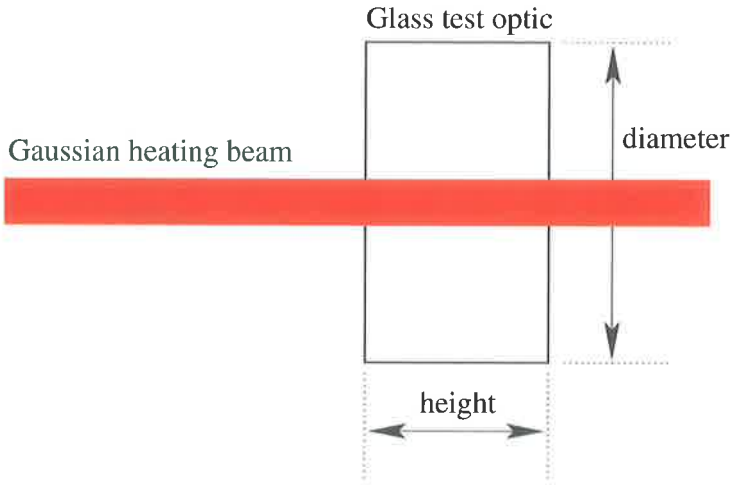

Figure 2.1: A cylindrical test optic exposed to a Gaussian beam expected to absorb optical power in the substrate and produce a wavefront distortion as described by Hello and Vinet

been performed to date.

2.2 Objective

The aim of this chapter, therefore, is to describe a bench-top test of the temporal and steady-state Hello-Vinet model for substrate absorption using a glass test optic, as depicted in Figure 2.1, which produces a wavefront distortion that is similar in magnitude to that expected in Advanced LIGO and satisfies the assumptions of Hello and Vinet (H-V). The design and choice of the test optic is discussed in Section 2.3. The system used to produce the wavefront distortion and its measurement using a Mach-Zehnder (MZ) interferometer are described in Section 2.4. The results of the measurement are reported in Section 2.5.

2.3 Design and choice of test optic

Why is this objective difficult to meet? The primary difficulty in this experiment is creating an absorption-induced distortion in the test optic that is

measurable on a benchtop with, ideally, an amplitude similar to Advanced LIGO. A secondary difficulty is controlling the experiment and environment such that the signal is capable of being measured by an interferometer.

2.3.1 Design

The size of the volumetric-absorption-induced wavefront distortion expected in Advanced LIGO across the width of the cavity mode is, to first order, approximately λ, where $\lambda = 1064$ nm. This is determined using the formulae of Hello and Vinet (H-V) and knowing the power incident on the 20 cm thick fused silica optics in Advanced LIGO is of the order of 2 kW, the expected volumetric absorption in these optics is of the order of 50 ppm per cm [28] [29] (giving a total absorbed power of approximately 2 Watts) and the thermo-optic coefficient, $\mathrm{d}n/\mathrm{d}T$, is approximately 6×10^{-6}.

The maximum power available in the Gaussian beam for this benchtop test was 500 mW @ 1064 nm. In order to produce a distortion of similar size to Advanced LIGO, it was necessary to find a material with a higher coefficient of volumetric absorption, α, than the fused silica used in Advanced LIGO. Additionally, this coefficient could not be so large that the Hello-Vinet assumption of constant optical flux along the optical axis was no longer valid; a concern that is addressed in Section 2.3.3.

2.3.2 Choice of material

Filter glasses typically have a well-defined absorption spectrum and are available with many different values of volumetric absorption @ 1064 nm.

Schott BG20 filter glass [30] was chosen because the volumetric absorption @ 1064 nm (0.33% per mm) was large enough to produce a thermal lens approximately 10% - 20% of the size expected in Advanced LIGO, but not so large as to completely negate the assumption in Hello-Vinet of uniform optical flux through the material, as discussed in Section 2.3.3. The thermal conductivity was not specified, but was expected to be in the range $0.9 - 1.05$

Property	Value
Diameter	65.0 mm
Average Height	29.1 mm
Heat capacity	727 J $kg^{-1}K^{-1}$ [31]
Density	2848 ± 0.5 kg m^{-3} (measured)
Thermal conductivity	0.9 – 1.05 W $m^{-1}K^{-1}$ @18°C [31]
Emissivity	0.9 [35]
Volumetric absorption	0.33% mm^{-1} (measured)

Table 2.1: Properties of the BG20 glass cylinder used for measuring absorption induced wavefront distortion

W $m^{-1}K^{-1}$ @ 18°C [31] because of its chemical composition (50-60% SiO_2, 11-20% Na_2O, 11-20% Pr:Nd, 1-10% B_2O_3, 1-10% BaO [32]). The thermo-optic coefficient, dn/dT, is typically in the range 1-6 $\times 10^{-6}$ [33] [34]. Accurate knowledge of this coefficient is not required, however, as the Hello-Vinet theory was tested using the temporal development of the shape of the thermal lens, as discussed in more detail in Section 2.4.1.

Two cylinders of BG20 glass were cut and polished. The first had a diameter-to-length ratio (65 mm : 20 mm) similar to that for an Advanced LIGO fused silica mass. The second was 9.1 mm thicker in order to absorb more power and produce a larger thermal lens. This latter cylinder is depicted in Figure 2.2 and its relevant properties are listed in Table 2.1. This cylinder was used as the glass test optic (GTO) in the wavefront distortion experiment.

2.3.3 Comparison of induced WD with H-V prediction

The H-V model assumes that the optical flux and beam-size are uniform along the optical axis. In reality, the intensity, I, at any point along the optical axis is given by

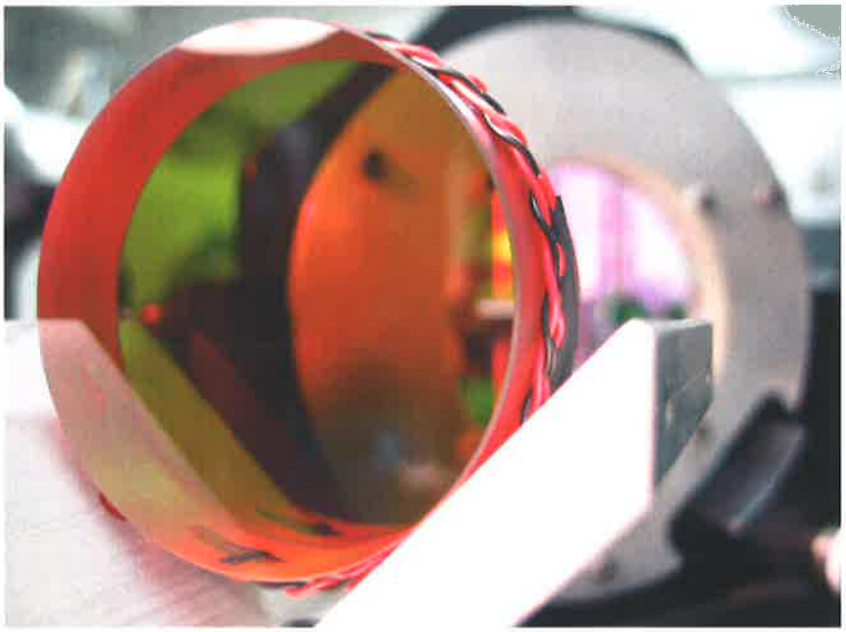

Figure 2.2: Schott BG20 filter glass cylinder. The absorption spectrum is such that the glass appears pink under natural or incandescent light and appears green under florescent light; hence the pink edges where the camera flash is illuminating the material and the green transmission in the upper left hand side. The twisted wire around barrel of the glass cylinder is attached to a temperature probe that was not used in the experiment described in this chapter.

$$\begin{aligned} I(z) &= I_{\text{inc}} \exp(-\alpha z) \\ &= I_{\text{inc}} \left(1 - \alpha z + \frac{(\alpha z)^2}{2} - \ldots\right) \\ &\approx I_{\text{inc}} \quad \text{for} \quad \alpha z << 1 \end{aligned}$$

where I_{inc} is the incident intensity. For Advanced LIGO, the assumption $\alpha z << 1$ is valid. For larger α, such as in this experiment, higher order terms are required to maintain accuracy in a Taylor-series expansion of the absorbed intensity, for example:

$$I_{\text{abs}}(z) \approx \alpha I_{\text{inc}} (1 - \alpha z).$$

The effect of this z dependence on the absorption-induced WD was modelled using a finite element simulation, a variant of the one described in Appendix B.3, and compared to the predictions of H-V. Two H-V scenarios were modelled using the parameters listed in Table 2.1. In the first simulation, the volumetric absorption was 0.33% mm^{-1}, the same as that in the BG20 glass. In the second simulation, the absorption was 1000× smaller than this. The incident power was adjusted in the second simulation such that the total absorbed power was the same as that in the first simulation. Note that the simulation code described in Appendix B.3 assumed constant flux throughout the glass, whereas the code for these simulations assumed an exponential decrease in the flux as it was absorbed by the glass. The code used for these simulations is identical in all other respects to the code in Appendix B.3.

The results from the finite-element model: the temperature distribution along the z-axis and the total WD are shown in Figure 2.3 a) and b), respectively. Also shown are the magnitude of the differences between the high-absorption and low-absorption scenarios. As expected, there is a slight variation in the temperature distribution with the high-absorption coefficient scenario being slightly warmer toward the input face (h = −14.5 mm). The

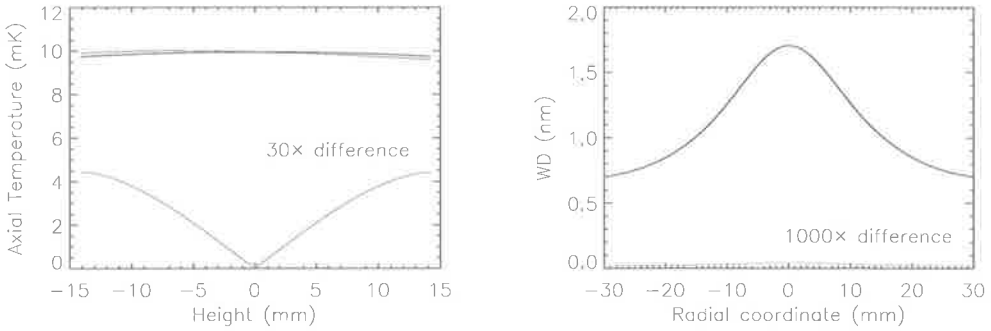

(a) Axial temperature (b) Radial WD

Figure 2.3: Predictions of the finite element model of absorption-induced WD: a) Temperature along cylindrical axis for low-absorption (blue curve) and high-absorption (red curve) coefficient scenarios. The green curve shows 30 × the difference between the two results. b) Radial WD ($dn/dT \times$ integrated temperature distribution) as a function of radius. The actual absorption curve (red) lies on top of the low absorption curve (blue). The green curve shows 1000 × the difference between the two.

difference in the overall WD is negligible. Hence the BG20 glass cylinder is appropriate for testing the H-V wavefront distortion equation.

2.4 Measurement and analysis of wavefront distortion in test optic

In this section, I start by describing the system used to produce the WD in the glass test optic (GTO), then I describe the measurement of the WD using a Mach-Zehnder interferometer and finally the analysis of the interference pattern.

2.4.1 Multiple heating beam sizes

The heating beam size is one of the easiest[1] parameters in the H-V solution to vary so as to change the size and shape of the expected wavefront distortion. As a result, the experiment was designed to be run with three different heating beam sizes and all other parameters kept constant to provide a more rigorous test of the Hello-Vinet solution. Additionally, this allowed one of the measurements to be used to calibrate the thermo-optic coefficient, since the absolute size of the wavefront distortion predicted by Hello-Vinet is directly proportional to the thermo-optic coefficient and this was not precisely known.

2.4.2 Experiment design

Figure 2.4 illustrates the experiment used to make an interferometric measurement of absorption induced WD in a cylindrical transmissive test mass. The 65.0 mm $\times$ 29.1 mm BG20 glass test optic was mounted on four small point contact sapphire balls to reduce conductive cooling and placed in a tent to reduce convective cooling so radiative cooling was the dominant heat loss mechanism.

A Mach-Zehnder (MZ) interferometer was created with a HeNe laser beam ($\lambda = 632.8$ nm) with the object and reference beams expanded to 75mm and 50mm by telescopes T2 and T3, respectively. The object and reference beams had intensity profiles I_{obj} and I_{ref}, respectively. The object beam was directed along the axis of the BG20 glass, demagnified by 4$\times$ by telescope T4 and then recombined with the reference beam by beamsplitter BS2. The interference pattern of the two beams at the exit plane of the glass test optic was imaged onto the CCD by lens L1 and a PC recorded the digital output from the CCD.

A mirror in the reference arm was tilted slightly, by an angle $\Delta\theta_x$, to introduce a carrier signal in the interference pattern, as required by the

[1]The easiest parameter to vary is the incident power, but the only effect of this is to scale the wavefront distortion without varying the shape.

Fourier analysis described in Section 2.4.4. The analytic expression for the central horizontal cross-section interference pattern between the two beams, $I_{int}(x)$, is thus given by

$$I_{int}(x) = I_{obj} + I_{ref} + 2\sqrt{I_{obj} I_{ref}} \cos\left[\frac{2\pi}{\lambda}(\psi(x) + \Delta\theta_x x)\right] \quad (2.1)$$

where $\psi(x)$ is the wavefront distortion introduced by the BG20 glass.

The laser beam from the Innolight 500 mW 1064 nm Mephisto NPRO [36] was passed through the PC-controlled shutter, S1, expanded by a telescope (T1) and directed along the axis of the BG20 glass cylinder. Immediately before the BG20 glass, the 1064 nm and 632.8 nm beams were combined by a dichoric beam splitter (DCBS) which reflected 1064 nm and transmitted 632.8 nm. After the BG20 glass, the 1064 nm beam was absorbed by an infra-red filter (IRF) that allowed visible light to pass through.

The telescope T1 was made using 150 mm and 50 mm lenses. The experiment was repeated three times, varying the configuration of T1 each time to change the heating beam size to test more rigourously the Hello-Vinet theory, as discussed in Section 2.4.1. The telescope configurations were varied:

1. 150 mm lens then 50 mm lens: heating beam $1/e^2$-radius $\approx$ 1.1 mm at the exit plane of the GTO.

2. No telescope: heating beam $1/e^2$-radius $\approx$ 5.8 mm at the exit plane of the GTO.

3. 50 mm lens then 150 mm lens: heating beam $1/e^2$-radius $\approx$ 10.6 mm at the exit plane of the GTO.

In the second configuration (no telescope), the heating beam propagated a distance of approximately 2.5 m from the NPRO to the GTO without passing through any intervening lenses. The waist size of the heating beam at the NPRO was approximately 150 μm. Hence, the beam was not completely collimated at the GTO because of the natural divergence of a Gaussian beam. However, the width varied by only 1-2% over the length of the glass test

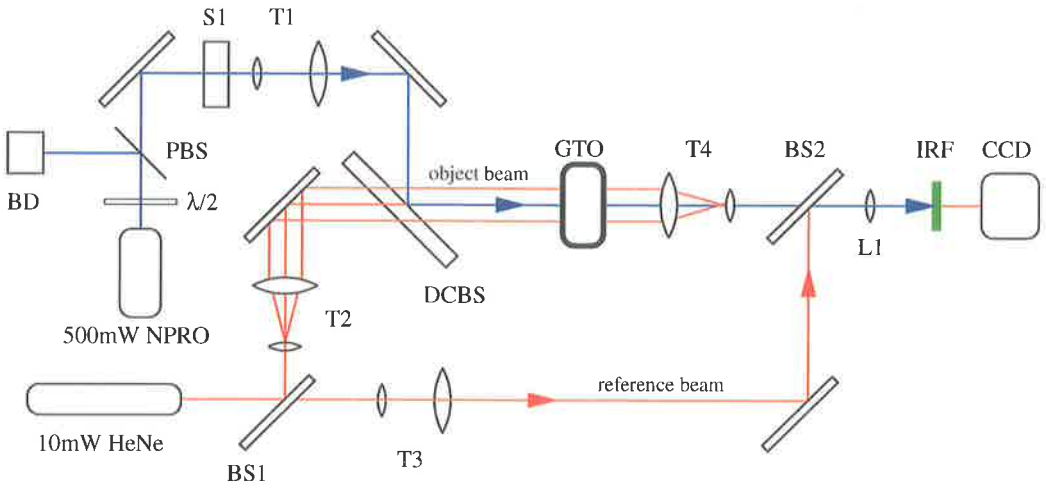

Figure 2.4: Schematic of experiment to measure thermal lensing in a cylindrical test optic. The output of a 500 mW 1064 nm laser is passed through a half-wave plate, $\lambda/2$, and a polarizing beam splitter (PBS) and is incident on a shutter S1. When the shutter is open, the beam passes through a telescope and is transmitted through the BG20 glass test optic (GTO). The remainder of the beam is absorbed by an IR filter, IRF, in front of the CCD. The output of a 10 mW HeNe laser is the input to a Mach-Zehnder interferometer, the object arm of which contains the BG20 optic. The object and reference arms are expanded by telescopes, T2 and T3, respectively. The object arm was demagnified by telescope T4 and recombined with the reference arm at the second beamsplitter, BS2. The interference pattern at the exit plane of the glass test optic was imaged onto the CCD with lens L1. A dichroic beam splitter, DCBS, immediately before the glass test optic was used to combine the two different wavelengths.

optic. This Gaussian divergence is also the reason that the beam size in configuration 2 was not 3× the beam size in configuration 1 and the beam size in configuration 3 was not 3× the beam size in configuration 2.

The flux of the 632.8 nm laser beam was at least 100× smaller than the 1064 nm laser beam in configuration 3 and over 10,000× smaller in configuration 1. Additionally, the absorption of the 632.8 nm light in the BG20 glass is of the same order of magnitude as the absorption of the 1064 nm light [30]. As such, the thermal lensing due to the absorption of the HeNe was not considered.

2.4.3 Measurement procedure

1. Adjust T1 and DCBS to direct an approximately collimated 1064 nm beam along the axis of the glass test optic. [1064nm ON, 632.8nm OFF].

2. Adjust $\lambda/2$ plate so that most of the 1064 nm is reflected from the polarising beam splitter (PBS) into the beam dump (BD). Remove IR filter (IRF) and open shutter. Record an image of the beam size. [1064nm Low Power, 632.8nm OFF].

3. Close shutter and adjust $\lambda/2$ plate so that all the power is transmitted through the PBS onto S1. [1064nm ON & Blocked, 632.8nm OFF].

4. Place an object of known size at the exit plane of the glass test optic. Measure the size of the image of the object on the CCD to determine the magnification. [1064nm Blocked, 632.8nm ON]. Remove the object of known size.

5. Start to record the interference patterns between the object and reference beams, $I_{\text{int}}(x, t_i)$, at times t_i, at a rate of 10Hz. At this stage i is designated as negative ($i < 0$) and these patterns are used to determine the rms background noise. [1064nm Blocked, 632.8nm ON].

6. Use the PC to open the shutter and allow the 1064 nm onto the glass test optic. This designates the time $t_0 = 0$ s of the zeroth interference pattern. [1064nm ON, 632.8nm ON].

7. Continue to record interference patterns ($i > 0$) on the CCD at a rate of 10Hz. The i^{th} pattern, recorded at time t_i, is designated $I_{\text{int}}(x, t_i)$. [1064nm ON, 632.8nm ON].

8. The last and M^{th} pattern, designated t_M, is the first one recorded after $t = 1000.0$ s. [1064nm ON, 632.8nm ON].

2.4.4 Analysis of MZ interference patterns

The following is a summary of phase profile extraction from the MZ interference patterns using Fourier transforms, described in detail by Malacara [37]. This discussion begins with the interference pattern at time t_i due to a wavefront distortion $\psi(x, t_i)$ with no tilt angle, $\Delta\theta_x$, between the object and reference beams:

$$\mathrm{I}_{\text{int}}(x, t_i) = \mathrm{I}_{\text{obj:}t_i} + \mathrm{I}_{\text{ref:}t_i} + 2\sqrt{\mathrm{I}_{\text{obj:}t_i}\,\mathrm{I}_{\text{ref:}t_i}}\,\cos\left[\frac{2\pi}{\lambda}\,\psi(x, t_i)\right] \tag{2.2}$$

where $\mathrm{I}_{\text{obj:}t_i}$ is the intensity profile of the object beam, $\mathrm{I}_{\text{obj:}t_i}$ is the intensity profile of the reference beam and $\psi(x, t_i)$ is the absorption-induced wavefront distortion to be extracted. Equation 2.2, can be rearranged as a sum of complex exponential terms

$$I_{\text{int}}(x, t_i) = g(x, t_i) + h_\psi(x, t_i) + h_\psi^*(x, t_i) \tag{2.3}$$

where

$$g(x, t_i) = \mathrm{I}_{\text{obj:}t_i} + \mathrm{I}_{\text{ref:}t_i} \tag{2.4}$$

is the background intensity in the interference pattern and

$$h_\psi(x,\, t_i) = \sqrt{\mathrm{I}_{\mathrm{obj}:t_i}\, \mathrm{I}_{\mathrm{ref}:t_i}}\, \exp\left[\mathrm{i}\, \frac{2\,\pi}{\lambda}\, \psi(x,\, t_i)\right] \tag{2.5}$$

is the complex form of the fringes in the interference pattern induced by the wavefront distortion in the object arm of the interferometer.

The Fourier transform, $S(f_x,\, t_i)$, of the interference pattern is thus

$$\begin{aligned} S(f_x,\, t_i) &= \int_{-\infty}^{+\infty} I_{\mathrm{int}}(x,\, t_i)\; e^{i\, f_x\, x}\, \mathrm{d}x \\ &= G(f_x,\, t_i) + H_\psi(f_x,\, t_i) + H_\psi^*(f_x,\, t_i) \end{aligned} \tag{2.6}$$

where $G(f_x,\, t_i)$, $H_\psi(f_x,\, t_i)$ and $H_\psi^*(f_x,\, t_i)$ are the Fourier transforms of $g(x,\, t_i)$, $h_\psi(x,\, t_i)$ and $h_\psi^*(x,\, t_i)$, respectively. For the discrete intensity data from the CCD, this is done using a discrete FFT. In IDL, the code is:

```
Fw = FFT(Iint)
```

The spectral components, $H_\psi(f_x,\, t_i)$, of the intensity-encoded phase information in $h_\psi(x,\, t_i)$ and the spectral components of the background intensity distribution, $g(x,\, t_i)$, are both centered around $f_x = 0$ and are therefore indistinguishable. Separation of these signals into two distinct peaks in frequency space is achieved by frequency shifting one signal with respect to the other.

To achieve such a frequency shift, a linear carrier signal, $2\pi\ (f_{\Delta\theta_x}\, x)$, where $f_{\Delta\theta_x} = \Delta\theta_x/\lambda$, is applied to the interference pattern by tilting a mirror in the reference arm so that the angle between object and reference beams becomes $\Delta\theta_x$. The complex representation of the fringes becomes

$$\begin{aligned} h_c(x,\, t_i) &= \sqrt{\mathrm{I}_{\mathrm{obj}:t_i}\, \mathrm{I}_{\mathrm{ref}:t_i}}\, \exp\left[\mathrm{i}\, \frac{2\,\pi}{\lambda}\ (\psi(x,\, t_i) + \Delta\theta_x\, x)\right] \\ &= h_\psi(x,\, t_i)\, \exp\left[i\, 2\pi\, f_{\Delta\theta_x}\, x\right] \end{aligned}$$

and the interference pattern becomes

$$\begin{aligned} I_{\text{int}}(x,\, t_i) &= g(x,\, t_i) + h_c(x,\, t_i) + h_c^*(x,\, t_i) \\ &= g(x,\, t_i) + h_\psi(x,\, t_i) \exp\left[i\, 2\pi\, f_{\Delta\theta_x}\, x\right] + h_\psi^*(x,\, t_i) \exp\left[-i\, 2\pi\, f_{\Delta\theta_x}\, x\right]. \end{aligned}$$

An example of such an interference pattern measured by the interferometer is shown in Figure 2.5 a).

The Fourier transform, $H_c(f_x,\, t_i)$, of $h_c(x,\, t_i)$ can be determined using the Fourier transform of the Dirac delta function

$$g(x) = \exp\left[-i\, 2\pi\, f_0\, x\right] \quad \Rightarrow \quad G(f) = \delta(f - f_0)$$

and the Convolution Theorem

$$\begin{aligned} \mathrm{F}\left\{g(x)\, h(x)\right\} &= G(f) * H(f) \\ &= \int_{-\infty}^{+\infty} G(\alpha) \times H(f - \alpha)\, \mathrm{d}\alpha, \end{aligned}$$

where $\mathrm{F}\left\{g(x)\, h(x)\right\}$ denotes the Fourier transform of $g(x) \times h(x)$, giving

$$H_c(f_x,\, t_i) = H_\psi(f_x - f_{\Delta\theta_x},\, t_i) \tag{2.7}$$

and the Fourier transform of the interference pattern becomes

$$S_c(f_x,\, t_i) = G(f_x,\, t_i) + H_\psi(f_x - f_{\Delta\theta_x},\, t_i) + H_\psi(f_x + f_{\Delta\theta_x},\, t_i).$$

The spectral components, $H_\psi(f_x,\, t_i)$, of the intensity-encoded phase information in $h_\psi(x,\, t_i)$ are thus centered around $f_{\Delta\theta_x}$, as illustrated by the amplitude spectrum in Figure 2.5 b). The spectral components of the phase information, the two lobes at $\pm f_{\Delta\theta_x}$, are now clearly separated from the spectral components of the background intensity, $G(f_x,\, t_i)$, centered around zero.

A band-pass filter, illustrated in Figure 2.6 a), is applied to one of the offset lobes to select the interference fringes and remove high spatial frequency

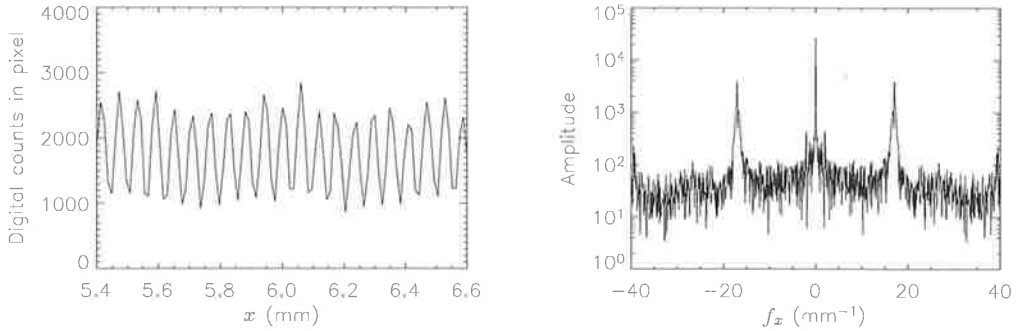

(a) Interference pattern cross-section

(b) FFT of interference pattern

Figure 2.5: Demonstration of phase extraction from interference pattern a) Original interference pattern, b) FFT of interference pattern.

noise. That lobe is then demodulated to zero frequency by $f_{\Delta\theta_x}$ as illustrated in Figure 2.6 b). The minimum width of the band-pass filter was determined by applying this analysis to the H-V model with the BG20 parameters and a heating beam width of 1.1 mm. The result of filtering the H-V signal with too narrow a bandwidth is a smoothing of the WD and the loss of high-frequency information and is illustrated in Figure 2.7 a). Shown in Figure 2.7 b) is the result of filtering the H-V with the bandwidth used in this experiment: there is virtually no smoothing of the signal.

The filtering and demodulation of the discrete data, using a full bandwidth of 70 spatial frequency units[2] as in Figure 2.7 b), was done in IDL using the following code:

```
bandwidth = 35.0
filter = exp(-2 * ((freq - fxc)/bandwidth)^8 )
Fw_filt = filter * Fw
Fw_demod = SHIFT(Fw_filt, fxc)
```

where `freq` is an array of indices corresponding to the spatial frequencies and

[2]If the interference pattern is sampled at N points with an interval of Δx, then the spatial frequency unit of the complex values returned by the FFT is $1/(N\,\Delta x)$. In this case, $N = 1024$ and $\Delta x = 12\,\mu$m is the width of one pixel and hence the sampling frequency unit is 0.0814 mm^{-1}.

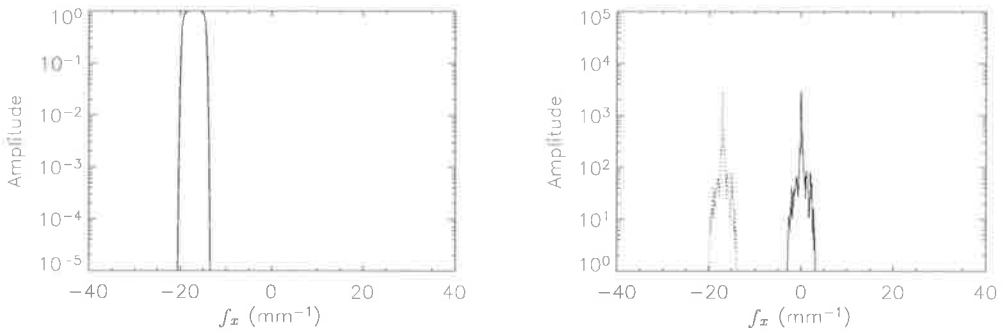

(a) Super-Gaussian bandpass filter (b) Demodulation of carrier signal

Figure 2.6: a) Super-Gaussian bandpass filter, b) Demodulation of filtered carrier signal in frequency space. The dashed curve is the original signal and the solid curve is the demodulated signal.

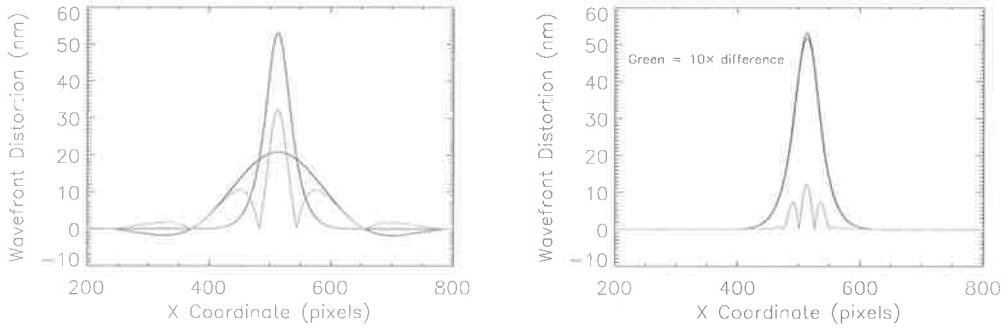

(a) Fullwidth of filter = 10 frequency units (b) Fullwidth of filter = 70 frequency units

Figure 2.7: a) Image filtering of sharpestH-V signal with bandwidth of 10 spatial frequency unit. b) Image filtering with bandwidth of 70 spatial frequency units. Original signal (red), filtered signal (blue) and a) magnitude of the difference (green) and b) 10× the magnitude of the difference (green). 1 spatial frequency unit = $1/(1024 \times 1 \text{ pixel}) = 0.0814 \text{ mm}^{-1}$.

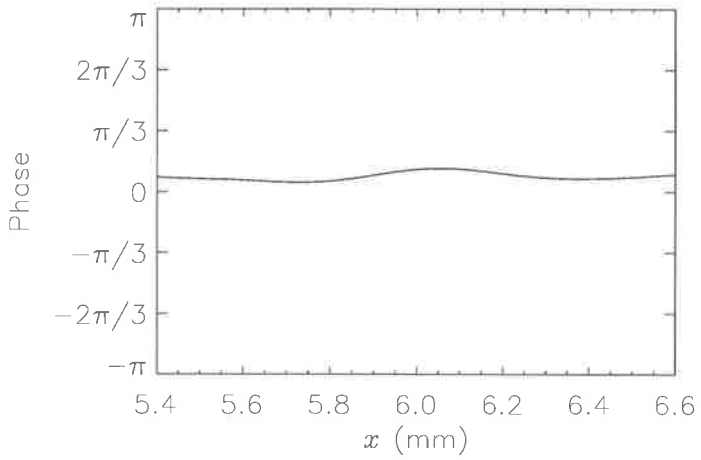

Figure 2.8: The reconstructed and filtered phase profile is given by the arctangent of the inverse FFT yields of the demodulated and filtered carrier signal.

`fxc` is the index of one of the offset lobes. The function `SHIFT(x, n)` moves all the values along in the array `x` by `n` units, which is the digital equivalent of demodulation. Note that the filter is a super-Gaussian, $\exp\left[-\left(f_x/\Delta f_x\right)^8\right]$.

After the filtering and demodulation, the inverse Fourier transform is applied using

```
hWD_filt = FFT(Fw_demod, /INVERSE)
```

to yield $h_{\mathrm{WD,\,filt}}(x)$. The phase profile is extracted by taking the arctangent

$$\frac{2\pi}{\lambda}\psi(x) = \arctan\left\{\frac{\mathrm{Im}\left(h_{\mathrm{WD,\,filt}}(x)\right)}{\mathrm{Re}\left(h_{\mathrm{WD,\,filt}}(x)\right)}\right\}$$

an example of which is illustrated in figure 2.8 a). The range of the arctangent function is $\{-\pi, +\pi\}$ and hence the return value $\frac{2\pi}{\lambda}\psi(x)$ is "wrapped" between these values. Unwrapping and extracting $\psi(x)$ is a straightforward process that is not described here.

The wavefront distortion in the i^{th} pattern, at time t_i, relative to the zeroth pattern, at time $t_0 = 0$ s, $\mathrm{WD}_{t_i}(x)$, is given by

$$\mathrm{WD}_{t_i}(x) = \psi_{t_i}(x) - \psi_{t_0}(x) \tag{2.8}$$

Once the wavefront distortion was found the residual tilt/prism in the x and y directions was removed.

2.5 Results

2.5.1 Background noise

The rms background noise was determined by measuring the temporal fluctuations in the interference patterns before the shutter was opened, $I_{\mathrm{int}}(x, t_i)$ with $i < 0$ in Step 5, using the Fourier analysis described above and was approximately $\lambda/150$ for $\lambda = 632.8$ nm.

2.5.2 Temporal development of measured wavefront distortion

The measured wavefront distortion profiles at times $t = 2.5$ s, 8.5 s, 29.2 s and 100.0 s and for beam sizes $\omega = 1.1$, 5.8 and 10.6 mm are plotted in Figures 2.9 and 2.10. The quasi-steady state at $t = 100.0$ s, in Figure 2.10 b), shows good agreement with the H-V predicted profile for which a thermal conductivity of 0.98 W m^{-1} K^{-1} was used. The measured profiles at the remaining times appear to have the same shape as the predicted profiles within the region of the heating beam albeit with marginally reduced magnitudes.

To illustrate the diffusion of heat through the material, the optical path difference between the center and $x = \pm \mathrm{GTO}_{\mathrm{diameter}}/4 = 16.25$ mm for the measurements and the Hello-Vinet prediction is shown in Figure 2.11 a). The temporal evolution of the OPD for $\omega = 1.1$ mm was used to determine the best-fit value of thermal conductivity, giving 0.98 W m^{-1} K^{-1}. As it has been used to fit a parameter, the red plot in Figure 2.11 a) cannot be used to validate the model. The data for the $w = 5.8$ mm and 10.6 mm agree

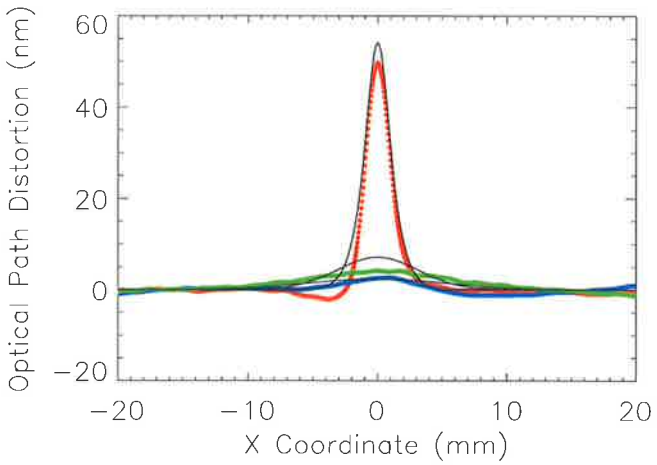

(a) $t_1 = 2.5$ s

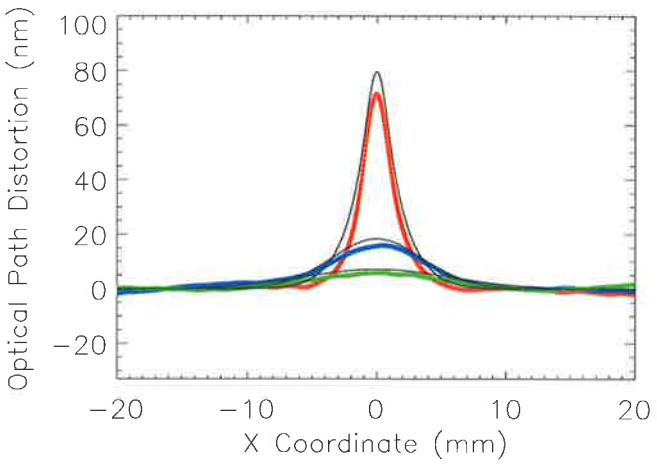

(b) $t_2 = 8.5$ s

Figure 2.9: The wavefront distortion measured by the interferometer when the test mass was heated with a laser beam of three different beam sizes: $w = 1.1$ mm (red), $w = 5.8$ mm (blue), $w = 10.6$ mm (green). The results were recorded at time t_1 from when the shutter was opened, where a) $t_1 = 2.5$ s, b) $t_1 = 8.5$ s. Note the different vertical scales on the figures. The black lines show the prediction of H-V for each beam size.

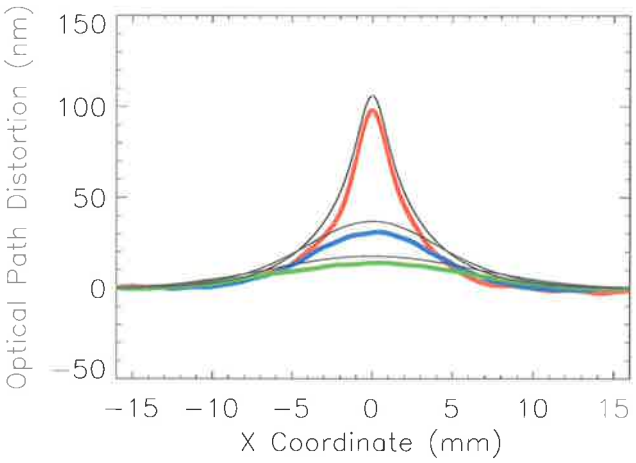

(a) $t_1 = 29.2$ s

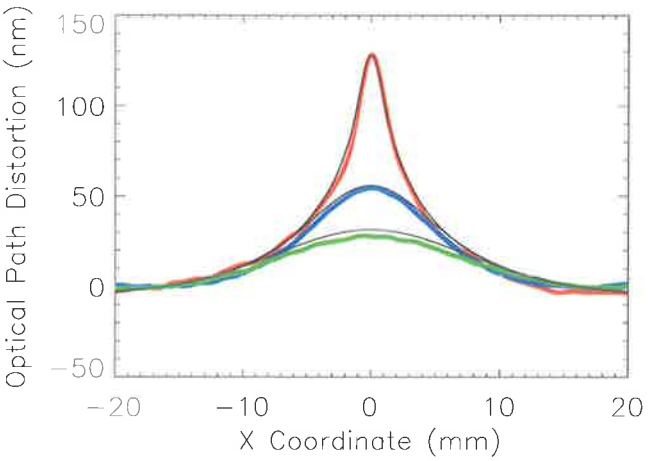

(b) $t_2 = 100.0$ s

Figure 2.10: The wavefront distortion measured by the interferometer when the test mass was heated with a laser beam of three different beam sizes: $w = 1.1$ mm (red), $w = 5.8$ mm (blue), $w = 10.6$ mm (green). The results were recorded at time t_1 from when the shutter was opened, where a) $t_1 = 29.2$ s, b) $t_1 = 100.0$ s. Note the varying scales on the figures. The black lines show the prediction of H-V for each beam size.

reasonably well with the H-V prediction.

To illustrate the development of a thermal lens, the average defocus across a beam width (calculated from the measured WD) and the H-V prediction of the development of the defocus is plotted in Figure 2.11 b). There is good agreement between the temporal development of the measured and predicted thermal lenses for beam sizes $\omega = 1.1$ mm and 5.8 mm and reasonable agreement for the very weak thermal lens when $\omega = 10.6$ mm.

These measurements show good agreement with the predictions of Hello and Vinet for longer times, however, there are small systematic differences between the predictions and the measurements. These discrepancies are most obvious in the central sections of the wavefront distortion profiles in Figures 2.9 a) and b) and Figures 2.10 a) and also in the blue curve in Figure 2.11 a) and, to a lesser extent, the green curve in Figure 2.11 b). It appears from Figures 2.9 and 2.10 that there is less thermal lensing than expected at earlier times. It is unlikely that this was due to less laser power/heating at earlier times as the intensity of the NPRO was observed to be very stable with time. A possible explanation is that, given the test optic is in a tent to minimize air currents and not a vacuum to eliminate them, there is a small amount of convective cooling of the glass test optic - a cooling mechanism not included in the Hello-Vinet model.

2.6 Conclusion

This chapter has described an interferometric measurement, with a precision of $\lambda/150$ for $\lambda = 632.8$ nm, to validate the formula of Hello and Vinet. A completely independent evaluation proved to be difficult because the value of thermal conductivity of the test material was not known well enough and had to be determined from one of the measurements. The remaining measurements show good agreement with the predictions of Hello and Vinet. It is possible that the small deviations from the predicted results are due to convective cooling of the glass test optic.

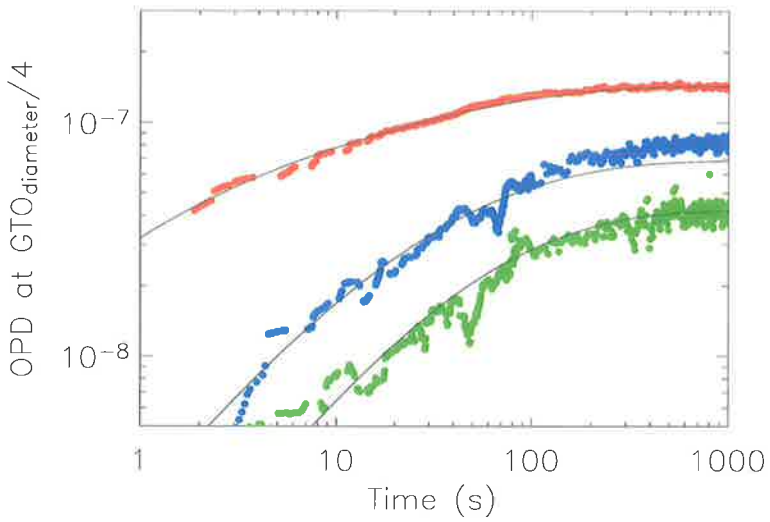

(a) OPD at w_i

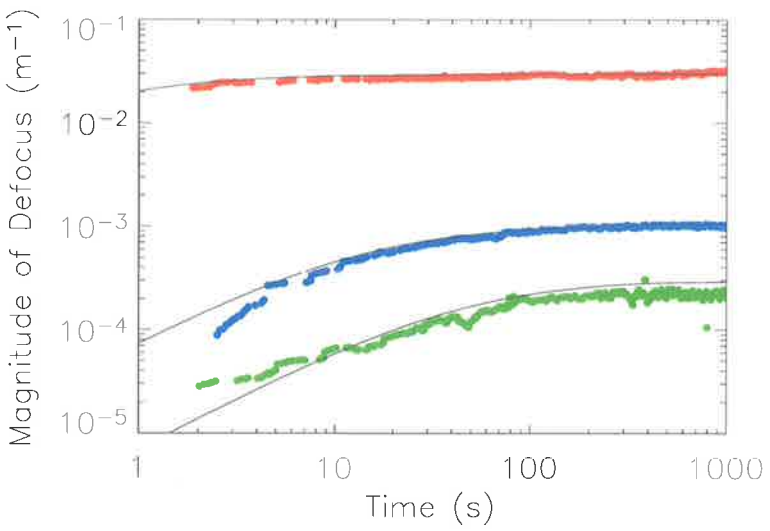

(b) Defocus at w_i

Figure 2.11: a) The optical path difference between $x = 0$ and $x =$ diameter/4 measured by the interferometer and the predicted result from Hello-Vinet and b) the average defocus across the heating beam width and the predicted result from Hello-Vinet. In both plots the three different beam sizes are $w = 1.1$ mm (red), $w = 5.8$ mm (blue), $w = 10.6$ mm (green) and the H-V predictions are the corresponding black curves.

The validation of the H-V model presented in this chapter increases the confidence in the validity of numerical models of GWI, such as MELODY [16], that employ the Hello-Vinet model, within the limitation of the systematic error discussed. A more strenuous validation of the Hello-Vinet theory would be possible with a stronger laser source, which would allow one to use a more precisely characterized test optic, and construction of the experiment in a vacuum chamber to eliminate convective cooling. Additionally, one could use a Hartmann wavefront sensor, the construction and development of which is described in the following chapter.

Chapter 3

Hartmann wavefront sensor - development

3.1 Introduction

The Hartmann Wavefront Sensor (HWS) was first used in 1900 [38] as a way to measure aberrations in spherical mirrors and has since then been applied to many more general wavefront sensing applications. Its popularity has dramatically increased in recent years due to the incorporation into its design of cheap and fast solid-state arrays [39]. This chapter discusses the operation of the HWS and describes its development for measuring thermal lensing in advanced Gravitational Wave Interferometers.

Section 3.2 begins by describing several applications of Hartmann-type sensors to familiarise the reader with the scenarios in which they can be used. The basic physics and operation of a HWS are described in Section 3.2.2 and potential configurations of a HWS in an experiment are discussed in Section 3.2.3. With the basic physics and operation covered, variants of the standard Hartmann theme are described in Section 3.2.4, including the popular Shack-Hartmann sensor. The suitability of these variants for measuring thermal lensing in GWIs is contrasted with the traditional HWS. Lastly, a short description of potential temperature induced limitations is

described in Section 3.2.5.

The development of the HWS for an advanced GWI is described in Section 3.3. The design of the hardware components (the light source, the Hartmann plate and the CCD) and the noise sources associated with these components are described in Sections 3.3.1 to 3.3.3. The software components (the centroiding and wavefront reconstruction algorithms) and the errors associated with these components are described in Sections 3.3.4 and 3.3.5. Finally, the total accumulated noise and error in the sensor are discussed in Section 3.3.6.

3.2 Hartmann sensor basics

3.2.1 Applications of the Hartmann sensor

The original purpose of the Hartmann sensor was to characterise aberrations in curved mirrors as illustrated in Figure 3.1 (reproduced from Ghozeil [40]). In this figure, a light source illuminates a plate containing a series of apertures, the Hartmann plate (HP), that is directly in front of a test optic (in this case, a mirror). The rays from the apertures are reflected from the mirror and are incident on a photographic plate forming a pattern of spots. The displacements of the spots, from the positions expected for an ideal optic, reveal the aberrations in the mirror. This process of characterizing reflective or transmissive optics with a HWS has been used since 1904 [41] [42] [43] [44] [45] [26] [46] [47]. Note that the light from the source that reflects off the mirror is often referred to as a "probe beam", a label that is used often in the latter parts of this chapter.

Of the myriad of other applications of Hartmann-type sensors, a particularly salient one for this thesis is the measurement of thermal lensing in optics. It is interesting to note that one might consider this application to be quite old; Plaskett employed a Hartmann sensor in 1920 to determine the change in the optics of a 72-inch mirror due to temperature [48]. More recently, Mansell *et al.* [27] measured the effect on laser beam quality with a Shack-Hartmann wavefront sensor with a reproducibility of $\lambda/100$ @ 633

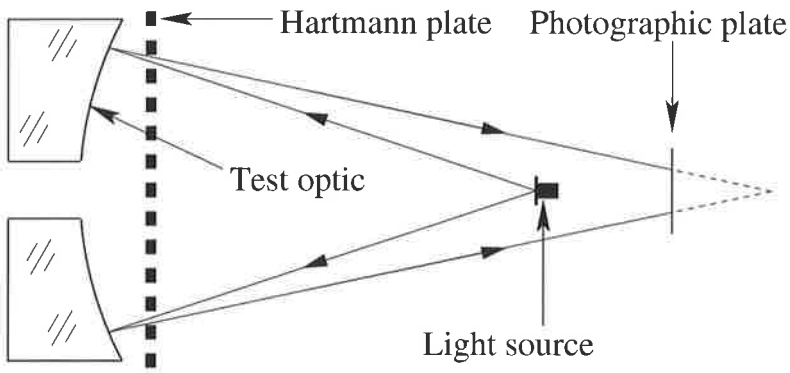

Figure 3.1: The original Hartmann test. A light source illuminates a Hartmann plate that is directly in front of a test optic. The resulting rays are reflected onto the photographic plate, forming a pattern of spots. Aberrations in the spot pattern reveal the aberrations in the test optic. Reproduced from Ghozeil [40]

nm. Also, Lawrence *et al.* [17] described a measurement of a radiative thermal corrector designed to compensate thermal lensing induced in an optic by absorption of a Gaussian beam. Lawrence *et al.* used a Wavefront Sciences CLAS-2D Shack-Hartmann sensor with a sensitivity of approximately $\lambda/100$ @ 633 nm [25]. While these examples illustrate the application of Hartmann sensor technology to thermal lensing problems, the sensors that were used do not meet the sensitivity requirement for use in Advanced LIGO (better than $\lambda/470$ @ 633nm) established in Section 1.3.2.

Hartmann type sensors have also been used in:

- Adaptive optic systems in large ground-based optical telescopes [49] [50] [51] [52]. Light from stars and other stellar bodies accumulates phase aberrations upon passage through atmospheric turbulence. The resolution of telescopes viewing this light has been improved by measuring the aberrations using Shack-Hartmann sensors and actuating upon the telescopes' optics to compensate for the effects.

- Ophthamology. Modified Hartmann tests have reflected rays off an aberrated cornea have been used to measure its topography [53] [54].

- The characterization of laser-beam parameters, such as M^2, divergence and beam widths [55] [56].

- The automatic alignment of a synchrotron beamline using a Hartmann sensor (operating at 0.414 nm) has been demonstrated at the SOLEIL synchrotron in France [57].

- The triangulation of a point-like source [58].

3.2.2 Overview of Hartmann sensor

Stated simply, a Hartmann sensor measures the change in the gradient of a wavefront relative to a reference wavefront. The gradient change is numerically integrated to give the wavefront change. The following description of the operation of a Hartmann sensor is a summary of the original Hartmann papers [38] [59] and the work by Ghozeil [40].

A Hartmann sensor consisting of an opaque plate containing an array of apertures and an intensity recording medium is shown in Figure 3.2. Originally, the recording medium was a photographic plate, but it is now almost exclusively a solid-state photo-sensitive array. The basic operation of a Hartmann sensor can be described succinctly by:

1. The wavefront, W′, or wavefront change, $\Delta W = W' - W$, to be measured is incident on the Hartmann plate (HP) which divides it into a set of rays, known as *Hartmann rays.*

   In a traditional Hartmann sensor the apertures are simply holes in a screen from which the rays diffract. There are a variety of commonly used arrangements of apertures: radial patterns [60], square arrays, or hexagonally closed-packed arrays. The process of optimizing the apertures in the Hartmann plate for measuring thermally-induced wavefront distortion in GWIs is discussed in Section 3.3.2.

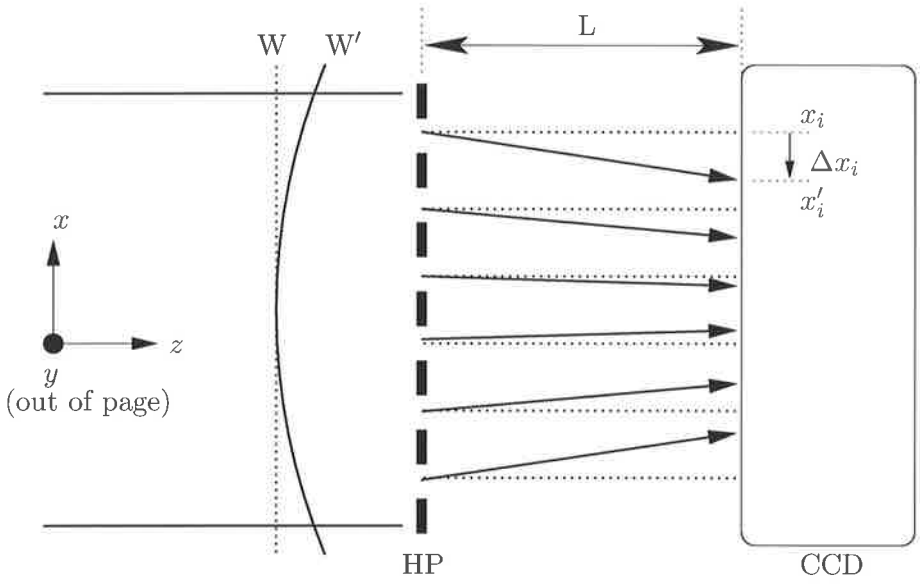

Figure 3.2: An aberrated wavefront W′ is incident on a Hartmann plate (HP). The resulting rays propagate a distance L, normal to the wavefront, and are incident on a CCD. The spot position, x_i', is determined by the centroid of that spot's intensity profile. The reference spot positions, x_i, (either measured using a non-aberrated wavefront, W or calculated using the hole positions in the HP) are indicated by the intersection of the dotted lines and the CCD. The gradient of the wavefront at the i^{th} aperture is given by the displacement, Δx_i, from the reference position divided by L.

2. The rays propagate a known distance L, normal to the wavefront, and are incident on the CCD.

   The process of optimization of L is also discussed in Section 3.3.2. The lever arm needs to be accurately known in order to prevent systematic errors in the gradient of the wavefront change. Fortunately, it can be calibrated by measuring an accurately known gradient as demonstrated in Section 4.2.

3. The pattern of spots on the CCD is recorded as a digital image.

   An example image of a recorded pattern of spots is shown in Figure 3.3. The operation of the CCD, the digitization and the noise are discussed in Section 3.3.3.

4. The position of the i^{th} spot, x_i', is determined by a centroiding algorithm.

   The optimization of centroiding algorithms is discussed in Section 3.3.4.

5. The displacement of each spot, Δx_i, from a previously measured reference position, x_i, for wavefront W is calculated.

6. The gradient of the wavefront change is calculated using

$$\frac{\partial \Delta \mathrm{W}}{\partial x} = \frac{\Delta x_i}{L}$$

   The angle between the i^{th} Hartmann ray and its reference ray is equal to the displacement, Δx_i divided by the lever arm, L. Rayces [61] showed that this angle is approximately proportional to the gradient of the wavefront aberration. Figure 3.4 shows an aberrated wave-front PC and a spherical reference wavefront SC of radius R centered at Q. The wave-

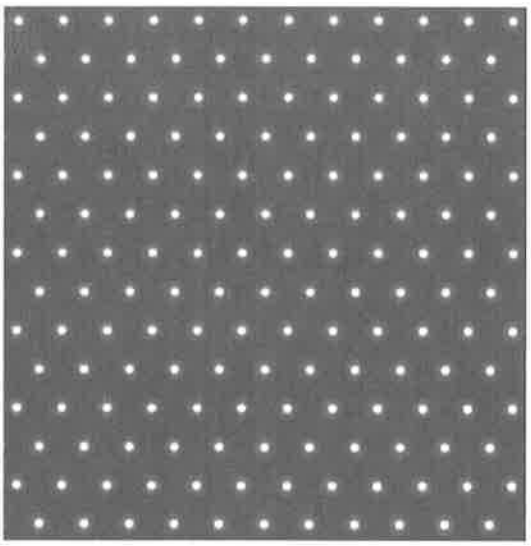

(a) Hartmann spots on a CCD

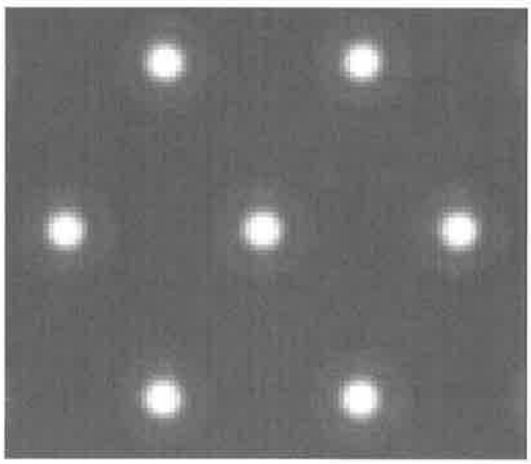

(b) Hartmann spots - closer view

Figure 3.3: a) An example of a Hartamnn spot pattern and b) a closer view of some of the spots.

front change (aberration), ΔW, is defined as the distance PS. Rayces determined the following relation:

$$\frac{\partial \Delta \mathrm{W}}{\partial x} = -\frac{|QT|}{|QS| - \Delta \mathrm{W}} \tag{3.1}$$

which can be simplified to

$$\frac{\partial \Delta \mathrm{W}}{\partial x} \approx -\frac{\Delta x}{\mathrm{L}} \tag{3.2}$$

if one assumes $\mathrm{L} \ll \mathrm{R}$ and $\Delta \mathrm{W} \ll \mathrm{L}$. For absorption-induced wavefront distortion in GWIs, $\Delta \mathrm{W} \approx 10^{-7}$ m, $\mathrm{L} \approx 10^{-2}$ m and the reference wavefront is approximately flat ($\mathrm{R} \approx \infty$). That is, these assumptions and thus Equation 3.2 are valid.

7. The wavefront change, ΔW, is calculated by integrating the discrete gradient field.

   The techniques used to integrate the field and the propagtion of errors in the integration are based largely on the work of Southwell [62] and are discussed in Section 3.3.5.

3.2.2.1 Absolute or differential operation

In a conventional HWS, an absolute measurement of that wavefront can be made by comparing the measured spot positions with the reference spot positions (Step 5) which are determined using the positions of the holes in the Hartmann plate, typically known with an accuracy of $\pm 1 \mu$m. Alternatively, the positions of those holes could be calibrated by illuminating the HWS with a flat wavefront and measuring the spot centroids on the CCD - except that the flatness of this wavefront must be verified with another method. The

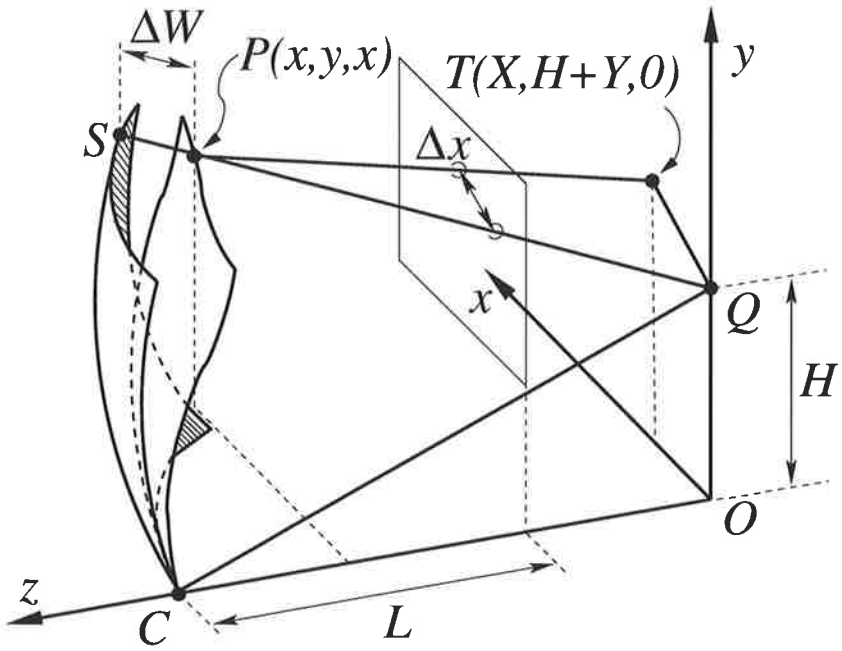

Figure 3.4: Reference sphere SC and wave-front PC (propagating to the right), QS = QC = R, PS = ΔW. Reproduced and revised version of the figure from Rayces [61].

uncertainty of the absolute positions of the reference spots therefore limits the accuracy of the HWS when used in the conventional absolute measurement.

For absorption-induced wavefront distortion in GWI, however, one is interested only in the differential wavefront change, ΔW, from an undistorted wavefront. The reference spots produced by the undistorted wavefront at an earlier time are measured accurately by the sensor. This removes a potential systematic error and allows much greater accuracy. All of the HWS measurements within this thesis are differential.

3.2.3 Hartmann plate - CCD configurations

When measuring the wavefront change in a large diameter beam, some demagnification of the beam is necessary to fit the region of interest onto the CCD of the HWS. For example, the wavefront sensor in Advanced LIGO must probe a 224 mm diameter region (see Section 1.3.2). In order to fit this onto a 12 mm $\times$ 12 mm CCD it must be demagnified by a factor of 18.7. Similarly, the beam probing the distortion in the 65 mm diameter BG20 glass test optic described in Section 2.3.2 must be demagnified by a factor of 5.4. To facilitate this, the Hartmann plate, CCD and demagnifying optics can be configured in several ways, as shown in Figure 3.5.

In Configuration A, a Hartmann plate is placed at the plane HP_O immediately after the test optic and before the telescope. The rays from the Hartmann sensor propagate through the telescope, which demagnifies them by M, and then are incident on the CCD. The effective lever arm of the Hartmann sensor, L_1, is the distance between the Hartmann plate and the conjugate plane of the CCD, CCD_I.

In Configuration B, a different Hartmann plate is placed at the plane HP_I, the conjugate plane of HP_O. The wavefront from the test optic propagates through the telescope and is incident on the Hartmann plate.

Configurations A and B are equivalent if the Hartmann plate in B is a demagnified version of the plate in A and $\mathrm{L}_2 = \mathrm{L}_1/M^2$. Thus, if the test optic introduces the primary aberration defocus, S, for example, given by

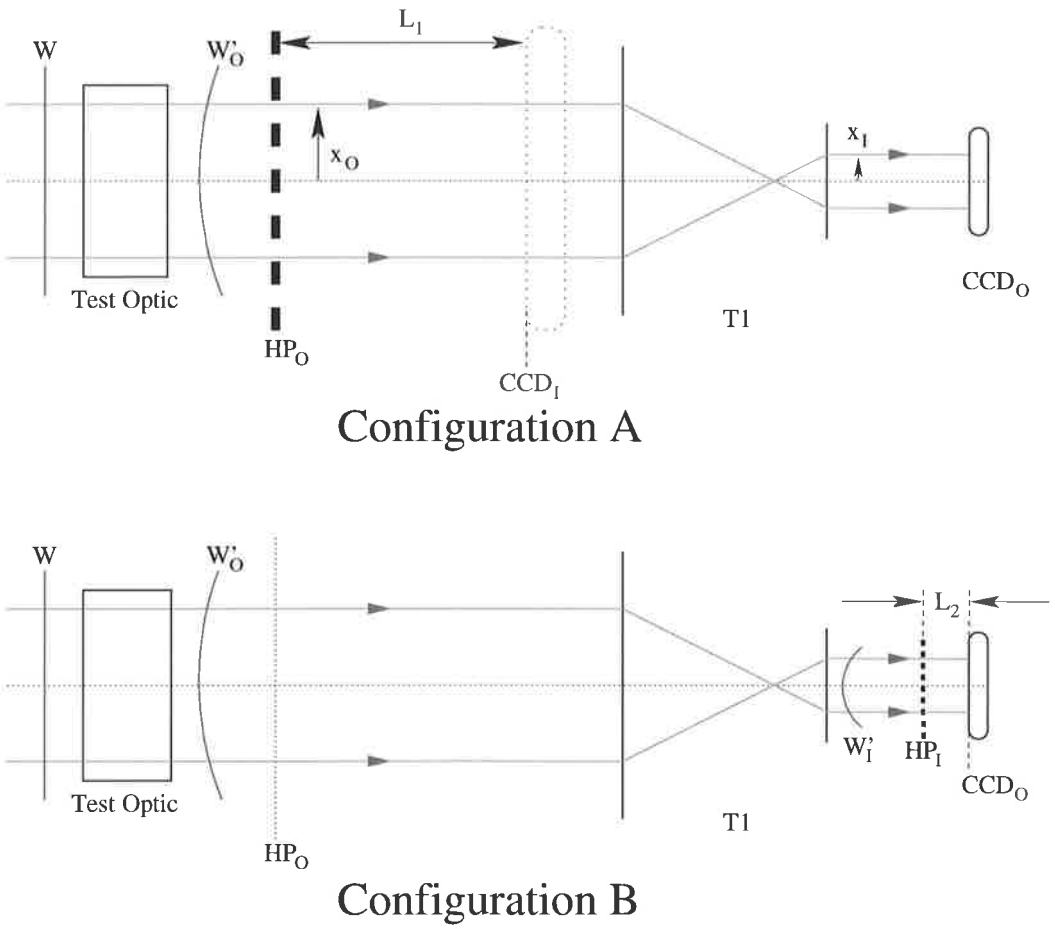

Figure 3.5: Two configurations of the Hartmann sensor. Configuration A: the Hartmann plate is placed at HP_O immediately after a test optic that changes the wavefront from W to W′. The beam propagates through a telescope, which demagnifies it by M onto a CCD. The effective lever arm of the Hartmann sensor, L_1, is the distance between the Hartmann plate and the conjugate plane of the CCD, CCD_I. Configuration B: the beam propagates through the test optic and telescope and is incident on the Hartmann plate at HP_I, the conjugate plane of HP_O, where the lever arm is $L_2 = L_1/M^2$.

$$\mathrm{W} = \frac{\mathrm{S}}{2} x^2$$

then the size of the aberration, S, at HP_I is M^2 times that at HP_O. In other words, if the test optic introduces a wavefront change with a radius of curvature R_O then the Hartmann sensor will measure a wavefront change with a radius of curvature $R_I = R_O/M^2$. This is important in the analysis of a thermal lens in a high optical power cavity and its effect on the cavity mode, discussed in Chapter 5.

3.2.4 Variants of the traditional Hartmann sensor

3.2.4.1 Shack-Hartmann

In the S-H sensor, the holes in the HP were replaced by a lenslet array by Shack [63]. Such a lenslet array is illustrated in Figure 3.6. A Shack-Hartmann sensor operates in largely the same way as a standard Hartmann sensor, except that the wavefront propagating through the lenslets are focussed onto the CCD rather than diffracting from the aperture. This results in spots that are smaller than those from apertures of the same diameter in a Hartmann sensor. The advantages and disadvantages of the Shack-Hartmann sensor are described below and summarised in Table 3.2.4.1.

- Flexibility: the lever arm distance between the array and the CCD may be varied easily in the Hartmann sensor, whereas in a Shack-Hartmann sensor it is approximately equal to the focal length of the lenslets [64].
- Light collection: The Shack-Hartmann array has a higher transmission per unit area and also concentrates the light onto the CCD, which is an advantage in astronomical adaptive optics applications when there are only a limited number of photons available [65].
- Spatial resolution: The spots in the Hartmann and Shack-Hartmann sensors need to be separated from one another to prevent cross-talk

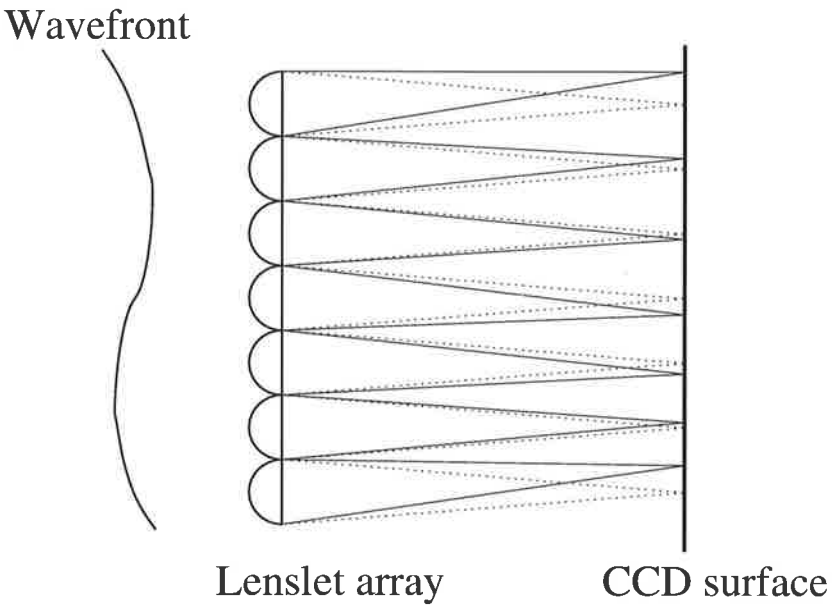

Figure 3.6: A distorted wavefront incident on a Shack-Hartmann lenslet array. The light through the each lenslet is focussed to a position on the CCD determined by the average gradient of the wavefront over the lenslet. The dotted lines show the reference positions of the spots when the incident wavefront is flat.

and the subsequent reduction in sensitivity. The area on the CCD occupied by a spot in a Hartmann sensor is larger than the area occupied by a spot in a Shack-Hartmann sensor (assuming the Hartmann aperture and Shack-Hartmann lenslet diameters are equal). Therefore the lenslets in a Shack-Hartmann sensor can be packed closer togther than in a Hartamnn sensor and achieve a higher spatial resolution.

- Both are susceptible to the misalignments between the array and the detector identified by Pfund *et al.* [66]. Of the misalignments identified (translation of the array in the x or y directions, translation of the array along the z axis, rotation of the array about the z axis and rotation of the array about the x and y axes) only rotation about the x and y axes poses any problems for a differential measurement [67] and this can be mitigated by careful assembly of the Hartmann sensor, as discussed in Section 3.3.2.3. For the orientation of the axes, see Figure 3.2.

- The spots in a Hartmann sensor will typically cover more pixels than a Shack-Hartmann sensor. This may average out the effects of any non-uniform response in the pixels of the CCD, but it does not improve the accuracy of the centroid. This can be shown using the theoretical result higlighted by Thomas *et al.* [68]: the minimum possible centroid noise in a Gaussian spot with rms size σ_{spot} and pure photon noise, is equal to

$$\sigma_{N_{\text{ph}}} = \frac{\sigma_{\text{spot}}}{\sqrt{N_{\text{ph}}}}$$

where N_{ph} is the average number of photons per spot. If the photon flux on the CCD is large enough, then the number of photons per spot will be proportional to the area of the spot, which is proportional to σ^2_{spot}, and hence $\sigma_{N_{\text{ph}}}$ will be a constant. Note that this only applies if a spot covers an area greater than one pixel. If a spot is smaller than a single pixel there is only a single data point and the location of the center of

Property	Shack-Hartmann	Hartmann
Best sensitivity at time of design	$\lambda/150$ @ 633 nm [25]	$\lambda/500$ @ 1064 nm [24]
Lever arm is variable	No	Yes
Higher transmission per unit area	Yes	No
More pixels per spot	No	Yes
Subject to lenslet aberrations	Yes	No
Ease of manufacture	Medium	Easy

Table 3.1: A comparison of the relative merits of Shack-Hartmann and Hartmann sensors.

the spot cannot be determined with sub-pixel precision. In this case, a Hartmann sensor with larger spots will offer an improvement on a Shack-Hartmann sensor with single pixel-sized spots.

- A Hartmann sensor is a simpler device and is easier and cheaper to manufacture than a Shack Hartmann lenslet array.
- A Shack-Hartmann array may suffer from aberrations in the lenslets [67]. Clearly, this will not be a problem for a Hartmann sensor as it contains no lenslets.

Ultimately, the large number of available photons, flexibility, low cost and the relative ease of manufacturing a Hartmann plate to exact specifications led to its choice over a commercially available Shack-Hartmann sensor.

3.2.4.2 Other variations

Other minor variations on the Hartmann sensor theme include:

- The scanning Hartmann sensor in which an incoming wave front is scanned by a moving aperture that is created using a programmable liquid-crystal display [69] [70] or a single beam is scanned across a CCD using a galvanometer-based rotating mirror [71]. In this configuration, cross-talk is not an issue. However, because of the sequential scanning, real-time operation is not possible making it unsuitable for use in a GWI.

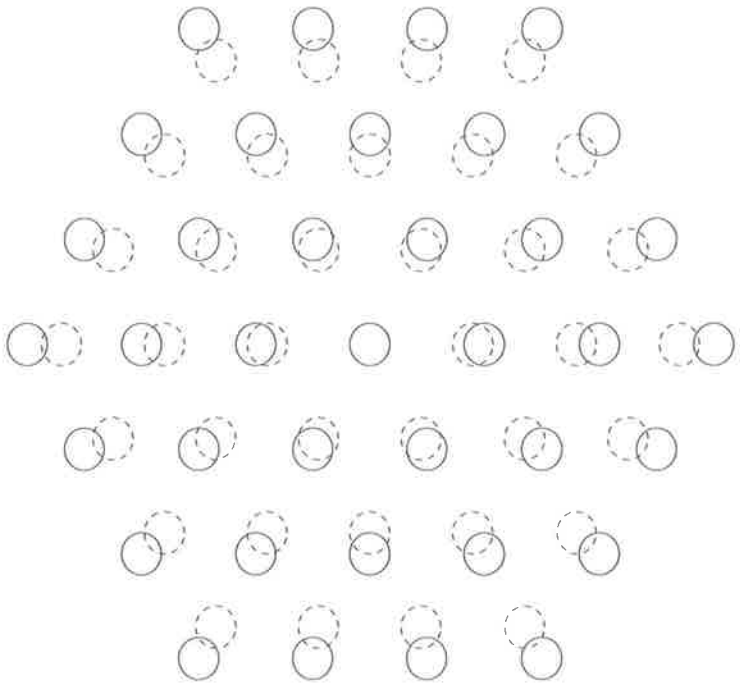

Figure 3.7: Apertures on the Hartmann plate move further apart as the temperature of the plate increases. The dashed circles represent the original positions and the solid circles represent the new positions after an increase in temperature.

- The interferometeric Hartmann sensor [52] [72]. The spots in the Hartmann sensor are deliberately brought closer together to create interference fringes between neighbouring spots. Changes in the fringes are used to extract the wavefront change. Using this method West [52] reliably measured wavefront distortions as small as 10 nm, which does not satisfy the Advanced LIGO sensitivity requirement of 1.35 nm = $\lambda/467$ @ 633 nm.

3.2.5 Temperature dependence of Hartmann sensors

As discussed by Chernyshov *et al.* [73], if the temperature of the Hartmann sensor changes then there will be thermal expansion in the components of the sensor. Thermal expansion of the HP causes an increased distance between the holes, as shown in Figure 3.7, which results in an increase in the distance between the spots on the CCD which increases the change in the wavefront gradient measured by the sensor. Thermal expansion of the CCD results in a decrease in the apparent distance between the spots.

For the HWS discussed in this chapter, the thermal effect is dominated by thermal expansion of the brass HP and leads to a systematic error equivalent to defocus, S, as shown below.

Assume that there is a uniform (and small) increase in temperature, ΔT, of the Hartmann plate. The increased distance between two Hartmann holes, $\Delta x_{\text{thermal}}$, is given by

$$\Delta x_{\text{thermal}} = \alpha \, h_{\text{p}} \, \Delta T \tag{3.3}$$

where h_{p} is the nominal distance between holes on the Hartmann plate. The distance between the two corresponding spots on the CCD increases by the same amount and the apparent change in gradient, $\partial\left(\Delta \text{W}\right)/\partial x$, is

$$\begin{aligned} \frac{\partial\left(\Delta \text{W}\right)}{\partial x} &= \frac{\Delta x_{\text{thermal}}}{\text{L}} \\ &= \frac{\alpha \, h_{\text{p}} \, \Delta T}{\text{L}} \\ &= \left(\frac{\alpha \, \Delta T}{\text{L}}\right) h_{\text{p}} \end{aligned} \tag{3.4}$$

or more generally

$$\frac{\partial\left(\Delta \text{W}\right)}{\partial x} = \left(\frac{\alpha \, \Delta T}{\text{L}}\right) x \tag{3.5}$$

for the distance, x, between any two points. The apparent change in gradient

is linear in x and, therefore, the apparent change in wavefront is quadratic in x. That is, thermal expansion of the HP results in a measurement of the primary aberration defocus [37], with a coefficient $S_{thermal}$, given by

$$S_{thermal} = \frac{\alpha \Delta T}{L} \tag{3.6}$$

3.3 Hartmann sensor for advanced GWI

As discussed in Section 1.3.2, the requirements for the wavefront sensor to be used in the thermal compensation system in Advanced LIGO [20] [74] are

1. A sensitivity of at least $\lambda/785$ @ 1064 nm

2. Spatial resolution sufficient to cover a 224 mm diameter circle with sampling points that are separated by less than 10 mm.

This section describes the design of a Hartmann sensor that exceeds these requirements. The description of the sensor hardware includes the probe beam light source in Section 3.3.1, the optimization of the Hartmann plate and lever arm distance in Section 3.3.2 and the choice of the CCD camera in Section 3.3.3. The analysis software is discussed in the following two subsections, and includes the description of a novel centroiding algorithm and discussion of the wavefront reconstruction algorithm. Finally, Section 3.3.6 collates the errors identified in earlier sections to determine the overall sensitivity.

3.3.1 Light source - coherent versus incoherent

The probe beam is an integral part of the use of a HWS to measure thermal lensing in an optic. The effect of intensity noise in the probe beam should thus be included in the overall noise of the sensor.

Property	Value
Product name	Agilent HFBR-1414 Transmitter
Emmiting Material	AlGaAs
Fibre Output Power	60 μW
Peak Wavelength	820 nm
Coherence Length (FWHM)	5.5 μm
Fibre size	50/125 μm

Table 3.2: Properties for Agilent fibre-coupled LED

The intensity of the light source will fluctuate due to photon shot noise and also due to time-varying coherent effects, such as interference fringes, that are present in the intensity distribution.

Photon shot noise, σ_{photon}, is simply the Poissonian fluctuations in the number of photons, N_p, arriving in a given time interval, given by

$$\sigma_{\text{photon}} = \sqrt{N_p} \tag{3.7}$$

This will be quantified in the discussion about the CCD in Section 3.3.3.

Coherent fluctuations, σ_{coherent}, in the intensity pattern depend entirely on the particular system under test. They are more likely to appear in a system with many transmissive optics, in which multiple reflections of the beam may occur, as opposed to one with purely reflective optics. As such, no attempt will be made to quantify them at this point.

It is possible to circumvent these effects entirely by using a source with a short coherence length. The feasibility of using an incoherent light source was discussed by Roddier in 1990 [75]. Additionally, an incoherent source will reduce the inteferometric cross-talk between neighbouring spots. This is modelled and discussed in Section 3.3.2.

Thus, a fibre-coupled AlGaAs LED, with the properties listed in Table 3.2, was chosen as the primary light source for the HWS. The coherence length of this source was measured using a path-matched Michelson interferometer and observing the Michelson visibility [76], V_M, given by

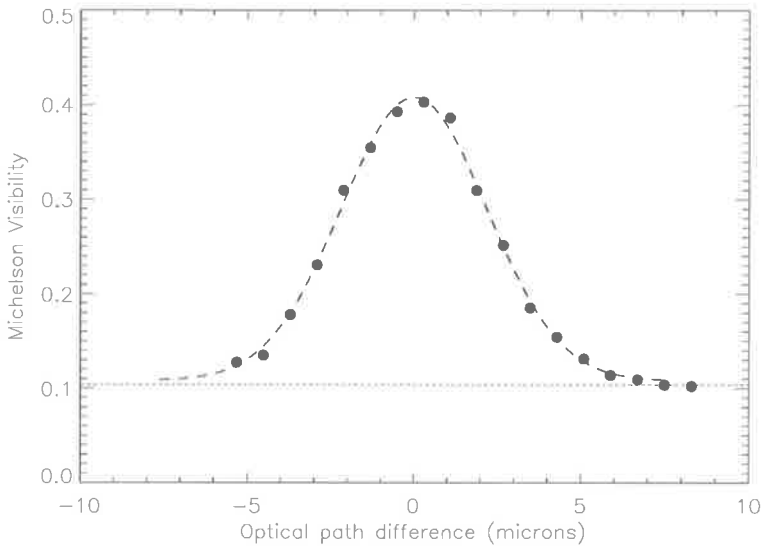

Figure 3.8: A plot of the Michelson visibility in the output of the interferometer as a function of the optical path difference. The horizontal dashed line is due background fluctuations in the object and reference intensity profiles. The best fit Gaussian, indicated by the dashed line, has a FWHM coherence length of 5.5 μm.

$$V_M = \frac{I_1 - I_2}{I_1 + I_2}$$

of interference fringes as a function of optical path difference, where I_1 and I_2 are the maximum and minimum intensities of the fringes, respectively. The results are plotted in Figure 3.8.

3.3.2 Optimization of Hartmann plate design

The optimum Hartmann plate design for measuring thermally induced wavefront changes in the optics of a GWI is found by determining the best combination of hole size, h_s, hole spacing, h_p, and lever arm, L, that give a spatial resolution and sensitivity consistent with the Advanced LIGO requirements stated in Section 1.3.2.

For example, longer lever arms will yield greater displacements of the spots on the CCD in response to a given wavefront change, resulting in better sensitivity for a constant uncertainty in the centroid positions. However, diffraction from the holes increases the size of the spots on the CCD and, if the lever arm was long enough then there would be substantial cross-talk between neighbouring spots, reducing the sensitivity. Of course, cross-talk could be reduced by increasing the hole spacing of the holes in the array but this would decrease the spatial resolution. Alternatively, cross-talk could be reduced by varying the hole size: either increasing the hole size if L is large and there is substantial diffraction, or decreasing the hole size if L is small and there is minimal diffraction. The optimum balance between these, h_s, h_p and L must be found.

Unfortunately, the optimum balance cannot be found analytically because a typical Hartmann sensor is arranged such that the CCD is in the near field of the holes in the plate. Therefore, numerical simulation of the diffraction patterns for various Hartmann plate configurations was used to find the optimum solution.

The modelling simulated a Hartmann sensor operating in Configuration A, shown in Figure 3.5. It calculated the wavefront change induced by absorption of a 8 mm ($1/e^2$-radius) Gaussian beam in a 30 mm high, 50 mm diameter cylinder of Schott FK51 glass, which was a potential candidate glass for the thermal lensing experiment described in the previous chapter at the time of design.

3.3.2.1 Modelling

The simulation, described below, determined the RMS noise, σ_{sim}, in the centroid measurements for a Hello-Vinet thermal lens for a variety of Hartmann sensor configurations. The smallest noise occurs when the separation of the holes, h_p, in the Hartmann plate is large and the lever arm is long, but this is undesirable because of the low spatial resolution. Ideally, the RMS noise should be small, i.e. $1/\sigma_{\text{sim}}$ should be large, and the density of holes, $\propto 1/h_p^2$, should also be large. Therefore, a figure of merit (FOM) was defined by

$$\text{FOM} = \left(\sigma_{\text{sim}}\, h_p^2\right)^{-1}.$$

The configuration with the largest figure of merit was then manufactured. Note that only close-packed hexagonal arrays were modelled because the density of spots is approximately 15% larger than in square arrays of the same hole spacing, improving the spatial resolution and reducing the error in the reconstruction of the wavefront as discussed in Section 3.3.5.

The simulation used the physical optics propagation package in the ZEMAX Optical Design program [77] [78]. The code used for this simulation is listed in Appendix B.1.

The procedure used for each simulation was:

1. Choose the parameters for the Hartmann plate and lever arm from the following sets :

$$\begin{aligned} \frac{h_s}{2} &= 0.2, 0.4, 0.6, 0.8 \text{ or } 1.0 \text{ mm radius} \\ h_p &= 2.25, 2.50, 2.75, 3.00, 3.25, 3.50, 3.75 \text{ or } 4.00 \text{ mm} \\ \mathrm{L} &= 100, 300, 500, 700 \text{ or } 900 \text{ mm}. \end{aligned}$$

2. Create a 1024×1024 numerical mask representing a 60 mm $\times$ 60 mm square Hartmann plate, slightly larger than the 50 mm diameter of the FK51 glass cylinder, with 4 rings of holes in a close-packed hexagonal arrangement (61 holes). Weight each pixel in the array by the fraction of its area that is covered by an aperture.

3. Create a 1024×1024 array representing the phase front incident on the Hartmann plate in Mathematica.

4. Calculate the phase across the array, given by $2\pi/\lambda$ times the optical path distortion due to an 8 mm ($1/e^2$-radius) laser beam heating a cylindrical piece of FK51 Schott Glass using Hello-Vinet.

5. Combine the mask and phase front to calculate the electric field immediately after transmission through the Hartmann plate.

6. Use the diffraction propagation code in ZEMAX to propagate the field array through the chosen lever arm distance to an output plane.

7. Convert the field at the output plane to intensity and digitize into an 8-bit TIFF image.

8. Calculate spot centroids, using Equation 3.10 (see Section 3.3.4), and centroid displacements from their nominal position.

9. Determine the magnitude of the measured gradient as a function of radial position.

10. Compare to the known theoretical gradient of the Hello-Vinet distortion, calculated by the gradient mutiplied by the lever arm and divided by the pixel size.

11. Calculate the standard deviation of the difference between the measured and known gradients.

The intensity patterns, resulting from Step 7, for $h_s = 2.0$ mm, $h_p = 2.75$ mm, $L = 300$ mm is shown in Figure 3.9 a) and for $h_s = 0.8$ mm, $h_p = 2.25$ mm, $L = 900$ mm is shown in Figure 3.10 a). Plots for the simulated (points) and known (line) spot displacements, resulting from Step 10, for $h_s = 2.0$ mm, $h_p = 2.75$ mm, $L = 300$ mm, and for $h_s = 0.8$ mm, $h_p = 2.25$ mm, $L = 900$ mm are shown in Figure 3.9 b) and Figure 3.10 b).

The five best Hartmann sensor parameter sets and their figures of merit are listed in Table 3.3. The parameter set: (hole diameter of 0.8 mm diameter and hole spacing of 2.25 mm) was chosen for fabrication as a Hartmann plate. Subsequently, it was decided that the sensor would be more robust if the Hartmann plate was physically attached to CCD, as shown in Configuration B in Figure 3.5. Thus the hole spacing and hole size were demagnified by a factor, $M \approx 5.3$, the demagnification of the telescope in Figure 3.5, and the lever arm was demagnified by M^2. The parameter sets for Configurations A and B are listed in Table 3.4.

A hexagonally-close-packed array of 150 μm diameter holes spaced 430 μm apart was laser drilled in a 50μm thick piece of brass plate to cover a 12.5 $\times$ 12.5 mm area. The laser drilling process could position holes to within ± 1 μm [79].

The plate, as viewed under a microscope, is shown in Figure 3.11. The small diameter holes have a tendency to get clogged with dust when the plate is stored in a dirty environment. The two images in this figure show that plate before and after cleaning in an ultrasonic bath. Also indicated is the hexagonal unit cell.

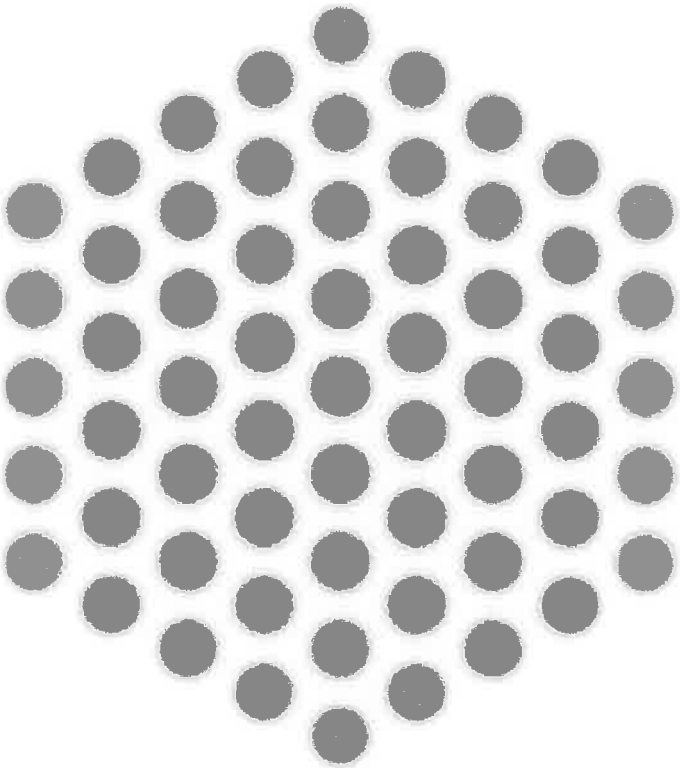

(a)

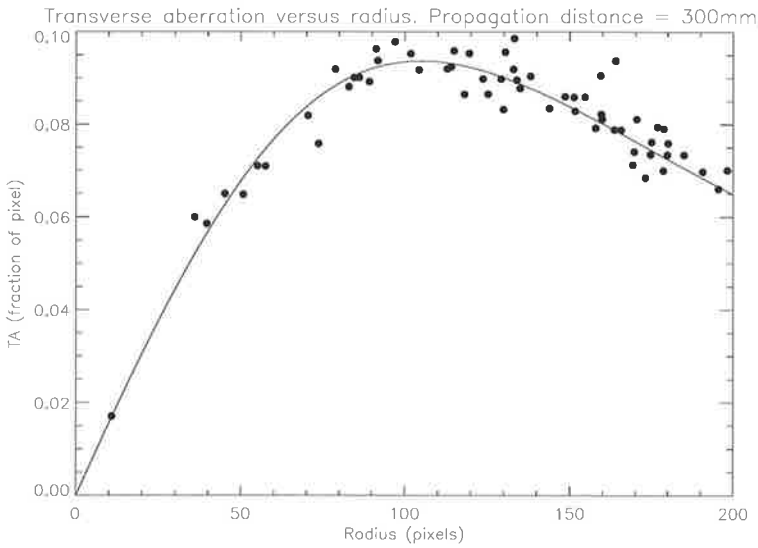

(b)

Figure 3.9: a) Numerically determined diffraction pattern from a Hartmann plate with $h_s = 2.0$ mm, $h_p = 2.75$ mm, $L = 300$ mm and b) the simulated (points) and known (solid line) centroid displacements.

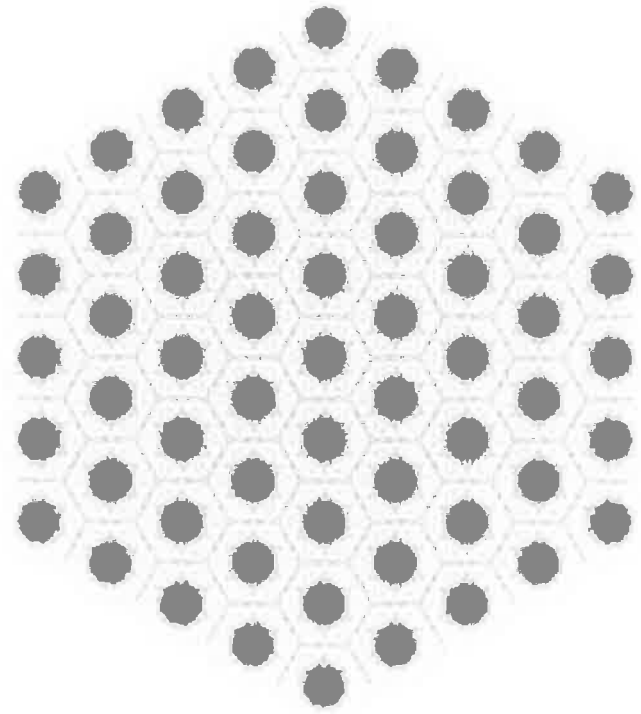

(a)

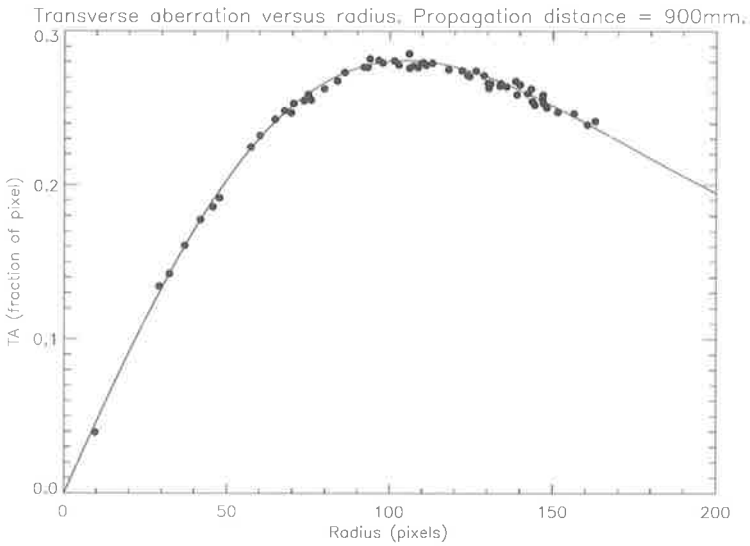

(b)

Figure 3.10: a) Numerically determined diffraction pattern from a Hartmann plate with $h_s = 0.8$ mm, $h_p = 2.25$ mm, $L = 900$ mm and b) the simulated (points) and known (solid line) centroid displacements.

Hole diameter, h_s (mm)	Hole Spacing, h_p (mm)	Lever Arm, L (mm)	FOM
0.8	2.25	900	92.1
0.8	2.25	700	67.5
0.8	2.75	900	66.1
0.8	2.50	500	57.8
0.8	2.50	700	55.9

Table 3.3: Best five Hartmann plate configurations as rated by the figure of merit (FOM).

	Configuration A	Configuration B
Hole diameter	0.8 mm	150 μm
Hole Spacing	2.25 mm	430 μm
Lever Arm	$\leq$ 900 mm	$\leq$ 31 mm

Table 3.4: Final design parameters for the Hartmann sensor

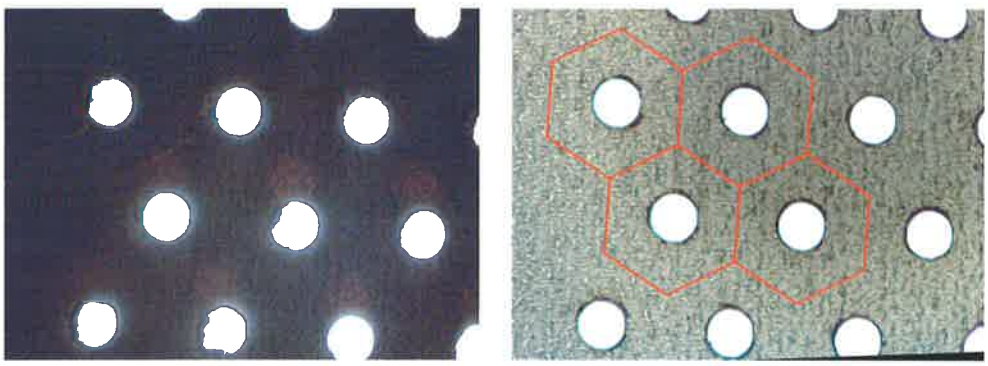

Figure 3.11: Hartmann plate as viewed under microscope. a) as delivered, b) after cleaning in an ultrasonic bath and with hexagonal unit cells highlighted. Note that the second image is brighter because the plate was more highly illuminated.

3.3.2.2 Simulations of cross-talk

If the array of holes in the HP is is illuminated by a spatially varying intensity and/or wavefront, then centroid pulling due to cross-talk will occur and result in systematic errors in the centroid displacements. The magnitude of these errors will also be affected by the length of the lever arm and the coherence length of the light source, particularly if spurious interference fringes are produced by transmissive optics between the light source and HWS.

Numerical simulations were used to quantify the effect of cross-talk for Configuration B. The simulations used two different lever arms, 31 mm and 10 mm, and coherent light, with a wavelength of 820 nm, and incoherent light with a central wavelength of 820 nm and a FWHM spectral width of 120 nm (the width of a source with a coherence length of 5.5μm).

The systematic error due to cross-talk was calculated by comparing the displacement of a spot centroid due to wavefront defocus for an isolated spot and a spot at the centre of 6 hexagonally-coordinated neighbouring spots. The procedure used for this simulation was:

1. Single hole HP, shown in Figure 3.12 a)
   (a) Illuminate the HP with a flat wavefront and simulate numerically the diffraction pattern at the lever arm distance using Fourier diffraction propagation [80] (see Appendix B.2 for the source code of this simulation). Determine the centroid.
   (b) Repeat step 1 (a), but illuminate with a wavefront aberrated by a small, randomly-selected, amount of the primary aberration defocus that is centered at a random position within the vicinity of the hole in the HP.
2. Seven hole HP, shown in Figure 3.13 a)
   (a) Repeat step 1 (a).
   (b) Repeat step 2 (a), but illuminate with the aberrated wavefront used in step 1 (b).

The resulting diffraction patterns for the single hole HP are shown in Figure 3.12 b) and c) coherent and incoherent, respectively, for the 31 mm lever arm and d) and e) coherent and incoherent, respectively, for the 10 mm lever arm. The diffraction patterns for the seven hole HP are shown in Figure 3.13 b) - e), arranged in the same order as the previous figure.

The cross-talk is defined to be that part of the spot displacement that is due to the presence of neighbouring spots. The two quantities required to calculate this are:

- The displacement of the spot for the single hole HP, $\Delta x_{1\mathrm{h}}$, given by the difference between the centroid calculated in step 1 (b) and the centroid calculated in step 1 (a).
- The displacement of the central spot for the seven hole HP, $\Delta x_{7\mathrm{h}}$, given by the difference between the centroid calculated in step 2 (b) and the centroid calculated in step 2 (a).

Recall that $\Delta x_{1\mathrm{h}}$ and $\Delta x_{7\mathrm{h}}$ are simulations of the same wavefront curvature. Thus, the cross-talk, ϵ_{CT}, is given by

$$\epsilon_{\mathrm{CT}} = \frac{\Delta x_{7\mathrm{h}} - \Delta x_{1\mathrm{h}}}{\Delta x_{1\mathrm{h}}} \tag{3.8}$$

The results of the cross-talk simulations are summarised in Table 3.5. The cross-talk shown in this table is the result of averaging over many defocus aberrations. They show that the contribution of cross-talk is much more significant with a lever arm of 30 mm than 10 mm. They also show that better results are obtained with the incoherent source, which is not unexpected because of the reduced interference between neighbouring spots.

As a result of these simulations, the nominal lever arm in the design was reduced to 10 mm. It should be noted that this is a departure from the optimized design reached in Section 3.3.2.1, however, the reduction of the lever arm by a factor of only 3 in order to reduce the systematic cross-talk for the incoherent source by a factor of 18.75 was deemed to be worthwhile.

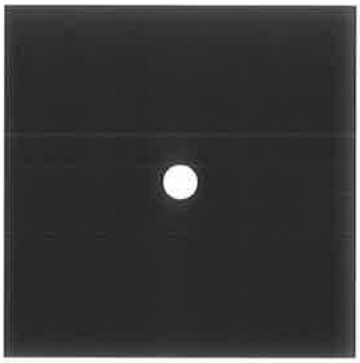

(a) Hartmann mask

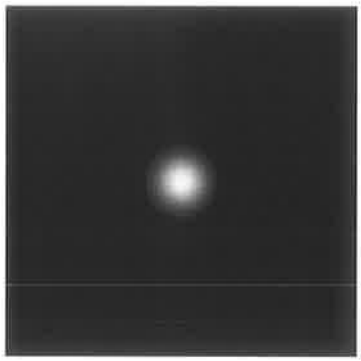

(b) Coherent: L=31mm

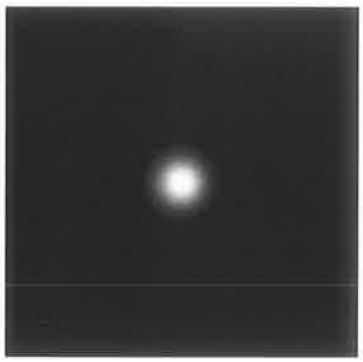

(c) Incoherent: L=31mm

(d) Coherent: L=10mm

(e) Incoherent: L=10mm

Figure 3.12: a) Simulated Hartmann plate with a single hole. b) calculated diffraction pattern from the Hartmann plate at a distance of 31 mm when illuminated with a coherent 820 nm light source and c) with an incoherent 820 nm light source with a coherence length of 5.5 μm. d) diffraction pattern at a distance of 10 mm when illuminated with a coherent 820 nm light source and e) with an incoherent 820 nm light source with a coherence length of 5.5 μm.

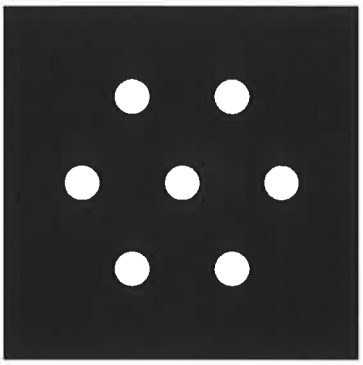

(a) Hartmann mask

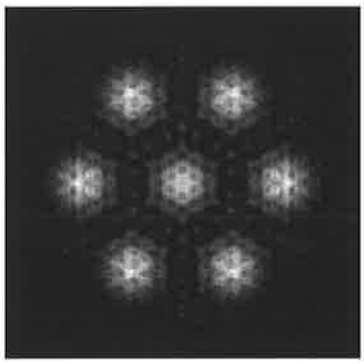

(b) Coherent: L=31mm

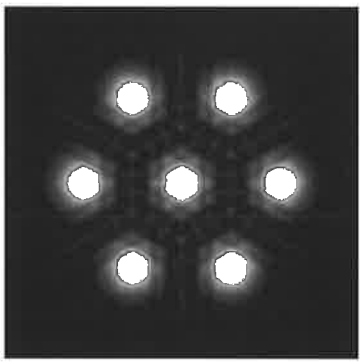

(c) Incoherent: L=31mm

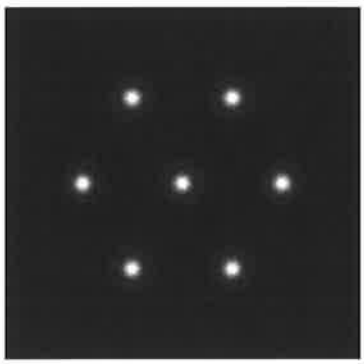

(d) Coherent: L=10mm

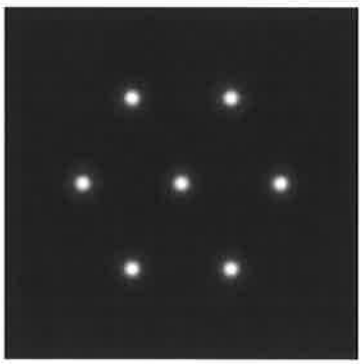

(e) Incoherent: L=10mm

Figure 3.13: a) Simulated Hartmann plate with multiple holes. b) calculated diffraction pattern from the Hartmann plate at a distance of 31 mm when illuminated with a coherent 820 nm light source and c) with an incoherent 820 nm light source with a coherence length of 5.5 μm. d) pattern at a distance of 10 mm when illuminated with a coherent 820 nm light source and e) with an incoherent 820 nm light source with a coherence length of 5.5 μm.

Lever Arm Length	Crosstalk - Coherent	Crosstalk - Incoherent
10 mm	0.18%	0.08%
31 mm	2.7%	1.5%

Table 3.5: Level of cross-talk error in the centroid displacement of a single Hartmann spot for coherent and incoherent sources at two different lever arm lengths

3.3.2.3 HWS construction

An exploded view of the final Hartmann sensor is illustrated in Figure 3.14. A 4 mm thick spacer containing a 36 mm diameter hole is bolted to the front of the CCD camera (the CCD is discussed in detail in Section 3.3.3). A front plate, also containing a 36 mm diameter hole, is bolted to the spacer. The Hartmann plate is sandwiched between the spacer and the front plate in a 30 μm recessed region. The CCD is nominally 6 mm behind the front face of the camera body. In combination with the spacer, this yields a lever arm, L, of approximately 10 mm.

This construction addresses problems of CCD-HP alignment. Rotations of the HP about the x or y axes will cause errors in the HWS measurement. Either of these rotations cause the CCD and HP not to be parallel. Therefore, the lever arm distance between the CCD and HP will not be constant across the face of the HP. This is not a problem here because, as shown in Figure 3.14, the CCD is nominally parallel to the front face of the camera housing and the sandwich construction should minimize misalignments between the HP and the CCD.

3.3.2.4 Estimated temperature dependent defocus error

For a brass Hartmann plate (with a linear thermal expansion coefficient, α_{brass}, of $20.3\,\mu\text{m}\,\text{m}^{-1}\,\text{K}^{-1}$ [81]) and a lever arm length of 10.43 mm (the measurement of which is described in the next chapter), the temperature dependent defocus error can be determined using Equation 3.6

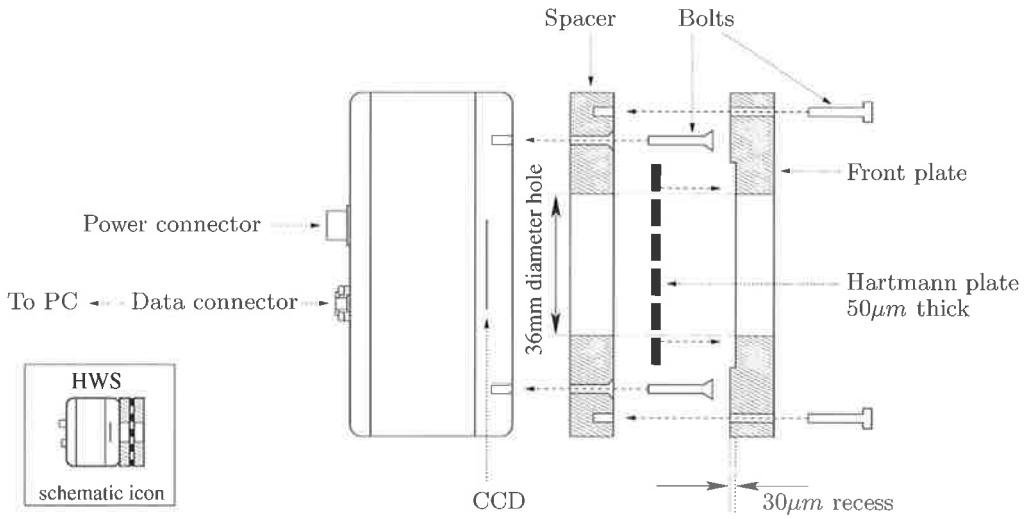

Figure 3.14: A 4mm wide spacer is bolted to the front of the Dalsa 1M60 camera. The Hartmann plate is positioned in a 30 μm recess in the front plate which is then bolted onto the camera. 36mm diameter holes in both plates allow the the rays to propagate onto the CCD. The inset shows the icon used to represent the HWS in schematic diagrams.

$$\frac{\mathrm{S_{thermal}}}{\Delta T} = \frac{\alpha_{\mathrm{brass}}}{\mathrm{L}} = 0.00195\,\mathrm{m^{-1}\,K^{-1}} \tag{3.9}$$

3.3.3 CCD camera

The CCD records a digital image of the intensity distribution of the Hartmann spots by accumulating photoelectrons, produced by the incident light in an $N_x \times N_y$ array of picture elements (pixels). Once exposure is complete, the CCD transfers the accumulated charge in each pixel out of the array and converts the output into a measurable voltage [82]. This voltage is passed through an n-bit A/D converter to yield the digital numbers (DN) that make up the digital image. The recording, transfer and digitization processes can introduce noise which degrades the image fidelity and reduces the ability of Hartmann sensor to locate accurately the centroids of the each of the spots in the image.

One additional problem during exposure is the leakage of charge from a

Parameter	Value
Array size	1024×1024 pixels
Pixel size, p_s	$12\,\mu m \times 12\,\mu m$
Digitization	12 bits
Quantum efficiency @ 820 nm	$\approx 6\%$
Full well capacity (linear operation)	350,000 electrons
Dark current @ 45°C	1.3×10^{-16}A per pixel
Random Readout noise (rms)	1.2 DN
Fixed pattern noise	3.8 % rms
Random non-uniformity	0.3 % rms
Antiblooming	$> 100\times$ saturation level

Table 3.6: Specifications of Dalsa 1M60 CCD camera using an FTT 1010-M image sensor [85] [86]. Note that the operating temperature of the CCD array is approximately 45°C when the room temperature is approximately 20°C.

full pixel well into the wells of adjacent pixels. This effect is known as blooming and it will reduce the quality of the digital image. Fortunately, modern scientific grade CCDs have antiblooming features that use an overflow drain below each pixel to prevent blooming for reasonable exposure levels. Charge flows into the drain before it is able to flow into adjacent pixels and is constantly removed [82] [83] [84]. The magnitude of the anti-blooming in a CCD refers to the multiple of the saturation level that can be applied to a pixel before any charge leaks into a neighbouring pixel. Ultimately, this feature allows the CCD to be used close to saturation level, improving the sensitivity, without any danger of adjacent pixels contaminating one another.

A Dalsa 1M60 CCD camera [85], the relevant parameters of which are listed in Table 3.6, was chosen as the image sensor in the Hartmann wavefront sensor. The substantial technical and diagnostic information available on this CCD indicates that it should be shot-noise limited (see below). A measurement that tested and verified this conclusion is described in this section after a brief discussion of the various noise sources in the CCD. The magnitudes of these noise sources are collated in Table 3.7 for convenience.

3.3.3.1 Expected noise in CCD

The dominant noise sources, in order of their appearance in the measurement process, are:

- Photon shot noise. This arises because of the non-uniform arrival of the photons at the pixels. It can be calculated by dividing the number of electrons per pixel, N_e, by the quantum efficiency (QE $\approx$ 6%) to determine the approximate number of photons, N_p, required to produce N_e electrons. For the Dalsa 1M60, $N_p \approx 5.8 \times 10^6$ when N_e is equal to the maximum value of 350,000. The rms noise in the number of photons is $\sqrt{N_p}$. This can be expressed in electrons by multiplying by the QE. The maximum rms fluctuation due to photon shot noise is 145 electrons.

- Photoelectron shot noise arises because of the random nature of the photoelectric conversion process and is given by $\sqrt{N_e}$. For the maximum number of electrons in a pixel ($N_e = 350,000$) the rms fluctuation due to electron shot noise is 592 electrons.

- Readout noise is due to random noise sources within the sensor, including dark current and amplifier noise. Dark current refers to electrons which are thermally generated, rather than photo-generated. The HWS typically uses a short integration time ($\leq$ 50 ms) and thus dark current can be ignored. Amplifier noise is simply the noise introduced by the sensor electronics. The specified value [85] in Table 3.6 is 1.2 digital numbers (DN). This can be converted into electrons assuming a gain of 4096 DN per 350,000 electrons. The readout noise is thus 103 electrons.

- Digitization noise is the uncertainty in the measurement of the number of electrons in a pixel because of quantization into an n-bit scale. This is calculated using Equation A.4:

$$\sigma_{\text{digital}} = \frac{1}{\sqrt{3}} \frac{N_{e_{\max}}}{2^n}$$

Noise Type	RMS Value (el)	% of total variance
Photon shot noise	145	5.40 %
Photoelectron shot noise	592	91.2 %
Random readout noise	103	2.76 %
Digitization noise @ 12-bits	49.3	0.63 %
Fixed Pattern noise	3.9	0.004%
Random non-uniformity	0.3	2×10^{-5} %

Table 3.7: Noise from each source expressed in electrons.

which gives a value of 49.3 electrons when $N_{e_{\max}} = 350,000$ electrons and $n = 12$.

The remaining noise sources specified by the camera manufacturer, fixed pattern noise and photoresponse non-uniformity, were small enough, see Table 3.7, to be safely ignored.

It is clear from Table 3.7 that digitization noise is negligible and that the total noise is dominated by photoelectron shot noise for the Dalsa 1M60 CCD. The contribution of the digitization noise for a reduced number of bits is shown in Table 3.8, indicating that 10-bits, as opposed to 12-bits, would not increase the total noise significantly. The total relative error, σ_{tot}/N_e, in this Table is calculated using

$$\frac{\sigma_{tot}}{N_e} = \frac{\sqrt{\sigma^2_{\text{others}} + \sigma^2_{\text{digital}}}}{N_e}$$

where σ^2_{others} is the total variance from all the other noise sources as presented in Table 3.8. In summary, using a CCD with more than 10-bits of digitization is worthwhile only if the photoelectron shot noise is also reduced. This would be accomplished by increasing the maximum number of electrons per pixel.

3.3.3.2 CCD: Measurement of noise

To confirm that the CCD was indeed shot noise limited, it was illuminated at three different intensity levels by the LED described in Section 3.3.1. The RMS fluctuations in the DN of the pixels were measured and are plotted as

Number of bits	Total var. (el^2)	% of total var.	Total relative error
Other sources	3.82×10^5	-	-
8	10.0×10^5	62%	0.29%
9	5.38×10^5	29%	0.21%
10	4.21×10^5	9.3%	0.19%
11	3.92×10^5	2.5%	0.18%
12	3.85×10^5	0.63%	0.18%

Table 3.8: The contribution of digitization noise to the total variance in the pixel measurement using 8 to 12-bit digitization. All other noise sources are assumed to be fixed at the levels shown in Table 3.7. Also shown is the overall relative error in the measurements in each pixel.

a function of digital number in Figure 3.15 on a log-log scale. A line with slope -1/2, the dependence expected for Poissonian statistics, is also plotted in Figure 3.15. The good agreement indicates that the noise in the CCD is, indeed, Poissonian and therefore that the CCD is random. From this plot, the relative error at DN = 4095 is estimated to be 2.5×10^{-3} ($\approx 10^{-2.6}$). This is equivalent to the noise in a Poissonian distribution with a mean of $\approx 160,000$ counts, assumed to be the equivalent number of electrons in the pixel well when full. This value is slightly less than the nominal full well capacity of 350,000 electrons.

3.3.3.3 Pixel size measurement

Since all centroid positions are calculated in units of pixels, the wavefront reconstruction is only as accurate and precise as the pixel size, p_s . Therefore, the pixel size was measured as outlined below.

The CCD was illuminated with the diffraction pattern from the edge of a razor blade and the image recorded. The CCD was then translated horizontally and perpendicular to the illuminating beam by 6.001 ± 0.003 mm using a micrometer-controlled translation stage. A second image of the diffraction pattern was recorded. The two images are shown in Figure 3.16. Horizontal cross-sections of each image are plotted in Figure 3.17. The second fringe in the diffraction pattern was chosen as a well defined feature to locate

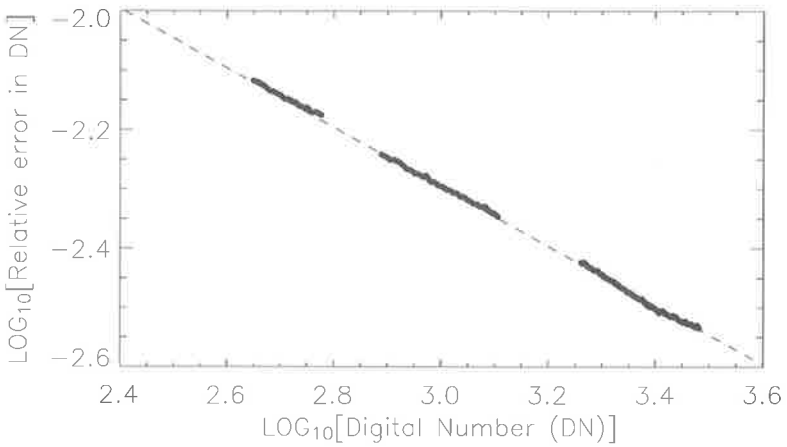

Figure 3.15: RMS fluctuation in intensity vs intensity. The dashed line has a slope of $-1/2$.

on the CCD when it was in the two positions and its peak was found for both images. The data points marked by the square boxes in Figure 3.16 indicate the data that were used to calculate the peaks. The difference between the two peaks was 500.9 pixels. This yielded an average apparent pixel size of $11.975 \pm 0.005\,\mu$m.

3.3.4 Centroiding algorithms

As discussed in Section 3.2.2, a centroid algorithm is normally used to locate the centres of the spots in a Hartmann image. The conventional form of this algorithm is

$$(x_c, y_c)_m = p_s \left(\frac{\sum_{i=N_m^{\min}}^{i=N_m^{\max}} \sum_{j=M_m^{\min}}^{j=M_m^{\max}} i\ I_{ij}}{\sum_{i=N_m^{\min}}^{i=N_m^{\max}} \sum_{j=M_m^{\min}}^{j=M_m^{\max}} I_{ij}}, \frac{\sum_{i=N_m^{\min}}^{i=N_m^{\max}} \sum_{j=M_m^{\min}}^{j=M_m^{\max}} j\ I_{ij}}{\sum_{i=N_m^{\min}}^{i=N_m^{\max}} \sum_{j=M_m^{\min}}^{j=M_m^{\max}} I_{ij}} \right) \quad (3.10)$$

where p_s is the pixel size, i and j are the CCD pixel indices in the horizontal

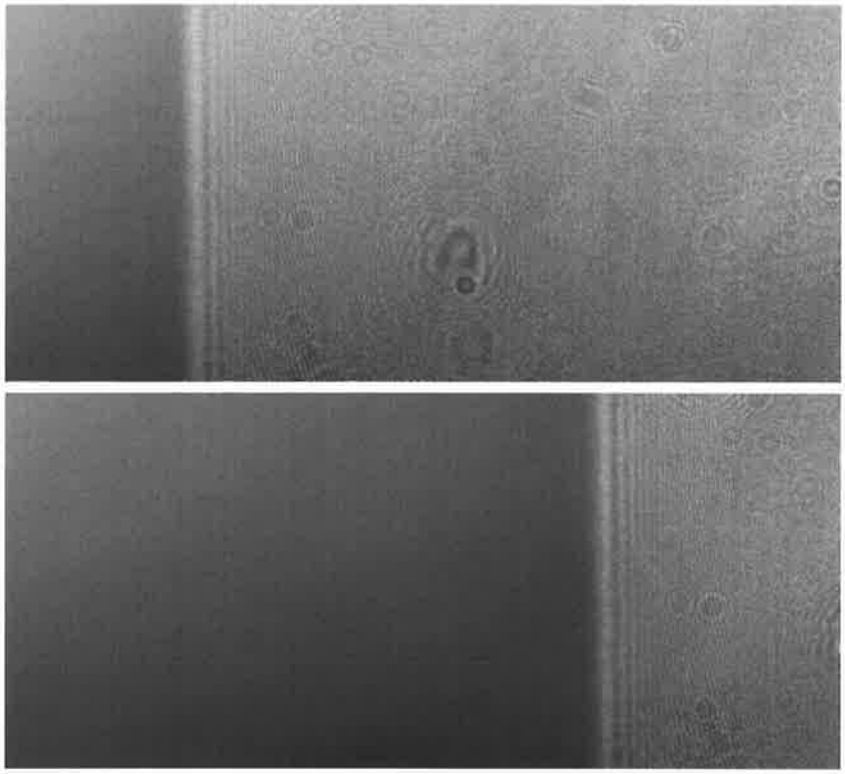

Figure 3.16: Fixed diffraction pattern on the CCD before (top) and after (bottom) a lateral translation of the CCD by 6.001 mm as measured on a micrometer-controlled translation stage.

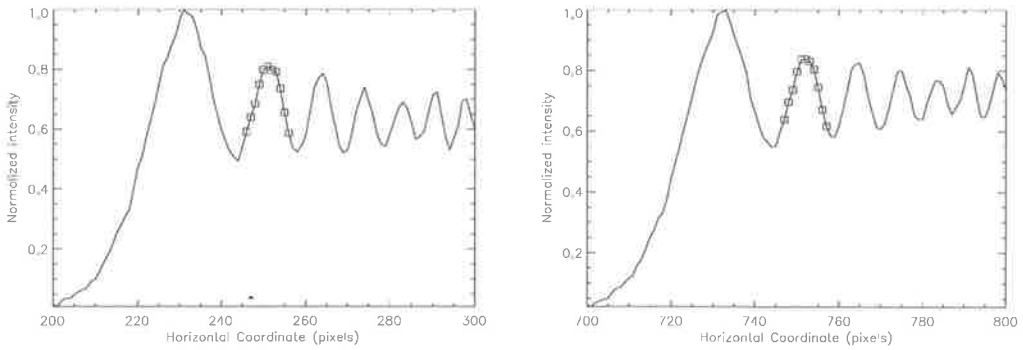

(a) Position 1

(b) Position 2

Figure 3.17: Average horizontal cross section of 1.0 mm vertical slice of both images shown in Figure 3.16 in the vicinity of the edge of the shadow. The peak of the second fringe in the diffraction pattern was determined for both images over the range indicated by the square data points.

and vertical directions, respectively, and $\mathrm{I}_{i\,j}$ is the intensity of the ij^{th} pixel.

This algorithm can give rise to significant systematic errors depending on the limits of summations, especially if the centroid of the spot is not at the center of the detection area [87]. Many variations on this algorithm have therefore been developed to minimize systematic and random errors in the centroid. Much of this work was concerned with the performance of the algorithm (and any variations) for a low photon flux [88] [89], such as might be used in adaptive optics in astronomy. However, much brighter light sources can be used for metrology and thermal lens measurement. Therefore, rather than considering all the various centroiding algorithms, this discussion will be limited to those that perform best in high photon flux: the weighted center of gravity algorithm [87] [88] [68] and a novel 'fractional pixel' algorithm of the author's design.

3.3.4.1 Weighted center of gravity (WCoG)

The WCoG algorithm applies a mask to the intensity distribution such that a weighting, $(F_w)_i$, is given to different pixels depending on their digital value. The basic 1-D form is

$$x_{\mathrm{WCoG}} = p_{\mathrm{s}} \frac{\sum_{i=i_{\min}}^{i_{\max}} i\,\mathrm{I}_i\,(F_w)_i}{\sum_{i=i_{\min}}^{i_{\max}} \mathrm{I}_i\,(F_w)_i} \tag{3.11}$$

The weighting function is quite often chosen to be a Gaussian that is centered around an *a priori* estimate of the spots center [68]. Alternatively, it can chosen to be the intensity in the pixel raised to a power $P-1$ [87]:

$$(F_w)_i = \mathrm{I}_i^{P-1}$$

and thus

$$x_{\mathrm{WCoG}} = p_{\mathrm{s}} \frac{\sum_{i=i_{\min}}^{i_{\max}} i\,\mathrm{I}_i^{P}}{\sum_{i=i_{\min}}^{i_{\max}} \mathrm{I}_i^{P}}. \tag{3.12}$$

Note that the summation range $i_{\min} \leq i \leq i_{\max}$ about a spot is chosen

such that the central pixel is that pixel with the maximum intensity. Additionally, the summation range extends by the same amount, n_1, in the positive and negative directions from the central pixel, resulting in $2\,n_1 + 1$ pixels, an odd number, in the range.

3.3.4.2 Fractional pixel centroiding (FPC)

An iterative algorithm to locate the centroid of a symmetric intensity distribution was developed. A vaguely similar method was suggested by Topa [90] for use in a Shack-Hartmann sensor.

The premise for this algorithm is derived from the problem identified by Topa [90] of a symmetric spot being located asymmetrically about a pixel on the CCD array. The center of the range of summation for the centroid calculation is not coincident with the center of the spot and there is a systematic error in the centroid calculation. In general, it is very unlikely that the true center of a spot will lie in the center of a pixel. If, however, the range of summation can be altered such that the true center lies at the center of the range of summation, then the systematic error should be removed. Therefore, we must treat the data from the CCD as a continuum and consider fractional pixels. Thus, *the true centroid is defined to be that centroid which is coincident with the center of the rectangular region (boxcar) used to calculate it.*

Since the coordinates on the CCD are considered to be a continuum, but the individual pixels still need to be identified with discrete indices, the following scheme applies. The coordinates in the continuum, $(\bar{i}, \bar{j})$, are labelled with a bar to signify their continuous nature and the indices of the pixels remain the same, i and j. In the ij^{th} pixel, therefore, the continuum ranges from $(\bar{i}, \bar{j})$ in the bottom left corner to $(\bar{i}+1, \bar{j}+1)$ in the top right corner.

The algorithm used to locate the true centroid, (illustrated schematically in figure 3.18) is:

1. Define a boxcar of ranging from $\bar{i_0}$ to $\bar{i_1}$ in the horizontal direction and

$\bar{j}_0$ to $\bar{j}_1$ in the vertical direction, that is approximately centered over a spot in the digital image.

2. Apply equation 3.13 to determine the centroid. The numerator of the equation is the sum of a series of values. Each value in that sum is the weighted intensity, I_{ij}, of the ij^{th} pixel multiplied by the fraction of the area, A_{ij}, of that pixel that is covered by the boxcar and the center, $(\bar{i}_{\text{mid}}, \bar{j}_{\text{mid}})$, of the intersection between the pixel and the boxcar. The denominator is the sum of the weights, A_{ij}, multiplied by the intensities, I_{ij}. If the boxcar range is restricted to the discrete indices, this centroid algorithm becomes the same as the conventional centroid algorithm in Equation 3.10.

$$
\begin{aligned}
(x_c,\, y_c) &= \mathrm{p_s}\, FC\left(I_{ij} : \bar{i}_0,\, \bar{i}_1,\, \bar{j}_0,\, \bar{j}_1\right) \qquad (3.13)\\
&= \mathrm{p_s}\left(\frac{\sum_{i,j=\text{floor}(\bar{i}_0,\bar{j}_0)}^{\text{ceiling}(\bar{i}_1,\bar{j}_1)} \bar{i}_{\text{mid}}\, A_{ij}\, I_{ij}}{\sum_{ij=\text{floor}(\bar{i}_0,\bar{j}_0)}^{\text{ceiling}(\bar{i}_1,\bar{j}_1)} A_{ij}\, I_{ij}}, \frac{\sum_{i,j=\text{floor}(\bar{i}_0,\bar{j}_0)}^{\text{ceiling}(\bar{i}_1,\bar{j}_1)} \bar{j}_{\text{mid}}\, A_{ij}\, I_{ij}}{\sum_{ij=\text{floor}(\bar{i}_0,\bar{j}_0)}^{\text{ceiling}(\bar{i}_1,\bar{j}_1)} A_{ij}\, I_{ij}}\right)
\end{aligned}
$$

where $\bar{i}_{\text{mid}}$ and $\bar{j}_{\text{mid}}$ are defined

$$
\bar{i}_{\text{mid}} = \begin{cases} \frac{\bar{i}_0 + (i+1)}{2} & \text{for} \quad i = \text{floor}\left(\bar{i}_0\right) \\ i + \frac{1}{2} & \text{for} \quad \text{ceiling}\left(\bar{i}_0\right) \le i < \text{floor}\left(\bar{i}_1\right) \\ \frac{i + \bar{i}_1}{2} & \text{for} \quad i = \text{floor}\left(\bar{i}_1\right) \end{cases}
$$

$$
\bar{j}_{\text{mid}} = \begin{cases} \frac{\bar{j}_0 + (j+1)}{2} & \text{for} \quad j = \text{floor}\left(\bar{j}_0\right) \\ j + \frac{1}{2} & \text{for} \quad \text{ceiling}\left(\bar{j}_0\right) \le j < \text{floor}\left(\bar{j}_1\right) \\ \frac{j + \bar{j}_1}{2} & \text{for} \quad j = \text{floor}\left(\bar{j}_1\right) \end{cases}
$$

and A_{ij} is defined

$$
A_{ij} = \begin{cases} (i\,+\,1) - \bar{i}_0 & \text{for} \quad i = \text{floor}\left(\bar{i}_0\right) \\ 1 & \text{for} \quad \text{ceiling}\left(\bar{i}_0\right) \le i < \text{floor}\left(\bar{i}_1\right) \\ \bar{i}_1 - i & \text{for} \quad i = \text{floor}\left(\bar{i}_1\right) \end{cases} \times
$$

$$\begin{cases} (j+1) - \bar{j}_0 & \text{for} \quad j = \text{floor}\,(\bar{j}_0) \\ 1 & \text{for} \quad \text{ceiling}\,(\bar{j}_0) \leq j < \text{floor}\,(\bar{j}_1) \\ \bar{j}_1 - j & \text{for} \quad j = \text{floor}\,(\bar{j}_1) \end{cases} .$$

3. Center the new boxcar at this centroid.

4. Repeat steps 2 and 3 until the difference between the calculated centroid of a boxcar and the center of that boxcar differ by less than a specified error value.

3.3.4.3 Comparison of algorithms

A numerical simulation was used to compare the accuracy of the WCoG and FPC algorithms in determining the centroid of a 2D Gaussian intensity distribution with a $1/e^2$ full-width of 8.4 pixels, in the presence of realistic noise sources. The width of 8.4 pixels was chosen because this is the width for the best fit Gaussian to a spot 10 mm from the Hartmann plate designed in Section 3.3.2.

A Gaussian spot with a known center, x_{G_1}, was produced. Shot noise (SN) was added at the realistic levels determined in Section 3.3.3.2 and readout noise (RN) at the levels in Table 3.7 were added and the spot was quantized using 12-bit digitization. The centroid of the spot was found with both algorithms for a given summation range in the WCoG algorithm and a boxcar of the same width in the FPC algorithm. In this instance the optimum summation range/boxcar width was determined to be 19 pixels. The Gaussian spot was moved to a new location, x_{G_2}, and the procedure was repeated. The difference between the centroids from the first and second spots was determined for both algorithms and was compared to the known displacement. The results are summarised in Table 3.9.

The FPC is, ultimately, limited in precision because all pixels are weighted by the same amount. Those pixels with higher levels of shot noise, due to less electrons in the pixel well, will increase the overall noise in the centroid calcu-

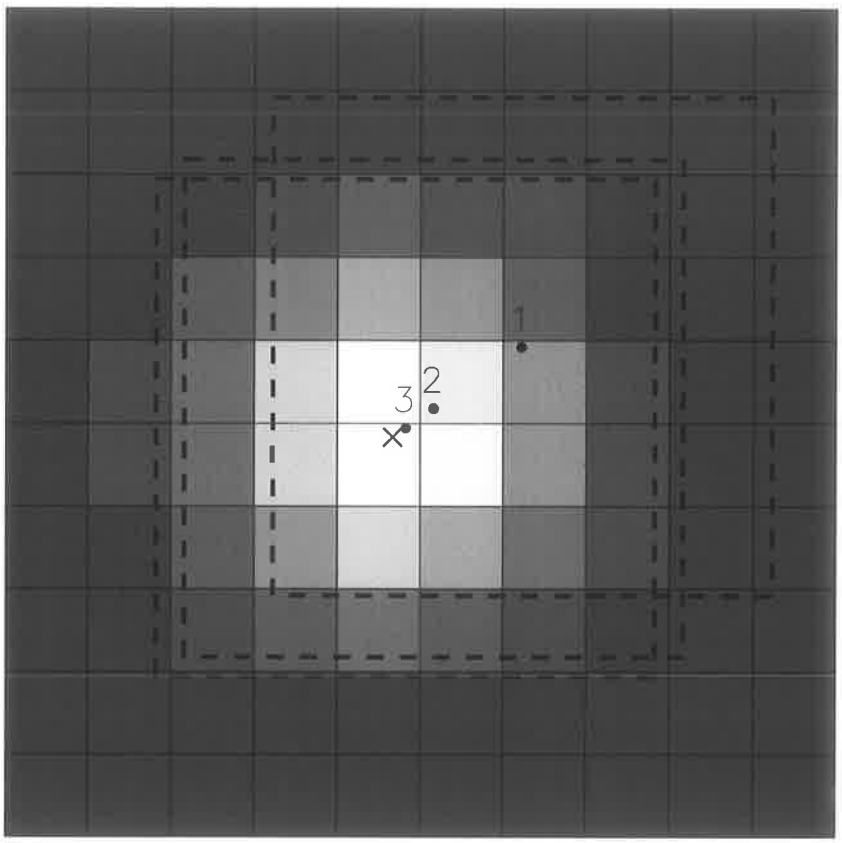

Figure 3.18: A cartoon of the pixels on a CCD and the integration regions. The centroid is determined for a boxcar of fixed width that is positioned to include fractional parts of pixels. The true center is illustrated by the cross. The *center* of each boxcar is the *centroid* of the previous boxcar. The successive boxcars and their numbered central spots are seen approaching the true center.

Algorithm	SN & RN
Fractional Pixel Centroiding	0.34 % pixel
Weighted Center of Gravity	0.19 % pixel

Table 3.9: RMS error in the FPC and WCoG centroiding algorithms measurements of displacements in the presence of realistic noise sources, shot noise (SN) and readout noise (RN).

lation. Conversely, the WCoG algorithm preferentially weights those pixels with higher intensities, and, therefore, lower levels of shot noise reducing the overall noise in the centroid calculation.

The FPC algorithm was used for earlier HWS measurements described in Section 4.3 and in Chapter 6. Later measurements, the remaining HWS measurements in Chapter 4 and all measurements in Chapter 5, used the WCoG algorithm.

3.3.5 Wavefront reconstruction algorithm

For most applications the discrete gradient field output from the HWS must be converted, via numerical or analytic integration, into a wavefront map for additional post-processing[1]. Most of the material published on wavefront reconstruction is based on the work of Southwell [62] who applied reconstruction techniques that were developed for shearing interferometers to Hartmann-type sensors and described the two basic types of wavefront reconstruction algorithms: modal and zonal.

3.3.5.1 Modal wavefront reconstruction

In modal reconstruction the wavefront is represented by the sum of continuous functions

$$\mathrm{W}(x,\, y) = \sum_{i=1}^{n} a_i\, f_i(x,\, y)$$

and its gradient is represented by

$$\vec{\nabla}\mathrm{W}(x,\, y) = \sum_{i=1}^{n} a_i\, \vec{\nabla} f_i(x,\, y)$$

The coefficients a_i are found by performing a least-squares fit of the gradient functions, $\vec{\nabla} f_i(x,\, y)$, to the discrete gradient field measured by the HWS.

[1]Sometimes full wavefront reconstruction is unnecessary and the analysis can be done with the gradient data directly, for example in the measurement of defocus [91].

Zernike polynomials are a particularly popular choice for SHWS used in adaptive optics [92] [93] and ophthalmology [94] because they are orthogonal over circular apertures, or approximately orthogonal over a discretely sampled circular aperture. However, unless many polynomials are used, which becomes computationally expensive, the result is generally a smooth wavefront map.

The smooth nature of the reconstructed wavefront tends to mask localized thermal blooming. Ryan Lawrence [12] found that Zernikes were inappropriate for describing point absorbers and scanning CO_2 laser compensation. Recall from the requirements for the wavefront sensor, Section 1.3.2, that after wavefront reconstruction one must be able to resolve the thermal lensing from a point absorber. For this reason modal reconstruction is considered to be inappropriate for use in a Hartmann sensor measuring thermal lensing in the optics of a GWI.

3.3.5.2 Zonal wavefront reconstruction

Zonal wavefront reconstruction determines the best fit wavefront at the center of each of the holes in the Hartmann plate. The advantage of this technique is that it typically provides richer information than the modal technique [95]. Numerical integration can produce rounding errors when there are sharp peaks in the wavefront. The following is a description of a reconstruction technique reported by Southwell, which uses the Gauss-Seidel iteration.

An iterative algorithm can be used to reconstruct the wavefront, W_m, at each of the M points on the Hartmann sensor from the discrete gradient field, G_m, given by

$$G_m = \left\{ (x,\, y)\ ,\ \left(\frac{\partial \mathrm{W}}{\partial x}\ ,\ \frac{\partial \mathrm{W}}{\partial y} \right) \right\}_m .$$

First, the nearest neighbours of each point must be found. The nearest neighbours of a point are defined as those points the distance to which lies within the range $h_\mathrm{p} \pm \varepsilon/2$, as illustrated in Figure 3.19, where h_p is the hole

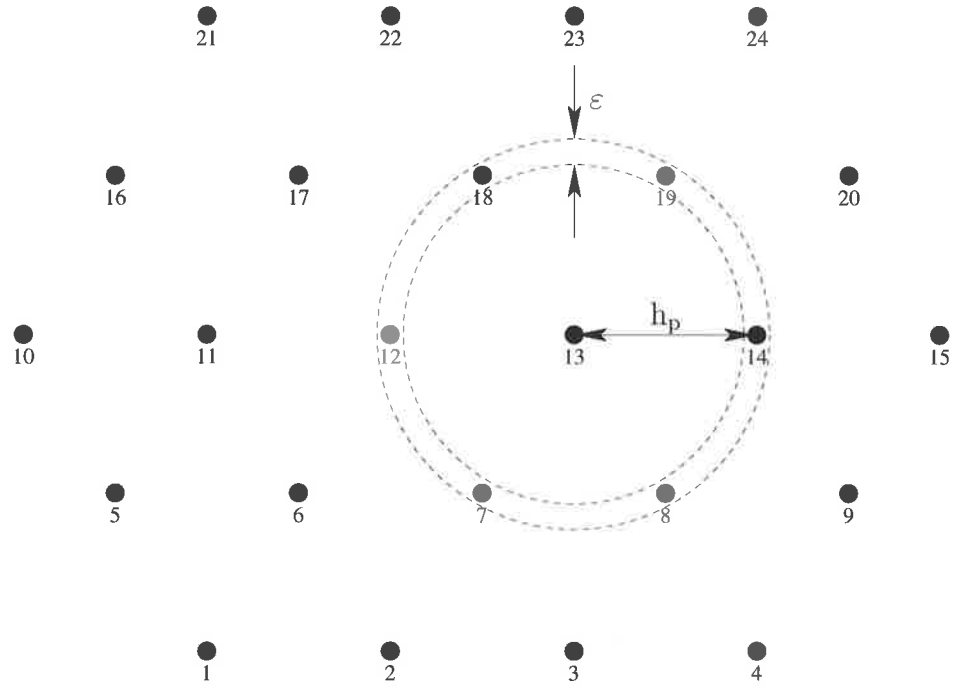

Figure 3.19: Hartmann spots arranged in a hexagonal grid and numbered from 1 to 24. The nearest neighbours of the 13^{th} spot are those lying within the dashed annular region of inner radius $h_{\text{p}} - \varepsilon$ and outer radius $h_{\text{p}} + \varepsilon$.

spacing of the array of spots. This can be expressed as an $M \times M$ matrix, Λ_{mn}:

$$\Lambda_{mn} = \begin{cases} 1 & \text{if} \quad |\,\vec{x}_m - \vec{x}_n\,| - h_{\text{p}} \leq \varepsilon \\ 0 & \text{if} \quad |\,\vec{x}_n - \vec{x}_n\,| - h_{\text{p}} > \varepsilon \end{cases}$$

where $\vec{x}_m$ designates the m^{th} point, $\vec{x}_n$ designates the n^{th} point and where the tolerance value, ε, is included to allow for any small deviations from a hexagonal array.

Next, a matrix of wavefront differences between nearest neighbours, $\Delta\mathbf{w}^{\text{neighbours}}$ is defined:

$$\Delta \text{w}_{mn}^{\text{neighbours}} = \begin{cases} \Delta \text{w}_{mn} & \text{if} \quad |\,\vec{x}_m - \vec{x}_n\,| - h_{\text{p}} \leq \varepsilon \\ 0 & \text{if} \quad |\,\vec{x}_m - \vec{x}_n\,| - h_{\text{p}} > \varepsilon \end{cases},$$

where the wavefront difference, Δw_{mn}, between a point, $\vec{x}_m$, and its neigh-

bour, $\vec{x}_n$, is found using the Improved Euler-Cauchy method (Heun's method) [96]:

$$\begin{aligned} \Delta \mathrm{w}_{m\,n} &= \frac{1}{2}\left[\left(\frac{\partial \mathrm{W}}{\partial x}\right)_m + \left(\frac{\partial \mathrm{W}}{\partial x}\right)_n\right] \times (x_m - x_n) + \\ &\quad \frac{1}{2}\left[\left(\frac{\partial \mathrm{W}}{\partial y}\right)_m + \left(\frac{\partial \mathrm{W}}{\partial y}\right)_n\right] \times (y_m - y_n) \end{aligned} \tag{3.14}$$

The wavefront can be now be reconstructed using Gauss-Seidel iteration as follows:

1. Begin with a flat wavefront map as a zeroth guess, such that

$$\mathrm{W}_{m,\,0} = 0$$

2. Determine the k^{th} wavefront map, $\mathrm{W}_{m,\,k}$, by updating each value in the map, $\mathrm{W}_{m,\,k-1}$, using the matrix $\Delta\mathbf{w}^{\mathrm{neighbours}}$:

$$\mathrm{W}_{m,\,k} = \frac{\sum_{j=1}^{N} \Delta \mathrm{w}_{m\,j}^{\mathrm{neighbours}} + \sum_{j=1}^{N} \Lambda_{m\,j} \times \mathrm{W}_{j,\,k-1}}{\sum_{j=1}^{N} \Lambda_{m\,j}} \tag{3.15}$$

   In the Jacobi method, the wavefront is updated as a whole. That is, all the wavefront values, $\mathrm{W}_{m,\,k}$ are updated from a previous set of values

$$\{\mathrm{W}_{1,\,k-1}, \mathrm{W}_{2,\,k-1}, \ldots, \mathrm{W}_{m-1,\,k-1}, \mathrm{W}_{m,\,k-1}, \ldots, \mathrm{W}_{N,\,k-1}\}$$

   In Gauss-Seidel method, the wavefront value $\mathrm{W}_{m,\,k}$ is updated from a set including the most recently updated values

$$\{\mathrm{W}_{1,\,k}, \mathrm{W}_{2,\,k}, \ldots, \mathrm{W}_{m-1,\,k}, \mathrm{W}_{m,\,k-1}, \ldots, \mathrm{W}_{N,\,k-1}\}$$

3. Repeat step 2 until the change between successive iterations is less than a previously defined error value.

4. Once the wavefront, W_m, has been reconstructed at the discrete points, $\vec{x}_m$, use linear interpolation to convert the discrete hexagonal array of wavefront values into a 2D Cartesian array suitable for display as a contour plot.

In certain cases, the wavefront is such that it appears likely that rounding error will occur in the numerical integration. The wavefront may contain a sharp peak, for example. In this case, the rounding error can be reduced by artificially adding points into the discrete gradient field, such that a new point lies between two of the original points in the gradient field and the gradient of the new point is determined by interpolating the gradients of several of the surrounding points.

3.3.5.3 Error propagation - From gradient to wavefront

The mean square error (variance) in the reconstructed wavefront, σ^2_{W}, depends on the variance in the wavefront difference between adjacent holes, $\sigma^2_{\Delta\mathrm{W}}$. It can be predicted using

$$\sigma^2_{\mathrm{W}} = C_{\Delta\mathrm{W}}\,\sigma^2_{\Delta\mathrm{W}} \tag{3.16}$$

where $C_{\Delta\mathrm{W}}$ is the Southwell noise coefficient, [62], and the variance in the wavefront difference between adjacent holes, $\sigma^2_{\Delta\mathrm{W}}$, is given by

$$\sigma^2_{\Delta\mathrm{W}} = \left[\frac{h_{\mathrm{p}}}{L}\left(\frac{\sigma_{x_c} + \sigma_{y_c}}{2}\right)\right]^2 \tag{3.17}$$

where σ_{x_c} and σ_{y_c} are the rms errors in the x and y centroids, respectively, h_{p} is the distance between the holes in the Hartmann plate and L is the lever arm of the Hartmann sensor.

As pointed out by Southwell [62], $C_{\Delta\mathrm{W}}$ is dependent on the number and arrangement of holes. Following Southwell's methodology, the noise coefficient was numerically determined as a function of the number of holes in a hexagonal close-packed arrangement and the results are shown in Figure 3.20.

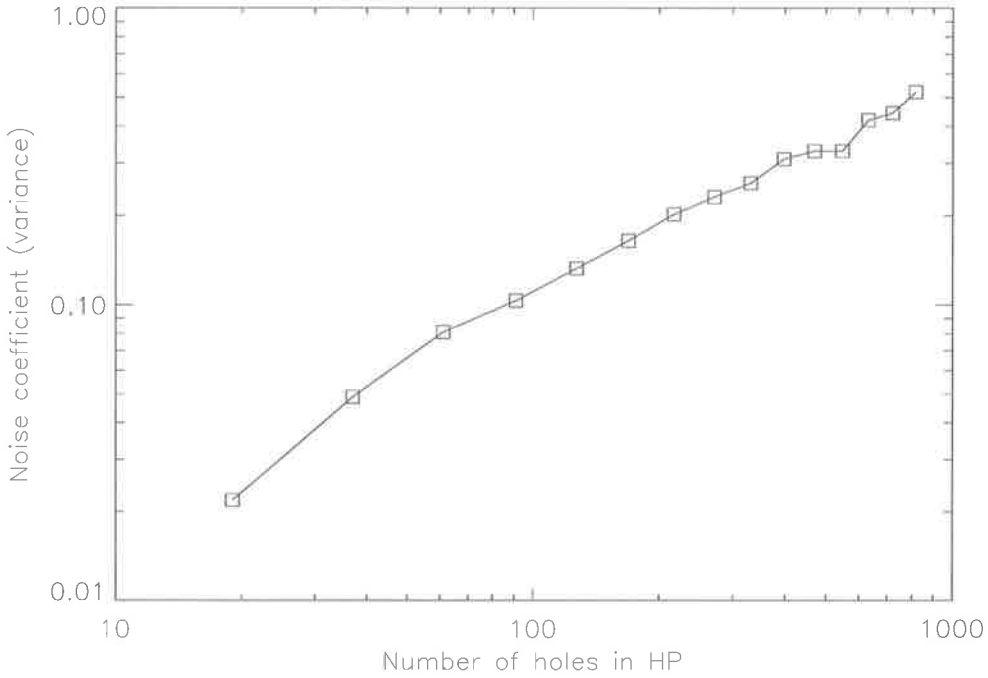

Figure 3.20: The Southwell noise coefficient of the Gauss-Seidel iterative matrix wavefront reconstruction versus the number of holes in the HP. A hexagonal close-packed arrangement of spots was used. Note that this result assumes that the noise in the gradient field is uncorrelated.

This coefficient allows one to predict the noise in the overall reconstructed wavefront if the noise in the gradient field is uncorrelated. The actual noise is determined by analyzing the reconstructed wavefront. Note that $C_{\Delta W} < 1$ for the approximately 700 holes required for a HWS for advanced GWI and thus the zonal reconstruction reduces the effect of uncorrelated noise in the gradient field on the reconstructed wavefront.

3.3.6 Summary of noise sources

The noise sources discussed in the previous sections are summarized below for convenience.

- Coherent Noise: An incoherent source was chosen to mitigate the effects

of noise due to parasitic interference fringes caused by transmissive beam-control optics.

- Cross-talk: It was established in Section 3.3.2 that the level of cross-talk between neighbouring spots is about 0.08% of the signal size, or one part in 1250. Hence, for a signal with a maximum size of 200 nm, the cross-talk is not expected to produce an error greater than 0.16 nm.

- Random noise: (shot noise, readout noise and digitization). The error in the centroid due to these random noise sources is expected to be about 0.19% pixel using the WCoG algorithm and 0.34% using the FPC algorithm, (see Table 3.9). Using Equations 3.16 and 3.17 and a noise coefficient for the variance of approximately 0.4 (see Figure 3.20 for 700 gradient measurements) the rms wavefront error is estimated to be 0.6 nm for the WCoG algorithm and 1.1 nm for the FPC algorithm. Since these noise sources are random, this can be improved by averaging.

- $S_{\text{thermal}}(T)$: One can specify the maximum permissible temperature fluctuation, $\Delta T_{\max}$, such that the error from this source is not greater than $W_{\varepsilon_{\max}} = \lambda/467$ @ 633 nm = 1.35 nm.

$$\begin{aligned} \Delta T_{\max} &= W_{\varepsilon_{\max}} \left(\frac{2}{d^2 \frac{S_{\text{thermal}}}{\Delta T}} \right) \\ &\approx 0.04\,\text{K} \end{aligned}$$

The largest source or error in the sensor is expected to be random noise in the CCD (shot noise, readout noise and digitization uncertainty). This will contribute an error of approximately 0.6 nm, or about $\lambda/1050$ @ 633nm, to a wavefront measurement of thermal lensing in a GWI, which is substantially better than the sensitivity required for the wavefront sensor in Advanced LIGO. If, in addtion, there is a signal of approximately 200 nm to be measured, cross-talk will also contribute and the total error will be approximately

0.76 nm or about $\lambda/830$ @ 633nm.

3.4 Conclusion

The design and development of a HWS for advanced GWI has been presented in this chapter. Random noise in the CCD has been identified as the major error source in the HWS limiting the sensitivity to about $\lambda/1050$ @ 633nm - a value that can be improved with averaging due to the random nature of the noise. In the next chapter, diagnostic testing of and measurements using this sensor are described and the improvement of the sensitivity with averaging is demonstrated.

Chapter 4

Testing the sensor

4.1 Introduction

This chapter focusses on the calibration and testing of the Hartmann wavefront sensor (HWS) described in Chapter 3. The accuracy of the sensor is determined by that of the pixel spacing, p_s, and the lever arm, L, used to convert the transverse displacement of the Hartmann spots to the gradient field corresponding to the wavefront change. The measurement of p_s was described in Section 3.3.3.3, yielding $11.975 \pm 0.005\mu$m. The measurement of L will be discussed in Section 4.2. The sensitivity (precision) of the HWS is expected to be affected by the light source used for the HWS, see Section 3.3.1, and fluctuations in the temperature of the HWS, see section 3.3.2.4. In Sections 4.3 and 4.4, therefore, a comparison of the noise floor of the centroids in the HWS for different light sources and a measurement of its temperature sensitivity are described.

For a suitable light source and temperature stability, the sensitivity of the HWS is expected to be limited by photoelectron shot noise. Thus, in Section 4.5, a measurement is described of the noise floor of the HWS and the improvement that can be obtained by averaging the centroid positions over multiple Hartmann images. The measurement of a small known wavefront change to determine the accuracy of the HWS is described in Section 4.6.

4.2 Lever arm calibration

The nominal value of the lever arm, L, the distance between the Hartmann plate and the CCD, in the fully assembled Hartmann sensor is approximately 10 mm. Given that every gradient measurement of the sensor relies on this value, any error in it reduces the *accuracy* of the sensor. As this error is common to all measurements it thus represents a systematic error. It was therefore necessary to refine the value of the lever arm.

An experiment that precisely and accurately determines the lever arm of the Hartmann wavefront sensor is illustrated in Figure 4.1. Vertical needles that could be bolted coaxially to tapped holes were designed. These were bolted, at various times, into the regular grid of holes in a Newport RS Series Research Grade Optical Table at positions A, B, C and D. Position E, shown in Figure 4.1, contained no vertical needle, but was the intersection of the line through BD and the line parallel to AB that passed through C. The HWS was placed at the point of intersection of the line through AB and the line through CD and was approximately normally incident to AB, the precise angle of incidence not being critical.

A HeNe laser beam was aligned to needles at A and B by overlapping their shadows. The needles were removed and the resulting spot pattern was recorded and centroided 25 times. The mirrors M1 and M2 were then used to align the beam to needles at positions C and D, again by overlapping their shadows. The needles were removed and the new spot pattern was recorded and centroided 25 times. This procedure was repeated 4 times.

Figure 4.2 shows the horizontal translation of the measured centroids. The average measured horizontal displacement, Δx, was 286.1 ± 0.3 pixels, approximately $4.6\times$ the horizontal-hole-spacing. Using this value and similar triangles, it is straightforward to determine L

$$L = \Delta x \, p_s \frac{|\mathrm{AB}|}{|\mathrm{BD}| - |\mathrm{AC}|}$$

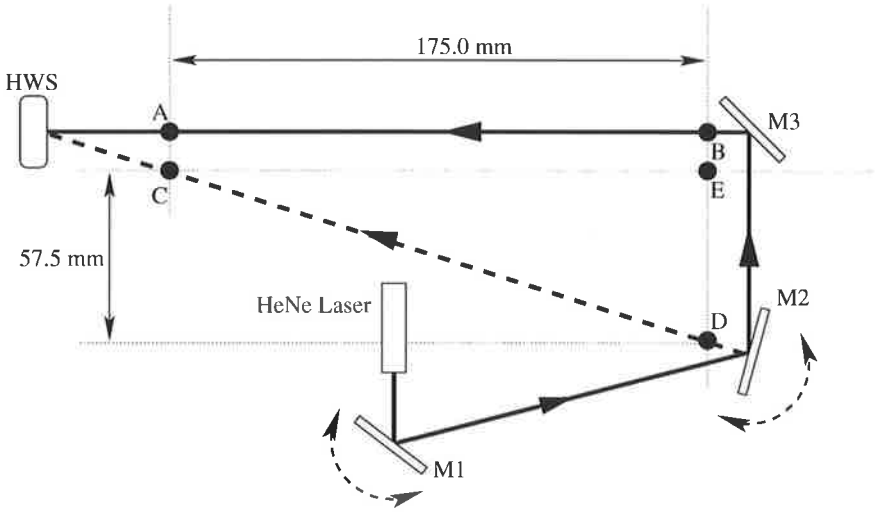

(a) Lever arm measurement experiment

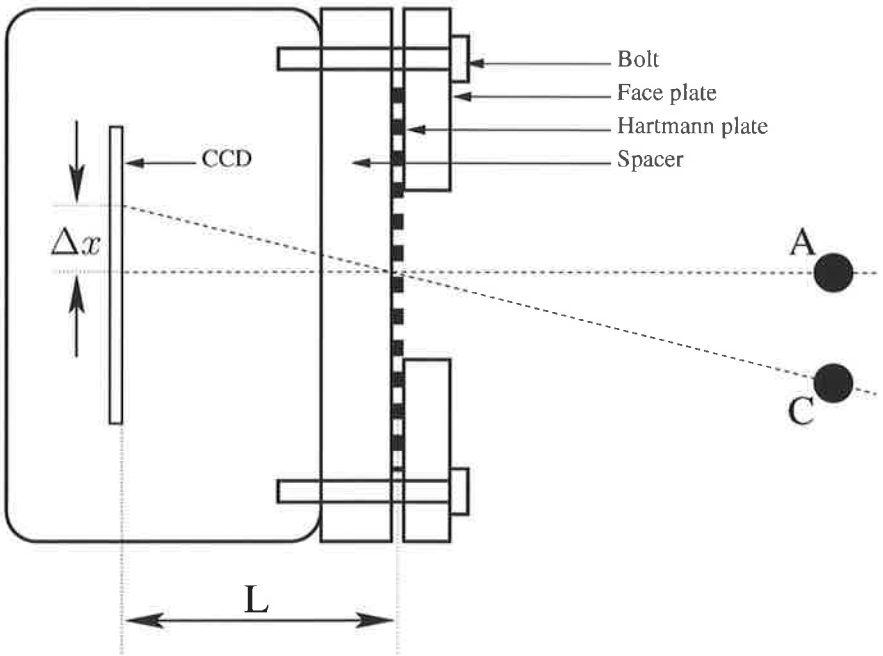

(b) Lever arm measurement experiment - zoom

Figure 4.1: Schematic of the experiment used to calibrate the lever arm.

$$= \Delta x \, p_{\mathrm{s}} \frac{|\mathrm{AB}|}{|\mathrm{DE}|} \tag{4.1}$$

where p_{s} is the previously determined value of the pixel size (see Section 3.3.3.3). Since $|\mathrm{AB}| = 1750.0 \pm 0.5$ mm and $|\mathrm{DE}| = 575.0 \pm 0.5$ mm, $L = 10.43 \pm 0.02$ mm. The errors in $|\mathrm{AB}|$ and $|\mathrm{DE}|$ are given by the error in the placement of the tapped holes in the optical table and is set, rather conservatively, to 0.5 mm.

The assumption of similar triangles is limited by the degree to which the HWS is not normally incident to the beam $|\mathrm{AB}|$. If the HWS is rotated away from normal incidence by a small angle $\delta\theta$, then there will be a scaling error in the similar triangles assumption of the order of $\delta\theta^2/2$ when $\delta\theta$ is given in radians. For instance, if $\delta\theta = 2.5$ degrees then the scaling error is approximately 0.1%. Since the HWS can easily be aligned to better than 2.5 degrees the similar triangles assumption is assumed to be completely valid.

The accuracy of L is determined by the accuracy of Δx, p_{s}, $|\mathrm{AB}|$ and $|\mathrm{DE}|$. However, in a wavefront measurement, transverse spot displacements, Δx_i, are converted to wavefront gradients, $\partial \mathrm{W_i}/\partial x$, using

$$\frac{\partial \mathrm{W_i}}{\partial x} = \frac{\Delta x_i \, p_{\mathrm{s}}}{L} = \frac{\Delta x_i}{\Delta x} \frac{|\mathrm{DE}|}{|\mathrm{AB}|}$$

It is clear that the accuracy of a gradient measurement is limited by Δx_i, $|\mathrm{AB}|$ and $|\mathrm{DE}|$.

4.2.1 Discounting other solutions due to pattern degeneracy

The other possible, though unlikely, solutions, corresponding to spot pattern displacements of 3.6× and 5.6× the horizontal-hole-spacing, would give $L = 8.17$ mm and $L = 12.71$ mm. These solutions were discounted by comparing the spot profile with numerical predictions as described below. The cross-sections of measured spots at two different wavelengths, $\lambda = 632.8$ nm

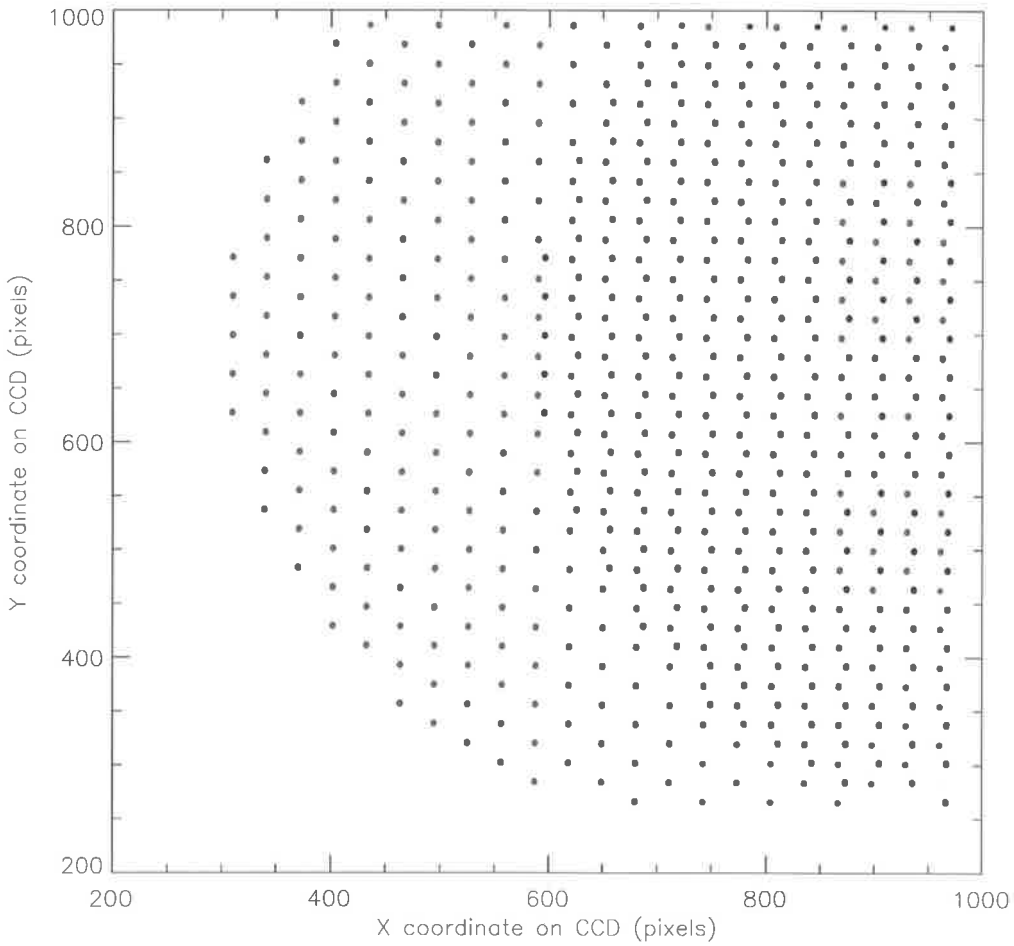

Figure 4.2: The measured centroids on the CCD for the HeNe aligned with needles A and B (red) and with needles C and B (blue). Note that the circular mask was digitally added after the measurement as a visual aid.

(coherent) and $\lambda = 820$ nm (incoherent), were compared to the cross-sections of a simulation using ZEMAX for the three potential solutions for the lever arm. The results are shown in Figure 4.3. The best matches between the measured and simulated diffraction patterns are in Figure 4.3 c) and d) corresponding to a lever arm of 10.43 mm, thus verifying the previous result. Additionally, this result is consistent with a lever arm of approximately 11 mm, determined using a schematic diagram of the CCD camera and a measurement of the spacer thickness.

The comparison of the measured and simulated diffraction patterns to verify the lever arm measurement provides some interesting information about the diffraction of the rays from the Hartmann plate. However, it would have been unnecessary to verify the lever arm measurement using this comparison in the absence of pattern degeneracy. A simpler measurement would have covered all holes except for a single column and used the displacement of the spots from that column to measure the lever arm.

4.3 Comparison of incoherent and coherent light sources

The Hartmann sensor should have lower noise when illuminated with light from a broadband source because this light is free of coherent effects that can cause fluctuations in the intensity pattern illuminating the sensor. To test this, the distribution of centroid fluctuations in the Hartmann sensor was investigated when it was illuminated with different light sources, coherent and incoherent, and operated under different conditions as shown in Figure 4.4. The incoherent source was the fibre-coupled super luminescent diode (SLD) described in Section 3.3.1 and the coherent source was a HeNe laser beam.

In Tests 1 & 2 the wavefront from a light source diverged from the source onto a Hartmann sensor placed a short distance away. In Tests 3 & 4 the light propagated through a series of transmissive optical elements before be-

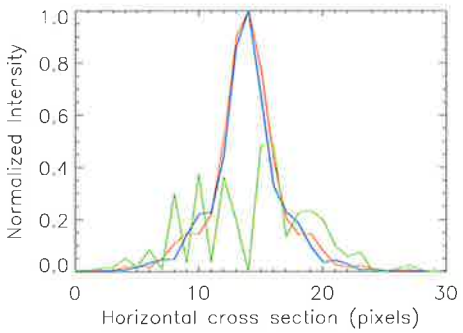

(a) L = 8.17 mm, λ = 632.8 nm

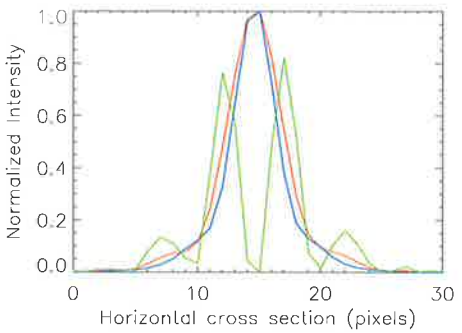

(b) L = 8.17 mm, λ_{peak} = 820 nm

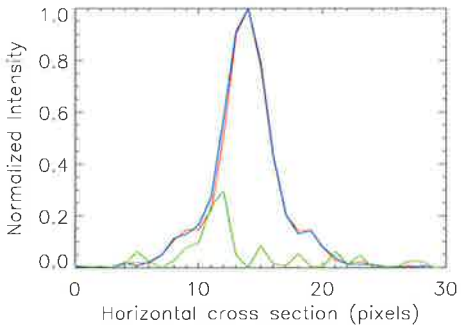

(c) L = 10.43 mm, λ = 632.8 nm

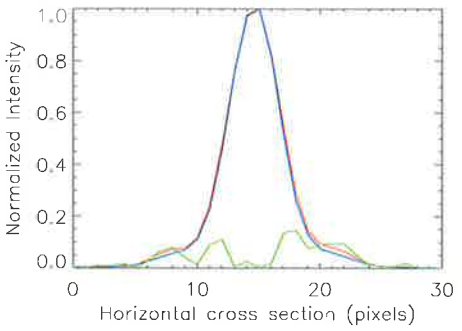

(d) L = 10.43 mm, λ_{peak} = 820 nm

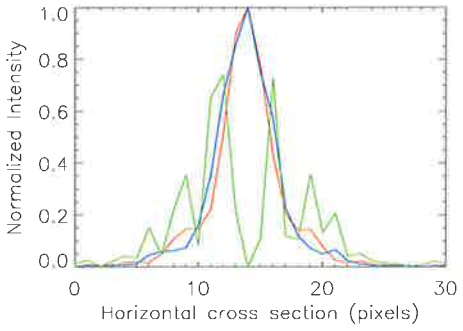

(e) L = 12.71 mm, λ = 632.8 nm

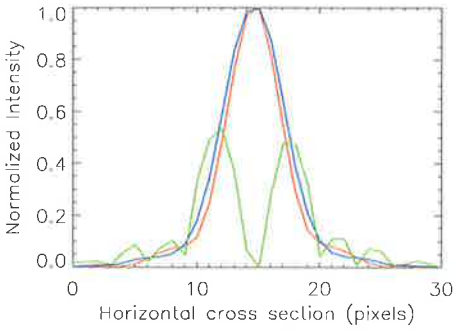

(f) L = 12.71 mm, λ_{peak} = 820 nm

Figure 4.3: Intensity cross sections from measured Hartmann spots (red) illuminated with a), c), e) 632.8 nm coherent light and b), d), f) 820 nm incoherent light. Physical optics simulations by ZEMAX (blue) are also plotted. 5 $\times$ the magnitude of the difference is also shown (green). The best match between measured and simulated is at 10.43mm.

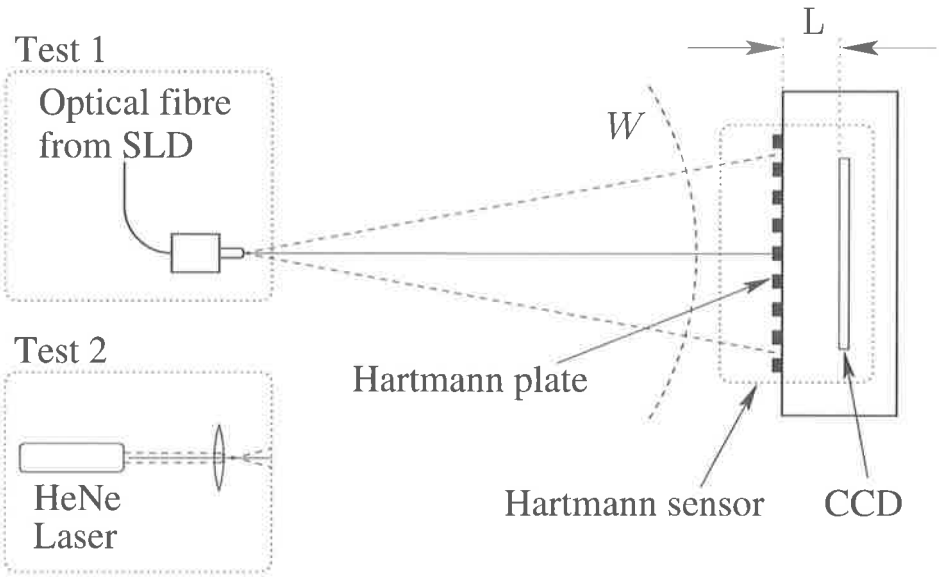

(a) Tests 1 & 2 - no intermediate optics

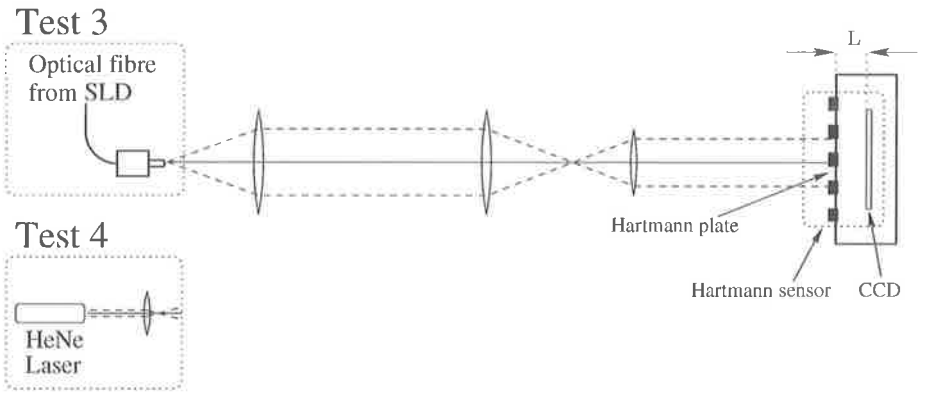

(b) Tests 3 & 4 - multiple intermediate optics

Figure 4.4: Experimental setup to test the precision of the Hartmann sensor. a) Test 1: An incoherent source (output from a fibre coupled SLD) directly illuminates the Hartmann wavefront sensor. Test 2: A HeNe laser beam focussed to form a waist that directly illuminates the Hartmann wavefront sensor. b) Test 3: An incoherent source that propagates through multiple transmissive optics illuminates the Hartmann wavefront sensor. Test 4: A HeNe laser beam that propagates through multiple transmissive optics illuminates the Hartmann wavefront sensor.

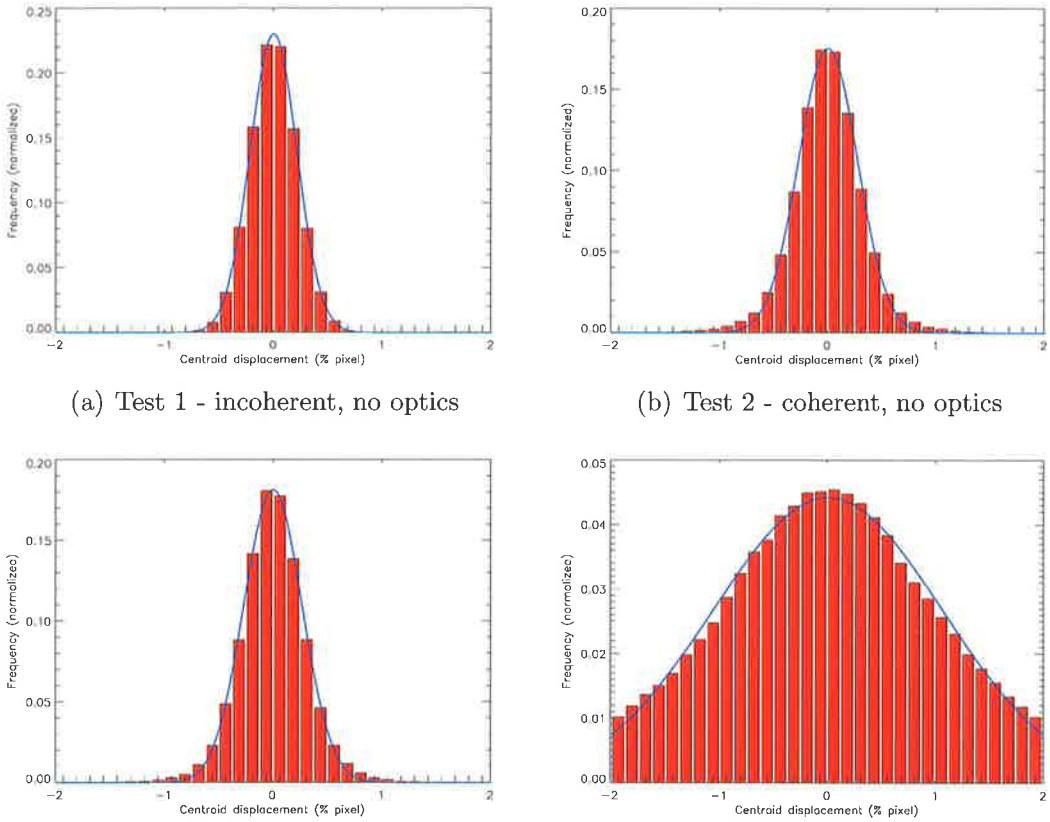

(a) Test 1 - incoherent, no optics

(b) Test 2 - coherent, no optics

(c) Test 3 - incoherent, multiple optics

(d) Test 4 - coherent, multiple optics

Figure 4.5: The distribution of the deviations of each of the M centroids from its average value for each Test and best fit Gaussians. a) Test 1: incoherent illumination and no optics between source and Hartmann sensor, b) Test 2: coherent illumination and no optics, except a single imaging lens, between source and Hartmann sensor, c) Test 3: incoherent illumination and multiple optics between source and Hartmann sensor, d) Test 4: coherent source and multiple optics between source and Hartmann sensor.

ing incident upon the Hartmann sensor. A series of N images of the M Hartmann spots was recorded over a short period of time for each set-up. The patterns were analyzed using the FPC algorithm described in Section 3.3.4.2 to obtain a list of all centroids over all images. For simplicity, the analysis only considered the x component of the centroids.

For each test, the average centroids for the j^{th} spot from N images, $\overline{x_j}$, was calculated using

$$\overline{x_j} = \frac{\sum_{i=1}^{N} x_{ij}}{N}, \quad \text{where} \quad j = 1, \ldots, M.$$

The deviations, Δx_{ij}, of each of the M centroids from its average value for all images were determined using

$$\Delta x_{ij} = x_{ij} - \overline{x_j}, \quad \text{where} \quad i = 1, \ldots, N.$$

The distributions of the deviations for the four tests are plotted in Figure 4.6 and are compared to a best fit Gaussian. The width of the distribution in Tests 1-3 is consistent with the shot noise limit, 0.34% of a pixel for the FPC algorithm, established in Section 3.3.4.3, and the good agreement with the Gaussian distributions shows that the distribution of centroid deviations are largely random. The distribution of centroid deviations in Test 4 is much wider, indicating an additional noise source.

The RMS deviation of the centroids in the i^{th} image, from those in the initial image, is defined as

$$\sigma_{\text{cent}_i} = \sqrt{\frac{\sum_{j=1}^{M} (x_{ij} - x_{0j})^2}{M-1}}.$$

and the temporal variation of this RMS deviation is shown in Figure 4.6. Since the graphs for Test 1,2 & 3 are independent of i, the fluctuations in the centroids are random. Futhermore, the RMS deviation for these tests is similar to the 0.34% shot-noise floor predicted in the previous chapter. For

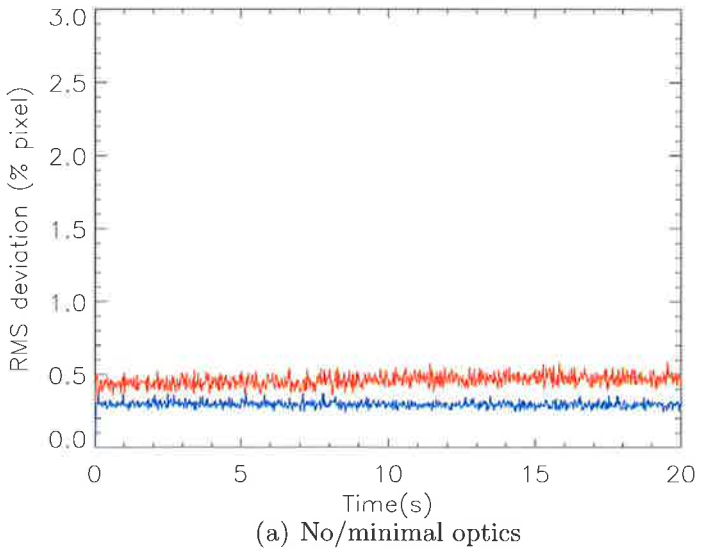

(a) No/minimal optics

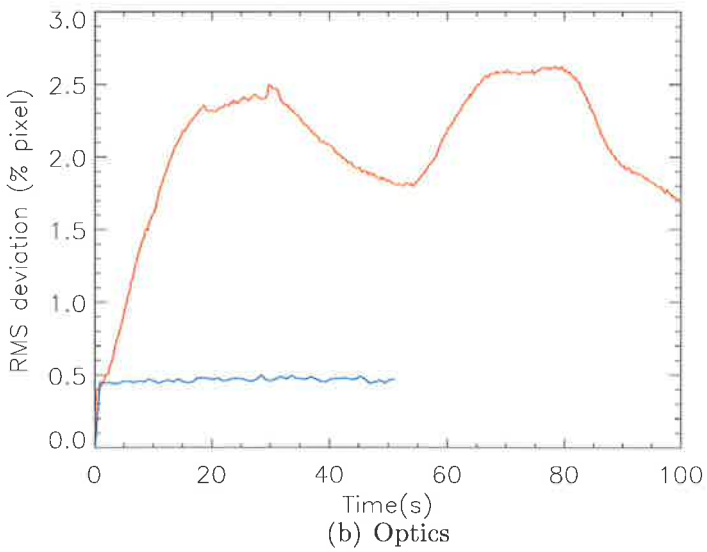

(b) Optics

Figure 4.6: RMS centroid difference between each set of centroids and the first image set vs time. a) Tests 1 & 2: incoherent source (blue) and coherent source (red), no optics between source and Hartmann sensor. b) Tests 3 & 4: incoherent source (blue) and coherent source (red), multiple optics between source and Hartmann sensor. Note that the incoherent source test (blue) was run for approximately 50 s and the coherent source test (red) for approximately 100 s.

Test 4, however, it is clear that there is a large temporal variation in the RMS deviation. This is further evidence for some non-random noise component. The most plausible explanation for this component is the presence of interference fringes in the intensity pattern, acquired from multiple reflections in the transmissive optics, resulting in fluctuations in the Hartmann spots that are not due to the variations in phase of the wavefront.

These results clearly demonstrate that using an incoherent source as a probe beam yields a more robust Hartmann wavefront sensor as the incoherent source remains shot-noise limited in scenarios where a coherent source does not.

4.4 Temperature dependence of HWS

As discussed in Section 3.2.5, if Hartmann sensor measurements are made before and after a temperature change then there could be an apparent change in the wavefront where none exists. This change would appear as the primary aberration defocus.

A measurement was made of this temperature dependent error using a system very similar to that shown in Figure 4.4 a). The HWS was turned on, at t = 0, and illuminated with light from the SLD. Two temperature sensors, one on the A/D converter and the other on the CCD sensor board, recorded the temperature of the camera from t = 22.5 s. Centroiding the Hartmann patterns and calculating the apparent defocus, relative to the first pattern, commenced at t = 34.0 s.

The results of these measurements are plotted in the semi-logarithmic plot in Figure 4.7. The red and blue data show the temperature at the A/D converter and CCD sensor, respectively. Notice that the temperature of the A/D converter starts increasing immediately, while the intial increase in the temperature of the CCD is much slower and ultimately settles on a lower value. The initial increase in the resultant apparent defocus (green data) is delayed further still. This indicates that the heat in the camera is generated

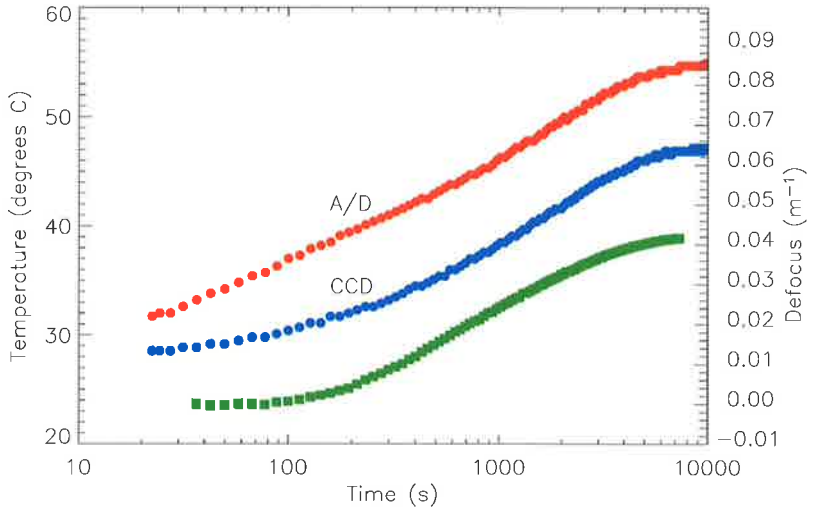

Figure 4.7: Temperature on the A/D board of the camera (red) and temperature on the CCD sensor (blue). Apparent defocus, relative to the initial state, measured by HWS (green).

in the immediate vicinity of the A/D converter and diffuses first to the CCD and, subsequently, to the Hartmann plate.

Figure 4.8 is a scatter plot of the defocus and the temperature on the A/D converter for measurements that were recorded at the same time. Notice that there is a one-to-one and approximately linear relationship between defocus and temperature. Also shown is the line of best fit, with a slope of $0.0025\,\mathrm{m}^{-1}\,\mathrm{K}^{-1}$. Recall that an estimate, $0.00195\,\mathrm{m}^{-1}\,\mathrm{K}^{-1}$, of this coefficient was determined in Section 3.3.2.4.

The approximate linear relationship between defocus and temperature and the reasonable agreement between the expected and measured values of the coefficient of the temperature dependence of defocus are strong evidence for the existence of a temperature dependent error in the Hartmann sensor that is consistent with the physical argument presented in Section 3.2.5. Also illustrated by this experiment is the necessity of allowing the Hartmann sensor approximately 3 hours to reach a steady state temperature before it should be used.

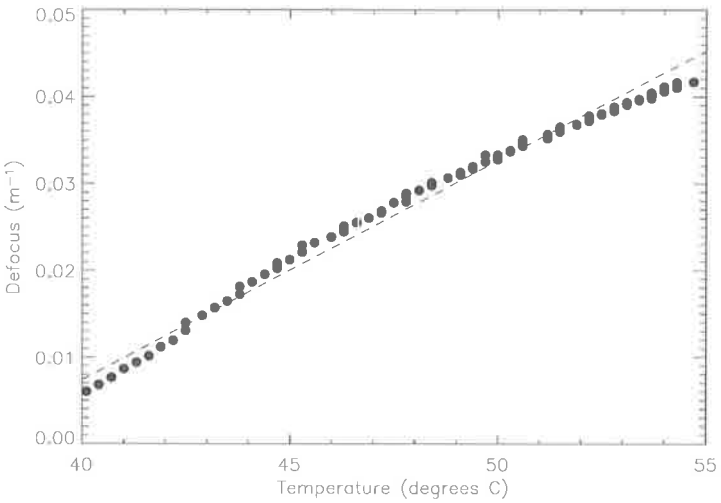

Figure 4.8: Scatter plot of the measured defocus vs temperature. The dashed line is the best linear fit and has a slope = $0.0025\,\mathrm{m}^{-1}\,\mathrm{K}^{-1}$

4.5 Noise floor of the Hartmann sensor

The equivalent wavefront error due to noise in the sensor was measured using the system shown in Figure 4.4 a) using the 820nm fibre-coupled superluminescent diode (SLD). Spot centroids[1] were calculated for consecutive Hartmann images separated in time by 15 s and the average prism (tip/tilt) in each image was removed. These zero-prism centroids were used to calculate the error in the discrete gradient field and subsequent wavefront change. A typical gradient field and map of the wavefront change, which has an RMS error of $\lambda/1450$, are shown in Figure 4.9 a) and b), respectively. The RMS error for these maps varied between $\lambda/1000$ and $\lambda/2000$ which is consistent with the shot noise limit, established in Section 4.3, and the Southwell noise coefficient (see Section 3.3.5.3), $C_{\Delta \mathrm{W}} = 0.2$, calculated for $N_{\mathrm{holes}} = 263$ used in this example. In general, the RMS wavefront error for a zonal reconstruction across *all holes*, assuming uncorrelated noise, is given by $C_{\Delta \mathrm{W}}^{1/2} \times \sigma_{\Delta W}$, where $\sigma_{\Delta W}$ is the RMS wavefront difference between *adjacent holes*, which was defined in Equation 3.17 and is repeated here.

[1] All the remaining experiments in this chapter used the WCoG algorithm to calculate the spot centroids.

$$\sigma_{\Delta W} = \frac{h_{\mathrm{p}}}{L}\,\sigma_{\Delta y} \tag{4.2}$$

where $\sigma_{\Delta y}$ is the average RMS error in the individual centroids.

If the statistical characteristics of the noise do not vary with time (i.e. the noise is stationary) then the wavefront error should be reduced by averaging over multiple Hartmann images. To test this, a sequence of 2000 Hartmann images was recorded at 30 images/second and the global prism was removed from each image. A set of reference centroids was then calculated by averaging over $N_{\mathrm{ref}} = 1000$ images, consisting of the first and last 500 images. The central 1000 images were used to calculate sets of centroids averaged over N_{avg} images, where $N_{\mathrm{avg}} = 1, \ldots, 990$. This process ensured that the reference and average centroids were statistically independent. The procedure was repeated 5 times. The dependence of $\sigma_{\Delta W}$ on N_{avg} is plotted in Figure 4.10, showing that $\sigma_{\Delta W} < \lambda/15,500$ at $N_{\mathrm{avg}} = 990$.

The prediction of a numerical simulation that assumes stationary random noise given by

$$\sigma^2_{\Delta W}\left(N_{\mathrm{avg}}\right) = \sigma^2_{\Delta W,1}\left(\frac{1}{N_{\mathrm{avg}}} + \frac{1}{N_{\mathrm{ref}}}\right) \tag{4.3}$$

is also plotted in Figure 4.10, where $\sigma_{\Delta W,1}$, the $N_{\mathrm{avg}} = 1$ error, is the only free parameter. For small N_{avg}, the error decreases as $N_{\mathrm{avg}}^{1/2}$, as expected and it asymptotically approaches a value that is $N_{\mathrm{ref}}^{1/2}$ below the $N_{\mathrm{avg}} = 1$ error, the limit due to noise in the reference centroids. Note the good agreement between the measurement and the numerical prediction, except for $N_{\mathrm{avg}} > 300$ where the measured error is slightly larger than that predicted.

The RMS wavefront error was approximately $\lambda/15,500$, which is larger than the $\lambda/21,000$ predicted using the Southwell noise coefficient appropriate to this measurement. These discrepancies are probably due to the effect of a low-frequency temperature fluctuation, which is described in Section 4.6.

These results demonstrate that the dominant noise in the Hartmann wavefront sensor is random and well described by Poissonian statistics, which

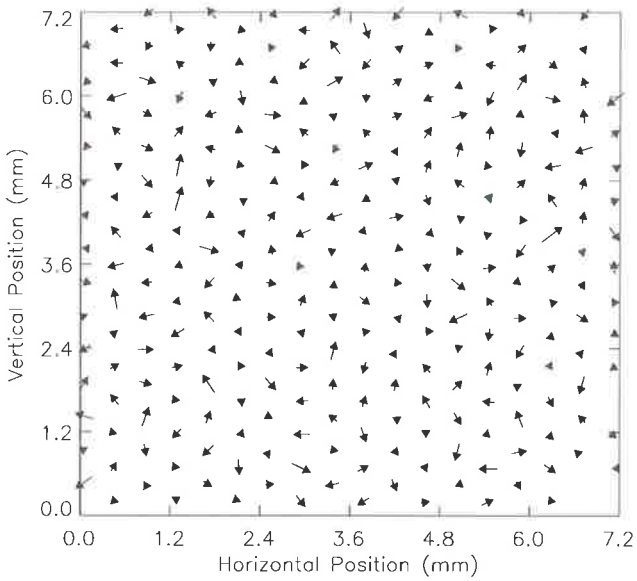

(a) Vector plot of gradient field

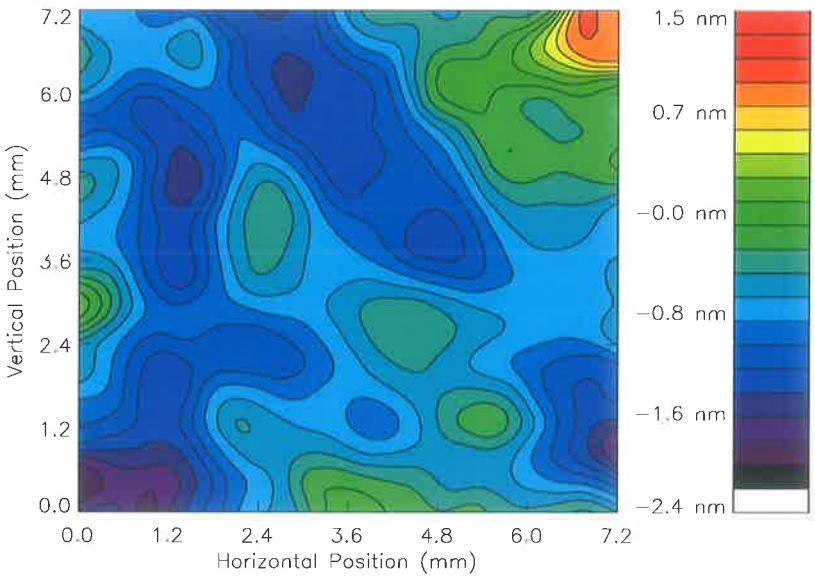

(b) Contour plot of reconstructed wavefront

Figure 4.9: Hartmann sensor measurement of the background shot-noise level made by comparing two Hartmann patterns separated in time by approximately 15 s. Shown here are a) the gradient field of the apparent wavefront change and b) a reconstruction of the apparent wavefront change.

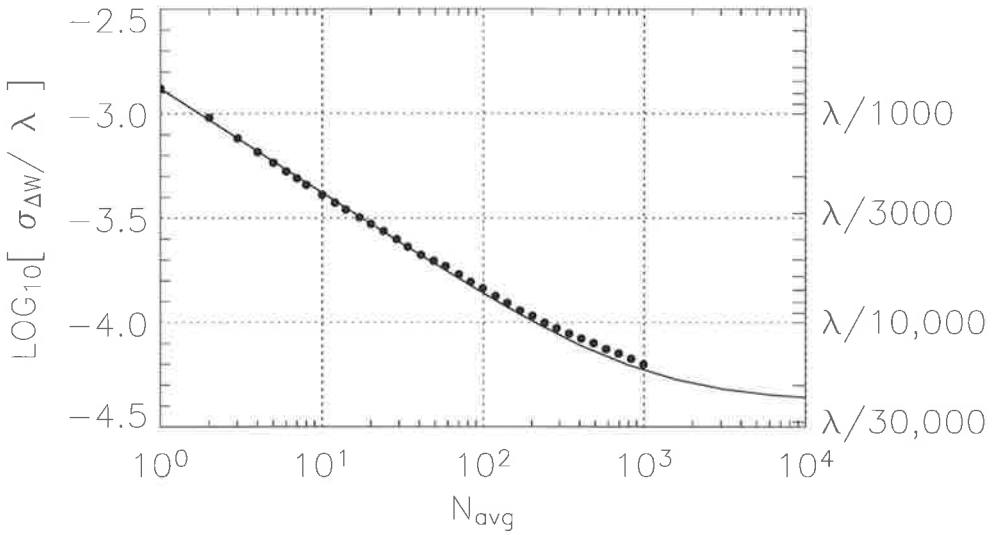

Figure 4.10: The improvement in HWS sensitivity due to averaging over N_{avg} Hartmann images. The solid curve shows the improvement predicted assuming only random, stationary noise in the spot centroids

is consistent with the HWS being shot-noise limited as predicted in Section 3.3.3. The sensitivity is limited when averaging, implying an additional small noise source. It is plausible that thermal expansion of the HP may be a contributing factor to this noise.

4.6 Accuracy test using known wavefront change

A simultaneous measurement of the accuracy and precision of the HWS can be tested by measuring a well-known, and preferably small, wavefront change. Therefore, an experiment was developed to create a small quadratic wavefront change, the primary aberration defocus.

4.6.1 Analytic form of known wavefront change

Consider a wavefront diverging from a point source and incident on a Hartmann sensor a distance z_0 away, as illustrated in Figure 4.11. The equation for the wavefront at height h is

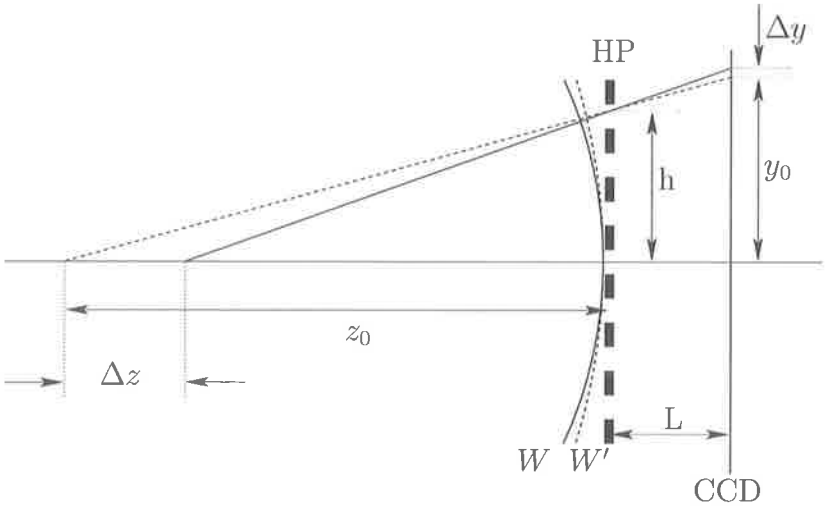

Figure 4.11: Schematic showing the change in direction of a Hartmann ray in the presence of defocus.

$$W(h) = z_0 - \sqrt{z_0^2 + h^2}, \tag{4.4}$$

and the gradient of the wavefront in the paraxial limit is

$$\frac{\partial W}{\partial h} = \frac{h}{z_0}. \tag{4.5}$$

If the source is translated toward the HWS by Δz, the new wavefront W', equal to the original wavefront plus the wavefront change ΔW, has a gradient at height h given by

$$\frac{\partial W'}{\partial h} = \frac{h}{z_0 - \Delta z} \tag{4.6}$$

The gradient of the wavefront change is then given by

$$\begin{aligned} \frac{\partial(\Delta W)}{\partial h} &= \frac{h}{z_0} - \frac{h}{z_0 - \Delta z} \\ &= \frac{-\Delta z\, h}{z_0 (z_0 - \Delta z)} \qquad (4.7) \\ &= S\, h \qquad (4.8) \end{aligned}$$

where S is the primary aberration defocus. The gradient can also be expressed as

$$\frac{\partial(\Delta W)}{\partial h} = \frac{\Delta y}{L} \tag{4.9}$$

$$= \frac{\Delta z}{(z_0 - \Delta z)\,(z_0 + L)}\, y_0 \tag{4.10}$$

The measured wavefront change, which can be made arbitrarily small by reducing Δz, is characterized by plotting $\partial(\Delta W)/\partial h$ versus y_0, determining the slope of the line-of-best-fit and the deviation of the data points about this line. The predicted wavefront change is, therefore, known with the accuracy with which z_0, L and Δz are known.

4.6.2 Experiment design

The layout of the system used to measure Δz and the resulting wavefront change is shown in Figure 4.12. The HWS was illuminated by light emitted from the optical fiber coupled to the 820 nm Agilent HFBR-1414 superluminescent diode described in Section 3.3.1. The fiber was mounted on a micrometer-controlled translation stage to allow the distance, z_0, between the light source and the HWS to be adjusted precisely.

Translation of the fibre end, Δz, was measured using a Michelson interferometer, in which the input beam was split at point A. The object beam of the interferometer was formed by the path A-M_{obj}-A, where $\mathrm{M_{obj}}$ was a mirror mounted on the fibre holder on the translation stage. The reference beam was formed by the path A-B-C-M_{ref}-C-B-A, where M_{ref} was a mirror mounted on the front of the HWS. These beams were recombined on a CCD, and the horizontal cross-section of the interference pattern was recorded as rapidly as the CCD would allow, approximately 13 Hz. To assist in measuring Δz, a small amount or horizontal tilt was introduced between the object and reference beams resulting in vertical fringes on the CCD and a sinusoidal intensity pattern in the horizontal direction, which moved across on the CCD

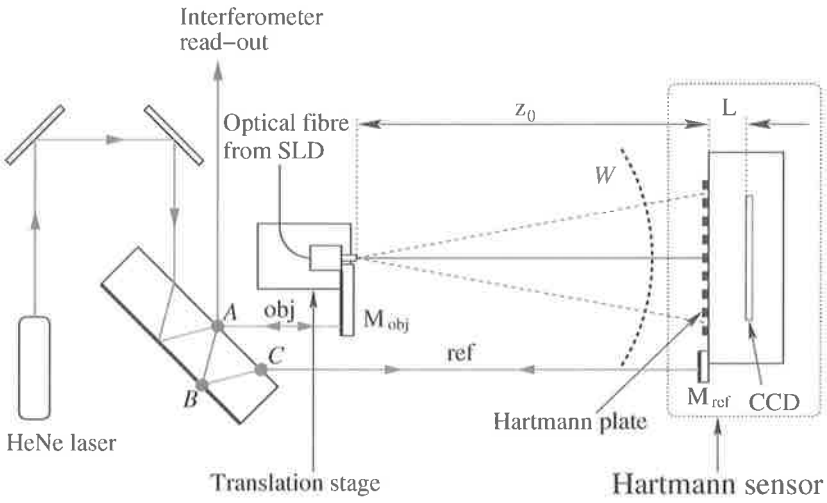

Figure 4.12: A schematic of the Hartmann wavefront sensor and the system used to test the sensor. The sensor was illuminated using a fiber-coupled super luminescent diode (SLD), the free end of which was mounted on a translation stage. Changes in the distance between the fiber end and the Hartmann plate were measured using a Michelson interferometer.

in response to a translation Δz. Fourier analysis was used to filter out all the noise, leaving only the sinusoidal signal. An example of the interference pattern measured by the CCD and the filtered signal are shown in Figure 4.13.

A change, Δz, in the distance between HWS and the fibre holder results in a horizontal translation of the sinusoid by a phase, $\Delta\phi$, given by

$$\Delta\phi = \frac{4\,\pi\,\Delta z}{\lambda} \tag{4.11}$$

If the phase change per CCD frame was less than π then the translation of the sinusoid per frame was unambiguous (i.e. avoided any modulo $2\,\pi$ ambiguity) and the change in phase and thus Δz over time could be tracked. Provided it was varied slowly, Δz could be recorded with approximately 10 nm precision for small translations.

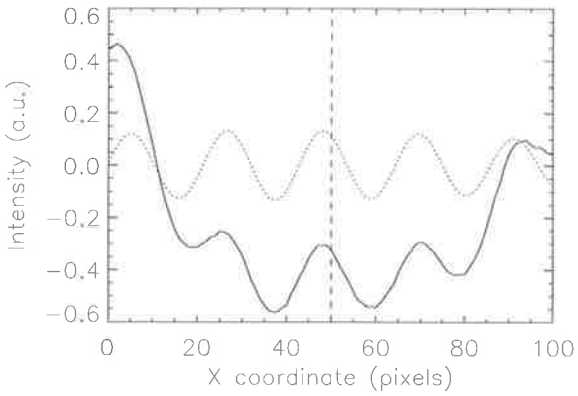

Figure 4.13: A cross-section of the interference pattern output from the Michelson interferometer measured on the CCD. The solid line shows the measured fringes and the dotted line shows the filtered sinuosidal modulation due to the tilt introduce into the reference beam. The vertical dashed line indicates the position at which the phase is measured in every frame.

4.6.3 Calibration of the origin for z_0

The accuracy of the defocus measurement can be determined by comparing the measured defocus with that predicted using Equation 4.10, but this comparison requires an accurate determination of the origin of z_0. The nominal distance between the HP and the fibre end, z_{nom}, can be measured with a ruler with a precision of ± 1 mm. A micrometer or calipers could not be used to measure the nominal because the HP was not a rigid surface. The true distance between the HP and the fibre end is z_0 and will differ from this nominal value by a systematic offset ε_z such that

$$z_0 = z_{\text{nom}} + \varepsilon_z$$

Therefore, if ε_z can be determined and a measurement of z_{nom} exists, then the origin of z_0 can be determined. This can be accomplished by exploiting the non-linear dependence of the gradient of the wavefront change on z_0. Equations 4.7 and 4.9 can be combined to give

$$\frac{\Delta y}{L} = \frac{\Delta z}{z_0 \left(z_0 - \Delta z\right)} h.$$

where the theoretical slope, $\mathrm{m}_{\mathrm{theory}}$, of $\Delta y/L$ versus h is thus

$$\begin{aligned} \mathrm{m}_{\mathrm{theory}} &= \frac{\Delta z}{z_0 \left(z_0 - \Delta z\right)} \\ \mathrm{m}_{\mathrm{theory}}\left(\varepsilon_z\right) &= \frac{\Delta z}{\left[z_{\mathrm{nom}} + \varepsilon_z\right]\left(\left[z_{\mathrm{nom}} + \varepsilon_z\right] - \Delta z\right)}. \end{aligned}$$

If a translation, Δz, from an initial nominal distance, z_{nom}, is made, with HWS measurements of N spots taken before and after, then the slope of the line-of-best-fit, $\mathrm{m}_{\mathrm{fit}}$, of $\left(\Delta y/L\right)_i$ versus h_i, where $1 \leq i \leq N$, can be determined. The corresponding value of $\mathrm{m}_{\mathrm{theory}}\left(\varepsilon_z\right)$ can be determined at this nominal distance.

Multiple, large translations were made, $\Delta z \approx 1$ mm, for a series of nominal distances, z_{nom}, between the HP and the fibre end. The resulting theoretical and fitted slopes, $\mathrm{m}_{\mathrm{theory}}$ and $\mathrm{m}_{\mathrm{fit}}$, respectively, were plotted versus the nominal distances z_{nom} *plus* an estimate of ε_z. This resulted in two non-linear curves that were offset from one another. The value ε_z was varied to displace the curves until they lay on top of one another, as illustrated in Figure 4.14, thereby yielding a value for the systematic offset ε_z, and hence calibrating the origin of z_0.

In this way, z_0 for the measurement in Section 4.6.5 was determined to be 91.7 ± 0.2 mm. Note that, although the best fit of z_0 gives an error of approximately ± 0.03 mm, the error here is set to 0.2 mm because the relative error in the lever arm L, which is used in the calculation of z_0, is approximately 0.2% (recall that $L = 10.43 \pm 0.02$ mm).

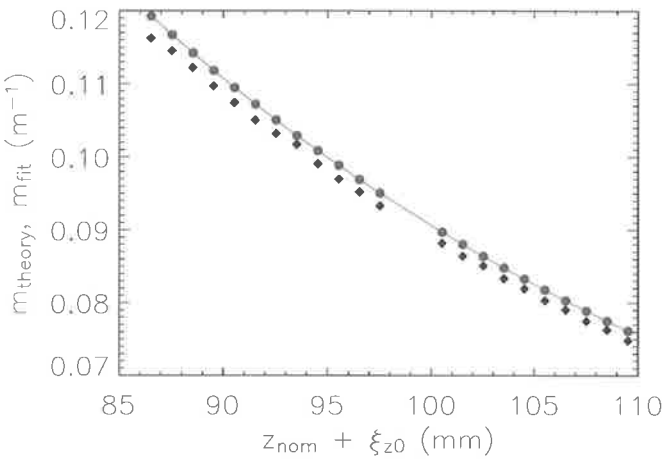

(a) $\varepsilon_{z_0} = 0.0$ mm low

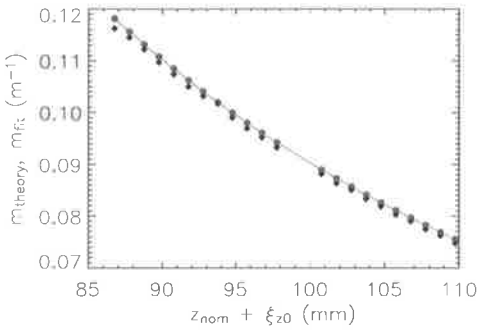

(b) $\varepsilon_{z_0} = -0.23$ mm low

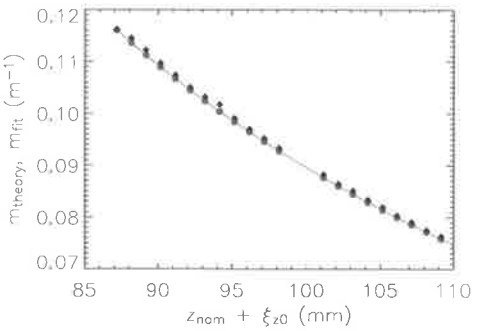

(c) $\varepsilon_{z_0} = -0.63$ mm high

Figure 4.14: Multiple measurements of m_{theory} (red) and m_{fit} (blue) at different approximate distances, $z_{nom}+\varepsilon_{z_0}$, from the HP. The only fitting parameter is the error in the distance from the HP, ε_{z_0}. a) Shows the comparison using only the nominal value z_{nom} with $\varepsilon_{z_0} = 0$. By varying the fitting parameter, ε_{z_0}, the measurements (blue) could be made to lie on top of the theory curve (red). In this way the distance from the fibre to the HP could be calibrated. b) shows an example where this distance has been underestimated and c) shows an example where this distance has been overestimated.

4.6.4 Mitigating cyclic temperature fluctuations

Since ΔW was intended to be very small to simultaneously test precision as well as accuracy, the temperature dependence of the HWS, discussed in Section 3.2.5, was expected to introduce a significant error in response to any changes in temperature. Recall that the change in wavefront due to a change in temperature appears to be quadratic - the same form as the signal to be measured in this defocus experiment!

Periodic fluctuations in the temperature of the CCD ($\pm$150 mK @ 0.5 mHz) were observed due to the laboratory air-conditioning (if the air- conditioning was turned off the laboratory was subject to diurnal temperature variations, approximately $\pm 5,500$mK per day). The air-conditioning induced temperature fluctuations were periodic and the translations could be timed to coincide with a maxima or a minima such that the average temperature before and after translation was the same and the net effect of these fluctuations would thus be minimal. This was done by performing multiple translations of the fibre end and then leaving the system for another 2-3 hours to record the period and phase of the background fluctuations. Knowing these values, the periodic signal could be traced back in time and the translation that occurred closest to a turning point of the periodic signal could then be selected.

4.6.5 Experiment procedure

The experimental procedure was:

1. t_{expt} = -180:00 minutes. The HWS was turned on 3 hours in advance of any measurements to allow it to reach a steady-state temperature.

2. t_{expt} = 000:00 minutes. The Michelson interferometer started recording interference patterns at approximately 13 Hz and ran continuously for the 6 hour duration of the experiment.

3. $t_{\text{expt}} = 000{:}10$ minutes. A temperature record of the HWS sensor was started and ran continuously for the 6 hour duration of the experiment. This was read from the the on-board sensors with a frequency of 33 mHz (every 30 s).

4. $t_{\text{expt}} = 000{:}20$ minutes. The HWS sensor started and ran continuously for the 6 hour duration of the experiment. Centroid patterns were recorded at approximately 33Hz.

5. $t_{\text{expt}} \approx 000{:}20 \rightarrow 006{:}30$ minutes. 10,000 centroids were recorded at the intial position.

6. $t_{\text{expt}} \approx 006{:}30 \rightarrow 007{:}30$ minutes. The fibre was translated approximately 10μm closer to the HWS by adjusting the translation stage. This was done extremely carefully and slowly to enable successful tracking of the fringes in the interference pattern.

7. $t_{\text{expt}} \approx 007{:}30 \rightarrow 014{:}00$ minutes. 10,000 centroids were recorded at the new position.

8. $t_{\text{expt}} \approx 014{:}00 \rightarrow 143{:}00$ minutes. Steps 6 and 7 were repeated a further 18 times.

9. $t_{\text{expt}} \approx 143{:}00 \rightarrow 360{:}00$ minutes. The equipment was left recording data for a further 3.5 hours.

10. $t_{\text{expt}} = 360{:}00$ minutes. All data recording ceased.

4.6.6 Results

The defocus measured in Step 9 is plotted in Figure 4.15 a), the OPD measured by the interferometer for this Step in Figure 4.15 c) and the temperature measured by the on-board temperature sensors on the HWS in Figure 4.15 e). A sinusoidal variation in defocus with a frequency of 0.5 mHz can be seen in the defocus data, the OPD measurements and the on-board temperature. The spectral components of this signal are shown for the defocus,

OPD and temperature in Figures 4.15 b), d) and f), respectively. Given that it has been established, Section 3.2.5, that the HWS produces a temperature dependent systematic error that appears to be defocus and that the temperature and defocus oscillations have the same frequency, it is concluded that the observed periodic fluctuations in defocus are caused by the cycling laboratory temperature. Periodic thermal expansion of the optical table would also explain the fluctuations in OPD observed in Figure 4.15 c).

The defocus measurements were made by comparing measurements immediately before and after maxima or minima in the temperature cycle, with the fibre translation itself coinciding with the maxima or minima. The fluctuations in temperature were slowest at these points and the average temperature of the measurements before and after the displacement were approximately the same. The sinusoidal signal measured after the last measurement was traced backward in time to determine the displacement which occurred closest to a maxima or minima and therefore had the smallest systematic error. This is illustrated Figure 4.16. The displacement at 68 minutes coincided with a maximum of the sinusoid and hence the centroids immediately before and after this measurement were used in the following analysis. The change in the optical path length, measured by the interferometer, was $19.2 \pm 0.1\,\mu$m, giving $\Delta z = 9.60 \pm 0.05\,\mu$m.

The vertical gradient field of the wavefront distortion was determined from the difference between the Hartmann centroids before and after the displacement at $t = 68$ minutes. This was done for centroids averaged over N_{avg} measurements for $N_{\text{avg}} = 1, 100, 1000, 5000$. Figure 4.17 shows plots of the vertical component of the gradient field for the four averages. The predicted value of vertical gradient is also plotted. These plots show a linear relationship between the local gradient and transverse position, y_0, as predicted by Equation 4.10, and the improvement in sensitivity due to averaging.

The defocus due to the source translation can be calculated using the slope, m, of the line-of-best-fit to this data and $S = m\,(z_0 + L)\,/z_0$ and the results are summarised in Table 4.1. Linear regression analysis was used to

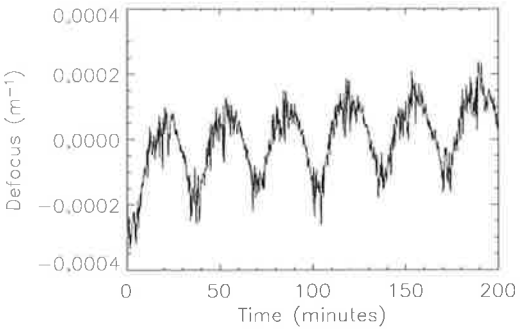

(a) Hartmann defocus measurement

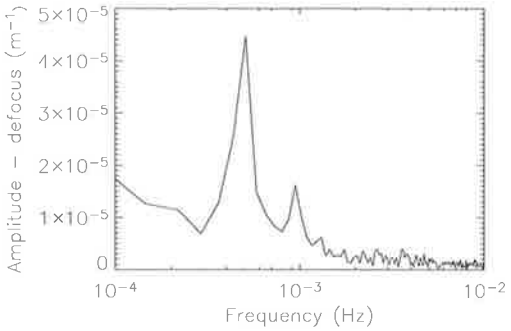

(b) Hartmann defocus frequency spectrum

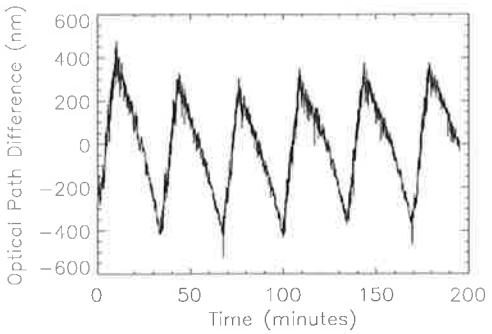

(c) Interferometer measurement

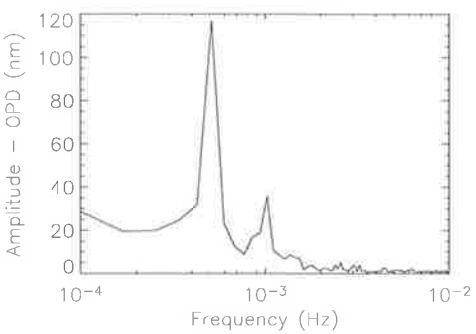

(d) Interferometer frequency spectrum

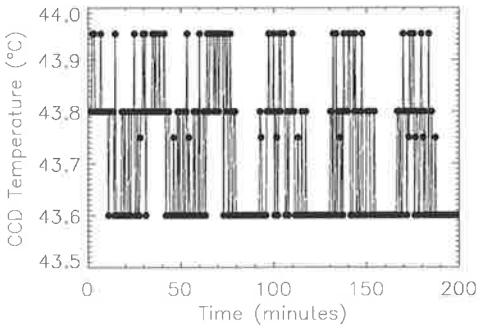

(e) CCD temperature measurement

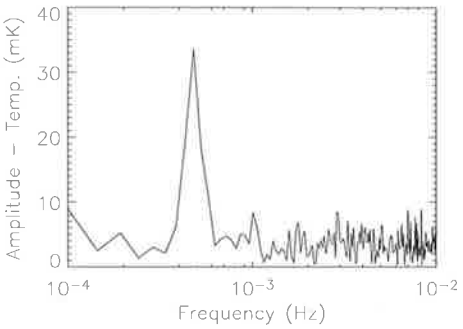

(f) CCD temperature frequency spectrum

Figure 4.15: a) Hartmann sensor defocus measurement and b) its temporal spectrum. c) Mach-Zehnder interferometer optical path distortion measurement and d) its temporal spectrum. e) Average temperature measured by the two CCD temperature sensors and f) its temporal spectrum. These plots show a 0.5 mHz sinusoidal signal common to the defocus, interferometer and temperature measurements.

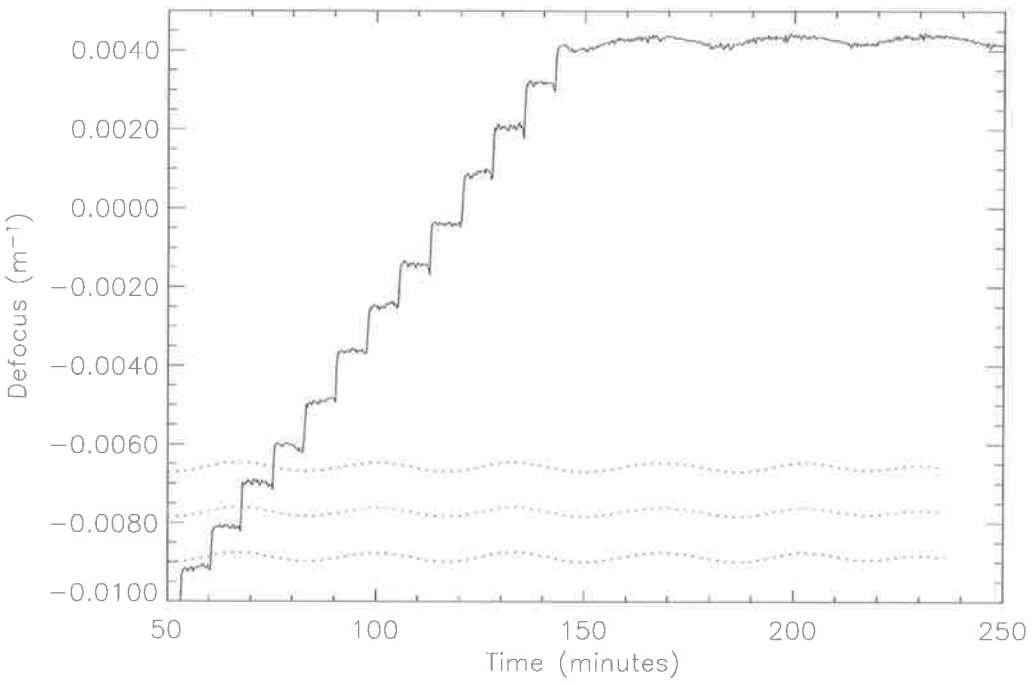

Figure 4.16: The defocus measured by the Hartmann sensor, relative to an average background, versus time where the fibre end is displaced multiple times by approximately 10μm every 7.5 minutes. The dotted lines are sinusoidal curves that have the same frequency and phase as the cyclic fluctuation of the laboratory temperature and are traced backward in time. Notice that the displacement at 68 minutes coincides with a peak.

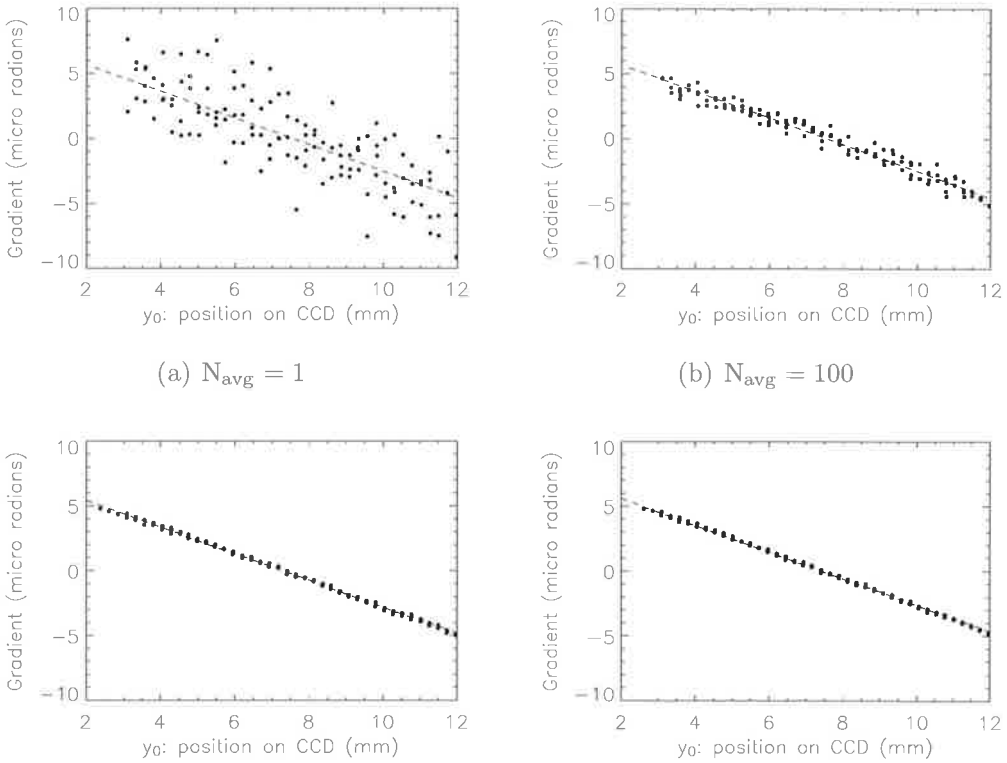

(a) $N_{avg} = 1$ (b) $N_{avg} = 100$

(c) $N_{avg} = 1000$ (d) $N_{avg} = 5000$

Figure 4.17: Measured local gradient of the wavefront change versus spot position at the CCD, y_0, due to translation of the fiber light source, averaged over a) 1, b) 100, c) 1000 and d) 5000 Hartmann images.

N_{avg}	**Defocus, S**	**Accuracy**	**Precision**
1	$-1.3 \pm 0.2 \times 10^{-3}\,\text{m}^{-1}$	$\lambda/860$	$\lambda/330$
100	$-1.127 \pm 0.036 \times 10^{-3}\,\text{m}^{-1}$	$\lambda/3700$	$\lambda/1800$
1000	$-1.150 \pm 0.008 \times 10^{-3}\,\text{m}^{-1}$	$\lambda/5200$	$\lambda/8200$
5000	$-1.159 \pm 0.007 \times 10^{-3}\,\text{m}^{-1}$	$\lambda/3300$	$\lambda/9300$
Expected value	$-1.14 \pm 0.01 \times 10^{-3}\,\text{m}^{-1}$	-	-

Table 4.1: Summary of the defocus measurements with the HWS averaged over N_{avg} measurements, where $N_{\text{avg}} = 1$, 100, 1000 and 5000. Precision is given by the 95% confidence interval.

determine the slope and precision of the line-of-best-fit. The uncertainty in S when averaged over 5000 images is equivalent to an uncertainty in the wavefront sag of 0.1 nm ($\lambda/9300$) over the CCD aperture (≈ 10 mm), which is roughly twice the previously measured $\lambda/15,500$ due probably to non-stationary noise during the extended acquistion time.

The accuracy of the defocus measurement over the aperture of the HWS (≈ 10 mm) is determined by comparing the measured defocus with the predicted value of $-1.14 \pm 0.01 \times 10^{-3}\,\text{m}^{-1}$, which differs from the measurement by about $2 \times 10^{-5}\,\text{m}^{-1}$ or 1.7%, for $N_{\text{avg}} = 5000$. This error is equivalent to $\lambda/3300$ and could be explained by a change in average temperature of the HWS of order 10 mK.

These results show that the HWS is ideal for high precision and high accuracy measurement of wavefront changes, and represent a large improvement in the state-of-the-art. The application to the measurement of a small wavefront change due to defocus, S, with a precision of $7 \times 10^{-6}\,\text{m}^{-1}$ (see Table 4.1 for $N_{\text{avg}} = 5000$) was demonstrated. It was also established that the sensor measures this aberration with an accuracy of about $2 \times 10^{-5}\,\text{m}^{-1}$.

4.7 Conclusion

The sensitivity and accuracy of the Hartmann sensor has been demonstrated by the results reported in this chapter. In Section 4.3, the choice of an incoherent light source was shown to be crucial in reducing the uncertainty

in centroid measurements to a shot-noise limit. A high precision and accuracy calibration of the effective lever arm of the Hartmann sensor was described in Section 4.2. In Section 4.5, the background noise in the Hartmann sensor was shown to be dominated by Poissonian shot-noise and capable of being reduced to at least $\lambda/15{,}500$ by averaging multiple measurements. Evidence of another, potentially temperature related, noise source was observed at this level. An observation of the temperature dependent error in the Hartmann sensor was described in Section 4.4 and a simple measurement of the size of this effect yielded a result relatively close to the expected value. Section 4.6 described the measurement of the accuracy using a novel experiment to induce very small, yet well-defined, wavefront aberrations and the results from this experiment demonstrated the measurement of a very small defocus, equivalent to an 850m lens, with an accuracy of 1.7% and a precision of 0.7%.

Chapter 5

Direct measurement of wavefront distortion at the High Optical Power Test Facility

5.1 Background

The High Optical Power Test Facility (HOPTF), operated by the Australian Consortium for Interferometric Gravitational Astronomy (ACIGA), is a test facility designed to investigate critical issues associated with high power optical cavities, such as the measurement and compensation of absorption-induced wavefront distortion and the effect of parametric instabilities on cavity stability [97].

The high optical power cavity at the facility has previously been used to investigate the effect of absorption-induced thermal lensing in the cavity optics on the cavity mode size by Zhao *et al.* [18]. This was accomplished by measuring the spatial profile of the light emitted from the cavity and comparing it with that predicted by a FEM, assuming the dominant thermal time constants expected for the intra-cavity optics and that the cavity power

was constant. Whilst there appeared to be reasonable agreement between measurement and model in that investigation, such a technique could not be used to produce a signal suitable for a thermal compensation system (TCS) in Advanced LIGO, as described in Section 1.3 and illustrated in Figure 1.7, as it a) estimates only the defocus (thermal lens) component of the wavefront distortion (WD), and b) could not determine the WD of individual optics within a GWI.

5.2 Objectives

In this chapter, I describe the first direct measurement of wavefront distortion in an optical cavity that has high stored power using a sensor that meets the sensitivity and spatial resolution criteria specified for Advanced LIGO (see Section 1.3.2).

The installation of the sensor at the HOTPF and the properties of the cavity itself are discussed in Section 5.3, as well a measurement of the sensor noise floor. The experimental procedure and analysis of the data from the sensor are discussed in Section 5.4. This discussion is particularly detailed because the sensor measures the absorption-induced WD of multiple intra-cavity optics off-axis and this measurement must be converted to the on-axis distortion that is experienced by the cavity mode. The results of the wavefront measurement and their validation using two independent measurements are reported in Section 5.5 and concluding remarks are made in Section 5.6.

5.3 Description of measurement system

5.3.1 The HOPTF high-optical-power cavity in detail

The current optical configuration is a 77 m Fabry-Perot cavity in which the substrate of the input coupler or 'input test mass' (ITM) is inside the cavity to enhance the absorption-induced wavefront distortion in that mirror, as

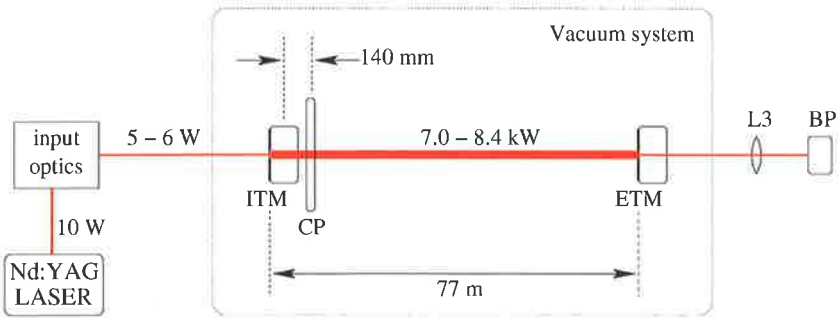

Figure 5.1: Schematic of the Fabry-Perot cavity with high stored power, located at the HOPTF.

	ITM	ETM	CP
Material	Sapphire	Sapphire	Fused Silica
Diameter	100 mm	150 mm	160 mm
Thickness	46 mm	80 mm	17 mm
Radius of curvature	flat	720 ± 100 m	flat
HR transmission	1840 ± 100 ppm	20 ppm	n/a
AR reflectivity	30 ± 20 ppm	12 ± 10 ppm	100 ppm
Volumetric absorption	≈ 51 ppm/cm	n/a	≈ 2 ppm/cm

Table 5.1: Physical parameters of the HOPTF Fabry-Perot cavity optics

shown in Figure 5.1. The cavity also contains a fused-silica compensation plate (CP) that can be heated via a heating coil wrapped around its barrel surface, which is used by other members of ACIGA.

The optical and physical parameters of the ITM, CP and the end test mass (ETM) are shown in Table 5.1. The cavity has a measured finesse of approximately 1400 [98], which is consistent with the losses due to the AR coatings and absorption of the CP and ITM substrates. A laser beam from a 10W Nd:YAG single frequency 1064 nm laser [99] is passed through a series of input optics (a pre-mode cleaner, isolator, mode-matching and alignment optics) and the remaining 5 - 6W is coupled into the 77 m Fabry-Perot cavity, resulting in approximately 7.0 - 8.4kW of intra-cavity power. A small amount of the cavity mode is transmitted through the end test mirror (ETM) and is imaged onto a beam profiler (BP) with a demagnification = 2.92 ± 0.05, thereby recording the cavity mode size and power level at the ETM.

5.3.2 Installation of the HWS at HOPTF

A HWS was installed at the HOPTF to measure the wavefront distortion in the ITM and the CP at an off-axis angle as illustrated in Figure 5.2. The HWS was identical to the one described in Chapters 4 and 5, the only modification being a more powerful light source (QPhotonics QSDM-790-2 2mW 800 nm fibre-coupled superluminescent diode [100]). The output of the fibre was collimated into an approximately 80 mm diameter beam, steered into the vacuum system and through the ITM and the CP at an angle of 10°. The interior of the vacuum system, the beam steering mirrors, M2, M3, and M4, the CP and the ITM are shown in the photograph in Figure 5.3. After transmission through the ITM and CP, the beam was steered out of the vacuum system, through an imaging lens, L2 (f = 500 mm), and was incident on the HWS. The imaging lens was adjusted such that the exit plane of the ITM, p_{obj}, was imaged onto the Hartmann plate.

The ITM suspension assembly [101] can be seen surrounding the ITM in Figure 5.3 and also in Figure 5.4 a). Part of the Hartmann probe beam was obscured by several components of this suspension assembly, as illustrated in the computer-generated rendering of the ITM and suspension assembly, from the point-of-view of the probe beam, shown in Figure 5.4 b). The top and bottom cross beams, on which the magnetic actuators used to align the ITM are mounted, which cannot be removed, obscure a substantial fraction of the ITM but a region about 3 × the cavity mode diameter around the center of the cavity mode remains unobscured. This is sufficient for measuring the wavefront distortion in the region of the cavity mode. Additionally, there were two brackets to the left and right of the ITM center that obscured part of the HWS probe beam. The front LH and rear RH brackets were removed as their removal had little to no effect on the suspension system (these brackets housed two safety stops and their removal left 12 remaining stops). This final configuration is illustrated in the computer-generated rendering in Figure 5.4 c).

The aperture is highlighted in the computer-generated rendering in Figure

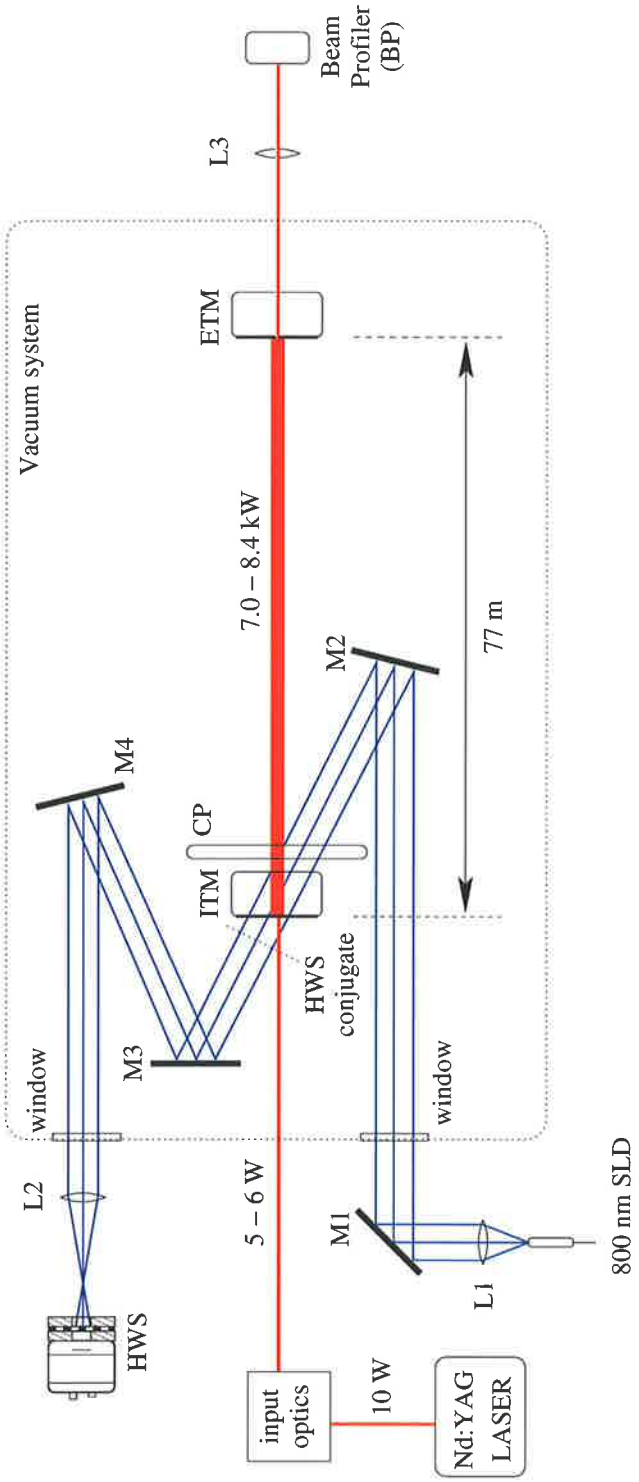

Figure 5.2: Schematic showing HWS installed to measure thermal lensing in the ITM and CP.

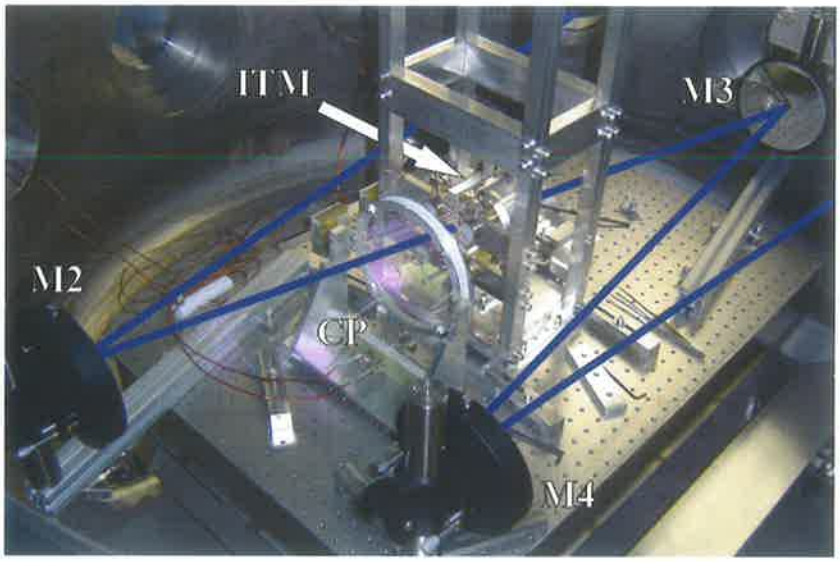

Figure 5.3: Photograph showing interior of the vacuum system, the beam steering mirrors, M2, M3, and M4, the CP and the ITM.

5.5 a) with the positions of the centers of the ITM and CP indicated by red and blue crosses, respectively. An image of the probe beam at p_{obj} is shown in Figure 5.5 b).

5.3.3 Reduction of environmental noise coupling into HWS

The wavefront distortion across the whole aperture was measured with the Nd:YAG laser off so that there was no stored power in the cavity. The RMS error when the HWS was first installed, averaged over 10 contiguous Hartmann images, as a function of time is shown in Figure 5.6 in curve a), exhibiting much higher average RMS wavefront error than the theoretical shot-noise limit for the sensor: $\lambda/45$ vs $\lambda/3000$. The additional noise was primarily due to air filters creating turbulence in the vicinity of the experiment. Additionally, the volume of air through which the probe beam passed was significantly greater than for the shot-noise limited measurements described in Chapter 4 and hence the contribution from air currents was greater.

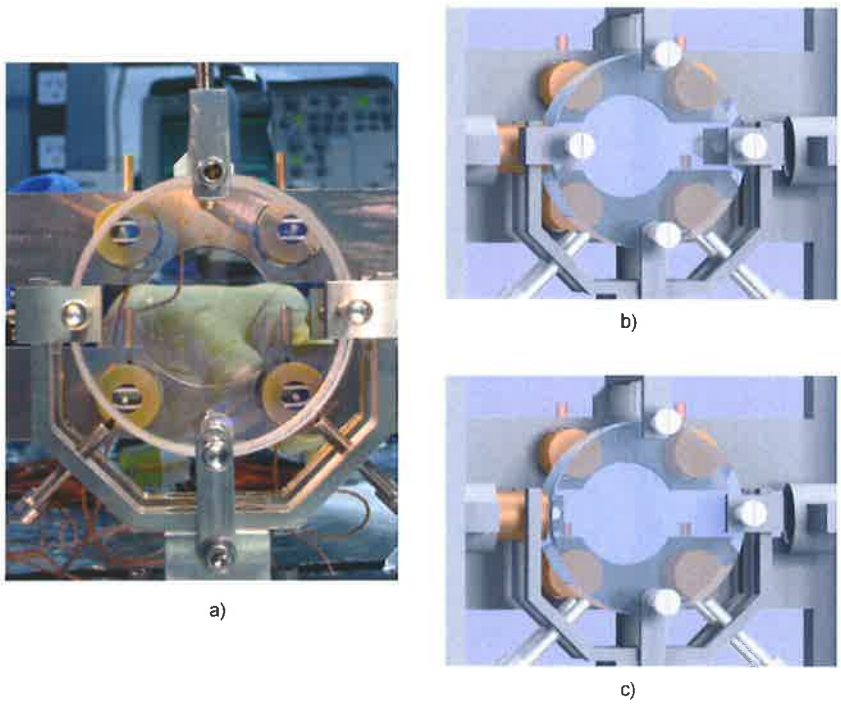

Figure 5.4: a) Photograph of the ITM installed in its suspension system. b) Computer-generated rendering of the ITM and suspension system from the point-of-view of the probe beam. c) Computer-generated rendering of the ITM and suspension system from the point-of-view of the HWS with the corner brackets removed.

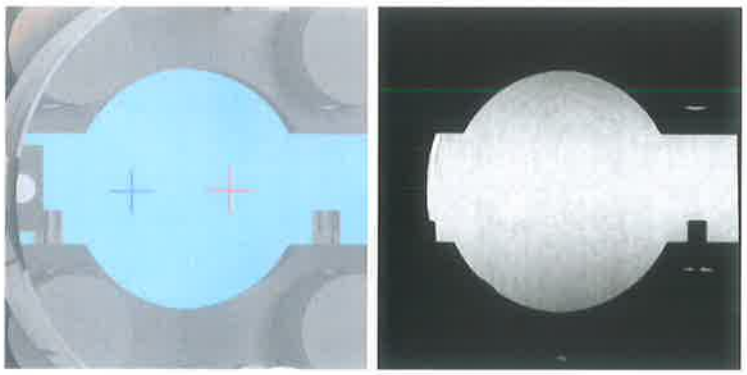

(a) (b)

Figure 5.5: a) computer-generated rendered view of ITM and suspension system at 10 degrees with aperture highlighted and the positions of the ITM and CP centers indicated by red and blue crosses, respectively. b) Image of the probe beam shadow at p_{obj}.

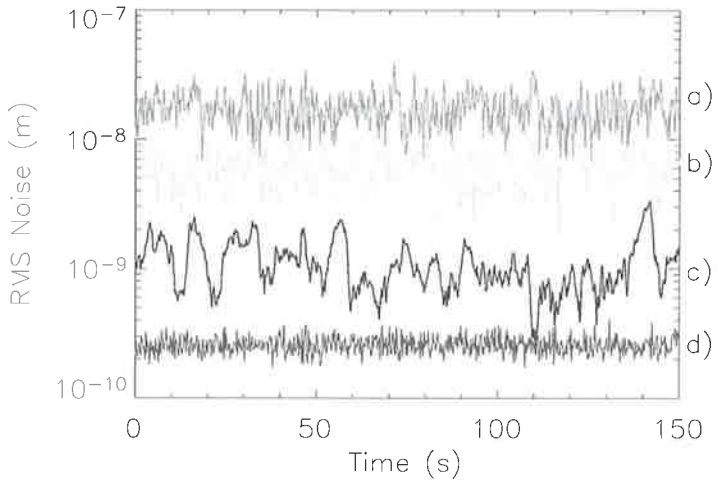

Figure 5.6: RMS noise in HWS measurement versus time. a) With all air filters on, b) with air filters off, c) with air filters off and beam tubes enclosing the majority of the beam path and d) shot-noise limit (simulated).

When the air filters were turned off to reduce air currents, the RMS wavefront error decreased to an average value of $\lambda/130$. The time dependence of the RMS wavefront error for that configuration is displayed in Figure 5.6 in curve b). The RMS wavefront error was further decreased by isolating a substantial fraction of the probe beam with beam tubes, as illustrated in the photographs in Figure 5.7. The final average RMS wavefront error was $\lambda/730$ and this error as a function of time is shown in Figure 5.6 in curve c). Also shown in this figure, curve d), is the RMS wavefront error expected for purely random noise, with an average of $\lambda/3000$. The large excursions from the mean RMS level in curve c) indicate that there is probably still some correlated noise in the wavefront. Indeed, the wavefront difference for curve c) at $t \approx 75$ s indicates evidence of correlated noise as shown in Figure 5.8. This is most likely due to residual air currents and the large volume of air in the probe beam, although it could also be acoustic vibration of the optical components. To alleviate this in future the probe beam could be expanded inside the vacuum system reducing the volume of air to which it is exposed. Nevertheless, the sensor as installed in this experiment still satisifes the Advanced LIGO sensitivity specification.

5.4 Measurement procedure and analysis

5.4.1 Measurement procedure

The procedure for measuring the thermal lensing in the sapphire (ITM) and fused silica (CP) as a function of time, where t_{expt} is the experiment time, is as follows:

1. $t_{\text{expt}} \approx -15$ s. Start recording Hartmann images to establish reference centroids before the 1064 nm beam is coupled into the cavity.

2. $t_{\text{expt}} = 0$ s. Couple 10W laser into cavity. Start recording the transmitted power and beam size with the beam profiler (BP).

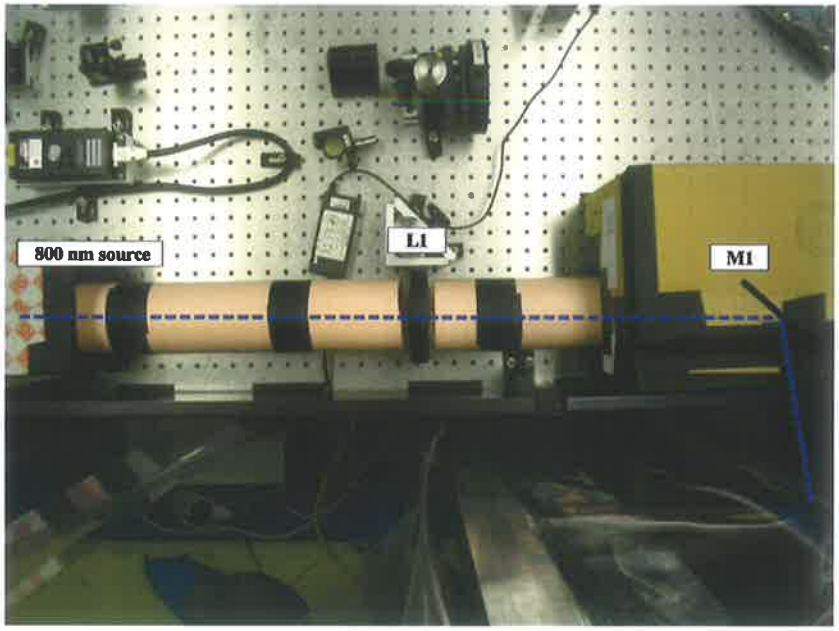

(a)

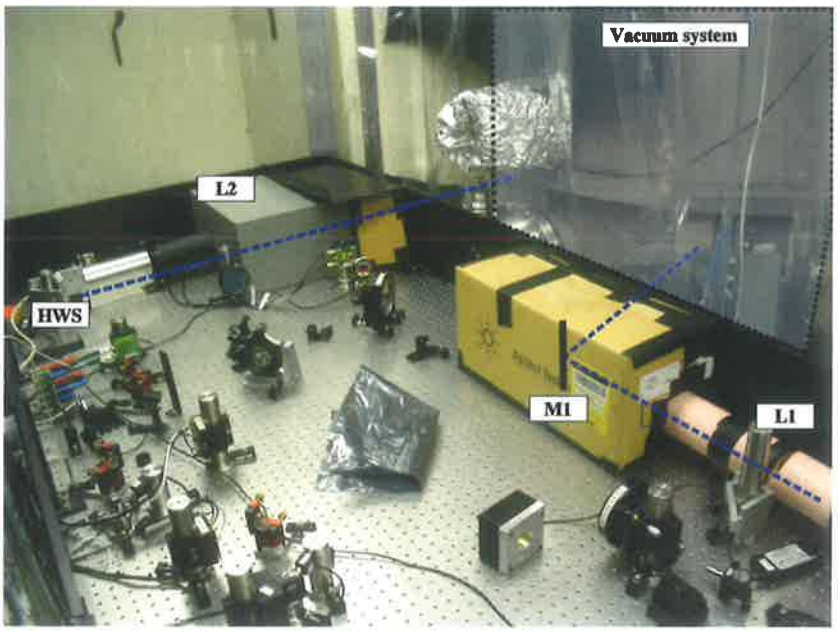

(b)

Figure 5.7: Photographs showing some of the (improvised) beam tubes that attenuated background noise in the HWS.

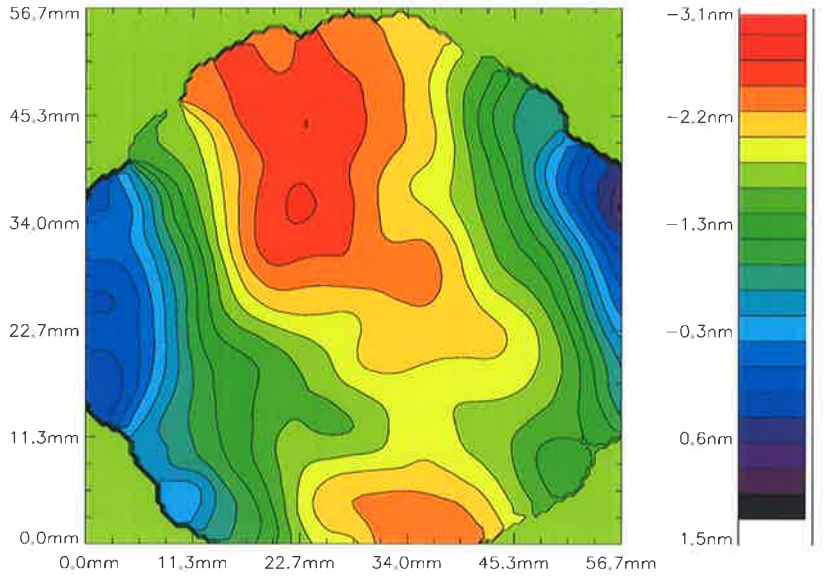

Figure 5.8: An example of correlated noise in the background wavefront difference for curve c) in Figure 5.6 at $t \approx 75$ s.

3. $t_{\text{expt}} = 0$ s $\rightarrow$ $t_{\text{expt}} \approx 300$ s. Continue recording Hartmann images to measure the temporal development of thermal distortions in the ITM and CP.

4. $t_{\text{expt}} \approx 300$ s. Turn off 1064 nm beam.

5. $t_{\text{expt}} \approx 300$ s $\rightarrow$ $t_{\text{expt}} \approx 400$ s. Continue recording Hartmann images to observe the decay of thermal distortions in the ITM and CP.

6. $t_{\text{expt}} \approx 400$ s. Cease recording with the HWS and the BP.

This procedure was repeated on 13 separate occasions. The power level in the cavity was noticeably more stable on some occasions than others due to variations in the mode-matching of the 1064 nm laser into the Fabry-Perot cavity.

5.4.2 Analysis of wavefront distortion

As indicated earlier, the Hartmann probe beam is incident on the CP and the ITM with a 10° angle of incidence so that the wavefront distortions can be measured separately. In Section 5.4.2.1, I show how this off-axis HWS measurement of distortion is transformed into the distortion that would be measured by an on-axis probe beam. The on-axis WD is measured in transmission through the CP and ITM, however, while the cavity mode is reflected from the high-reflecting surface of the ITM. Thus, in Section 5.4.2.2, I show how the on-axis distortion can be used to determine the distortion experienced by the cavity mode. Lastly, in Section 5.4.2.3, I show how to determine, from the distortion experienced by the cavity mode, the thermally induced defocus, which can be used to calculate the cavity mode size at the ETM. In Section 5.5 the calculated mode size is compared with the measurements from the BP to show that the wavefront distortion measurement is accurate.

Note that the off-axis to on-axis transformation described here is valid only because the CP and ITM are separated by a distance that is large compared to the thickness of the ITM and CP, and the angle of incidence is small. More generally, a tomographic analysis should be used to achieve this transformation as described in Chapter 6.

5.4.2.1 Converting off-axis distortion to on-axis distortion

A schematic illustrating the off-axis probe beam propagating through the CP and ITM is shown in Figure 5.9 a). The results of a numerical simulation of the expected off-axis wavefront distortion due to Hello-Vinet thermal gradient inside the optics is shown in Figure 5.9 b), where this off-axis distortion is labelled $\mathbf{WD}^{(\mathbf{off})}$. Two lobes are clearly seen, indicating the distortion in the two optics. Due to the shallow viewing angle, a vertical cross-section through each lobe is approximately equivalent to what would have been measured in that component in an on-axis view. These cross-sections are indicated by dashed lines in Figure 5.9 b) and are labelled $\mathrm{WD}^{(\mathrm{off})}_{\mathrm{SAPH}}$ and $\mathrm{WD}^{(\mathrm{off})}_{\mathrm{FS}}$ for the sapphire and fused silica cross-sections, respectively.

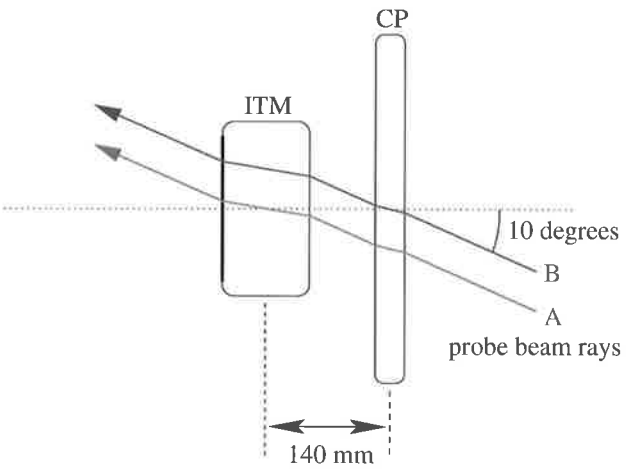

(a)

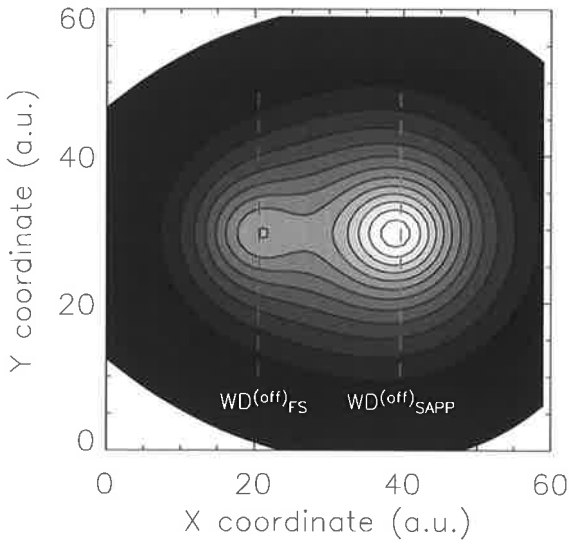

(b)

Figure 5.9: a) Off-axis probe beam refracting through sapphire ITM and fused silica CP. b) Simulated off-axis wavefront distortion, $\mathbf{WD^{(off)}}$, showing the two vertical cross-sections, $WD_{FS}^{(off)}$ and $WD_{SAPH}^{(off)}$, used to determine the defocus in the fused-silica and sapphire, blue and red respectively.

The on-axis and off-axis distortions differ because of two effects. Firstly, each lobe is smeared or elongated slightly in the horizontal direction due to the axial extent of the thermal lenses. Secondly, each lobe is contaminated slightly by the signal from the other lobe. This can be seen by considering ray A in Figure 5.9 a): despite the fact that it is dominated by the strong thermal lens at the center of the sapphire, there is still a contribution to the total distortion from the thermal lens in the compensation plate. Thus, the vertical cross-sections through each lobe represent a sum of on-axis wavefront distortions which can be expressed as

$$\mathrm{WD}_{\mathrm{SAPH}}^{(\mathrm{off})} = \mathrm{K}_{\mathrm{E1}}(t)\ \mathrm{WD}_{\mathrm{SAPH}}^{(\mathrm{on})} + \mathrm{K}_{\mathrm{C1}}(t)\ \mathrm{WD}_{\mathrm{FS}}^{(\mathrm{on})} \tag{5.1}$$

$$\mathrm{WD}_{\mathrm{FS}}^{(\mathrm{off})} = \mathrm{K}_{\mathrm{E2}}(t)\ \mathrm{WD}_{\mathrm{FS}}^{(\mathrm{on})} + \mathrm{K}_{\mathrm{C2}}(t)\ \mathrm{WD}_{\mathrm{SAPH}}^{(\mathrm{on})} \tag{5.2}$$

where $\mathrm{WD}_{\mathrm{SAPH}}^{(\mathrm{on})}$ and $\mathrm{WD}_{\mathrm{FS}}^{(\mathrm{on})}$ are the on-axis distortions of the sapphire and fused silica, respectively, $\mathrm{K}_{\mathrm{E1}}(t)$ and $\mathrm{K}_{\mathrm{E2}}(t)$ describe the elongation of the sapphire and fused silica distortion, respectively, and $\mathrm{K}_{\mathrm{C1}}(t)$ and $\mathrm{K}_{\mathrm{C2}}(t)$ describe the contribution of the fused-silica and sapphire distortion to the opposite cross-section, respectively.

The parameters $\mathrm{K}_{\mathrm{E1}}(t)$, $\mathrm{K}_{\mathrm{E2}}(t)$, $\mathrm{K}_{\mathrm{C1}}(t)$ and $\mathrm{K}_{\mathrm{C2}}(t)$ can be determined using the geometry of the ITM-CP-probe-beam arrangement and assuming the temporal development of the wavefront distortion as described by Hello and Vinet (see Appendix A.1) to first order.

The on-axis distortion is determined by solving the Equations 5.1 and 5.2 to yield

$$\begin{aligned}\mathrm{WD}_{\mathrm{SAPH}}^{(\mathrm{on})} &= \frac{\mathrm{K}_{\mathrm{E2}}\,\mathrm{WD}_{\mathrm{SAPH}}^{(\mathrm{off})} - \mathrm{K}_{\mathrm{C1}}\,\mathrm{WD}_{\mathrm{FS}}^{(\mathrm{off})}}{\mathrm{K}_{\mathrm{E1}}\,\mathrm{K}_{\mathrm{E2}} - \mathrm{K}_{\mathrm{C1}}\,\mathrm{K}_{\mathrm{C2}}} \\ &= \mathrm{b}_{1\,1}\,\mathrm{WD}_{\mathrm{SAPH}}^{(\mathrm{off})} + \mathrm{b}_{1\,2}\,\mathrm{WD}_{\mathrm{FS}}^{(\mathrm{off})}\end{aligned} \tag{5.3}$$

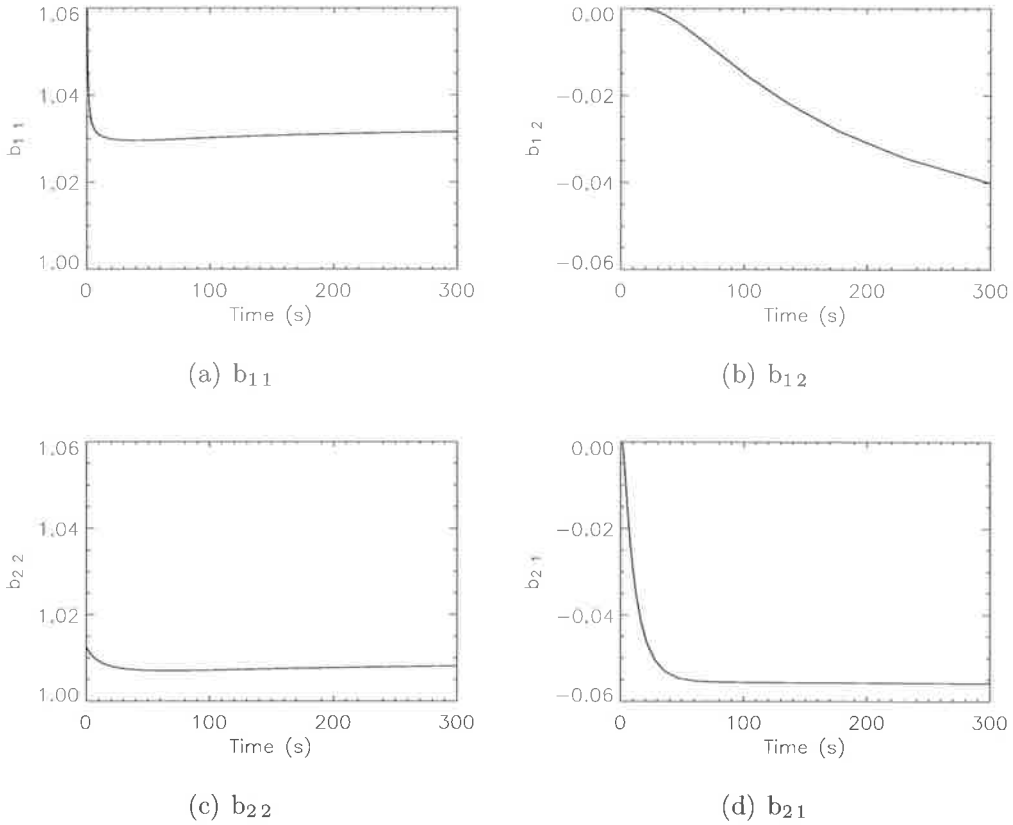

(a) b_{11} (b) b_{12}

(c) b_{22} (d) b_{21}

Figure 5.10: Conversion parameters for off-axis distortion, calculated using the Hello-Vinet equation and known geometry of ITM, CP and probe beam

$$\begin{aligned} \mathrm{WD}_{\mathrm{FS}}^{(\mathrm{on})} &= \frac{\mathrm{K_{E1}\,WD_{FS}^{(off)} - K_{C2}\,WD_{SAPH}^{(off)}}}{\mathrm{K_{E1}\,K_{E2} - K_{C1}\,K_{C2}}} \\ &= \mathrm{b_{22}\,WD_{SAPH}^{(off)} + b_{21}\,WD_{FS}^{(off)}} \end{aligned} \tag{5.4}$$

where the conversion parameters, b_{11}, b_{12}, b_{21} and b_{22}, are plotted in Figure 5.10.

5.4.2.2 Converting on-axis WD to round-trip cavity-mode WD

As noted by Ryan Lawrence [12] and others, and discussed in Section 1.2.3, absorption in the substrate of a mirror leads to wavefront distortion via the thermo-optic, elasto-optic and thermo-elastic effects. The first two effects

	Sapphire	Fused Silica
Thermooptic Effect (SUB1, SUB2)	1	1
Elastooptic Effect (SUB1, SUB2)	0.2	-0.01
Thermoelastic expansion (CS1, ..., CS4)	0.8	0.06

Table 5.2: Sizes of thermoelastic deformation and the elastooptic effect relative to the size of the thermooptic effect. SUB1, SUB2 and CS1, ..., CS4, refer to the locations at which these effects occur as indicated in Figure 5.11.

result in volumetric distortions that are acquired on transmission through the substrate, while thermo-elastic distortion leads to surface deformation and thus is acquired on reflection or refraction at the surface. The relative sizes of the thermo-optic, elasto-optic and thermo-elastic distortion for sapphire and fused silica are listed in Table 5.2 (reproduced from Table 2.1 in Ryan Lawrence's Ph.D thesis [12]).

A schematic diagram showing the cavity mode and the Hartmann beam probing these distortions is illustrated in Figure 5.11. With the exception of the distortion at curved surface 4 (CS4), the cavity mode experiences every distortion twice that the probe beam experiences once. Therefore, the major difference between the distortion experienced by the cavity mode and probe beam arises at CS4, due to the thermo-elastic effect, which the cavity mode experiences on reflection and the probe beam on transmission. The relative sizes of the distortions accumulated by the probe beam and the cavity mode can be determined using a simple ABCD matrix description of the reflection of the cavity mode from and the transmission of the probe beam through the ITM and knowing the relative sizes of the thermo-optic, thermo-elastic and elasto-optic effects (see Appendix A.3 for details). This modelling shows that the wavefront distortion experienced by the cavity mode in the ITM is a factor of 2.53 larger than that measured by the HWS probe beam. Hence, the distortion experienced by the cavity mode, $\mathrm{WD}_{\mathrm{cavity}}$, can be expressed

$$\mathrm{WD}_{\mathrm{cavity}} \approx 2.53 \times \mathrm{WD}^{(\mathrm{on})}_{\mathrm{SAPH}} + 2.0 \times \mathrm{WD}^{(\mathrm{on})}_{\mathrm{FS}} \tag{5.5}$$

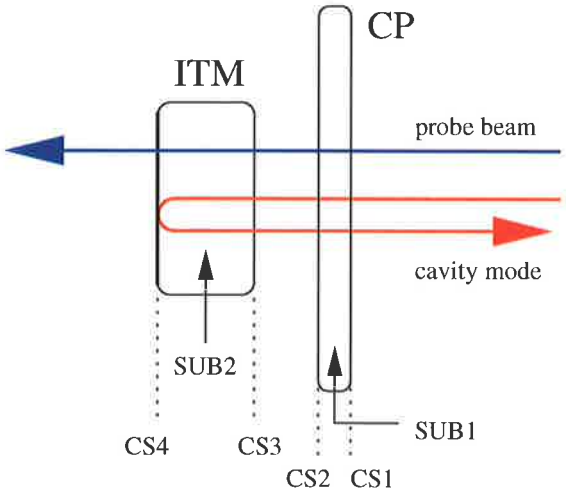

Figure 5.11: The probe beam (blue) is transmitted through both substrates, SUB1 and SUB2, and through all curved surfaces, CS1 to CS4. The cavity mode (red) is transmitted through both substrates, SUB1 and SUB2, and through curved surfaces, CS1 to CS3 and is reflected from CS4.

5.4.2.3 Defocus of cavity-mode WD and ETM beam size

The characterization of the distortion by the defocus, S, is achieved using the method of Arain *et al.* [102] which determines the maximum overlap integral, $\mathrm{I}(S)$, between the distortion experienced by the cavity mode and a spherically curved mirror, where

$$\begin{aligned} \mathrm{I}(S) \;=\; & \int_{-\infty}^{+\infty} \sqrt{\left(\frac{2}{\pi}\right)} \frac{1}{w_{\mathrm{ITM}}(S)} \times \\ & \exp\left(-x^2 \left[\frac{2}{w_{\mathrm{ITM}}^2(S)}\right]\right) \times \\ & \exp\left(i \left[\frac{4\pi}{\lambda} \mathrm{WD}_{\mathrm{cavity}}(x) - \frac{4\pi}{\lambda} S\, x^2\right]\right) \mathrm{d}x \end{aligned} \tag{5.6}$$

where $w_{\mathrm{ITM}}(S)$ is the calculated cavity mode size at the ITM and the defocus of the cavity, S_{cavity}, is the value of S which maximizes the integral in Equation 5.6 and is, therefore, a solution of

$$\frac{\mathrm{d}\,\mathrm{I}(S)}{\mathrm{d}\,S} = 0. \tag{5.7}$$

The cavity mode can then be found from the cavity g-parameters (see Seigman [103] for full details) given by

$$g_{\mathrm{ETM}} = 1 - \frac{L_{\mathrm{cav}}}{R_{\mathrm{ETM}}}$$

and

$$g_{\mathrm{ITM}}(S) = 1 - S\,L_{\mathrm{cav}},$$

where R_{ETM}, R_{ITM} are the radii of curvature of the end test mass and input test mass, respectively, and L_{cav} is the length of the cavity. The mode size at the ITM, $w_{\mathrm{ITM}}(S)$, is given by

$$w_{\mathrm{ITM}}(S) = \sqrt{\frac{L_{\mathrm{cav}}\,\lambda}{\pi}\sqrt{\frac{g_{\mathrm{ETM}}}{g_{\mathrm{ITM}}(S)\left[1 - g_{\mathrm{ITM}}(S)\;g_{\mathrm{ETM}}\right]}}}$$

Note that since the cavity mode size at the ITM, $w_{\mathrm{ITM}}(S)$, depends on the calculated cavity defocus, S, this procedure must be iterated several times to reach a convergent solution. It is first run using $w_{\mathrm{ITM}}(0)$ equal to the cold cavity (nominal) mode size at the ITM to determine the new cavity mode and then iterated several times, using the updated cavity mode sizes at the ITM. Once a convergent solution is found, the cavity mode size at the ETM, $w_{\mathrm{ETM}}(S)$, is then calculated using

$$w_{\mathrm{ETM}}(S) = \sqrt{\frac{L_{\mathrm{cav}}\,\lambda}{\pi}\sqrt{\frac{g_{\mathrm{ITM}}(S)}{g_{\mathrm{ETM}}\left[1 - g_{\mathrm{ITM}}(S)\;g_{\mathrm{ETM}}\right]}}}$$

5.5 Results

This section describes the results of the HWS measurement of wavefront distortion. The comparison of the measured off-axis distortion with that ex-

pected is discussed in Section 5.5.1, and the temporal development of vertical cross-sections are compared to H-V in Section 5.5.2. The measured distortion is also validated by comparing it to that predicted using a FEM and the measured stored power and by comparing the predicted mode size with that measured.

5.5.1 Measured off-axis wavefront distortion

The discrete gradient fields measured by the HWS at successively later times are shown in Figure 5.12 a) - f), and the corresponding off-axis wavefront profiles, $\mathbf{WD}^{(\mathbf{off})}$, are shown in Figure 5.13 a) - f). The wavefront profiles clearly show two wavefront distortions forming at different rates, where the lens in the sapphire (RHS lobe) is the larger and forms more quickly. The distance between the centers of the two distortions ($\approx$ 23 mm) is consistent with the projection of the centers of the two optical elements separated by 140 mm and viewed at 10°, as previously illustrated in Figure 5.9 a).

The vertical cross sections of the distortions, $\mathrm{WD}_{\mathrm{SAPH}}^{(\mathrm{off})}$ and $\mathrm{WD}_{\mathrm{FS}}^{(\mathrm{off})}$, at time $t_{\mathrm{expt}} \approx 300$ s are plotted in Figure 5.14. The ratio of the wavefront distortion on transmission due to the sapphire compared to that due to the fused silica is 1.62. Assuming that this distortion is the steady-state value and using the theory of Hello and Vinet (see Section A.1), the ratio of the absorbed power in the sapphire and fused silica is 40, which is significantly different to the ratio of 93 determined indirectly by Zhao *et al.* [18]. This provides an additional demonstration that direct measurement of thermal lensing with a wavefront sensor provides more accurate information about the behaviour of the cavity than can be inferred without such a measurement.

5.5.2 Temporal development of cavity defocus

The cavity defocus produced by the measured off-axis wavefront distortion was calculated using the procedure described in Section 5.4.2. The time dependence of the cavity defocus is shown in Figure 5.15 a). Also plotted

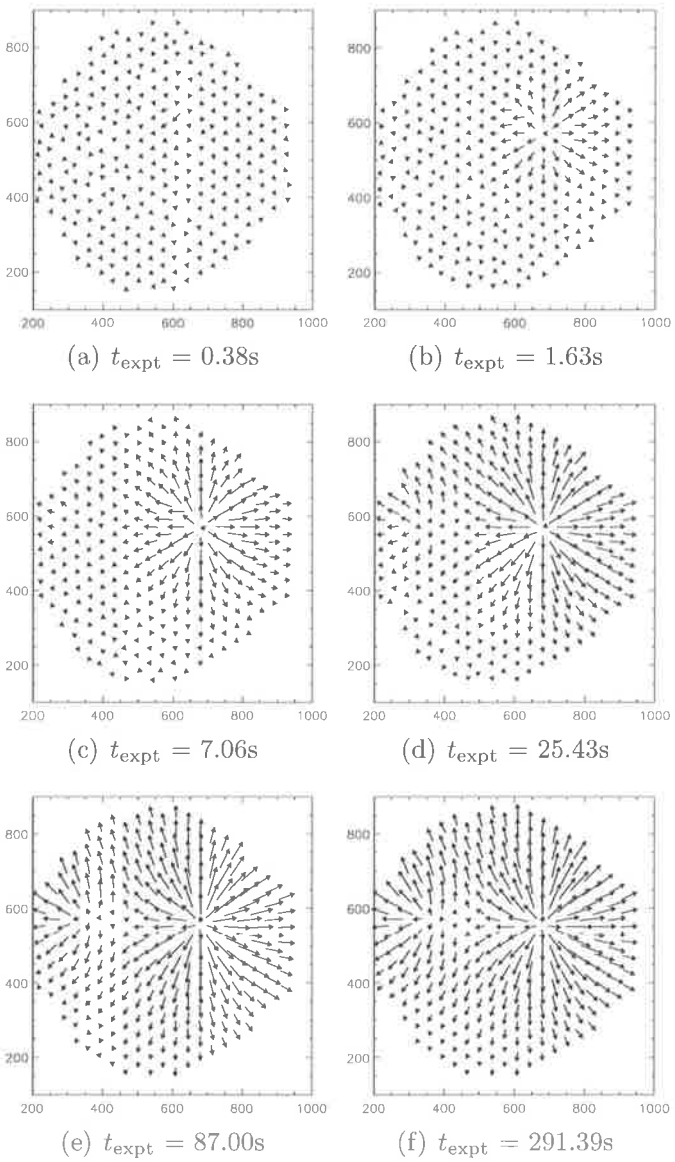

(a) $t_{\text{expt}} = 0.38$s (b) $t_{\text{expt}} = 1.63$s

(c) $t_{\text{expt}} = 7.06$s (d) $t_{\text{expt}} = 25.43$s

(e) $t_{\text{expt}} = 87.00$s (f) $t_{\text{expt}} = 291.39$s

Figure 5.12: Vector fields showing the gradient of the wavefront distortion in sapphire and fused silica at various times from $t_{\text{expt}} = 0$ s, at which the laser was locked to the cavity. The magnitude of the gradient is proportional to the length of a vector (from the tip of the arrow to the end of the line) at that point. The numbers on the axes indicate the coordinates on the HWS CCD in pixels (1 pixel = 12 μm) and the magnfication between the HWS and its conjugate plane at the ITM is approximately a factor of 7, indicating that 1 pixel corresponds to $\approx 72\,\mu$m at the ITM.

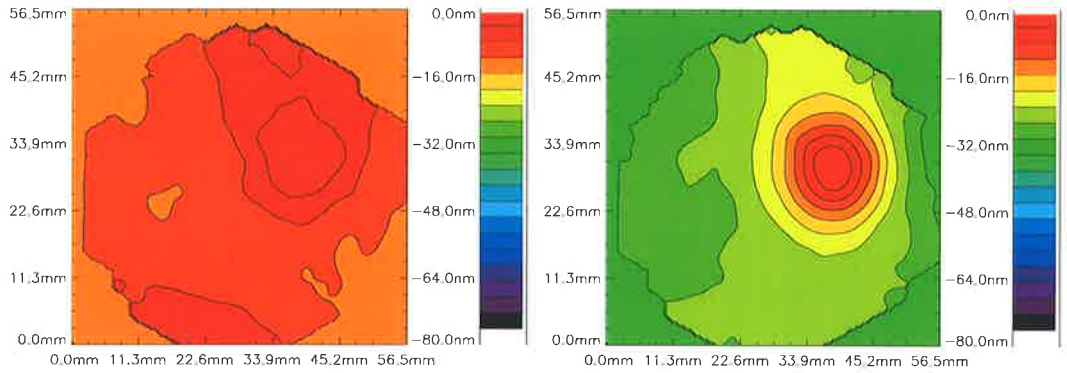

(a) $t_{\text{expt}} = 0.38$s (b) $t_{\text{expt}} = 1.63$s

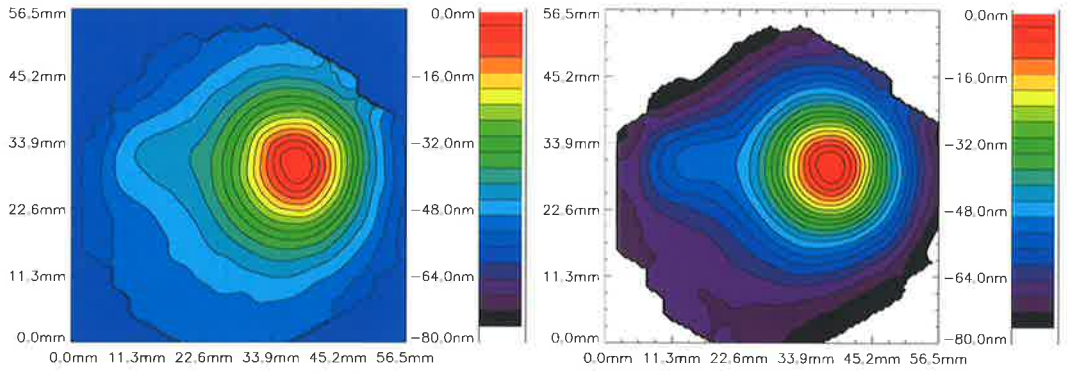

(c) $t_{\text{expt}} = 7.06$s (d) $t_{\text{expt}} = 25.43$s

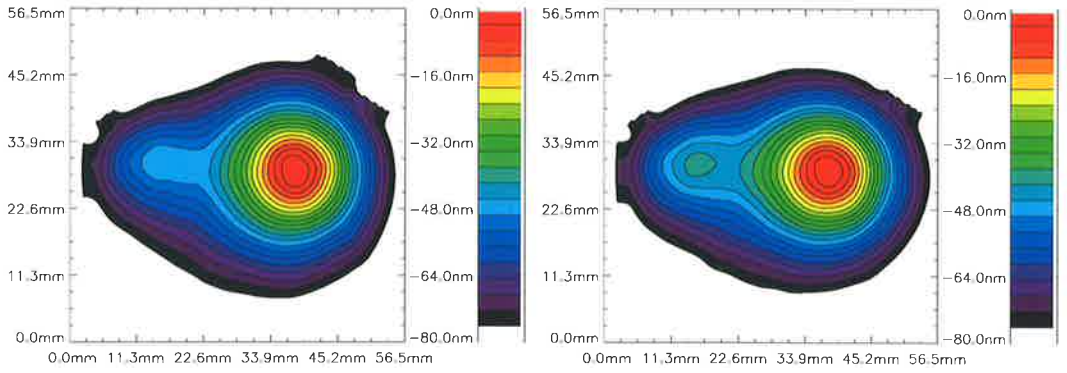

(e) $t_{\text{expt}} = 87.00$s (f) $t_{\text{expt}} = 291.39$s

Figure 5.13: Contour plots of the wavefront distortion in sapphire and fused silica, $\mathbf{WD}^{(\mathbf{off})}$, at various times from $t_{\text{expt}} = 0$ s, at which the laser was locked to the cavity. In order to compare the wavefront distortion at different times, all plots share the same colour scale. As such, parts of the distortion saturate the scale at later times resulting in an apparent reduction of spatial extent with time.

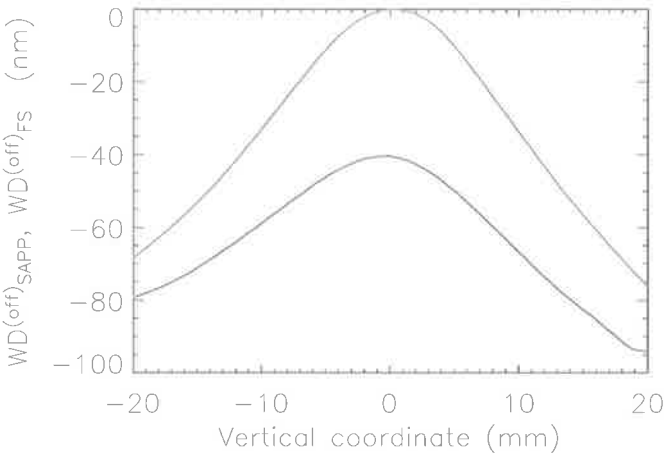

Figure 5.14: Vertical cross-sections of wavefront distortion in the sapphire ITM, $WD^{(off)}_{SAPH}$, (red) and fused silica CP, $WD^{(off)}_{FS}$, (blue). Some residual tilt is present on the WD.

is the temporal development of the defocus predicted by the theory of Hello and Vinet. This theory, however, assumes that the power is constant, which it is not in this case as shown in Figure 5.15 b). The difference between the measured and theoretical curves illustrates the advantage of having a wavefront sensor: the temporal development of the thermal lensing in the two optics may be measured directly and individually in each of the optics, rather than inferred from the behaviour of the cavity and an idealized model of the thermal lensing. This does not imply that the Hello-Vinet theory is incorrect, merely that this scenario does not lie within the range of the assumptions of the theory. Therefore, it would be inappropriate to apply the Hello-Vinet theory to this cavity to diagnose its properties.

5.5.3 Correlation of measured distortion and stored power

A finite element simulation was run to model the temporal development of the thermal lenses in the sapphire and fused silica using the temporal

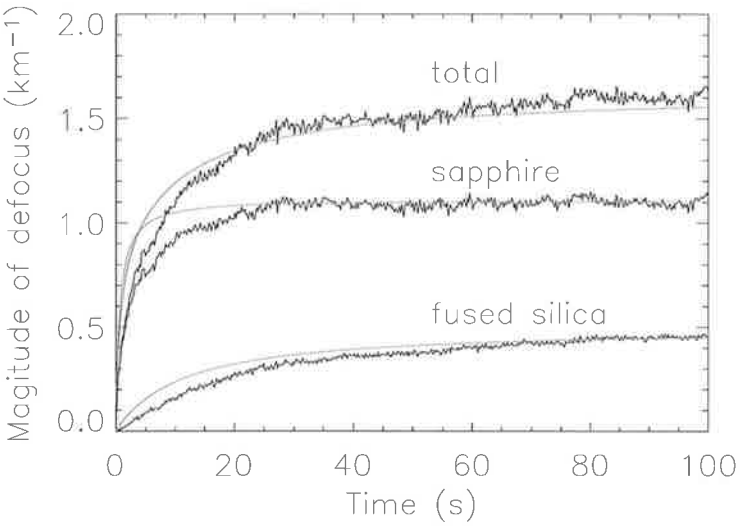

(a)

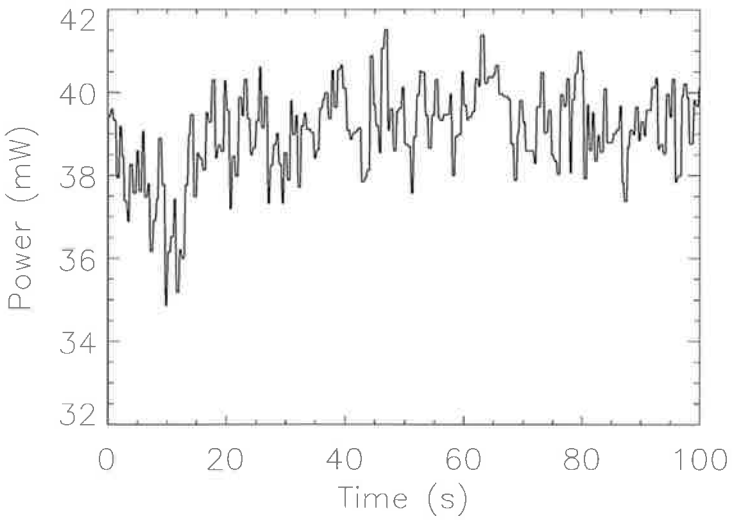

(b)

Figure 5.15: a) Time dependence of the sapphire, fused silica and total (sapphire + fused silica) thermal lenses as measured by the Hartmann sensor and experienced by the cavity mode. Also plotted is the prediction of the temporal development from the theory of Hello and Vinet. b) Time dependence of the power transmitted through the ETM, as recorded by the beam profiler.

development of the intra-cavity power and beam size measured by the beam profiler. The source code for the model can be found in Appendix B.3. The normalized defocus of this lens is plotted as a function of time in Figure 5.16 a) (red). Also plotted is the normalized defocus measured by the Hartmann sensor (blue). The difference between the two curves is plotted in Figure 5.16 b) and has an rms value of approximately 0.03. The curves were normalized by setting the average value between $t_{\mathrm{expt}} = 100$ and $t_{\mathrm{expt}} = 300$ s to 1. This was necessary because that the transmittance through the end mirror is not known accurately and, hence, the absolute power in the cavity can not be determined accurately. There is clearly good agreement between the finite element model of the defocus and the defocus measured by the HWS sensor.

5.5.4 Correlation of measured distortion and cavity mode size

The cavity mode size at the ETM, as measured by the beam profiler, and the mode size predicted by the measured distortion were compared for a measurement that had particularly unstable mode-matching. The results are plotted in Figure 5.17 a). There is excellent agreement between the magnitudes of the predicted and measured cavity mode sizes and a clear correlation between fluctuations in the measured and predicted mode sizes. The difference between the measured and predicted cavity mode size is plotted in Figure 5.17 b) and has an rms value of approximately 0.05 mm.

5.6 Conclusion

The results presented in this Chapter show that the HWS described in Chapters 3 and 4 can be used to measure absorption-induced wavefront distortion in optics that are suspended in a large vacuum system. The sensitivity of the sensor was $\lambda/730$ where $\lambda = 800$ nm (average of 10 frames), which was worse than the shot-noise limited sensitivity, probably due to residual air

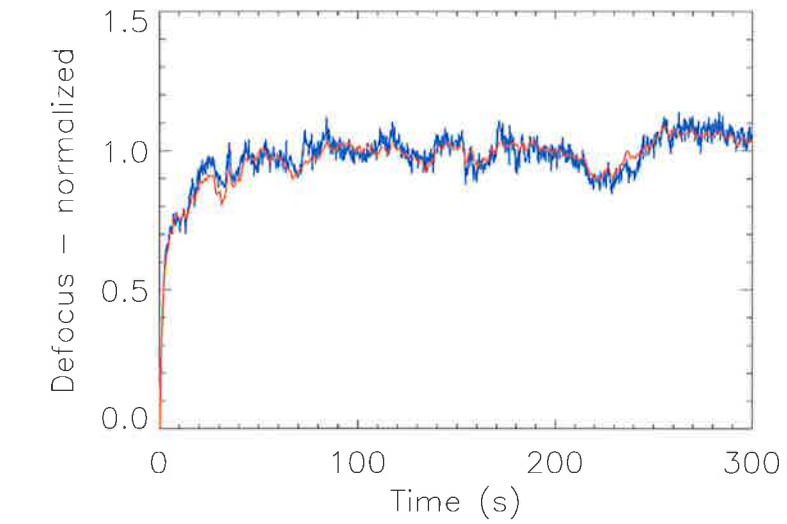

(a)

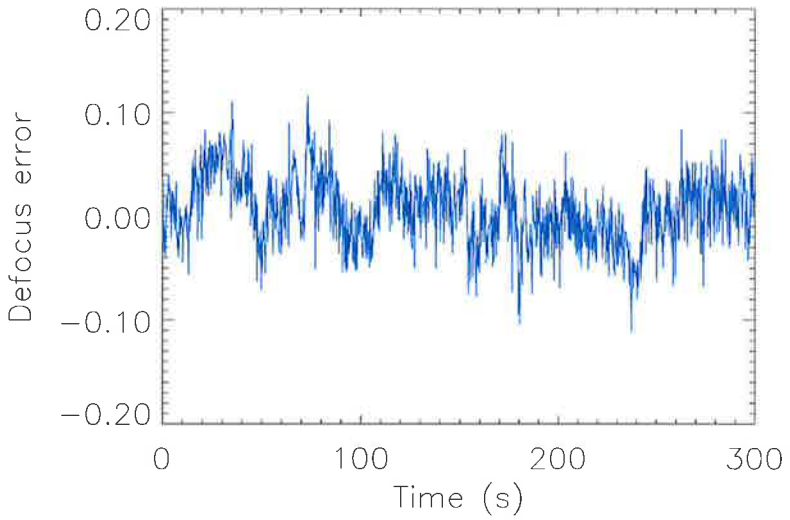

(b)

Figure 5.16: a) Finite element prediction of the total defocus using the measured of intracavity power versus time (red curve) and the measured defocus (blue curve). Both plots were normalized to remove any scaling issues. b) the difference between the red and blue curves which has an rms value of approximately 3%.

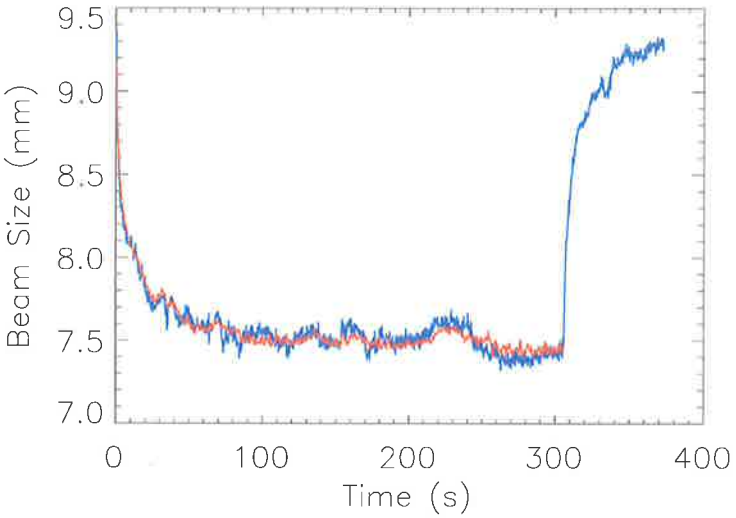

(a)

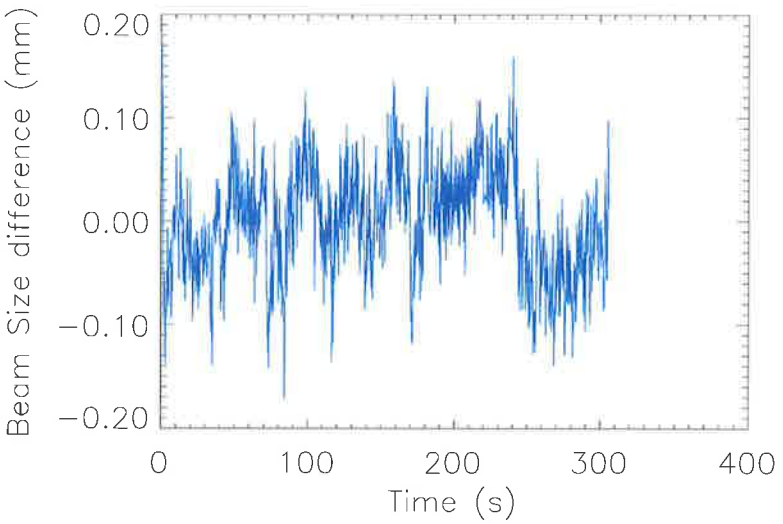

(b)

Figure 5.17: a) Cavity mode size versus time. The red curve is the measurement from the beam profiler. The blue curve is the prediction from the measurement of the Hartman sensor. b) the difference between the red and blue curves which has an rms value of approximately 0.05 mm.

currents. The HWS was validated by showing that the measured distortion was consistent with the predictions of a FEM of the ITM and CP and the measured cavity power, and by showing that the cavity mode size predicted using the measured distortion agreed to within 0.05 mm (rms), about 0.7%, with the measured mode size.

These results thus indicate that the installed HWS is both sufficiently sensitive for the measurements of absorption-induced wavefront distortion in advanced GWI, concordant with the requirements stated in Section 1.3.2, and is accurate. Importantly, the HWS provides a direct, detailed measurement of the variation of the WD, rather than a measurement that relies on the validity of assumptions and models. Although the wavefront distortion was characterized by the defocus in this instance, the profile is rich in spatial information that is necessary for any future directed compensation system, such as the scanning CO_2 heating laser described in Section 1.3.1.

Chapter 6

Off axis measurement of wavefront distortion

6.1 Background

The measurement of three-dimensional index-of-refraction distributions with an optical wavefront sensor was described by Roggemann *et al.* [104]. They framed the problem to cover arbitrary three dimensional index-of-refraction distributions and, as such, required multiple views of the variations in accordance with traditional tomography. The solution presented in this chapter takes advantage of the cylindrical symmetry inherent in the thermal lensing problem in a GWI to solve for the refractive index distribution in the glass test masses using only a single view approximately $20 - 40°$ off-axis. Tomographic reconstruction of cylindrically symmetric refractive index distributions using a single view has previously been discussed by Miranda *et al.* [105]. However, their solution relied on a view that was perpendicular to the axis of symmetry. This view is not possible with a temperature distribution in a cylindrical glass optic and hence their solution is not applicable to this problem.

6.2 Objective

In this chapter I will describe the measurement of absorption induced wavefront distortion (WD) using an off-axis HWS. I begin by discussing, in Section 6.3, the *analysis* of a measured off-axis wavefront distortion to determine the axially-symmetric temperature distribution in a test mass, and thus calculate the on-axis wavefront distortion. The objective of the remainder of the chapter is the proof-of-principle of the analysis under ideal conditions using a numerical simulation, described in Section 6.5, and under practical conditions using a bench-top experiment, described in Section 6.5.3.

6.3 Analysis of wavefront distortion measured off-axis

A probe beam transmitting through an axially-symmetric temperature distribution $T(r,z)$ in a test optic is shown in Figure 6.1. The temperature distribution results in a refractive index distribution, $n(r,z) + n_2$, which is a deviation from the nominal refractive index, n_0. The resulting wavefront distortion, $\mathrm{WD}(x\prime, y\prime)$, is measured at the plane $\mathrm{P_{meas}}$. The projection of this wavefront distortion onto the exit plane of the optic, $\mathrm{P_{exit}}$, is denoted $\mathrm{WD}(x,y)$ and is determined by the path integral through $T(r,z)$, where the path, $\vec{\sigma}(z)$, is defined parametrically

$$\begin{aligned} \vec{\sigma}(z) &= \{x_p(z), y_p(z), z\} \\ x_p(z) &= x + z\tan(\theta) \\ y_p(z) &= y \end{aligned}$$

where x and y are the coordinates of the path as it crosses the plane $z = 0$ and are related to the coordinates $x\prime$ and $y\prime$, by

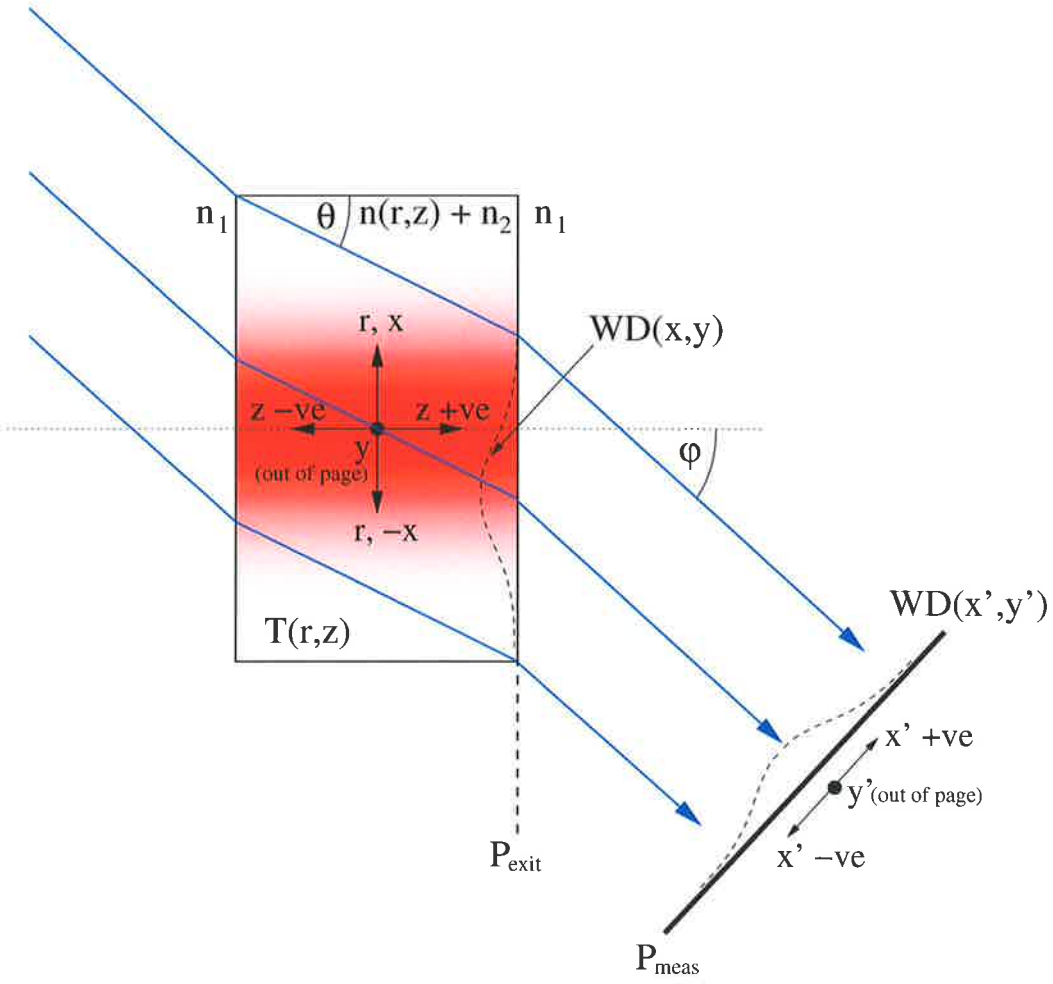

Figure 6.1: Schematic showing off-axis transmission through an axially symmetric thermo-refractive index distribution, $n(r,z) = \mathrm{d}n/\mathrm{d}T \times T(r,z)$ in a test optic with nominal refractive index n_2. The accumulated wavefront distortion, WD$(x\prime, y\prime)$, is measured at the plane $\mathrm{P_{meas}}$. The accumulated wavefront distortion projected onto the exit plane of the optic, $\mathrm{P_{exit}}$, is denoted WD(x,y).

$$\begin{aligned} x\prime &= x\cos(\varphi) \\ y\prime &= y \end{aligned}$$

Thus, the path integral that returns the projected wavefront distortion, $\mathrm{WD}(x,y)$, is given

$$\mathrm{WD}(x,y) = \frac{\mathrm{d}n}{\mathrm{d}T}\int_{z_0}^{z_1} T(x(z),y(z),z)\,|\vec{\sigma}'(z)|\,\mathrm{d}z$$

where $|\vec{\sigma}'(z)|$ is the infinitesimal length of a path element given by

$$\begin{aligned} |\sigma'(z)| &= \sqrt{\left(\frac{\mathrm{d}x_p(z)}{\mathrm{d}z}\right)^2+\left(\frac{\mathrm{d}y_p(z)}{\mathrm{d}z}\right)^2+\left(\frac{\mathrm{d}z}{\mathrm{d}z}\right)^2} \\ &= \sqrt{\tan^2(\theta)+1} \end{aligned}$$

6.3.1 A zonal representation of $T(r,z)$

In a zonal representation, the region of the temperature distribution is spanned by a set of discrete volume elements, or voxels, $V_{ij}(r,z)$, that are discontinuous in r and z and have a uniform internal density, defined as

$$V_{ij}(r,z) = \begin{cases} 1 & \text{for} \quad r_i \le r < r_{i+1} \text{ and } z_j \le z < z_{j+1} \\ 0 & \text{otherwise} \end{cases}$$

The boundaries of these functions in the cut-away of a cylinder are illustrated in Figure 6.2. For reference, the volume elements that were used by Roggemann *et al.* [104] were not cylindrically symmetric and had a non-uniform density defined by a three-dimensional Gaussian refractive index distribution within the region of the volume element. The path integral through the function $V_{ij}(r,z)$ is given by:

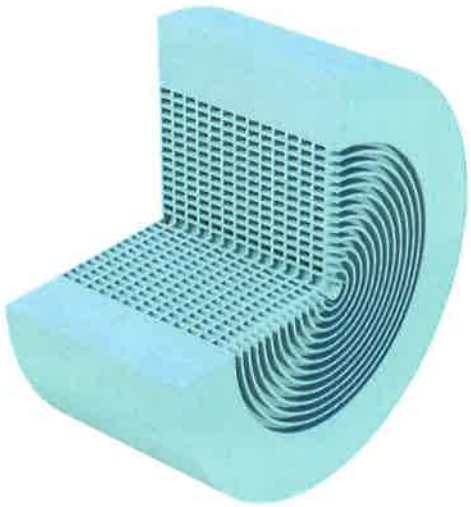

Figure 6.2: Cut-away of a cylinder containing 14×14 annular voxels

$$w_{ij}(x,y) = \int_{z_0}^{z_1} V_{ij}(r,z)\,\mathrm{d}z \tag{6.1}$$

$$= \int_{Z_{ij}^{\text{lower}}(x,y)}^{Z_{ij}^{\text{upper}}(x,y)} 1\,\mathrm{d}z \tag{6.2}$$

where $Z_{ij}^{\text{lower}}(x,y)$ and $Z_{ij}^{\text{upper}}(x,y)$ are the limits of integration through the ij^{th} volume element for a ray passing through the coordinates $(x,y,0)$. Provided one chooses a fine enough mesh, one can ensure a good approximation to all axially symmetric temperature distributions.

Physically, the functions $w_{ij}(x,y)$ can be thought of as the wavefront distortion measured at the exit plane, P_{exit}, resulting from transmission through a uniform density annular volume element, $V_{ij}(r,z)$. An example of a single annular volume element in a mesh is shown in Figure 6.3 a) and the corresponding wavefront distortion is shown as a greyscale image in Figure 6.3 b).

To prevent large numbers of indices in the following discussion, the functions $V_{ij}(r,z)$ and $w_{ij}(x,y)$ where $1 \leq i \leq N_r$ and $1 \leq j \leq N_z$ will be re-labelled $V_k(r,z)$ and $w_k(x,y)$ where $1 \leq k \leq N_r \times N_z$.

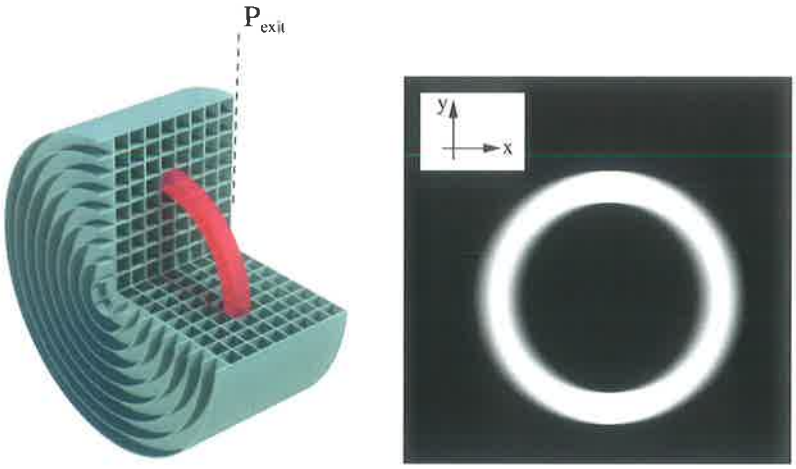

(a) (b)

Figure 6.3: a) An example of a single annular volume element, $V_{ij}(r,z)$, and b) a greyscale map of the corresponding wavefront distortion, $w_{ij}(x,y)$, measured at the exit plane, $\mathrm{P_{exit}}$.

Recovery of the temperature distribution from the off-axis measurement becomes a straightforward process. The coefficients, A_k, of the best fit of $w_k(x,y)$ to the measured wavefront distortion are determined. If the wavefront distortion is measured at m positions (x_α, y_α), where $1 \leq \alpha \leq m$, the best fit is determined using the fitting method described by Bevington [106].

The calculation of a least squares fit to a set of functions, $w_k(x,y)$, begins by determining a vector, $\mathbf{B}$, containing the overlap of the measured wavefront distortion projected onto $\mathrm{P_{exit}}$, the exit plane, $\mathrm{WD}(x,y)$, and each $w_k(x,y)$, where the B_k component of the vector is given by

$$B_k = \sum_\alpha \left[\mathrm{WD}(x_\alpha, y_\alpha)\ w_k(x_\alpha, y_\alpha)\right]. \tag{6.3}$$

Next one determines a square matrix $\mathbf{M}$, representing the overlap of every combination of $w_k(x,y)$, where the lk^{th} component of the matrix, M_{lk}, is given by

$$M_{lk} = \sum_\alpha \left[w_l(x_\alpha, y_\alpha)\ w_k(x_\alpha, y_\alpha)\right]. \tag{6.4}$$

Thus, the coefficients, A_k, of the best fit of $w_k(x,y)$ to $\mathrm{WD}(x,y)$ are the components of the vector $\mathbf{A}$, given by

$$\mathbf{A} = \mathbf{B}\,\mathbf{M}^{-1} \tag{6.5}$$

where $\mathbf{M}^{-1}$ is the inverse of $\mathbf{M}$. The fitted refractive index distribution, $n_{\mathrm{fit}}(r,z)$, is then

$$n_{\mathrm{fit}}(r,z) = \sum_k A_k\, V_k(r,z)\,, \tag{6.6}$$

the temperature distribution, $T_{\mathrm{fit}}(r,z)$, is

$$T_{\mathrm{fit}}(r,z) = \left(\frac{\mathrm{d}n}{\mathrm{d}T}\right)^{-1} \sum_k a_k\, V_k(r,z)\,, \tag{6.7}$$

and, finally, the fitted on-axis wavefront distortion, $\mathrm{WD}_{\mathrm{fit}}(r)$, is given by

$$\begin{aligned} \mathrm{WD}_{\mathrm{fit}}(r) &= \int_{z_0}^{z_1} n_{\mathrm{fit}}(r,z)\,\mathrm{d}z \\ &= \int_{z_0}^{z_1} \sum_k A_k\, V_k(r,z)\,\mathrm{d}z. \end{aligned} \tag{6.8}$$

6.4 Numerical simulation of voxel analysis

6.4.1 Simulation procedure

In this simulation, I compare the on-axis wavefront distortion, for a realistic temperature distribution, by a) directly calculating the on-axis distortion, and b) calculating the off-axis distortion and then using the voxel reconstruction to determine the best-fit temperature distribution and its resulting on-axis distortion.

1. Using the substrate absorption solution of Hello and Vinet, specify a temperature distribution, $T(r,z)$, in a 200 cm diameter, 100 cm thick glass cylinder [1] heated by a Gaussian beam with a $1/e^2$ radius of 25 cm

[1] The optic is large by realistic standards but does not affect the results of the voxel analysis.

propagating along the cylindrical axis. For this simulation, the glass had the same thermal properties as the BG20 filter glass described in Chapter 2.

2. Integrate $T(r,z)$ along the z-axis to determine the on-axis wavefront distortion, $\mathrm{WD}_{\mathrm{on}}(r)$.

3. Determine the off-axis path integral of $T(r,z)$:

   (a) Determine the off-axis path integral projected onto, $\mathrm{P}_{\mathrm{exit}}$, the exit plane of the optic, $\mathrm{WD}_{\mathrm{off}}(x_\alpha, y_\alpha)$, through the distribution at angle $\theta = 32.6°$ by taking the sum of a series of axial slices of the temperature distribution of thickness $\mathrm{d}z$ that are offset from each other in the x-direction by $\mathrm{d}z\tan(\theta)$ at the m coordinates (x_α, y_α), where $1 \leq \alpha \leq m$. Note that the path integral (projection) through a distribution at angle θ is known as the Radon Transform of that distribution [107].

   (b) Determine the aperture created by the front and back faces. Set $\mathrm{WD}_{\mathrm{off}}(x,y)$ to be zero outside this aperture.

4. Determine the functions, w_k:

   (a) Specify the limits of each of the $N_r \times N_z$ volume elements, $V_k(x,y)$, where there are N_r elements in the radial direction and N_z elements in the axial direction. Note that because of the aperturing, some areas of the cylinder are undersampled and some are not sampled at all. Hence the extent of the voxels in the radial direction is set to be less than the actual radius of the cylinder.

   (b) Determine the path integral through each uniform density volume element, w_k where $1 \leq k \leq N_r \times N_z$, using Equation 6.1.

   (c) Determine the overlap of $\mathrm{WD}_{\mathrm{off}}(x_\alpha, y_\alpha)$ with the functions w_k, using Equation 6.3 to yield $\mathbf{B}$.

5. Determine the square matrix $\mathbf{M}$, representing the overlap of every combination of $w_k(x_\alpha, y_\alpha)$, using Equation 6.4.

6. Invert $\mathbf{M}$ to determine $\mathbf{M}^{-1}$.

7. Determine the best fit coefficients $\mathbf{A}$ using Equation 6.5:

8. Reconstruct the temperature distribution $T_{\text{fit}}(r, z)$ using Equation 6.7.

9. Determine the on-axis distortion, $\text{WD}_{\text{fit}}(r)$, by integrating the reconstructed temperature distribution along the axis using Equation 6.8.

10. Compare the reconstructed on-axis distortion, $\text{WD}_{\text{fit}}(r)$, with the known on-axis distortion, $\text{WD}_{\text{on}}(r)$, calculated in Step 2.

6.4.2 Simulation results

The given and reconstructed temperature distributions from the simulation are shown as false color images in the left and right cells, respectively, of Figure 6.4 a). Note that the full width of the temperature distribution can't be reconstructed due to aperturing and thus the reconstructed temperature distribution does not span the full width and has grey edges. The reconstruction qualitatively agrees with the given temperature distribution.

The directly calculated and reconstructed on-axis wavefront distortions are shown in Figure 6.4 b). There is clearly very good agreement between the two distortions within the constraint of the quantization inherent in the analysis.

The results of the simulation demonstrates that the off-axis voxel analysis is, in principle, capable of reconstructing the temperature distribution and on-axis distortion under ideal conditions.

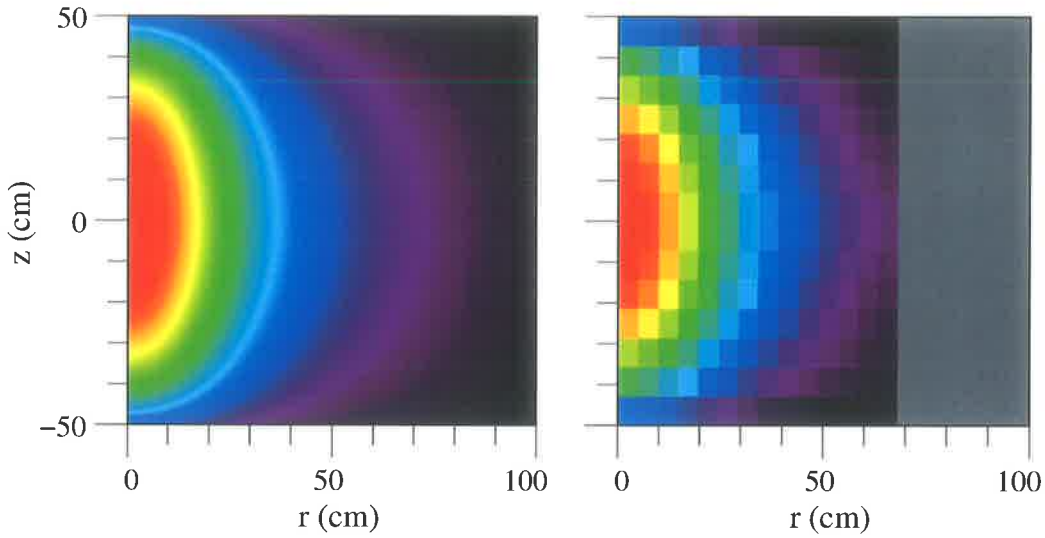

(a)

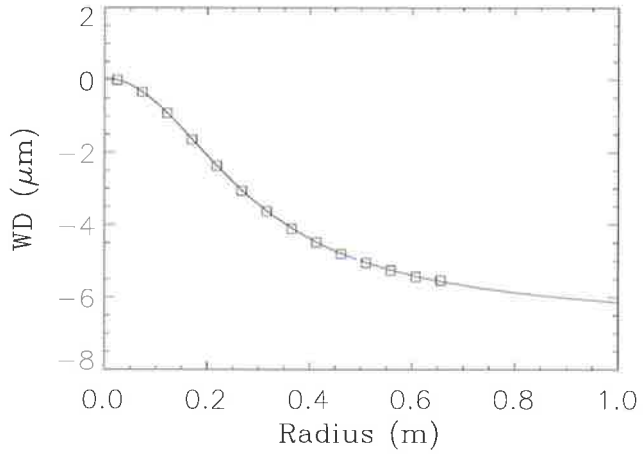

(b)

Figure 6.4: Simulation results: a) (left) False colour image of temperature distribution in simulated BG20 glass (arbitrary units) and (right) false colour image of 14×14 voxel reconstruction of temperature distribution. Grey area indicates the region not reconstructed. b) Wavefront distortion (WD): directly calculated on-axis distortion, $\mathrm{WD}_{\mathrm{on}}(r)$, (line) and reconstructed on-axis distortion, $\mathrm{WD}_{\mathrm{fit}}(r)$, (points).

6.5 Proof-of-principle demonstration of off-axis voxel reconstruction

6.5.1 System layout

The measurement system for the proof-of-principle of the off-axis voxel analysis is shown in Figure 6.5. The BG20 glass test optic (GTO) described in Chapter 2 was placed in the object arm of a Mach-Zender interferometer that was constructed using a 10mW HeNe laser beam. A 3W Nd:YAG cw laser beam was propagated along the axis of the GTO to produce wavefront distortion in the GTO. The on-axis WD was measured using the MZ interferometer in which the exit plane of the GTO was imaged onto CCD_{MZ}.

The off-axis wavefront distortion, WD $(x\prime, y\prime)$ at P_{meas}, was measured using a HWS similar to that described in Chapters 3 and 4. The output from the 820 nm Agilent fibre-coupled SLD was expanded and collimated into a beam by the lenses in telescope T5. This probe beam was incident on the GTO at an angle of $57.2 \pm 0.2°$ and transmitted through the optic with an internal angle of $32.8° \pm 0.2°$ assuming the nominal refractive index is 1.55. The probe beam was then demagnified with a Galilean telescope, T6, and was incident on the HWS.

6.5.2 Procedure

The procedure for measuring the on-axis and off-axis WD in the GTO was:

1. Place a grid of holes at the exit plane of the GTO and record image of 632.8 nm transmission through the grid on CCD_{MZ} to determine the scale of the GTO image on the CCD.

2. Repeat step 1 with the 820 nm transmission through the grid and record an image on the HWS CCD but with the Hartmann plate removed, to determine the scale of the GTO image at the HWS.

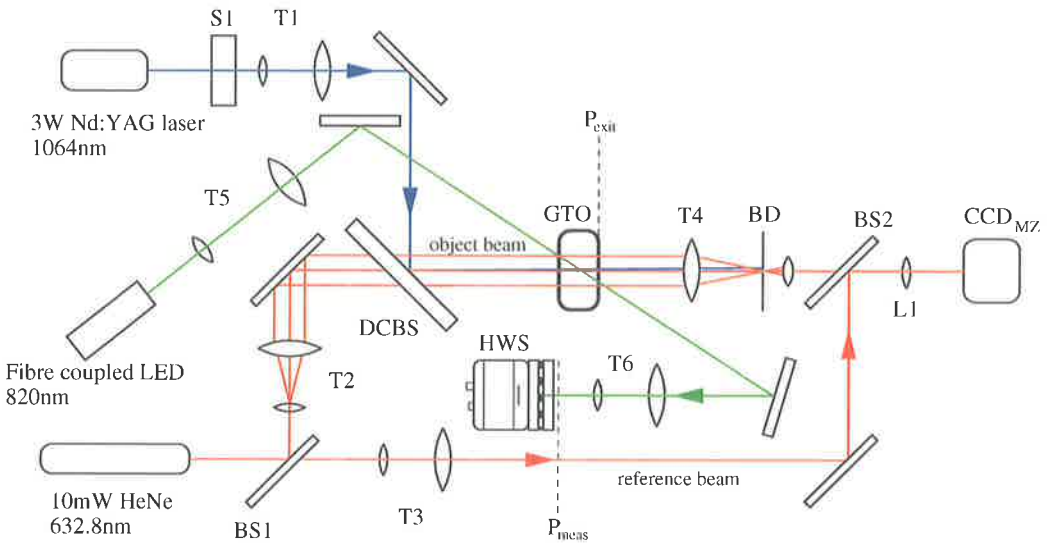

Figure 6.5: Schematic of experiment to measure thermal lensing in a cylindrical test optic. The output of a 3W 1064 nm Nd:YAG laser is incident on shutter S1. When the shutter is open, the beam passes through telescope, T1, and is transmitted through the BG20 glass test optic. The 1064nm is incident on telescope T4 at an angle very close to normal incidence. A beam dump with a small hole in it is placed at the focal plane of T4 and is adjusted such that normally incident rays on T4 pass through the hole and those rays at a small angle are blocked. The 1064 nm beam is blocked by the beam dump. The output of a 10 mW HeNe laser is the input to a Mach-Zehnder interferometer, the object arm of which contains the BG20 optic. The object and reference arms are expanded by telescopes, T2 and T3, respectively. The object arm is normally incident on telescope T4, is demagnified and recombined with the reference arm at the second beamsplitter, BS2. The interference pattern at the exit plane of the glass test optic is imaged onto the CCD with lens L1. A dichroic beam splitter, DCBS, immediately before the glass test optic is used to combine the two different wavelengths. The output from the 820 nm Agilent fibre-coupled SLD is expanded and collimated into a beam by the lenses in telescope T5. This probe beam is incident on the GTO at an angle of $57.2 \pm 0.2°$. The transmitted probe beam is demagnified with a Galilean telescope, T6, and is incident on the HWS. The exit and measurement planes described in Figure 6.1 are indicated on this figure by P_{exit} and P_{meas}, respectively.

3. Record a series of reference interference patterns, with no heating of the GTO, with $\mathrm{CCD_{MZ}}$.

4. Record a series of reference measurements with the HWS (with the Hartmann plate replaced).

5. $t_{\mathrm{expt}} = 0$ s. Turn on the 3W 1064 nm Nd:YAG laser to induce a thermal lens in the GTO.

6. $t_{\mathrm{expt}} \approx 500$ s. Record a series of distorted interference patterns with $\mathrm{CCD_{MZ}}$. Simultaneously, record a series of distorted Hartmann images with the HWS.

7. Turn off 1064nm laser and cease recording with $\mathrm{CCD_{MZ}}$ and the HWS.

6.5.3 Results

The on-axis and off-axis wavefront distortions are shown in Figures 6.6 a) and b) respectively, where the scale was established by the images recorded in Step 1. The off-axis distortion is clearly elongated in the x direction due to propagation through the temperature distribution at a large angle. The shape of the aperture (tall and thin) seen in Figure 6.6 b) is consistent with viewing the GTO at a large external angle in the horizontal plane.

The off-axis wavefront distortion, $\mathrm{WD}(x\prime, y\prime)$, was projected onto the coordinate system at exit plane of the optic, $\mathrm{P_{exit}}$. The off-axis voxel analysis was applied to the projected-off-axis-distortion, $\mathrm{WD}(x, y)$, to reconstruct the on-axis distortion, $\mathrm{WD_{fit}}(r)$, using a variety of different voxel configurations (N_r, N_z and $r_{V_{max}}$). Two reconstructions are plotted in Figures 6.7 a) and b), respectively. Also plotted is the radial on-axis distortion, $\mathrm{WD_{on}}(r)$, measured by the interferometer. These plots show that the off-axis voxel analysis is, in principle, capable of reconstructing the on-axis wavefront distortion.

The accuracy of the reconstruction is dependent upon the configuration of the voxels. For example, the quality of the reconstruction improves when the range in the radial direction is reduced. This is to be expected because

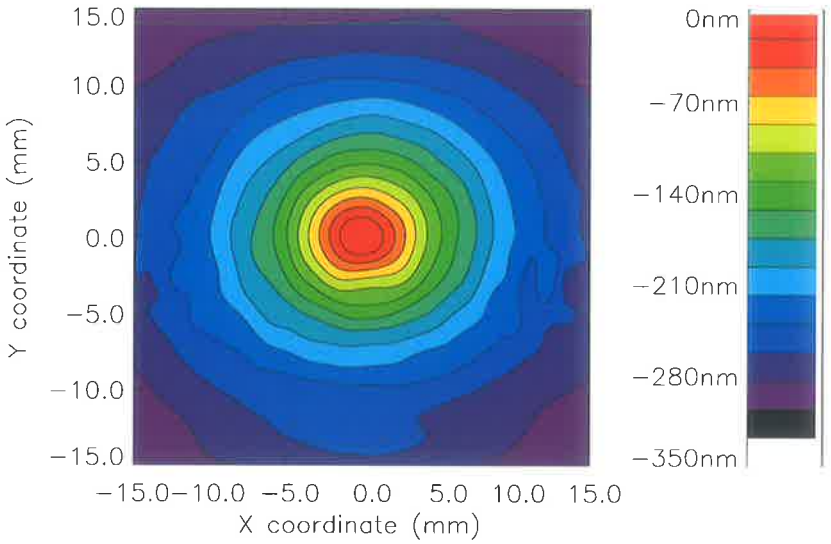

(a) Interferometer WD measurement

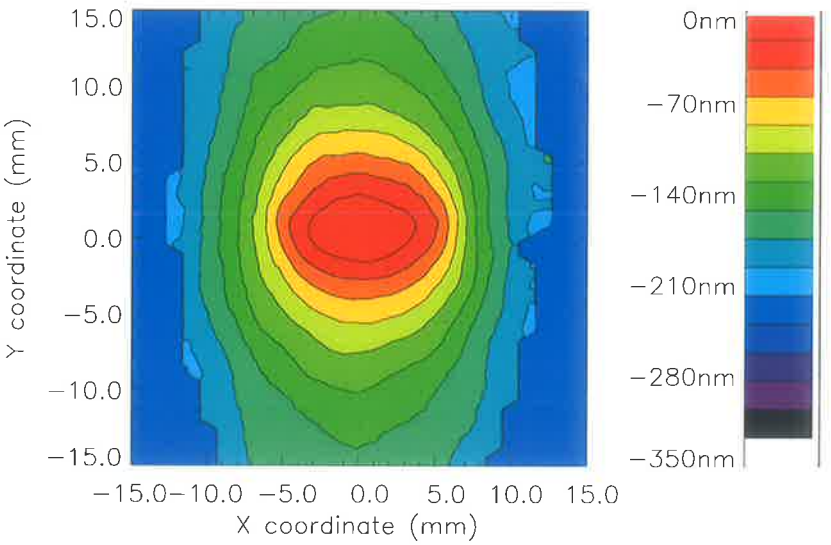

(b) HWS WD measurement

Figure 6.6: Contour plots of a) on-axis and b) off-axis wavefront distortion as seen at the plane P_{meas}.

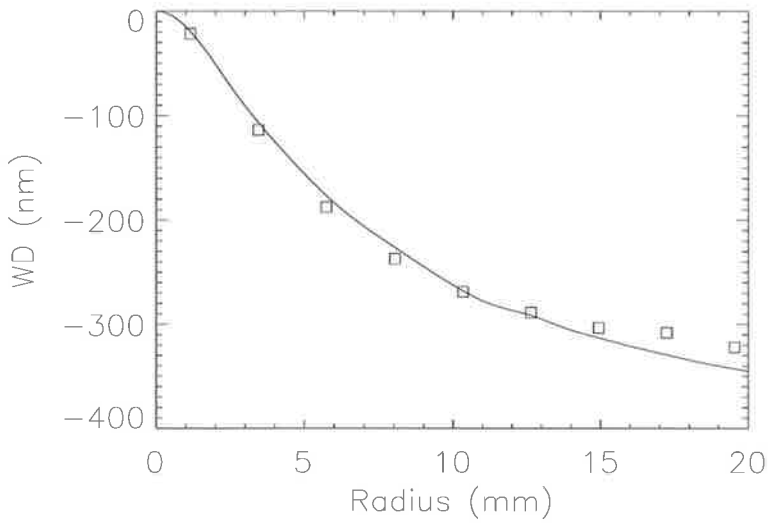

(a) $N_r = 10$, $N_z = 7$, $r_{V_{max}} = 23.0$ mm

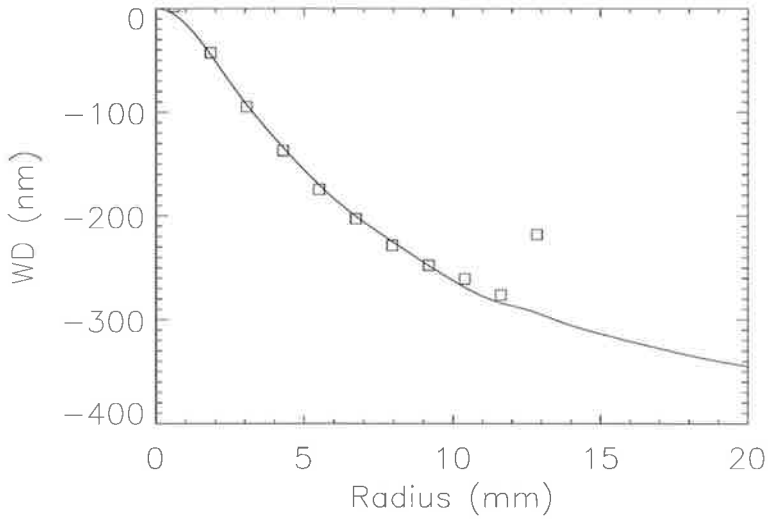

(b) $N_r = 11$, $N_z = 4$, $r_{V_{max}} = 13.5$ mm

Figure 6.7: On-axis measured and off-axis reconstructed wavefront distortion. a) Reconstruction with 10 annular × 7 axial volume elements to a radius of 23.0 mm with an RMS wavefront error of 11 nm. b) Reconstruction with 11 annular × 4 axial volume elements to a radius of 13.5 mm with an RMS wavefront error of 4.5 nm.

the aperture reduces the sampling of extreme radial values. Also, the quality of the reconstruction decreases when the number of voxels is increased. Once again, this is an expected effect of trying to fit a higher spatial resolution model to a finite spatial resolution measurement.

6.6 Conclusion

The off-axis voxel analysis described here has been demonstrated to work under ideal conditions in the simulation presented in Section 6.4.1 and in practice in the experiment results presented in Section 6.5.3. There is scope in future work to examine the efficacy of this technique under a variety of conditions, such as the dependence on noise sources and the optimum model configuration at a given angle. As such, this technique has been demonstrated to be a promising area of research.

Chapter 7

Conclusion

7.1 Review of aims

The objective of the research described in this thesis is the development of a wavefront sensor with sufficient sensitivity and spatial resolution for use in a closed-loop active thermal compensation system in an advanced GWI. The use of such a sensor contributes to solving one of the problems associated with upgrading from initial to advanced gravitational wave interferometry, as required for the realisation of gravitational wave astronomy. The specific aims, therefore, were

1. to validate the Hello-Vinet solution for absorption induced wavefront distortion. This solution has been used extensively in the modelling of GW interferometers,

2. to develop and test a wavefront sensor with a sensitivity sufficient for use in advanced GWI: at least $\lambda/467$ @ 632.8 nm with a spatial resolution of at least 23×23 sample points over the region of interest [21], and to investigate the limits of sensitivity possible with the wavefront sensor,

3. to deploy the wavefront sensor in a long-baseline high optical power

cavity and measure the thermal lensing within the input-coupling mirror, or ITM, of that cavity,

4. and the development and proof-of-principle demonstration of a single view tomographic algorithm for reconstruction of axially symmetric wavefront distortion.

7.2 Summary of results

A high-precision interferometric measurement of absorption-induced wavefront distortion was described in Chapter 2. The results showed good agreement with the predicitions of Hello and Vinet for longer times, but there was a small systematic difference, possibly due to convective cooling of the glass test optic - a cooling mechanism not included in the Hello-Vinet model. The validation of this model, within this limitation, increases the confidence in the validity of numerical models of GWI, such as MELODY [16], that employ the Hello-Vinet model.

The design and development of a Hartmann wavefront sensor (HWS) for advanced GWI was presented in this Chapter 3. Extensive modelling and diffraction simulations were used to optimize the Hartmann sensor, including an investigation of the systematic error introduced by cross-talk between neighbouring spots in the HWS. In the final HWS design, random noise associated with the photoelectrons in the pixels of the CCD was identified as the major noise source, limiting the single-shot sensitivity to about $\lambda/1050$ @ 633nm based on the nominal properties of the CCD.

The measurement of the sensitivity and accuracy of the HWS was discussed in Chapter 4. The choice of an incoherent light source was shown to be effective in reducing the uncertainty in centroid measurements to the Poissonian shot-noise limit, thereby enabling the wavefront error to be reduced to at least $\lambda/15{,}500$ by averaging multiple measurements. Evidence of another noise source, due probably to fluctuations in the temperature of the HWS, was observed at this level. The measurement of a very small defocus,

equivalent to the change in wavefront curvature that would be caused by an 850m lens, with an accuracy of 1.7% and a precision of 0.7% was also described.

Chapter 5 described the use of the HWS for the measurement of absorption-induced wavefront distortion in optics that were remotely suspended in a large vacuum system as part of a high optical power cavity. The sensitivity of the HWS was $\lambda/730$ at $\lambda = 800$ nm (average of 10 frames), limited somewhat by the noisy environment and residual air currents. The HWS measurements were validated by showing that the measured distortion was consistent with the predictions of a FEM of absorption-induced wavefront distortion, using the measured cavity power. The cavity mode size predicted using the measured distortion agreed to within 0.05 mm (rms) with the mode size measured by a beam profiler. The results in that chapter also illustrated that the HWS provides a direct, detailed measurement of the variation of the absorption-induced wavefront distortion, rather than an indirect measurement that relies on the validity of assumptions and models to infer information about the intra-cavity optics.

In Chapter 6, a single-view off-axis tomographic technique was described. A numerical simulation was used to demonstrate that a Hello-Vinet temperature and refractive index distribution could be recovered with good fidelity using a single off-axis view. The technique was validated by showing that the on-axis results of the tomographic analysis agreed well with the wavefront distortion measured on-axis using a Mach-Zehnder interferometer.

7.3 Future directions

It was evident from the results presented in Chapter 4 that the temperature dependence of the current Hartmann sensor design probably limits the long-term accuracy of the sensor. Work on future designs will most likely focus on reducing this temperature dependent error. A passive reduction in the temperature dependence can be made by replacing the brass Hartmann plate

with one made from a material with a low coefficient of thermal expansion, for example, invar. Alternatively or concurrently, active stabilization of the temperature, using a combination of high precision thermistors and thermo-electric coolers, could be employed to maintain a constant temperature in the Hartmann sensor. Although this would require more development than passive solutions, it would most likely allow the Hartmann sensor to operate with high precision accuracy in many more environments.

I would also suggest further investigation of the tomographic technique, presented in Chapter 6, to optimize its sensitivity and explore its application under a variety of conditions. The generalization of this technique to non-axially symmetric wavefront distortions may be important for identifying point absorbers in test masses of advanced GWI or for the measurement of wavefront distortion in the beam-splitter of a GWI.

"Our imagination has driven us to listen for the music of the cosmos. The opening movement entertains us with familiar themes, but the remainder is an undiscovered symphony, infinitely richer and more nuanced than we can possibly imagine."

Aidan F. Brooks

Appendix A

Additional derivations

A.1 Analytic form of Hello-Vinet solution

Substrate absorption

Only the temporal Hello-Vinet substrate absorption case was considered in Chapter 2, although that solution asymptotes to the steady-state case. The solution is as follows.

For a Gaussian intensity distribution, $I(r)$, of waist w and power P, given by

$$I(r) = \frac{2\,P}{\pi\,w^2}\,\exp\left[-2\frac{r^2}{w^2}\right]$$

transmitted through a cylindrical test optic of radius a, length h, volumetric absorption α, density ρ, specific heat C, thermal conductivity K, and thermo-optic coefficient $\mathrm{d}n/\mathrm{d}T$, and assuming only radiative boundary conditions, the total wavefront distortion, $\psi\,(r,t)$, as a function of time is:

$$\psi\,(r,t) = \frac{\mathrm{d}n}{\mathrm{d}T}\int_{-h/2}^{h/2}\left[\,T(t,r,z) - T_{\mathrm{ext}}\,\right]\mathrm{d}z.$$

The temperature distribution, $T(t,r,z)$, is given by

$$T(t,r,z) = T_{\text{ext}} + \sum_{p,m} C'_{p\,m}\left[1 - \exp\left(-\alpha_{p\,m}\,t\right)\right]\cos\left(u_p\,z/a\right)\;J_0\left(\zeta_m\,r/a\right),$$

where T_{ext} is the external temperature, where

$$C'_{p\,m} = \frac{4\,\alpha\,a}{K\,h}\,\frac{p_m}{\zeta_m^2}\left[\frac{\sin\left(u_p\,h/2\,a\right)}{u_p} - \frac{\tau\cos\left(u_p\,h/2\,a\right)}{\zeta_m^2 + u_p^2}\right]\frac{1}{c_p},$$

where $\alpha_{p\,m}$ is given by

$$\alpha_{p\,m} = \frac{K}{\rho\,C\,a^2}\left(\zeta_m^2 + u_p^2\right),$$

where u_p is the p^{th} solution of

$$u = \tau\,\cot\left[\frac{u\,h}{2\,a}\right],$$

where ζ_m is the m^{th} solution of

$$x\,J_1\left(x\right) - \tau\,J_0\left(x\right) = 0,$$

where p_m is given by

$$p_m = \frac{2\,\zeta_m^2}{\zeta_m^2 + \tau^2}\,\frac{1}{J_0\left(\zeta_m\right)^2}\,\frac{1}{a^2}\int_0^a I(r)J_0\left(\zeta_m\,\frac{r}{a}\right)\,r\,\mathrm{d}r,$$

where τ is given by

$$\tau = 4\,\sigma'\,T_{\text{ext}}^3\,a/K,$$

and, finally, where c_p is given by

$$c_p = 1 + \frac{a}{u_p\,h}\,\sin\left(u_p\,h/a\right).$$

A.2 Variance of a digitized value

Determination of the variance in a digitized value. Suppose ones wishes to determine the variance in a value, N_e, which has been digitized on an n-bit scale. The gain, g_{D}, of this digitization is the ratio of the highest possible value of N_e, $N_{e_{\max}}$, and the total number of digital values, 2^n.

$$g_{\mathrm{D}} = \frac{N_{e_{\max}}}{2^n} \tag{A.1}$$

All values between $i\,g_{\mathrm{D}}$ and $(i+1)\,g_{\mathrm{D}}$ will be rounded down to $i\,g_{\mathrm{D}}$ in the digization process. Therefore the effective mean of these values is $i\,g_{\mathrm{D}}$. If a series of M measurements, x_{e_i}, are made, such that they are all rounded to $i\,g_{\mathrm{D}}$, then the variance is given by

$$\begin{aligned} \sigma^2_{\mathrm{digital},M} &= \sum_{j=1}^{M} \frac{\left(x_{e_j} - i\,g_{\mathrm{D}}\right)^2}{M-1} \\ &= \frac{1}{g_{\mathrm{D}}} \sum_{j=1}^{M} \left(x_{e_j} - i\,g_{\mathrm{D}}\right)^2 \frac{g_{\mathrm{D}}}{M-1} \end{aligned} \tag{A.2}$$

In the limit that $M \to \infty$, the set of values $\left(x_{e_j} - i\,g_{\mathrm{D}}\right)$ approaches a continuum, x, that ranges between 0 and g_{D}, the value $g_{\mathrm{D}}/(M-1)$ approaches $\mathrm{d}x$, and the variance calculation becomes an integral

$$\begin{aligned} \lim_{M\to\infty} \sigma^2_{\mathrm{digital},M} &= \frac{1}{g_{\mathrm{D}}} \int_0^{g_{\mathrm{D}}} x^2 \mathrm{d}x \\ &= \frac{g_{\mathrm{D}}^2}{3} \end{aligned} \tag{A.3}$$

Hence the standard deviation, $\sigma_{\mathrm{digital}}$ is given by

$$\sigma_{\mathrm{digital}} = \frac{1}{\sqrt{3}} \frac{N_{e_{\max}}}{2^n} \tag{A.4}$$

A.3 ABCD cavity calculation

Determine the relative size of transmission and reflection from distorting optics

Treat WD as defocus: the C component in ABCD matrices
Note that the thickness of the ITM is ignored: the thermal lens is of the order of kilometers and the thickness of the ITM is only 46 mm, hence ignoring the thickness for simplicity is OK.

```
ABCD Matrix representing beam entering ITM (thermo-elastic)
nITM = refractive index of ITM = 1.75
nVac = refractive index of vacuum = 1.0
DS1 = 1/curvature of surface
```

$$\text{MintoITM} = \begin{pmatrix} 1 & 0 \\ \frac{\text{nITM}-\text{nVac}}{\text{nVac}} * \text{DS1} & \frac{\text{nITM}}{\text{nVac}} \end{pmatrix};$$

```
ABCD Matrix representing beam transmission through wavefront distortion
(thermo-optic and elasto-optic)
Characterized by defocus: WDdef
```

$$\text{MtransWD} = \begin{pmatrix} 1 & 0 \\ \text{WDdef} & 1 \end{pmatrix};$$

```
ABCD Matrix representing beam exiting ITM (thermo-elastic)
DS2 = 1/curvature of surface = -DS1
```

$$\text{MexitWD} = \begin{pmatrix} 1 & 0 \\ \frac{\text{nVac}-\text{nITM}}{\text{nITM}} * \text{DS2} & \frac{\text{nVac}}{\text{nITM}} \end{pmatrix} = \begin{pmatrix} 1 & 0 \\ -\frac{\text{nVac}-\text{nITM}}{\text{nITM}} * \text{DS1} & \frac{\text{nVac}}{\text{nITM}} \end{pmatrix};$$

```
ABCD Matrix representing reflection from curved surface (thermo-elastic)
DS3 = 1/curvature of surface = DS1
```

$$\text{MreflectWD} = \begin{pmatrix} 1 & 0 \\ 2\,\text{DS3} & 1 \end{pmatrix} = \begin{pmatrix} 1 & 0 \\ 2\,\text{DS1} & 1 \end{pmatrix};$$

```
Determine the ABCD matrices for transmission and reflection in the ITM
```

```
MReflection = Simplify[MintoITM.MtransWD.MreflectWD.MtransWD.MexitWD] ;
MTransmission = Simplify[MintoITM.MtransWD.MexitWD] ;
```

```
Extract defocus components
```

```
reflect = MReflection[[2]][[1]]
trans = MTransmission[[2]][[1]]
```

Determine the coefficients multiplying WDef and DS1 on transmission = (1.5 and 1.75). The normalization of WDef with respect to DS1 on transmission is

$$\text{norm} = \frac{1.75}{1.5}$$

Adjust the size of DS1 such that the relative sizes contributions of the thermo-optic and elasto-optic effects and the thermo-elastic effects are consistent with the values in given in Table 5.2

$$\text{DS1} = \text{DS1} \to \frac{0.8}{1.0 + 0.2} (\text{norm} * \text{WDdef})$$

Determine the ratio of the reflection and transmission effects

$$\text{Simplify}\left[\text{reflect} / \text{trans} /. \left\{\text{nITM} \to 1.75,\ \text{nVac} \to 1,\ \text{DS1} \to \frac{0.8}{1.2}\ \frac{1.75\ \text{WDdef}}{1.5}\right\}\right]$$

Ratio = 2.533

Appendix B

Computer code

B.1 Hartmann plate optimization code

The following Mathematica file produced a complex array representing the transmission through a Hartmann plate of varying parameters of hole size and hole spacing, discussed in Steps 1 to 5 in Section 3.3.2.1.

The data array from Mathematica had some header information attached to convert it into a .ZBF file [77] suitable for importing into ZEMAX. The complex array was unchanged by this step.

The .ZBF file is loaded into ZEMAX via `POP_many.ZPL`. The command `THIC(count) = i*200.0 + 100.0` increases the thickness of the `count`-th surface in increments of 200.0 mm, from 100.0 mm to 900.0 mm. The index `count` simply identifies the 'surface' in ZEMAX which is being altered. In this case the surface is simply free space and, hence, its thickness is equal to the propagation distance or lever arm. The command `POP filename$ count` performs the physical optics propagation which uses the Fourier diffraction propagation discussed by Goodman [80]. This covers Step 6 in Section 3.3.2.1.

The output is saved to a .ZBF file from which the electric field is extracted and converted into an 8-bit TIFF image as described in Step 7 in Section 3.3.2.1.

■ **Define Function to determine the area of the intersection of a pixel with circular aperture**

```
CircIntensity[xpos1_, ypos1_ , xcent1_, ycent1_, holes1_, deltaxy1_] :=
  Module[{xylist, itemp, jtemp, Ntotal1, frac1},
   Ntotal1 = 16;
   xylist = Table[{xpos1 + (itemp / Ntotal1 - 1 / 2) * deltaxy1, ypos1 +
       (jtemp / Ntotal1 - 1 / 2) * deltaxy1}, {itemp, Ntotal1}, {jtemp, Ntotal1}];
   frac1 = 0.0;
   For[itemp = 1, itemp ≤ Ntotal1, itemp++, {
     For[jtemp = 1, jtemp ≤ Ntotal1, jtemp++, {
        frac1 = frac1 + If[Sqrt[(xylist[[itemp]][[jtemp]][[1]] - xcent1) ^
                2 + (xylist[[itemp]][[jtemp]][[2]] - ycent1) ^
                2] ≤ holes1, 1.0 / (Ntotal1 ^ 2), 0.0];
       }];
    }];
   Return[frac1];
  ];
```

```
General::spell1 : Possible spelling error: new symbol name "jtemp" is similar to existing symbol "itemp".
```

■ **Specify Parameters of Hartman plate to Iterate Over**

```
StrHoleSize = {"0.2", "0.4", "0.6", "0.8", "1.0"};
StrHoleSpacing =
  {"2.25", "2.50", "2.75", "3.00", "3.25", "3.50", "3.75", "4.00"};
```

■ **Loop Over all parameters. Save a data file of Hartmann plate intensity and phase array. Phase is calculated using Hello-Vinet solution.**

```
Count5 = 1;
For[KMaster = 2, KMaster ≤ 2, IMaster++, {
   For[JMaster = 1, JMaster ≤ 1, JMaster++, {
      For[IMaster = 0, IMaster ≤ 2, KMaster++, {
         Print["Executed Total = ", Count5, " of ", 5*8*3];
         Count5 = Count5 + 1;
         HoleSize = KMaster*0.2;
         HoleSpacing = 2.25 + (JMaster - 1)*0.25;
Print["Initial Time:- ",
          Date[][[4]], ":", Date[][[5]], ":", Date[][[6]]];
BeamMode = IMaster;
NGingin = 1.0;
h = 0.03;
a = 0.025;
Tx = 300;
K = 0.911;
σ = 0.76* 5.67*10^-8;
τ = 4 σ Tx^3 a / K;
w = 0.008;
α = .77;
P = 6.0*NGingin;
dndt = -7.05 * 10^-6;

λ = 0.6328 *10^-6;
         (*HoleSpacing = 2.25;*);
N1 = 30;
ApertureSize = HoleSpacing*4 + 0.5;
N3 = 1024;
TableSize = 60.0;
Waist = 50.0;
eq1 = x BesselJ[1, x] - τ BesselJ[0, x];
τ = 4 σ Tx^3 a / K;

soln = Table[0, {i, 46}, {j, 2}];
prev = {eq1 /. x → -65, -65};
j = 1;
For[i = 1, i ≤ 260, i++,
          {curr = {eq1 /. x → (-65 + i/2), -65 + i/2};
           If[Sign[curr] ≠ Sign[prev],
            {y3x3 = curr;
             y2x2 = curr;
             y1x1 = prev;
             While[Abs[ y2x2[[1]] ] ≥ 10^-10,
               {slope = (y2x2[[1]] - y1x1[[1]])/(y2x2[[2]] - y1x1[[2]]);
               y3x3[[2]] = y1x1[[2]] - y1x1[[1]]/slope;
               y3x3[[1]] = eq1 /. x → y3x3[[2]];
               y1x1 = y2x2;
```

```
            y2x2 = y3x3;}];
          soln[[j]] = y3x3;
          j = j + 1}];
        prev = curr;}];

len = Length[soln];
For[i = 1, i ≤ len - 1, i++,
        {If[Abs[soln[[i+1]][[2]] - soln[[i]][[2]]] ≤ 0.01,
          {soln = Delete[soln, i+1];
           len = len - 1;}]
        }];

ζm = Table[0, {i, Length[soln]}];
For[i = 1, i ≤ Length[soln], i++,
        {ζm[[i]] = soln[[i]][[2]];}];
ζm = Take[ζm, {22, 42}];
Tinf = 0;

ψr = 0;
ψtable = Table[0, {i, Length[ζm]}];
For[i = 1, i ≤ Length[ζm], i++, {
        ζ = ζm[[i]];
        pm = P/(π a^2) ζ^2/((ζ^2 + τ^2) (BesselJ[0, ζ])^2) Exp[-1/8 ζ^2 w^2/a^2];
        Tinfm = BesselJ[0, ζ r/a];
        Tinfm = Tinfm * (1 - 2 τ Cosh[ζ z/a]/((ζ + τ) Exp[ζ h/(2a)] - (ζ - τ) Exp[-ζ h/(2a)]));
        Tinfm = α a^2/K pm/ζ^2 * Tinfm;
        ψrm = dndt * Integrate[Tinfm, {z, -h/2, h/2}];
        ψtable[[i]] = ψrm;
        ψr = ψr + ψrm;

        Tinf = Tinf + Tinfm;
        }];


Print[i, " ", Date[]];
        If[IMaster == 0 && JMaster == 1, {
PhaseTable = Table[2π/λ ψr /. {r → a * (i - 1) / (4 N3 - 1)}, {i, 4 N3}];
        }];

Print[i, " ", Date[]];
AngularDist = D[ψr, r];

g1 = Table[0, {i, N1^2}];
DeltaX = HoleSpacing / 8;
DeltaY = HoleSpacing / 8;
For[i = 1, i ≤ N1, i++, {
```

```
            For[j = 1, j ≤ N1, j++, {
               ypos = (i - 1 - N1 / 2) * √3 HoleSpacing / 2 + DeltaY;
               xpos = Mod[i, 2] * HoleSpacing / 2 +
                 (j - 1 - N1 / 2) * HoleSpacing + DeltaX;
               g1[[j + N1 * (i - 1)]] = N[{xpos, ypos}];
              }];
            }];

          Total1 = Length[g1];
count = 1;
For[i = 1, i ≤ Total1, i++, {
           If[((g1[[count]][[1]] - DeltaX) ^2 + (g1[[count]][[2]] - DeltaY) ^2) ^0.5 <
              ApertureSize, count = count + 1,
             g1 = Delete[g1, count]];
           }];

          NPoints = Length[g1];

          data1 = Table[0, {i, N3}, {j, N3}];
DeltaSize = TableSize / N3;
DeltaIJ = Round[HoleSize / DeltaSize + 6];
          If[IMaster == 0, {
For[k = 1, k ≤ Length[g1], k++, {
             i1 = Round [N3 * (g1[[k]][[1]] / TableSize - 0.5) + 0.5];
             j1 =  Round [N3 * (g1[[k]][[2]] / TableSize - 0.5) + 0.5];

             For [i = i1 - DeltaIJ, i ≤ i1 + DeltaIJ, i++, {
               For[j = j1 - DeltaIJ, j ≤ j1 + DeltaIJ, j++, {
                  xpos = TableSize / 2 + (i - 1 / 2) / N3 * TableSize;
                  ypos = TableSize / 2 + (j - 1 / 2) / N3 * TableSize;

                  rxpos = xpos - g1[[k]][[1]];
                  rypos = ypos - g1[[k]][[2]];

                  If[Sqrt[rxpos^2 + rypos^2] / DeltaSize ≤
                    Round[HoleSize / (DeltaSize)] - 1.5, {
                    data1[[i, j]] = Exp[-((xpos^2 + ypos^2) ^.5) / Waist];}];

                  If[Sqrt[rxpos^2 + rypos^2] / DeltaSize ≥
                     Round[HoleSize / (DeltaSize)] - 1.5 && Sqrt[rxpos^2 + rypos^2] /
                      DeltaSize ≤ Round[HoleSize / (DeltaSize)] + 1.5,
                   {fraction1 = CircIntensity[xpos, ypos, g1[[k]][[1]],
                      g1[[k]][[2]], HoleSize, DeltaSize];
                    data1[[i, j]] = fraction1 * Exp[-((xpos^2 + ypos^2) ^.5) / Waist];
                   }];

                 }];
              }];
             }];
            datatemp2 = data1;
           },
           {data1 = datatemp2;}];

If[IMaster == 0 || IMaster == 1, ListDensityPlot[data1, Mesh → False]];
```

```
data2R = Table[0.0, {i, N3}, {j, N3}];
n1 = N3;
For[i = 1, i ≤ n1, i++, {
          For[j = 1, j ≤ n1, j++, {

             If[data1[[i, j]] ≠ 0, {
                xpos = -TableSize/2 + (i - 1/2)/N3 * TableSize;
                ypos = -TableSize/2 + (j - 1/2)/N3 * TableSize;
                r1 = Sqrt[xpos^2 + ypos^2]/1000.0;
                k1 = Round[((4 * N3 - 1) * r1)/a + 1];
                If[BeamMode == 0, data2R[[i, j]] = data1[[i, j]]];
                If[BeamMode == 1,
                 data2R[[i, j]] = Re[data1[[i, j]] * Exp[ i * PhaseTable[[k1]] ]]];
                If[BeamMode == 2, data2R[[i, j]] = Im[data1[[i, j]] *
                    Exp[ i * PhaseTable[[k1]] ]]];
              }];
            }];
         }];

NString = ToString[NPoints];
NSGingin = ToString[HoleSpacing];
LocationString = "O:\\Physics\\Optics\\abrooks\\HartFiles\\";
         If[JMaster < 10,
          {NString1 = "0" <> ToString[JMaster];}, {NString1 = ToString[JMaster];}];
If[BeamMode == 0, NameFile = LocationString <> "HolesA-Spacing-" <>
             StrHoleSpacing[[JMaster]] <> "MM-HoleSize-" <>
             StrHoleSize[[KMaster]] <> "MM-Radius.dat"];
If[BeamMode == 1, NameFile = LocationString <> "HolesB-Spacing-" <>
             StrHoleSpacing[[JMaster]] <> "MM-HoleSize-" <>
             StrHoleSize[[KMaster]] <> "MM-Radius.dat"];
If[BeamMode == 2, NameFile = LocationString <> "HolesC-Spacing-" <>
             StrHoleSpacing[[JMaster]] <> "MM-HoleSize-" <>
             StrHoleSize[[KMaster]] <> "MM-Radius.dat"];
         Print[NameFile];
         Print[" "];

Print["Pre-Save Time:- ", Date[][[4]], ":", Date[][[5]], ":", Date[][[6]]];
Time1 = Table[Date[][[i + 3]], {i, 3}];
Time1N = 3600 * Time1[[1]] + 60 * Time1[[2]] + Time1[[3]];
Time1N = Time1N + 594;
Time1[[1]] = Floor[Time1N / 3600.0];
Time1[[2]] = Floor[(Time1N - Time1[[1]] * 3600) / 60.0];
Time1[[3]] = Mod[Time1N, 60];
Print["Post-Save Time about:- ",
          Time1[[1]] , ":", Time1[[2]], ":", Time1[[3]]];
Export[NameFile, data2R, "Table"];

         Print["Post-Save Time:- ",
          Date[][[4]], ":", Date[][[5]], ":", Date[][[6]]];
```

```
        }];
    }];
}];
```

```
General::spell1 :
 Possible spelling error: new symbol name "IMaster" is similar to existing symbol "KMaster".

General::spell :
 Possible spelling error: new symbol name "JMaster" is similar to existing symbols {IMaster, KMaster}.

General::spell1 : Possible spelling error: new symbol name "Tinfm" is similar to existing symbol "Tinf".

General::spell1 : Possible spelling error: new symbol name "ψrm" is similar to existing symbol "ψr".

General::stop : Further output of General::spell1 will be suppressed during this calculation.

General::spell :
 Possible spelling error: new symbol name "rypos" is similar to existing symbols {rxpos, ypos}.

Executed Total = 1 of 120

Initial Time:- 14:58:28

22 {2003, 9, 12, 14, 58, 29}

22 {2003, 9, 12, 14, 59, 2}
```

Printed by Aidan Brooks

Jul 23, 07 9:22 POP_many.ZPL Page 1/2

```
! ZEMAX test file 1

! Clear All Surfaces
DelAll = NSUR()

IF (NSUR() > 2)
   FOR i = DelAll - 1, 2, -1
      DELETE (i)
   NEXT
ENDIF

! Create file to store locations
OUTPUT "centres.txt"

! Set-up System Parameters
ATYP = 0
AVAL = 60.0
WAVL 1 = 0.6328
WWGT 1  = 1.0

ApertureSize = 60


! Loop to create fully apertured Hartmann Plate
count = 2

INSERT (count)
APTP (count) = 0
THIC (count) = 1000.0

file1$ = "Holes-Spacing-"
file2$ = "MM-HoleSize-"
file3$ = "MM-Radius"
file4Y$ = "-DIST.ZBF"
file4N$ = "-UNDIST.ZBF"

FOR j = 1, 8, 1
        FOR k = 1, 5, 1
                FOR q2 = 1, 2, 1

                        ! Loop through q2 to run DIST and UNDIST respectively
                        IF (q2 < 2)
                         file4$ = file4Y$
                        ELSE
                         file4$ = file4N$
                        ENDIF

                        ! Loop through j to run through all the hole spacings
                        holespace = 2.25 + (j-1)*0.25
                        FORMAT 3.2
                holespace1$ = $STR(holespace)

                        ! Loop through k to run through all the hole sizes
                        holesize = 0.2*k
                      FORMAT 2.1
                        holesize1$ = $STR(holesize)

                        ! Create the input filename.
                        infile$ = file1$ + holespace1$ + file2$ + holesize1$ + f
ile3$ + file4$

                        infile1$ = "C:\Program Files\ZEMAX\POP\BeamFiles\" + infile$
```

Jul 23, 07 9:22 POP_many.ZPL Page 2/2

```
                        COPYFILE infile1$ "C:\Program Files\ZEMAX\POP\BeamFiles\input1.ZB
F"
                        OUTPUT SCREEN
                        PRINT infile1$

                        outfile$ = file1$ + holespace1$ + file2$ + holesize1$ +
file3$

                        FORMAT 1.0

                        FOR i = 1, 5, 1

                                ! Set propagation distance
                                THIC(count) = (i-1)*200.0 + 100.0

!                       IF (i < 10)
!                       filler$ = "00"
!                       ELSE
!                       filler$ = "0"
!                       FORMAT 2.0
!                       ENDIF


                                filler$ = "-PD-"
                                filenumber$ = $STR(THIC(count))
                                filename$ = outfile$ +  filler$ + filenumber$ +
file4$

                                OUTPUT SCREEN
                                PRINT filename$

                                ! Run physical optics propagation and save to ap
propriate filename.
                                POP filename$ count

                                ! Remove result from C: drive and place on O:\ d
rive
                                outfile1$ = "C:\Program Files\ZEMAX\POP\BeamFiles\" + f
ilename$
                                movedfile$ = "O:\PHYSICS\Optics\abrooks\HartFiles\" + fil
ename$
                                COPYFILE outfile1$ movedfile$
                                DELETEFILE outfile1$
                        NEXT
                NEXT

        NEXT
NEXT
```

B.2 Diffraction propagation for cross-talk analysis

The source code listed in this section was used to model the cross-talk between neighbouring spots in Figures 3.12 and 3.13.

`Chp4_Fresnel_diffraction_Broadband_centroid.pro`

The initial electric field, `EIn`, is created from an intensity array, `IntIn`, of hexagonally arranged circular apertures and a phase array, `phase`, which contains a randomly set amount of defocus. This is propagated over the lever arm distance, `deltaZ`, using the Fourier transform technique discussed by Goodman [80] to yield the output electric field, `Eout`. This is converted to an intensity array.

For the coherent source, the final intensity array, `outputArrPeak`, is only calculated for one wavelength. For the coherent source, the final intensity array, `outputArrFinal`, is made from a sum of intensity arrays, where each array is weighted by the amplitude of that wavelength in the spectrum of the incoherent source.

Jul 23, 07 3:48 **Chp4_Fresnel_diffraction_Broadband_centroid.pro** Page 1/3

```
; Chp4 - Fresnel approximation
; Written by Aidan Brooks, 9th May 2007

seedL = 845739L
NTest = 10
time1 = systime(1)
for test_number = 0, NTest-1 do begin
    ; get the center and defocus of the wavefront distortion
    xc = 1E-1*randomn(seedL, 2)
    defocus = (-1.0)^(floor(2.0*randomu(seedL)))
    defocus = defocus * (1.0D-5)*(randomu(seedL) + 1.0)

    for displacement = 0, 1 do begin
        for HoleConfig = 0, 1 do begin
            time0 = systime(1)
            ; spectral width
            dW = 100D-6
            dW = 55.26D-6
            dWTotal = 3.2*dW
            ndW = 200
            dWStep = dWTotal/ndW

            ;-------------------------------------------------------
            ; specify parameters of model: length units = (mm
            inputArrSize = (1.5D-3)*1024
            wavelengthPeak = 820D-6
            ;deltaZ = 31D0
            ;deltaZ = 10.43D0
            deltaZ = 10.00D0
            holesize = 150D-3
            N1 = 1024
            pi = acos(0.0D)*2.0D
            ;-------------------------------------------------------

            outputArrFinal = dblarr(N1, N1)
            outputArrPeak = outputArrFinal

            ;-------------------------------------------------------
            ; get spatial array coordinates
            dx = (inputArrSize)/N1
            x = (dindgen(N1)#replicate(1.0D, N1) - N1/2)*dx
            y = (dindgen(N1)##replicate(1.0D, N1) - N1/2)*dx
            OPD = (defocus/2.0)*((x - xc(0))^2.0 + (y - xc(1))^2.0)
            if (displacement eq 0) then OPD = OPD*0.0D
            ;-------------------------------------------------------


            ;-------------------------------------------------------
            ; get spectral array coordinates
            f0 = findgen(N1) - (N1/2 - 1)
            f1A = shift(f0, -(N1/2 - 1) )/(N1*dx)
            ;f1A = shift(f0, -511)/(N1*(dx*N1))
            freqX = f1A#replicate(1.0D, N1)
            freqY = f1A##replicate(1.0D, N1)
            freqR2 = freqX^2 + freqY^2
            ;-------------------------------------------------------

            ;-------------------------------------------------------
            ; get input mask
            IntIn = 0.0*x
```

Jul 23, 07 3:48 **Chp4_Fresnel_diffraction_Broadband_centroid.pro** Page 2/3

```
            r = sqrt((x)^2 + y^2)
            IntIn = IntIn + double(r le holesize/2.0)
            if (HoleConfig eq 0) then begin
                for i = 0, 5 do begin
                    angle = i*pi/3.0
                    pitch = 430E-3
                    r = sqrt((x - pitch*cos(angle))^2 + (y - pitch*sin(angle))^2
)
                    IntIn = IntIn + double(r le holesize/2.0)
                endfor
            endif
            ;-------------------------------------------------------

            window, 0
            window, 1

            for k = -ndW, ndW do begin
                wavelength = wavelengthPeak + k*dWStep
                ;amplitudeE = exp(-1.0*((wavelength - wavelengthPeak)/(dW))^2.0
)
                amplitudeE = exp(-0.25*((wavelength - wavelengthPeak)/(dW))^2.0
)


                ;-------------------------------------------------------
                ; get propagator
                PExponent = -1.0D*pi*wavelength*deltaZ*freqR2
                TDeltaZ = COMPLEX(cos(PExponent), sin(PExponent), /DOUBLE)
                ;-------------------------------------------------------


                ;-------------------------------------------------------
                ; get input field
                phase = OPD*2.0*pi/wavelength
                EIn = sqrt(IntIn) * COMPLEX(cos(phase), sin(phase), /DOUBLE)
                ;-------------------------------------------------------


                ;-------------------------------------------------------
                ; Perform propagation to get output field and intensity
                F1 = FFT(EIn, /DOUBLE)
                F2 = TDeltaZ*F1
                EOut = FFT(F2, /INVERSE, /DOUBLE)
                IntOut = (abs(EOut))^2
                ;-------------------------------------------------------
                if (k eq 0) then outputArrPeak = IntOut
                outputArrFinal = outputArrFinal + IntOut
                wset, 0
                plot, IntOut(N1/4:3*N1/4, N1/2)/max(IntOut(N1/4:3*N1/4, N1/2))
                wset, 1
                plot, outputArrFinal(*, N1/2)/max(outputArrFinal(N1/4:3*N1/4, N1
/2))

                timeNow = systime(1)
                print, [test_number, displacement, HoleConfig, k, wavelength, am
plitudeE^2, timeNow - time0, timeNow - time1]
                wait, 0.001

            endfor

            window, 0
            tvscl, IntIn(N1/4:3*N1/4, N1/4:3*N1/4)
            window, 1
```

Jul 23, 07 3:48 Chp4_Fresnel_diffraction_Broadband_centroid.pro Page 3/3

```
            tvscl, IntOut(N1/4:3*N1/4, N1/4:3*N1/4)


            wset, 0
            plot, outputArrPeak(3*N1/8:5*N1/8, N1/2)/max(outputArrPeak(3*N1/8:5*
N1/8, N1/2))
            wset, 1
            plot, outputArrFinal(3*N1/8:5*N1/8, N1/2)/max(outputArrFinal(3*N1/8:
5*N1/8, N1/2))
            window, 2
            x2 = dblarr(N1/8)
            for i = 0, N1/8 - 1 do x2(i) = total(outputArrPeak(i*8:(i+1)*8 - 1,
N1/2-4:N1/2+3))
            x3 = dblarr(N1/8)
            for i = 0, N1/8 - 1 do x3(i) = total(outputArrFinal(i*8:(i+1)*8 - 1,
N1/2-4:N1/2+3))
            N2 = N1/8
            plot, x2(3*N2/8:5*N2/8)/max(x2(3*N2/8:5*N2/8))
            window, 3
            plot, x3(3*N2/8:5*N2/8)/max(x3(3*N2/8:5*N2/8))

;            Final1 = outputArrFinal
;            Peak1 = outputArrPeak




            dirData = 'D:\SciWord\Thesis\data\chapter_4\cross_talk_broadband_L3'
            outfilename = dirData + '\cross_talk_displ_test_number_'  + string(test_numb
er, format = '(I3.3)') $
                                      + string(displacement, format = '(I2.2)') + $
                                      'HoleConfig_' + string(HoleConfig,  format = '
(I2.2)') + '.dat'
            openw, outunit, outfilename,  /GET_LUN
            writeu, outunit, long(N1)
            writeu, outunit, Ein
            writeu, outunit, OPD
            writeu, outunit, IntIn
            writeu, outunit, outputArrFinal
            writeu, outunit, outputArrPeak
            free_lun, outunit
;            writeu, outunit, long(N1)
;            writeu, outunit, Final1
;            writeu, outunit, Final2
;            writeu, outunit, Peak1
;            writeu, outunit, Peak2
;            free_lun, outunit

        endfor
    endfor
endfor
end
```

B.3 FEM of ITM and CP thermal lens at the HOPTF

The source code listed in this section was used to produce the finite element prediction of the wavefront distortion in the cavity at the HOPTF. The defocus was determined from this wavefront distortion and is plotted in Figure 5.16.

The five files listed here are as follows:

1. `FEM_Using_Spiricon.pro`

   The main code for that runs the finite element model.

2. `solvecrosssectionalareafem.pro`

   Solve the Cross Sectional Area on the end face.

3. `Create_V_FEM.pro`

   A procedure to create a variable to hold the volume elements.

4. `CreateSurfaceAreaArrayFEM.pro`

   Create an array storing the Surface Area elements seen by each cell in the 3D mesh of the FEM.

5. `CreateThermalConductM.pro`

   Procedure to determine the CrossSectional area between cells divided by the length between nodes of cells

```
N1k = 121
Fit1 = 0

Ntype = 1       ; if Ntype = 1 then set power to be constant
WType = 1       ; if Wtype = 1 then set beam size to be constant
mat1 = 1
if (mat1 eq 1 ) then material = 'sapphire' else material = 'fused_silca'

if (STRCMP(material, 'sapphire') eq 1) then begin
;    ThermalConductivity = 33.0
;    Text = 300.0
;    density = 3980.0
;    SpecificHeat = 757.0
    ThermalConductivity = 46.0
    Text = 300.0
    density = 3970.0
    SpecificHeat = 775.0
    SBConstant = 0.75*5.67E-8
    alpha = 3.6
    radius = 0.05
    height = 0.05
endif else begin
    ThermalConductivity = 1.38
    Text = 300.0
    density = 2202.0
    SpecificHeat = 745.0
    SBConstant = 0.75*5.67E-8
    alpha = 3.6
    radius = 0.08
    height = 0.017
endelse

;radius = 0.05
;height = 0.05
waistX =  0.0083
waistY = 0.0083


; determine cold cavity beam size
waistX = Get_Beam_Size(1D9, 720.0, 77.0, 1.064D-6)
waistY = waistX

if (WType eq 1) then begin
   waistX = 0.0080
   waistY = 0.0080
endif


NnodesR = N1k
NnodesZ = 27
dx = 2.0*radius/double(NnodesR-2.0)
dy = dx
dz = height/double(NnodesZ-2.0)

dNW = round(waistX/dx)

;dz = height/double(NnodesZ-2-1)
CrossX = - radius - dx + dx*(dindgen(NnodesR)+0.5)
CrossZ = -height/2.0 - dz + dz*(dindgen(NnodesZ)+0.5)
;CrossZ = -height/2.0 - dz + dz*(dindgen(NnodesZ))
```



```
window, 4

;-----------------------------------------------------------------
; Create the Volume and CrossSectional Area arrays
SolveCrossSectionalAreaFEM, AreaEnd, LocationArrXY, radius, CrossX
AreaEndOld = AreaEnd
AreaEnd = AreaEnd + double(AreaEnd eq 0.0)*10000.0
V = Create_V_FEM(AreaEnd, height, NNodesZ)

; Create the Surface Area Array
CreateSurfaceAreaArrayFEM, SurfaceArea, AreaEndOld, radius, CrossX, CrossZ

print, 'Starting thermal conductivity matrix'
wait, 0.001
; Create the Thermal Conductivity Matrix
CreateThermalConductM, ThermalConductM, radius, CrossX, CrossZ, LocationArrXY, A
reaEndOld
print, ' End thermal matrix'

; Clear unnecessary variables
;Delvar, LocationArrXY, AreaEndOld, AreaEnd
;-----------------------------------------------------------------

;-----------------------------------------------------------------



ThermalConductM = ThermalConductivity*ThermalConductM
SurfaceArea = SurfaceArea*SBConstant

TempArr = dblarr(NNodesR, NNodesR, NNodesZ) + Text
PArr = dblarr(NNodesR, NNodesR, NNodesZ)
;PArr(NNodesR/2-5:NNodesR/2+5, NNodesR/2-5:NNodesR/2+5, 1:NNodesZ-2) = 100000.0

OffsetXi = 0.000
OffsetXf = 0.000
Power = 1.0

time0 = systime(1)
for i = 1, NNodesZ - 2 do begin

    OffsetX = OffsetXi + (i-0.5)/(NNodesZ - 2.0)*(OffSetXf - OffSetXi)

    OffsetY = 0.000
    CrossX2 = CrossX#replicate(1.0D, NNodesR)
    XMin = sqrt(2.0)*(CrossX2 - OffSetX - dx/2.0)/waistX
    XMax = sqrt(2.0)*(CrossX2 - OffSetX + dx/2.0)/waistX
    CrossY2 = CrossX##replicate(1.0D, NNodesR)
    YMin = sqrt(2.0)*(CrossY2 - OffSetY - dx/2.0)/waistY
    YMax = sqrt(2.0)*(CrossY2 - OffSetY + dx/2.0)/waistY



    PArrEnd = 0.25*Power*(erf(Xmin) - erf(XMax))* $
                                    (erf(Ymin) - erf(Ymax))
    ;PArrEnd = PArrEnd * 0.5*(sin(2.0*CrossX2/0.005) + 1.0)
    ;PArrEnd = heat_Beam_FEM(NNodesR, Fit1)

    PArrEnd = ParrEnd * double(AreaEndOld gt 0.0)

    PArr(*, *, i) = height*alpha*PArrEnd(*, *)/(NNodesZ - 2.0)
endfor
```

```
time1 = systime(1)
print, time1-time0
;wait, 1000

;-------------------------------------------------------------------

print, 'hi'

;-------------------------------------------------------------------
; load spiricon data
DirToAnalyzeHS = string(dblarr(13))


nDirToAnalyze = size(DirToAnalyzeHS, /N_ELEMENTS)

SpiriconDataFiles = DirToAnalyzeHS
ThursFiles = FILE_SEARCH("D:\Hartmann - Shared Documents\Spiricon\2007-03-08", '2007*.txt', CO
UNT = ncount1)
SpiriconDataFiles(0:ncount1-1) = ThursFiles(*)
FriFiles = FILE_SEARCH('D:\Hartmann - Shared Documents\Fri Afternoon Folder', '2007-3*-9*.txt',
 COUNT = ncount2)
SpiriconDataFiles(ncount1:ncount1+ncount2-1) = FriFiles(*)
FriFilesCP = FILE_SEARCH('D:\Hartmann - Shared Documents\Fri Afternoon Folder', '2007-03-09.txt'
, COUNT = ncount2)
SpiriconDataFiles(nDirToAnalyze-1) = FriFilesCP(*)

DirIndex = 0
fileFEM = 'D:\Hartmann - Shared Documents\Spiricon\FEM_' + string(DirIndex, format = '(I3.3)
')
FILE_MKDIR, fileFEM

        ;-------------------------------------------------------------------
---------
        ; copy Spiricon file into a temporary directory and lose the time string
s at the start
        filenameSpir = SpiriconDataFiles(DirIndex)
        filenameTemp = "c:\Temp\Copied_Spiricon_file.txt"
        strIn = ""
        nLines = FILE_LINES(filenameSpir)

        openr, outunit1, filenameSpir, /GET_LUN
        openw, outunit2, filenameTemp, /GET_LUN
        for i = 0, nLines - 1 do begin
           readf, outunit1, strIn
           strIn = STRMID(strIN, 11)
           printf, outunit2, strIn
        endfor
        free_lun, outunit2
        free_lun, outunit1
        ;-------------------------------------------------------------------


        ;-------------------------------------------------------------------
        ; open temporary file and load data
        if (DirIndex eq 12) then nDims = 8 else nDims = 6
        dataSpir = dblarr(nDims, nLines)
        openr, outunit, fileNameTemp, /GET_LUN
        readf, outunit, dataSpir
        free_lun, outunit
        timeSpir = dblarr(nLines)
        timeSpir(*) = dataSpir(0, *)
        timeSpir = timeSpir - timeSpir(0)
```



```
        nSpirData = nLines
        ;-------------------------------------------------------------------

        print, timeSpir
;-------------------------------------------------------------------


dt = 0.0005
Q = dblarr(NNodesR, NNodesR, NNodesZ)
diffT = dblarr(1)
window, 0
window, 1
window, 2
TempOld = TempArr

TestDiff1 = 0.0
TestDiff2 = 0.0
count = 1
EnergyArr = TempArr*density*V*SpecificHeat

period = 200.0
w0 = 2.0*!Pi/period
TimeExpired = 0.0
TimeArr =[0.0]
NLimit = 7L*10L^6
TimeNew = 100.1

TimeNextRecord = 0.5
dtOld = 0.5
tCritical = density*SpecificHeat*radius^2.0/ThermalConductivity

RecordTempArrHot = 0
RecordTempArrCold = 0
RecordImage = 0


if (ntype eq 1) then begin
   n1 = nLines/2
   CurrentPower = dataSpir(1, n1)
endif else begin
   CurrentPower = dataSpir(1, 0)
endelse
CurrentTimeIndex = 0

OPDData = dblarr(4, NLimit)

;-------------------------------------------------------------------
; Start iteration of FEM
for i = 1L, NLimit do begin


    ;-------------------------------------------------------------
    ; Update energy-flow matrix
    Q = 0.0*Q
    Q(1 : NNodesR - 1, *, * ) = temporary(Q(1 : NNodesR - 1, *, * )) + (TempArr(
0 : NNodesR - 2, *, * ) - $
          TempArr(1 : NNodesR - 1, *, * ))*ThermalConductM(0, 1 : NNodesR - 1, *
, * )
    Q(0 : NNodesR - 2, *, * ) = temporary(Q(0 : NNodesR - 2, *, * )) + (TempArr(
1 : NNodesR - 1, *, * ) - $
          TempArr(0 : NNodesR - 2, *, * ))*ThermalConductM(2, 0 : NNodesR - 2, *
, * )
```

Printed by Aidan Brooks

Jul 19, 07 0:24 FEM_Using_Spiricon.pro Page 5/8

```
    Q(*, 1 : NNodesR - 1, * ) = temporary(Q(*, 1 : NNodesR - 1, * )) + (TempArr(
*, 0 : NNodesR - 2, * ) - $
          TempArr(*, 1 : NNodesR - 1, * ))*ThermalConductM(3, *, 1 : NNodesR - 1
, * )
    Q(*, 0 : NNodesR - 2, * ) = temporary(Q(*, 0 : NNodesR - 2, * )) + (TempArr(
*, 1 : NNodesR - 1, * ) - $
          TempArr(*, 0 : NNodesR - 2, * ))*ThermalConductM(1, *, 0 : NNodesR - 2
, * )

    Q(*, *, 0 : NNodesZ - 2) = temporary(Q(*, *, 0 : NNodesZ - 2 )) + (TempArr(*
, *, 1 : NNodesZ - 1 ) - $
          TempArr(*, *, 0 : NNodesZ - 2 ))*ThermalConductM(5, *, *, 0 : NNodesZ
- 2)
    Q(*, *, 1 : NNodesZ - 1) = temporary(Q(*, *, 1 : NNodesZ - 1 )) + (TempArr(*
, *, 0 : NNodesZ - 2 ) - $
          TempArr(*, *, 1 : NNodesZ - 1 ))*ThermalConductM(4, *, *, 1 : NNodesZ
- 1)
    ;-----------------------------------------


    ;-----------------------------------------
    ; Add power to energy-flow matrix
    Q = temporary(Q) + PArr*CurrentPower/100.0
    Q = temporary(Q) - SurfaceArea*(TempArr^4.0 - Text^4.0)


    ;-----------------------------------------------
    ; update energy and temperature arrays
    EnergyArr = temporary(EnergyArr) + Q*dt
    TempArr = EnergyArr/(density*SpecificHeat*V)
    ;-----------------------------------------------

    wset, 0
    if (count le 5) then begin
       TestDiff1 = TestDiff1 + max(abs(TempArr - TempOld)/TempOld)/10.0
    endif else begin
       TestDiff2 = TestDiff2 + max(abs(TempArr - TempOld)/TempOld)/10.0
    endelse
    count = count + 1
    TimeExpired = TimeExpired + dt


    ;-----------------------------
    ; update FEM with real data
    if (TimeExpired gt TimeSpir(CurrentTimeIndex + 1)) then begin
       if (CurrentTimeIndex lt nSpirData-1) then begin
          CurrentTimeIndex = CurrentTimeIndex + 1
          if (nType eq 1) then CurrentPower = CurrentPower else CurrentPower = d
ataSpir(1, CurrentTimeIndex)
          fileOUT = fileFEM + '\FEM_constW_' + material + string(ntype, format =
 '(I2.2)') + '_PRI_' + string(CurrentTimeIndex, format = '(I4.4)') + '.raw'

          openw, outunit, fileOUT, /GET_LUN
          writeu, outunit, byte(N1k)
          writeu, outunit, TimeExpired
          writeu, outunit, double(CrossX)
          OPD = total(TempArr(*, NNodesR/2, *), 3)
          OPD = OPD - OPD(1)
          writeu, outunit, OPD
          free_lun, outunit
          print, systime(0)
```

Jul 19, 07 0:24 FEM_Using_Spiricon.pro Page 6/8

```
          CurrentBeamSize = dataSpir(3, CurrentTimeIndex)
          if (CurrentBeamSize lt 3200.0) then begin
             ; solve for beam size at ITM
             mag = 0.00918612/(3145.0)
             q1Inv = COMPLEX(-1/720.0, (1.064E-6)/(3.14159*(CurrentBeamSize*mag)
^2.0))
             q1 = 1.0/q1Inv
             q2 = (q1 + 77.0)
             q2Inv = 1.0/q2
             ImgPart = IMAGINARY(q2Inv)
             w2 = sqrt( abs((1.064E-6)/(3.14159*ImgPart)) )

             print, "Beam Size at ITM = ", w2*1000.0
             ;waistX = w2
             ;waistY = w2

             for k1 = 1, NNodesZ - 2 do begin

                OffsetX = OffsetXi + (k1-0.5)/(NNodesZ - 2.0)*(OffSetXf - OffSe
tXi)


                OffsetY = 0.000
                CrossX2 = CrossX#replicate(1.0D, NNodesR)
                XMin = sqrt(2.0)*(CrossX2 - OffSetX - dx/2.0)/waistX
                XMax = sqrt(2.0)*(CrossX2 - OffSetX + dx/2.0)/waistX
                CrossY2 = CrossX##replicate(1.0D, NNodesR)
                YMin = sqrt(2.0)*(CrossY2 - OffSetY - dx/2.0)/waistY
                YMax = sqrt(2.0)*(CrossY2 - OffSetY + dx/2.0)/waistY



                PArrEnd = 0.25*Power*(erf(Xmin) - erf(XMax))* $
                                              (erf(Ymin) - erf(Ymax))
                ;PArrEnd = PArrEnd * 0.5*(sin(2.0*CrossX2/0.005) + 1.0)
                ;PArrEnd = heat_Beam_FEM(NNodesR, Fit1)

                PArrEnd = ParrEnd * double(AreaEndOld gt 0.0)

                PArr(*, *, k1) = height*alpha*PArrEnd(*, *)/(NNodesZ - 2.0)
             endfor


          endif
       endif
    endif
    ;-------------------------


    ;-----------------------------------
    ; record data at appropriate times
    if ((TimeExpired ge TimeNextRecord) OR (RecordImage eq 1)) then begin
       RecordImage = 0
       TimeNextRecord = TimeNextRecord * (tCritical/dtOld)^(1.0D/50.0)
       TempTotal = (total(TempArr, 3)*dz*(2.6*10.0^(-6.0)))/(6.33*10.0^(-7.0))
    endif
    ;-------------------------------


    if (i mod 10) eq 0 then begin
```

Printed by Aidan Brooks

Jul 19, 07 0:24 FEM_Using_Spiricon.pro Page 7/8

```
        ;-----------------------------
        ; check that time interval of FEM is small enough
        if (TestDiff2 lt TestDiff1) then dt = dt*1.1 else dt = dt/1.6
        if (dt le 0.0005) then dt = 0.0005
        if (TestDiff2 lt 1.0E-14) then i = NLimit + 20L
        ;-----------------------------


        ;-----------------------------
        ; print and plot updated data
        print, i, dt, TimeExpired, total(SurfaceArea*(TempArr^4.0 - Text^4.0))/to
tal(PArr) , $
                    max(TempArr) - TempArr(1, NNodesR/2, 1), max(TempArr) - Tex
t
        TestDiff2 = 0.0
        TestDiff1 = 0.0
        count = 1
        wset, 0
        plot, TempArr(1:NNodesR-2, NNodesR/2, NNodesZ/2) - TempArr(1, NNodesR/2,
NNodesZ/2)
        oplot, TempArr(1:NNodesR-2, NNodesR/2, NNodesZ/2) - TempArr(1, NNodesR/2,
 NNodesZ/2), PSYM = 6
        oplot, TempArr(NNodesR/2, 1:NNodesR-2, NNodesZ/2) - TempArr(NNodesR/2, 1,
 NNodesZ/2)
       ; print, k1
        ;print, TempArr(NNodesR/2, NNodesR/2, 3) - Text
        wait, 0.001
        diffT = [diffT, TempArr(NNodesR/2, NNodesR/2, NNodesZ/2) - Text]
        TimeArr = [TimeArr, TimeExpired]
        ;diffT = [diffT, alog10((max(TempArr) - TempArr(1, NNodesR/2, 1))/total(S
urfaceArea*(TempArr^4.0 - Text^4.0))) ]
;        wset, 1
;        plot, TimeArr, diffT
        ;dt = dt*1.05
       ; print, dt
        wset, 2
        plot, TempArr(NNodesR/2, NNodesR/2, *) - Text
        ;-----------------------------

    endif
    TEmpOld =TempArr
    result = total(FINITE(TempArr, /NAN)+FINITE(TempArr, /INFINITY))
    ;print, result
    wait, 0.001

    OPD = total(TempArr(*, NNodesR/2, *), 3)
    OPD = OPD - OPD(1)
    result = poly_fit(CrossX(NNodesR/2 - dNW:NNodesR/2 + dNW), OPD(NNodesR/2 - d
NW:NNodesR/2 + dNW), 2, STATUS = statRes)
    OPDData(0, i-1) = TimeExpired
    OPDData(1, i-1) = CurrentPower
    OPDData(2, i-1) = result(2)*2.0

    offset = 0.12*tan(10.0*acos(0.0D)/90.0)
    offsetX = round(offset/dx)

    OPD = total(TempArr(*, NNodesR/2 + offsetX, *), 3)
    OPD = OPD - OPD(NNodesR/2)
    result = poly_fit(CrossX(NNodesR/2 - dNW:NNodesR/2 + dNW), OPD(NNodesR/2 - d
NW:NNodesR/2 + dNW), 2, STATUS = statRes)
    OPDData(3, i-1) = result(2)*2.0
```

Jul 19, 07 0:24 FEM_Using_Spiricon.pro Page 8/8

```
    ;-----------------------------
    ; plot any remaining data
    if (i mod 10) eq 0 then begin
       wset, 1
       plot, OPDData(0, 0:i-1), OPDData(1, 0:i-1)
       wset, 4
       plot, OPDData(0, 0:i-1), OPDData(2, 0:i-1)
       oplot, OPDData(0, 0:i-1), OPDData(3, 0:i-1), THICK = 2
    endif
    ;-----------------------------

endfor


end
```

```
; Solve the Cross Sectional Area on the end face


pro SolveCrossSectionalAreaFEM, AreaEnd, LocationArrXY, radius, CrossX

s = size(CrossX)
Nnodes = s(1)

dx = CrossX(1) - CrossX(0)
x = CrossX#replicate(1.0, Nnodes)
y = CrossX##replicate(1.0, Nnodes)
r = sqrt(x^2 + y^2)

dxL = 2.0*radius/(NNodes - 3.0)
xLoc = -radius - dxL + dxL*findgen(NNodes)

LocationArrXY = dblarr(2, Nnodes, Nnodes)
LocationArrXY(0, *, *) = x
LocationArrXY(1, *, *) = y
;LocationArrXY(0, *, *) = xLoc#replicate(1.0D, NNodes)
;LocationArrXY(1, *, *) = xLoc##replicate(1.0D, NNodes)


rInside = double(r le radius)
area = rInside
rInSm = smooth(rInside, 3)

SumA = total(rInSm eq 1.0)*(dx*dx)
rEdge = (rInSm gt 0.0) AND (rInSm lt 1.0)
EdgeList = where(rEdge)
s = size(EdgeList)
s1 = s(1)


N3 = 800.0
for i = 0, s1 - 1 do begin
   xc = x(EdgeList(i))
   yc = y(EdgeList(i))
   XYPosn = ARRAY_INDICES(x, EdgeList(i))

   x1 = (dx*(dindgen(N3) + 0.5)/double(N3) - dx/2.0 + xc)#replicate(1.0D, N3)
   y1 = (dx*(dindgen(N3) + 0.5)/double(N3) - dx/2.0 + yc)##replicate(1.0D, N3)
   r1 = sqrt(x1^2 + y1^2)

   rTemp = double(r1 le radius)
   TempSum = total(rTemp)*(dx*dx)/double(N3^2)
   SumA = SumA + TempSum
   area(EdgeList(i)) = TempSum/(dx*dx)
   if (total(rTemp) ne 0.0) then begin
      LocationArrXY(0, XYPosn(0), XYPosn(1)) = total(rTemp*x1)/total(rTemp)
      LocationArrXY(1, XYPosn(0), XYPosn(1)) = total(rTemp*y1)/total(rTemp)
   endif
   print, i, " of ", string(s1, format = '(i4)'), " - Calculating surface area"
   wait, 0.0001

endfor

AreaEnd = double(area*dx*dx)


end
```

Nov 01, 05 16:04 **Create_V_FEM.pro** Page 1/1

```
; function to create variable V to hold the volume elements

function Create_V_FEM, AreaEnd, height, NnodesZ

s = size(AreaEnd)
s1 = s(1)

V = dblarr(s1, s1, NnodesZ)
for i = 0, NnodesZ - 1 do begin
   V(*, *, i) = AreaEnd(*, *)
endfor

return, V*height/(NNodesZ - 2.0)

end
```

Oct 24, 05 19:32 CreateSurfaceAreaArrayFEM.pro Page 1/4

```
; Create an array storing the Surface Area elements seen by each cell.

pro CreateSurfaceAreaArrayFEM, SurfaceArea, AreaEndOld, radius, CrossX, CrossZ


dx = CrossX(1) - CrossX(0)
dz = CrossZ(1) - CrossZ(0)

sR = size(CrossX)
sZ = size(CrossZ)
Nr = sR(1)
Nz = sZ(1)

; Create an array of the EDGES of the node boxes
;x0 = CrossX(0) - 0.5*dx
;z0 = CrossZ(0) - 0.5*dz


x = CrossX#replicate(1.0, Nr)
y = CrossX##replicate(1.0, Nr)




; surface area is nominally zero, except for those nodes whose grid cells inters
ect the radius
; determine the area in each cell by working through the list of cells given abo
ve

; Option A: Get list of fractional area elements from AreaEndOld. Search for the
 cross-sections from ListOut2
; Option B: Determine the cells which border the intersection points in ListOut2

; Option A
AreaEndNew = AreaEndOld/(dx*dx)
EdgeList = where( (AreaEndNew lt 0.999999) AND (AreaEndNew gt 0.0) )
;ListIndices = (ListOut2 - x0)/dx
s = size(EdgeList)
s1 = s(1)
;


SurfaceArea = AreaEndOld*0.0
for i = 0, s1 - 1 do begin

   ; get centre and edges of cell
   xc = x(EdgeList(i))
   yc = y(EdgeList(i))

   xmin = xc - dx/2.0
   xmax = xc + dx/2.0
   ymin = yc - dx/2.0
   ymax = yc + dx/2.0

   ; Determine the intercepts of the gridlines and the circle
   if (radius^2.0 ge xmin^2.0) then begin
      xminYVals = [sqrt(radius^2.0 - xmin^2.0), -sqrt(radius^2.0 - xmin^2.0)]
   endif else begin
      xminYVals = [10.0^6.0, 10.0^6.0]
```

Oct 24, 05 19:32 CreateSurfaceAreaArrayFEM.pro Page 2/4

```
   endelse

   if (radius^2.0 ge xmax^2.0) then begin
      xmaxYVals = [sqrt(radius^2.0 - xmax^2.0), -sqrt(radius^2.0 - xmax^2.0)]
   endif else begin
      xmaxYVals = [10.0^6.0, 10.0^6.0]
   endelse

   if (radius^2.0 ge ymax^2.0) then begin
      ymaxXVals = [sqrt(radius^2.0 - ymax^2.0), -sqrt(radius^2.0 - ymax^2.0)]
   endif else begin
      ymaxXVals = [10.0^6.0, 10.0^6.0]
   endelse

   if (radius^2.0 ge ymin^2.0) then begin
      yminXVals = [sqrt(radius^2.0 - ymin^2.0), -sqrt(radius^2.0 - ymin^2.0)]
   endif else begin
      yminXVals = [10.0^6.0, 10.0^6.0]
   endelse

   crossPts = dblarr(2, 4)
   crossN = 0

   ;-------------------------------------------------------------
   ; Check positions of intercepts - do they line on cell edges?
   if ((xminYvals(0) ge ymin) AND (xminYVals(0) le ymax)) then begin
      crossPts(*, crossN) = [xmin, xminYVals(0)]
      crossN = crossN + 1
   endif
   if ((xminYvals(1) ge ymin) AND (xminYVals(1) le ymax)) then begin
      crossPts(*, crossN) = [xmin, xminYVals(1)]
      crossN = crossN + 1
   endif

   if ((xmaxYvals(0) ge ymin) AND (xmaxYVals(0) le ymax)) then begin
      crossPts(*, crossN) = [xmax, xmaxYVals(0)]
      crossN = crossN + 1
   endif
   if ((xmaxYvals(1) ge ymin) AND (xmaxYVals(1) le ymax)) then begin
      crossPts(*, crossN) = [xmax, xmaxYVals(1)]
      crossN = crossN + 1
   endif
   ;-----
   ;-----
   if ((yminXVals(0) ge xmin) AND (yminXVals(0) le xmax)) then begin
      crossPts(*, crossN) = [yminXVals(0), ymin]
      crossN = crossN + 1
   endif
   if ((yminXVals(1) ge xmin) AND (yminXVals(1) le xmax)) then begin
      crossPts(*, crossN) = [yminXVals(1), ymin]
      crossN = crossN + 1
   endif

   if ((ymaxXVals(0) ge xmin) AND (ymaxXVals(0) le xmax)) then begin
      crossPts(*, crossN) = [ymaxXVals(0), ymax]
      crossN = crossN + 1
   endif
   if ((ymaxXVals(1) ge xmin) AND (ymaxXVals(1) le xmax)) then begin
      crossPts(*, crossN) = [ymaxXVals(1), ymax]
      crossN = crossN + 1
   endif
   ;-------------------------------------------------------------
```

Oct 24, 05 19:32 CreateSurfaceAreaArrayFEM.pro Page 3/4

```
   ; rearrange values so that the first two form and arc and the second two form
 an arc
   if (crossN gt 2) then begin
      crossPtsX = dblarr(4)
      crossPtsY = dblarr(4)
      crossPtsX(*) = crossPts(0, *)
      crossPtsY(*) = crossPts(1, *)

      XTrue = 0
      YTrue = 0
      Val = 0
      for j = 0, 2 do begin
         for k = j+1, 3 do begin
            if (crossPtsX(j) eq crossPtsX(k)) then begin
               XTrue = 1
               Val = [j, k]
            endif
            if (crossPtsY(j) eq crossPtsY(k)) then begin
               YTrue = 1
               Val = [j, k]
            endif
         endfor
      endfor

      rX = sqrt((crossPtsX - crossPtsX(Val(0)))^2.0 + (crossPtsY - crossPtsY(Val
(0)))^2.0)
      rX(Val(1)) = 100.0*radius
      NearList = sort(rX)

      crossOut = 0.0*crossPts
      crossOut(*, 0) = crossPts(*, Val(0))
      crossOut(*, 1) = crossPts(*, NearList(1))
      crossOut(*, 2) = crossPts(*, NearList(2))
      crossOut(*, 3) = crossPts(*, Val(1))

      crossPts = crossOut
   endif

   ; get the arc length - taking into account the fact that the arc might cross
 2Pi
   ArcLength = abs( atan(crossPts(1, 0), crossPts(0, 0)) - atan(crossPts(1, 1),
 crossPts(0, 1)) )
   if (ArcLength ge !Pi) then ArcLength = 2.0*!Pi - ArcLength


   ; if there are two points where the circle crosses the cell wall, then add th
e two arcs
   if (crossN gt 2) then begin
      ArcLength2 = abs( atan(crossPts(1, 2), crossPts(0, 2)) - atan(crossPts(1,
 3), crossPts(0, 3)) )
      if (ArcLength2 ge !Pi) then ArcLength2 = 2.0*!Pi - ArcLength2
      ArcLength = ArcLength + ArcLength2
   endif

   SurfaceArea(EdgeList(i)) = ArcLength*radius*dz
endfor

SurfaceAreaOut = dblarr(Nr, Nr, Nz)

for i = 1, Nz-2 do begin
   if ((i eq 1) OR (i eq Nz-2)) then begin
```

Oct 24, 05 19:32 CreateSurfaceAreaArrayFEM.pro Page 4/4

```
      SurfaceAreaOut(*, *, i) = AreaEndOld(*, *)
   endif

   SurfaceAreaOut(*, *, i) = SurfaceAreaOut(*, *, i) + SurfaceArea(*, *)
endfor

SurfaceArea = SurfaceAreaOut

end
```

Nov 05, 05 16:54 CreateThermalConductM.pro Page 1/4

```
; procedure to determine the CrossSectional area between cells divided by the le
ngth between nodes of cells

pro CreateThermalConductM, ThermalConductM, radius, CrossX, CrossZ, LocationArrX
Y, AreaEndOld

dx = CrossX(1) - CrossX(0)
dz = CrossZ(1) - CrossZ(0)

sR = size(CrossX)
sZ = size(CrossZ)
Nr = sR(1)
Nz = sZ(1)

ThermalConductM = dblarr(6, Nr, Nr, Nz)

CrossSectionBetweenCells = dblarr(4, Nr, Nr)

for i = 0, Nr - 1 do begin
   for j = 0, Nr - 1 do begin



      xmin = CrossX(i) - dx/2.0
      xmax = CrossX(i) + dx/2.0

      ymin = CrossX(j) - dx/2.0
      ymax = CrossX(j) + dx/2.0

      ; [South-West, North-West, North-East, South-East
      InsideR = [sqrt(xmin^2.0 + ymin^2.0) le radius, sqrt(xmin^2.0 + ymax^2.0)
le radius, $
                 sqrt(xmax^2.0 + ymax^2.0) le radius, sqrt(xmax^2.0 + ymin^2.0)
le radius]

      ; West
      if (InsideR(0) AND InsideR(1)) then begin
         CrossSectionBetweenCells(0, i, j) = dx
      endif else begin
         if ((xmin^2 le radius^2.0) AND ( abs(abs(xmin) - abs(radius))/abs(radiu
s) ge 1.0E-5  )) then begin
            MidPt = sqrt(radius^2.0 - xmin^2)
            MidPt = [MidPt, -MidPt]
            Select = where((MidPt lt ymax) AND (MidPt ge YMin))

         if (InsideR(0) OR InsideR(1) OR abs(MidPt(0) - MidPt(1)) le dx ) then b
egin
            if (InsideR(0)) then begin
               CrossSectionBetweenCells(0, i, j) = abs(ymin - MidPt(Select(0)) )
            endif
            if (InsideR(1)) then begin
               CrossSectionBetweenCells(0, i, j) = abs(ymax - MidPt(Select(0)) )
            endif
            if (abs(MidPt(0) - MidPt(1)) le dx ) then begin
               CrossSectionBetweenCells(0, i, j) = abs(MidPt(0) - MidPt(1) )
            endif
         endif
         endif
```

Nov 05, 05 16:54 CreateThermalConductM.pro Page 2/4

```
      endelse

      ; North
      if (InsideR(1) AND InsideR(2)) then begin
         CrossSectionBetweenCells(1, i, j) = dx
      endif else begin
         if ( (ymax^2.0 le radius^2.0) AND ( abs(abs(ymax) - abs(radius))/abs(ra
dius) ge 1.0E-5  )) then begin
            MidPt = sqrt(radius^2.0 - ymax^2)
            MidPt = [MidPt, -MidPt]
            Select = where((MidPt lt xmax) AND (MidPt ge xmin))

         if (InsideR(1) OR InsideR(2) OR abs(MidPt(0) - MidPt(1)) le dx ) then b
egin
            if (InsideR(1)) then begin
               CrossSectionBetweenCells(1, i, j) = abs(xmin - MidPt(Select(0)) )
            endif
            if (InsideR(2)) then begin
               CrossSectionBetweenCells(1, i, j) = abs(xmax - MidPt(Select(0)) )
            endif
            if (abs(MidPt(0) - MidPt(1)) le dx ) then begin
               CrossSectionBetweenCells(1, i, j) = abs(MidPt(0) - MidPt(1) )
            endif
         endif
         endif

      endelse

      ; East
      if (InsideR(2) AND InsideR(3)) then begin
         CrossSectionBetweenCells(2, i, j) = dx
      endif else begin
         if ((xmax^2.0 le radius^2.0) AND ( abs(abs(xmax) - abs(radius))/abs(rad
ius) ge 1.0E-5  )) then begin
            MidPt = sqrt(radius^2.0 - xmax^2)
            MidPt = [MidPt, -MidPt]
            Select = where((MidPt lt ymax) AND (MidPt ge ymin))

         if (InsideR(2) OR InsideR(3) OR abs(MidPt(0) - MidPt(1)) le dx ) then b
egin
            if (InsideR(2)) then begin
               CrossSectionBetweenCells(2, i, j) = abs(ymax - MidPt(Select(0)) )
            endif
            if (InsideR(3)) then begin
               CrossSectionBetweenCells(2, i, j) = abs(ymin - MidPt(Select(0)) )
            endif
            if (abs(MidPt(0) - MidPt(1)) le dx ) then begin
               CrossSectionBetweenCells(2, i, j) = abs(MidPt(0) - MidPt(1) )
            endif
         endif
         endif

      endelse

      ; South
      if (InsideR(3) AND InsideR(0)) then begin
         CrossSectionBetweenCells(3, i, j) = dx
      endif else begin
         if ((ymin^2.0 le radius^2.0) AND ( abs(abs(ymin) - abs(radius))/abs(rad
ius) ge 1.0E-5  )) then begin
            MidPt = sqrt(radius^2.0 - ymin^2)
            MidPt = [MidPt, -MidPt]
```

```
        Select = where((MidPt lt xmax) AND (MidPt ge xmin))

        if (InsideR(3) OR InsideR(0) OR abs(MidPt(0) - MidPt(1)) le dx ) then b
egin
           if (InsideR(3)) then begin
              CrossSectionBetweenCells(3, i, j) = abs(xmax - MidPt(Select(0)) )
           endif
           if (InsideR(0)) then begin
              CrossSectionBetweenCells(3, i, j) = abs(xmin - MidPt(Select(0)) )
           endif
           if (abs(MidPt(0) - MidPt(1)) le dx ) then begin
              CrossSectionBetweenCells(3, i, j) = abs(MidPt(0) - MidPt(1) )
           endif
        endif
        endif

     endelse




   endfor
   wait, 0.001
endfor


;ThermalConductM = [West, North, East, South, Back, Front]

West = [[1, Nr-1], [0, Nr-1], [0, Nr-2], [0, Nr-1]]
South = [[0, Nr-1], [1, Nr-1], [0, Nr-1], [0, Nr-2]]
East = [[0, Nr-2], [0, Nr-1], [1, Nr-1], [0, Nr-1]]
North = [[0, Nr-1], [0, Nr-2], [0, Nr-1], [1, Nr-1]]

for m = 1, Nz - 2 do begin
   for i = 0, 5 do begin
      ; Fill in the sides
      if (i le 3) then begin
         if (i eq 0) then Dist = West
         if (i eq 1) then Dist = North
         if (i eq 2) then Dist = East
         if (i eq 3) then Dist = South

         Imin1 = Dist(0, 0)
         Imax1 = Dist(1, 0)
         Jmin1 = Dist(0, 1)
         Jmax1 = Dist(1, 1)

         Imin2 = Dist(0, 2)
         Imax2 = Dist(1, 2)
         Jmin2 = Dist(0, 3)
         Jmax2 = Dist(1, 3)

         LArr = (LocationArrXY(*, Imin1:Imax1, Jmin1:Jmax1) - LocationArrXY(*, I
min2:Imax2, Jmin2:Jmax2))^2.0
         Larr2 = dblarr(Imax1-Imin1+1, Jmax1-Jmin1+1)
         LArr2(*, *) = sqrt(Larr(0, *, *) + Larr(1, *, *))

         ThermalConductM(i, IMin1:IMax1, Jmin1:Jmax1, m) = CrossSectionBetweenCe
lls(i, Imin1:Imax1, Jmin1:Jmax1)*dz/Larr2
      endif
```



```
      ; Fill in the back surface (except between cells 0 and 1 in z direction -
no thermal conduction)
      if ( i eq 4) then begin
         if (m ne 1) then begin
            ThermalConductM(i, *, *, m) = AreaEndOld(*, *)/dz
         endif
      endif

      ; Fill in the front surface (except between cells Nz-2 and Nz-1 in z dirn
- no thermal conduction)
      if ( i eq 5) then begin
         if (m ne Nz - 2) then begin
            ThermalConductM(i, *, *, m) = AreaEndOld(*, *)/dz
         endif
      endif
   endfor
endfor

;print, 'hi'
;wait, 10


end
```

Appendix C

Relevant papers

C.1 An off-axis Hartmann sensor for the measurement of absorption-induced wavefront distortion in advanced gravitational wave interferometers

A. Brooks, P.J. Veitch, J. Munch and T.L. Kelly, *Gen. Relativ. Gravit.*, **37**,1575-1580 (2005)

This paper was superseded by the work discussed in Chapter 6.

Gen. Relativ. Gravit. (2005) 37(9): 1575–1580
DOI 10.1007/s10714-005-0137-5

RESEARCH ARTICLE

Aidan Brooks · Peter Veitch · Jesper Munch · Thu-Lan Kelly

An off-axis Hartmann sensor for the measurement of absorption-induced wavefront distortion in advanced gravitational wave interferometers

Received: 13 December 2004 / Published online: 8 September 2005

Abstract We describe a novel off-axis Hartmann wavefront sensor, developed for the measurement of wavefront distortions induced in the mirrors (test masses) of advanced gravitational wave interferometers by residual absorption of the circulating laser power.

Keywords Hartmann sensor · Wavefront distortion · Gravitational wave interferometers

1 Introduction

Advanced gravitational wave interferometers will have circulating optical powers of order a few kW in the power-recycling cavity and about 500 kW in the arm cavities [1]. Even extremely small absorption by the substrates and coatings of the optical components in these cavities will result in thermal gradient within the optics, which will lead to significant distortion of the optical wavefront via the thermo-optic and elasto-optic effects and thermo-elastic deformation [2].

Absorption in the substrates of the input test masses (ITM), which are inside the power-recycling cavity, and in the coatings of the ITM and end test masses (ETM), which reflect the power in the arm cavities, are two particularly important sources of wavefront distortion [1]. These distortions could significantly reduce the sensitivity of an advanced interferometer by reducing the sideband power build-up in the power-recycling cavity and increasing the carrier power leaking out the dark port of the interferometer [3]. Thus, their effects must be compensated [3], which requires that the distortion in each mirror be measured independently, without interfering with the circulating power in the interferometer.

A Brooks · P. Veitch (✉) · J. Munch · T.-L. Kelly
Department of Physics, The University of Adelaide, Adelaide SA 5005, Australia
E-mail: peter.veitch@adelaide.edu.au

Fig. 1 A schematic of a prototypical Hartmann sensor. The Hartmann plate contains an array of apertures that produce a set of Hartmann rays. The transverse aberration of the Hartmann rays at the CCD is used to calculate the change in local slope of the wavefront due to the optic.

The High Power Test Facility (HPTF), a collaboration between the Australian Consortium for Gravitational Astronomy (ACIGA) and the LIGO project, located at Gingin in Western Australia, will be used to investigate the effect of the absorption in substrates and coatings in optical cavities that have high circulating power. The optical configuration of this facility has been designed to yield wavefront distortions with parameters that are directly relevant to advanced interferometers. Initially, we shall measure the effect of absorption in the substrate of the ITM, and investigate its compensation [4].

We are developing a novel off-axis Hartmann sensor that can be used to measure wavefront distortion without interfering with the circulating power. Hartmann sensors [5, 6], one variant of which is shown in Fig. 1, measure wavefront distortion by recording the positions of the "Hartmann rays" at the CCD camera before and after the distortion is introduced. Since the measured transverse displacement or aberration of each ray is proportional to the change in slope of the wavefront at the point at which the ray passes through the optic [7], the wavefront distortion can be determined by integration.

We have chosen to use a Hartmann sensor rather than a Shack–Hartmann sensor [8] to monitor the wavefront distortion. It does not require a micro-lens array, which could introduce interference between adjacent rays, as the light source is coherent, and it can have larger beam sizes at the CCD thereby reducing the effect of irregularities in pixel responsivity. Further, the effective optical 'lever arm' in a Hartmann sensor could be larger than for a Shack–Hartman sensor if a large area CCD were used, thereby further improving the sensitivity. The poorer spatial resolution of the Hartmann sensor is unimportant in this application as the wavefront distortion occurs over an area typically 2 cm diameter in the HPTF test and 10–20 cm diameter in an advanced interferometer, and is not expected to contain high spatial frequencies.

In this paper, we outline the development of the Hartmann sensor, including validation of the sensor, and preliminary measurements.

2 Hartmann sensor validation

The Hartmann sensor is validated by comparing the wavefront distortion measured using a stored-beam holographic interferometer [9], shown in Fig. 2, with that measured using an on-axis Hartmann sensor, shown in Fig. 3, and the off-axis Hartmann sensor, shown in Fig. 4.

In a stored-beam interferometer, the holographic beam-splitter is recorded while the heating beam is blocked, thereby recording and thus removing the effect

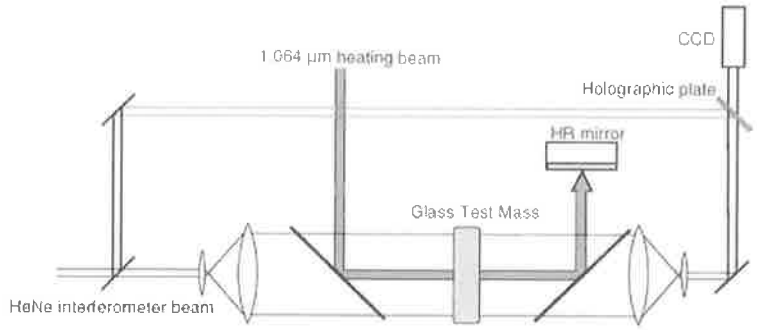

Fig. 2 A schematic of the stored-beam holographic interferometer. The holographic beamsplitter is recorded while the heating beam is blocked. The output surface of the glass test mass is imaged onto the CCD. Note that the glass used for the test mass is chosen to have a low absorption and the heating beam is retro-reflected through the test mass to provide a power absorption that is almost independent of the axial position. The glass was chosen to produce the distortion encountered in an advanced interferometer.

of the non-common static aberrations in the arms of the interferometer. Replaying the hologram while the heating beam is blocked results in a zero interference fringe as the beams transmitted through the hologram are identical to the holographically reconstructed beams. Unblocking the heating beam produces additional wavefront distortion as the interferometer beam passes through the glass test mass and thus the transmitted and reconstructed beams differ. The resultant interference pattern can be measured accurately by tilting one of the beams incident on the hologram prior to unblocking the heating beam, thereby introducing straight interference fringes. The added distortion is then determined by measuring the displacement of the fringes.

As indicated above, the reference spot positions for the Hartmann sensor are recorded with the heating beam blocked. It is then unblocked and the aberrated spot positions are recorded. An example of the calculated transverse aberrations is shown in Fig. 5. The ratio of the transverse aberration to the distance between the test mass and the CCD camera gives the change in the local slope of the wavefront, and is equal to the gradient of the wavefront distortion [7].

Since the Hartmann rays in the off-axis sensor propagate at an angle to the cylindrical axis of the test mass, the transverse aberration of each ray will not simply reflect the wavefront distortion that would be experienced by the eigenmode

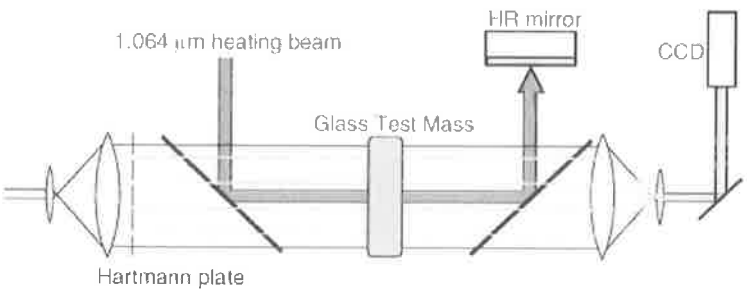

Fig. 3 A schematic of the on-axis Hartmann sensor. The reference spot positions are recorded with the heating beam blocked. It is then unblocked and the aberrated spot positions are then recorded.

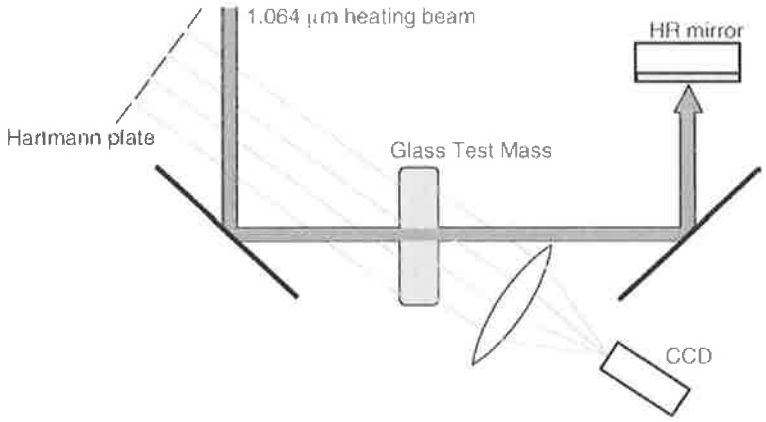

Fig. 4 A schematic of the off-axis Hartmann sensor.

of the interferometer, which propagates axially though the test mass. The distortion can be estimated, however, if it is assumed that the temperature increase due to the absorption is independent of the axial position in the cylindrical test mass, as occurs for substrate absorption in the ITM of advanced interferometers and in our tests. Then, the optical path difference (OPD) acquired by the Hartmann ray shown in Fig. 6 can be written, for small distortions:

$$OPD = \frac{\mathrm{d}n}{\mathrm{d}T} \int_{z=-h/2}^{z=h/2} \Delta T\,(x\,(z),\, y\,(z)) \sqrt{\tan^2\theta + 1}\,\mathrm{d}z \tag{1}$$

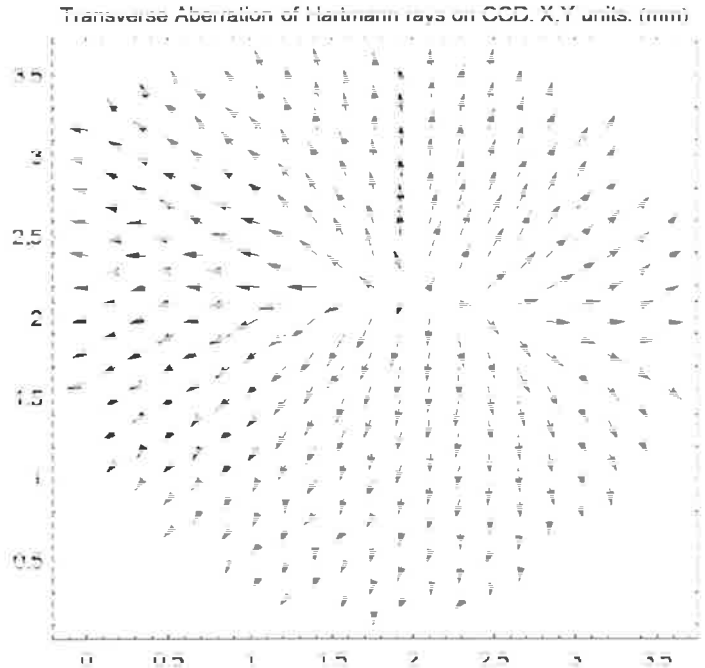

Fig. 5 An example of the measured transverse aberrations, shown as a vector field, recorded by the off-axis Hartmann sensor.

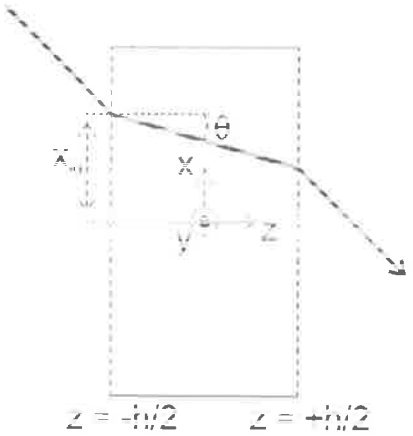

Fig. 6 The geometry used to determine the expected OPD of a particular Hartmann ray. The ray enters the test mass at $(x_{in}, y_{in}, z = -h/2)$. Transverse aberrations are measured in the coordinate frame of the CCD camera and transformed via a suitable rotation into the coordinate frame of the test mass.

where the temperature increase is given by

$$\Delta T\,(x, y) = \sum_{i=0}^{N} A_i (x^2 + y^2)^i, \tag{2}$$

and it is assumed that the distortion does not change the path within the test mass and thus $x\,(z) = z \tan\theta + x_{in}$ and $y\,(z) = y_{in}$.

Since the transverse aberration is proportional to the gradient of the OPD, we can use the measured transverse aberrations to determine the best estimate of the polynomial coefficients by defining

$$\chi^2 = \left[\left(\frac{\partial OPD}{\partial x} - TA_x\right)^2 + \left(\frac{\partial OPD}{\partial y} - TA_y\right)^2\right] \tag{3}$$

where TA_x and TA_y are the x and y components of the measured transverse aberration. The usual 'least squares' minimization of χ^2 is then used to determine the best estimate of the coefficients A_i.

A preliminary comparison of the wavefront distortion that would be experienced by a laser beam propagating along the axis of the test mass, as determined using the off-axis Hartmann sensor and the stored-beam interferometer is shown in Fig. 7. The discrepancy between the two curves in this result is believed due to the very noisy preliminary Hartmann data, caused by the poor dynamic range of the CCD camera used, which significantly limited the precision with which the centroids of the spots could be calculated.

3 Summary

We have described an off-axis Hartmann sensor for measuring wavefront distortion induced by absorption in the substrate of the input test masses of an advanced gravitational wave interferometer. We have shown how the wavefront distortion

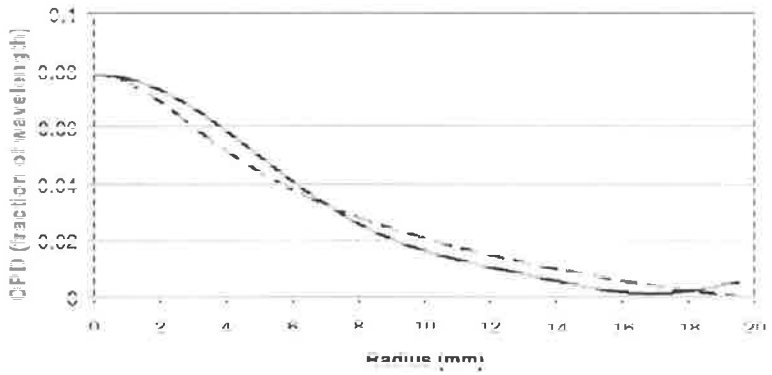

Fig. 7 A comparison of the wavefront distortion that would be experienced by a laser beam propagating along the axis of the test mass, as determined using the stored-beam interferometer (dashed line) and the off-axis Hartmann sensor (solid line). A HeNe laser, $\lambda = 632.8$ nm, was used for the measurement.

that would be experience by a laser beam propagating along the axis of the test mass can be extracted from the transverse aberrations measured using an off-axis Hartmann sensor. A preliminary measurements showing that the wavefront distortion measured using an off-axis Hartmann sensor is consistent with that measured using an interferometer has also been presented. We are currently replacing the CCD camera used for the Hartmann sensor.

Acknowledgements This work was supported by the Australian Research Council.

References

1. Lawrence, R., Ottaway, D.: (2002) [http://www.ligo.caltech.edu/docs/G/ G020502-00.pdf]
2. Hello, P., Vinet, J.-Y.: J. Phys. France **51**, 1267 (1990)
3. Lawrence, R. (2003) [http://www.ligo.caltech.edu/docs/P/P030001-00.pdf]
4. Degallaix, J., Slagmolen, B., Zhao, C., Ju, L., Blair, D.: Gen. Rel. Grav. this issue (2005)
5. Hartmann, J.: Zf. Instrumentenk. **20**, 4 (1900)
6. Ghozeil, I.: In Optical Shop Testing, D. Malacara (ed.): Ch. 10, Wiley, New York (1992)
7. Rayces, J. L.: Opt. Acta. **11**, 85 (1964)
8. Mansell, J. D., Hennawi, J., Gustafson, E. K., Fejer, M. M., Byer, R. L., Clubley, D., Yoshida, S., and Reitze, D. H.: Appl. Opt. **40**, 366 (2001)
9. Brooks, R. E., Heflinger, L. O., Weurker, R. F.: Appl. Phys. Lett. **7**, 248 (1965)

C.2 Ultra-sensitive wavefront measurement using a Hartmann sensor

Aidan F. Brooks, Thu-Lan Kelly, Peter J. Veitch, and Jesper Munch, *Opt. Express* **15** (16), 10370-10375 (2007).

Ultra-sensitive wavefront measurement using a Hartmann sensor

Aidan F. Brooks, Thu-Lan Kelly, Peter J. Veitch, and Jesper Munch
The University of Adelaide, Adelaide, SA, 5005
aidan.brooks@adelaide.edu.au

Abstract: We describe a Hartmann sensor with a sensitivity of $\lambda/15,500$ at $\lambda = 820$nm. We also demonstrate its application to the measurement of an ultra small change in wavefront and show that the result agrees with that expected to within $\lambda/3,300$.

OCIS codes: (120.4640) Optical instruments; (010.7350) Wave-front sensing; (350.4800) Optical standards and testing

References and links

1. J. Hartmann, "Bemerkungen uber den Bau und die Justirung von Spektrographen," Zt. Instrumentenkd. **20,** 47 (1900).
2. T. L. Kelly, P. J. Veitch, A. F. Brooks and J. Munch, "A differential Hartmann wavefront sensor for accurate and precise optical testing," Appl. Opt. **46,** 861–866 (2007).
3. C. Castellini, F. Francini and B. Tiribilli, "Hartmann test modification for measuring ophthalmic progressive lenses," Appl. Opt. **33,** 4120 (1994).
4. F. Roddier, ed., *Adaptive Optics in Astronomy* (Cambridge U. Press, Cambridge, England, 1999).
5. J. D. Mansell, J. Hennawi, E. K. Gustafson, M. M. Fejer, R. L. Byer, D. Clubley, S. Yoshida and D. H. Reitze, "Evaluating the effect of transmissive optic thermal lensing on laser beam quality with a Shack-Hartmann wavefront sensor," Appl. Opt. **40,** 366–374 (2001).
6. R. Lawrence, D. Ottaway, M. Zucker and P. Fritchel, "Active correction of thermal lensing through external radiative thermal actuation," Opt. Lett. **22,** 2635-2637 (2004).
7. M. Smith and P. Willems, "Auxiliary Optics Support System Conceptual Design Document, Vol. 1: Thermal Compensation System," (2006), http://www.ligo.caltech.edu/docs/T/T060083-00/T060083-00.pdf.
8. A. Chernyshov, U. Sterr, F. Riehle, J. Helmcke and J. Pfund, "Calibration of a Shack-Hartmann sensor for absolute measurements of wavefronts," Appl. Opt. **44,** 6419–6425 (2005).
9. J. L. Rayces, "Exact Relation between Wave Aberration and Ray Aberration," Opt. Acta. **11,** 85–88 (1964).
10. P. Mercere, P. Zeitoun, M. Idir, S. Le Pape, D. Douillet, X. Levecq, G. Dovillaire, S. Boucourt, K. A. Goldberg, P. P. Naullleau and S. Rekawa, "Hartmann wave-front measurement at 13.4 nm with $\lambda_{EUV}/120$ accuracy", Opt. Lett. **28,** 1534–1536 (2003).
11. A. Poteomkin, N. Andreev, I. Ivanov, E. Khazanov, A. Shaykin, and V. Zelenogorsky, "Use of a scanning Hartmann sensor for measurement of thermal lensing in TGG crystal," Proc. SPIE **4970,** 10–21 (2003).
12. M. Kasper, D. Looze, S. Hippler, R. Davies and A. Glindemann, "Increasing the sensitivity of a Shack-Hartmann sensor," in Proceedings of the Canterbury Conference on Wavefront sensing and its applications, Canterbury (1999), http://mpia-hd.mpg.de/ALFA/PAPERS/canterbury99MEK.pdf.
13. W. H. Southwell, "Wave-front estimation from wave-front slope measurements," J. Opt. Soc. Am. **70,** 998–1006 (1980).

1. Introduction

Hartmann wavefront sensors, first described in 1904 [1], and particularly the Shack-Hartmann derivatives, have enjoyed a recent surge of popularity due to improvements in the speed, quality and size of CCD arrays. They are currently used for a variety of applications, including lens metrology [2], ophthalmology [3], adaptive optics [4] and the measurement of thermal lensing

[5] [6]. The measurement of wavefront distortion induced by absorption in the optics of advanced gravitational wave interferometers is a particularly demanding application, requiring a sensitivity equivalent to at least $\lambda/600$ at $\lambda = 820\,\mathrm{nm}$ [7].

The type of Hartmann sensor used for an application is usually dictated by the intensity of the available light source. Shack-Hartmann sensors use micro-lens arrays to sample the wavefront and thus optimize the light collection efficiency but they are susceptible to imperfections in the micro-lens array [8]. A Hartmann wavefront sensor, by contrast, samples the wavefront, W, using an opaque plate containing an array of holes, the Hartmann plate, as shown schematically in part of Fig. 1. It is therefore less light efficient but it is simple to optimize and, as shown here, capable of superior performance.

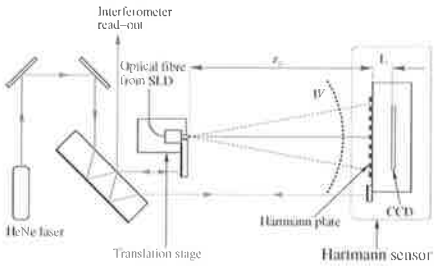

Fig. 1. A schematic of the Hartmann wavefront sensor and the system used to test it. The sensor consists of a Hartmann plate mounted a distance L from a CCD. It was illuminated by a wavefront W emitted from a fiber-coupled super luminescent diode (SLD), the free end of the which was mounted on a micrometer-controlled translation stage.

The rays created by the Hartmann plate propagate normal to the incident wavefront W, to the active surface of a CCD where they produce an array of spots. If the local slope of the wavefront changes then the positions of the spots will change. Dividing the transverse displacement of each spot by the 'lever-arm' propagation length L yields the gradient of the wavefront change at each hole (see [9] for example), and the wavefront change, ΔW, can be determined by numerically integrating this gradient field. While knowledge of the initial wavefront would then enable the new wavefront to be calculated, in this paper we do not make any assumptions about the initial wavefront but rather consider only the change, ΔW, in the wavefront as required for the measurement of thermal lensing in gravitational wave interferometers.

The position of each spot is specified by its centroid, the precision of which is maximized by ensuring that each spot consists of a large number of pixels and that each pixel acquires a large number of photoelectrons in the available integration time. This minimizes the effects of dark current, CCD read-out noise, non-uniformity in pixel response and photoelectron shot noise. Since Hartmann wavefront sensors naturally provide large spot sizes, they should be able to provide high sensitivity measurements of wavefront changes. Indeed, a Hartmann sensor that has a reproducibility (sensitivity) of $\lambda/1500$ at $\lambda = 13.4\,\mathrm{nm}$ [10] and a scanning Hartmann sensor that has a sensitivity of $\lambda/500$ at $\lambda = 1064\,\mathrm{nm}$ [11] have been reported. The accuracy of the scanning Hartmann sensor was estimated to be $\lambda/50$ at $\lambda = 1064\,\mathrm{nm}$. In this paper, we describe a detailed investigation of the optimization of a Hartmann wavefront sensor (H-WFS) and demonstrate large improvements in the sensitivity and accuracy of this type of sensor.

2. Hartmann wavefront sensor

The camera used in our sensor is a 12-bit digitized, 1024×1024 pixel CCD camera that has a nominal dynamic range of 66 dB (11 bits) and a nominal pixel spacing of $12\,\mu$m. The actual average pixel spacing was measured by translating the camera sideways using a micrometer-controlled translation stage and observing the displacement on the CCD of a fixed diffraction pattern, yielding a value of $11.975 \pm 0.005\,\mu$m.

The Hartmann plate was made from $50\,\mu$m thick brass plate into which $150\,\mu$m diameter holes in a uniform hexagonal-close-packed array spaced $430\,\mu$m apart were laser drilled. It was mounted on the body of the camera and the distance between the plate and the active surface of the CCD, the lever arm L, was calibrated by illuminating the sensor with two laser beams separated by a precisely measured angle and measuring the average displacement between the two spot patterns, giving $\mathrm{L} = 10.43 \pm 0.02$ mm. The hole diameter, pitch, pattern and value of L were chosen to ensure that cross-talk between neighbouring spots was negligible while maintaining sensitivity.

A weighted centroiding algorithm was used to determine the spot positions [12]: $x_c = \sum_i p_i^2 x_i / \sum_i p_i^2$ and $y_c = \sum_i p_i^2 y_i / \sum_i p_i^2$ where p_i is the digital number, directly proportional to the number of photoelectrons, and x_i and y_i are the coordinates of the i^{th} pixel. The summation range of the algorithm was adjusted to minimize the variance in the centroids. In practice, this meant using only pixels within a box that was 15 pixels square, which is 10% larger than the hole diameter. Simulations indicate that cross-talk due to diffraction should introduce a systematic error of less than 0.1% for the defocus measurement discussed in this paper.

All measurements reported here were recorded after a 3 hour warm-up period to reduce the effects of thermal expansion of the sensor. However, there was a residual 0.5 mHz oscillation in the output of the H-WFS due to a periodic variation in the temperature of the sensor with an amplitude of 150 mK, caused by the cycling of the room temperature. The magnitude of the oscillation is consistent with thermal expansion of the Hartmann plate. To reduce the effect of this variation, we used data recorded at the turning points of the oscillation for the analysis reported below.

The H-WFS was tested using the system shown in Fig. 1, in which it was illuminated by light emitted from an optical fiber with a $50\,\mu$m core and 0.36 NA that was coupled to an 820 nm super-luminescent diode, which had a full-width-half-maximum coherence length of about $5\,\mu$m. A Michelson interferometer was used to measure changes in the distance, z_0, between the light source and the H-WFS with a precision of 50 nm.

3. Results

The statistics of the noise in the H-WFS were investigated by illuminating the CCD with the output from the fiber at three different intensity levels. A short integration time was used to ensure that the dark current was negligible. We observed that the fluctuation, Δp, in the digital number in a pixel, p, was well described by $\Delta p \propto p^{0.5}$, and thus the noise has Poissonian statistics. A relative fluctuation of 0.25% was obtained for the maximum digital number (4095), indicating a maximum photoelectron count of approximately 1.6×10^5, which is similar to the specified electron well depth of each pixel, confirming that the dominant noise is photoelectron shot noise.

Numerical simulation predicts that the RMS uncertainty in the centroid position due to photoelectron shot noise in a single Hartmann image should be about 0.25% of a pixel, or about 30 nm, if the brightest pixel in each spot is full. If the noise in sequential Hartmann images is uncorrelated then the RMS error in the displacement of a centroid, $\sigma_{\Delta y}$, will be a factor of $2^{1/2}$ larger. The RMS wavefront difference between *adjacent holes*, $\sigma_{\Delta W}$, is given by

$\sigma_{\Delta W} = \sigma_{\Delta y} h_p / L$, where h_p is the spacing between adjacent holes in the Hartmann plate. The RMS wavefront error for a zonal reconstruction across *all holes*, assuming uncorrelated noise, is given by $C_{\rm pd}^{1/2} \times \sigma_{\Delta W}$, where $C_{\rm pd}$ is the noise coefficient developed by Southwell [13], which is dependent on the number, $N_{\rm holes}$, and arrangement of holes.

The wavefront error was measured using the system shown in Fig. 1 while keeping z_0 constant. Spot centroids were calculated for consecutive Hartmann images separated in time by 15 s and the average prism in each image was removed. These zero-prism centroids were used to calculate the error in the wavefront change. A typical map of the wavefront change, which has an RMS error of $\lambda/1450$, is shown in Fig. 2. The RMS error for these maps varied between $\lambda/1000$ and $\lambda/2000$ which is consistent with the shot noise limit and $C_{\rm pd} = 0.2$, calculated for $N_{\rm holes} = 263$ used in this example.

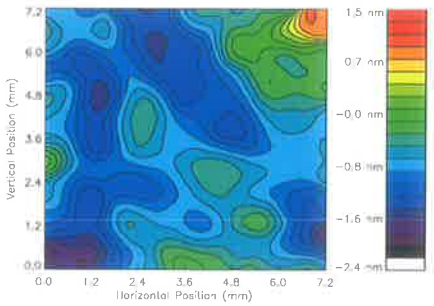

Fig. 2. Measured single-frame wavefront error map over a 7.2 mm × 7.2 mm region.

If the statistical characteristics of the noise do not vary with time then the wavefront error should be reduced by averaging over multiple Hartmann images. To test this, we recorded a sequence of 2000 Hartmann images at 30 images/second and removed the global prism from each image. A set of reference centroids was then calculated by averaging over $N_{\rm ref} = 1000$ images, consisting of the first and last 500 images. The central 1000 images were used to calculate sets of centroids averaged over $N_{\rm avg}$ images, where $N_{\rm avg} = 1, \ldots, 990$. This process ensured that the reference and average centroids were statistically independent. The $\sigma_{\Delta W}$ is plotted in Fig. 3, showing that $\sigma_{\Delta W} < \lambda/15,500$.

The $\sigma_{\Delta W}$ is plotted in Fig. 3. Also plotted is the result of a numerical simulation that assumes stationary random noise and in which the only free parameter is the $N_{\rm avg} = 1$ error. For small $N_{\rm avg}$, the error decreases as $N_{\rm avg}^{1/2}$, as expected, and it asymptotically approaches a value that is a factor $N_{\rm ref}$ times smaller than the $N_{\rm avg} = 1$, the limit due to the noise in the reference centroids. Note the good agreement between the measurement and the numerical simulation except for $N_{\rm avg} > 200$ where the measured error is slightly larger than that predicted.

The RMS wavefront error across all holes for $N_{\rm avg} = 990$ was $\lambda/15,500$, which is larger than the value $C_{\rm pd}^{1/2} \times \sigma_{\Delta W} = \lambda/21,000$ predicted using the simulated data and the Southwell noise coefficient appropriate for this measurement. These discrepancies are probably due to the effect of the low-frequency temperature fluctuation described above.

The ability of the H-WFS to measure a small (modal) change in the wavefront, ΔW, was demonstrated by translating the fiber light source. As shown in Fig. 4, translating the source a distance Δz from an initial position z_0 displaces the spot on the CCD by $\Delta y(h)$, assuming that the change in the slope of each wavefront across the hole is small. The expected local gradient

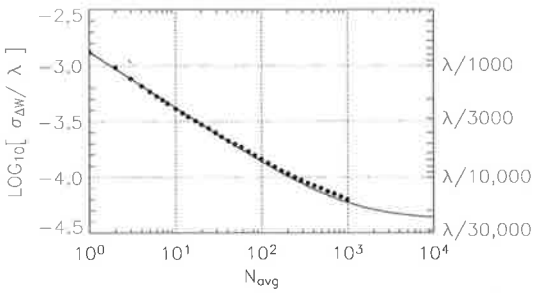

Fig. 3. The improvement in H-WFS sensitivity due to averaging over N_{avg} Hartmann images. The solid curve shows the improvement predicted by a numerical simulation assuming only random, stationary noise in the spot centroids.

of the wavefront change can then be calculated using

$$\frac{\partial(\Delta W)}{\partial h} = \frac{\Delta y}{L} = \frac{\Delta z\, y_0}{(z_0 - \Delta z)(z_0 + L)} = \frac{\Delta z\, h}{(z_0 - \Delta z)\, z_0} = Sh \tag{1}$$

where h is the position of the hole in the Hartmann plate, S is the primary aberration defocus and we have considered only one dimension for clarity.

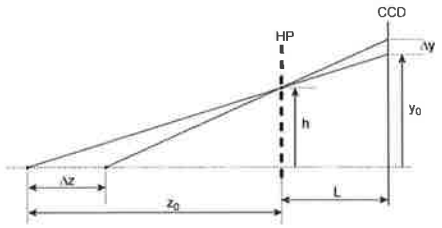

Fig. 4. Schematic diagram showing the displacement of the Hartmann spot on the CCD due to a change in the distance between the fiber end and the H-WFS.

Unfortunately, the 0.5 mHz oscillation in the output of the H-WFS resulted in a synchronous oscillation in the calculated defocus. We therefore continously recorded Hartmann images at 40 Hz and translated the fibre by about 10 μm every 5-10 minutes. The translation that occurred nearest a turning point of the 0.5 mHz oscillation was then selected for analysis, as this ensured that the average temperature of the H-WFS was the same before and after the translation. Plots of the local gradient of the wavefront change for $\Delta z = 9.60 \pm 0.05\,\mu$m, versus the transverse position, y_0, of each spot are shown in Fig. 5. They show a linear relationship between the local gradient and transverse position as predicted by Equation 1, and the improvement in sensitivity due to averaging.

The defocus due to the source translation can be calculated using the slope, m, of the line-of-best-fit to this data and $S = m(z_0 + L)/z_0$. The defocus for the 1-image and 5000-image averages are $-1.3 \pm 0.2 \times 10^{-3}\,\mathrm{m}^{-1}$ and $-1.159 \pm 0.007 \times 10^{-3}\,\mathrm{m}^{-1}$ at 95% confidence level. The uncertainty in S when averaged over 5000 images is equivalent to an uncertainty in the wavefront sag of 0.1 nm ($\lambda/9300$) over the CCD aperture (≈ 10 mm), which is roughly twice the

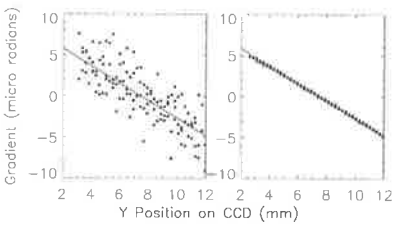

Fig. 5. Measured local gradient of the wavefront change versus spot position at the CCD, y_0, due to translation of the fiber light source, averaged over (left) 1 and (right) 5000 Hartmann images.

previously measured $\lambda/15,500$ due probably to the non-stationary noise during the extended acquistion time.

The accuracy of the defocus measurement can be determined by comparing the measured defocus with that predicted using Equation 1, but this comparison requires an accurate measurement of z_0. The distance between the source and the H-WFS was determined by exploiting the non-linear dependence of the local gradient on Δz: analyzing Hartmann images recorded with large Δz and determining the value of z_0 that would produce the best agreement between the measured local gradient and that predicted by Equation 1. With this approach, we found $z_0 = 91.7 \pm 0.2$ mm, giving an expected defocus of $-1.14 \pm 0.01 \times 10^{-3}\mathrm{m}^{-1}$, which differs from the measurement by about 1.7%. This error is equivalent to $\lambda/3,300$ and could be explained by a change in average temperature of the H-WFS of order 10 mK.

4. Conclusion

We have demonstrated that the H-WFS can measure changes in a wavefront with a single-frame sensitivity of $\lambda/1450$, which is primarily limited by shot noise. We have also shown that the sensitivity can be improved to $\lambda/15,500$ by averaging multiple Hartmann images. Finally, we demonstrated its application to the measurement of a small wavefront change due to defocus with a precision of $7 \times 10^{-6}\mathrm{m}^{-1}$ and established that the sensor is accurate to within about $2.0 \times 10^{-5}\mathrm{m}^{-1}$.

Together with the simplicity of the H-WFS, these results show that it is ideal for high precision and high accuracy measurement of wavefront changes, and represent a large improvement in the state-of-the-art. The H-WFS clearly exceeds the requirement for the measurement of absorption-induced wavefront distortion in advanced gravitational wave interferometers.

Acknowledgements

We acknowledge support from the Australian Research Council.

Bibliography

[1] A. Einstein, "On gravitational waves," *Abhandlungen der Preussischen Akademieder Wissenschaften*, vol. 8, pp. 154 – 167, 1918.

[2] R. A. Hulse and J. H. Taylor, "Discovery of a pulsar in a binary system," *Astrophys. J.*, vol. 195, no. 2, 1975.

[3] J. H. Taylor and J. M. Weisberg, "Further experimental tests of relativistic gravity using the binary pulsar PSR1913+16," *Astrophys. J.*, vol. 345, no. 1, pp. 434 – 450, 1989.

[4] S. A. Hughes, S. Marka, P. L. Bender, and C. J. Hogan, "New physics and astronomy with the new gravitational-wave observatories," Tech. Rep. P010029-00-D, LIGO Project, http://www.ligo.caltech.edu/docs/P/P010029-00.pdf, 2001.

[5] T. Creighton, "Advanced LIGO: Sources and astrophysics," *Classical Quant. Grav.*, vol. 20, no. 17, pp. S853 – S869, 2003.

[6] N. K. Glendenning, *Compact Stars.* Springer, New York, 2000.

[7] A. Abramovici, W. E. Althouse, R. W. P. Drever, Y. Gürsel, S. Kawamura, F. J. Raab, D. Shoemaker, L. Sievers, R. E. Spero, K. S. Thorne, R. E. Vogt, R. Weiss, S. E. Whitcomb, and M. E. Zucker, "LIGO: The Laser Interferometric Gravitational-Wave Observatory," *Science*, vol. 256, pp. 325 – 333, 1992.

[8] B. C. Barish and R. Weiss, "LIGO and the detection of gravitational waves," *Phys. Today*, vol. 52, no. 10, pp. 44–50, 1999.

[9] LIGO Scientific Community, "Livingston LIGO Electronic Logs: Detector Group." http://ilog.ligo-la.caltech.edu/.

[10] N. A. Robertson, "Laser interferometric gravitational wave detectors," *Classical Quant. Grav.*, vol. 17, no. 15, pp. R19–R40, 2000.

[11] G. Gonzalez, "Searches for gravitational waves from astrophysical sources - APS Meeting, April 14-17, 2007, Jacksonville, FL." http://www.ligo.caltech.edu/docs/G/G070232-00/G070232-00.pdf, 2007.

[12] R. Lawrence, *Active Wavefront Correction in Laser Interferometric Gravitational Wave Detectors*. PhD thesis, Massachusetts Institute of Technology, 2003.

[13] P. Hello and J.-Y. Vinet, "Analytical models of thermal aberrations in massive mirrors heated by high power laser beams," *J. Phys.-Paris*, vol. 51, no. 12, pp. 1267–1282, 1990.

[14] K. A. Strain, K. Danzmann, J. Mizuno, P. G. Nelson, A. Rudiger, R. Schilling, and W. Winkler, "Thermal lensing in recycling interferometric gravitational wave detectors," *Phys. Lett. A*, vol. 194, no. 1-2, pp. 124–132, 1994.

[15] P. R. Saulson, *Fundamentals of interferometric gravitational wave detectors*. World Scientific, Singapore, 1994.

[16] R. G. Beausoleil, E. K. Gustafson, M. M. Fejer, E. D'Ambrosio, W. Kells, and J. Camp, "Model of thermal wave-front distortion in interferometric gravitational-wave detectors. I. Thermal focusing," *J. Opt. Soc. Am. B*, vol. 20, no. 6, pp. 1247–1268, 2003.

[17] R. Lawrence, D. Ottaway, M. Zucker, and P. Fritschel, "Active correction of thermal lensing through external radiative thermal actuation," *Opt. Lett.*, vol. 29, no. 22, pp. 2635–2637, 2004.

[18] C. Zhao, J. Degallaix, L. Ju, Y. Fan, D. G. Blair, B. J. J. Slagmolen, M. B. Gray, C. M. Lowry, D. E. McClelland, D. J. Hosken, D. Mudge, A. Brooks, J. Munch, P. J. Veitch, M. A. Barton, and G. Billingsley, "Compensation of strong thermal lensing in high-optical-power cavities," *Phys. Rev. Lett.*, vol. 96, pp. 231101–1 – 231101–4, 2006.

[19] S. Ballmer, V. Frolov, R. Lawrence, W. Kells, G. Moreno, K. Mason, D. Ottaway, M. Smith, C. Vorvick, P. Willems, and M. Zucker, "Thermal compensation system description," Technical Note T050064-00-R, LIGO, 2005. http://www.ligo.caltech.edu/docs/T/T050064-00.pdf.

[20] M. Smith and P. Willems, "Auxiliary optics support system conceptual design document, vol. 1: Thermal compensation system," Technical Note T060083-00, LIGO, 2006. http://www.ligo.caltech.edu/docs/T/T060083-00/T060083-00.pdf.

[21] P. Willems, "Estimate of TCS sensor requirements," Technical Note T060068-00-D, LIGO, 2006.

[22] S. Wolfling, E. Lanzmann, N. Ben-Yosef, and Y. Arieli, "Wavefront reconstruction by spatial-phase-shift imaging interferometry," *Appl. Opt.*, vol. 45, no. 12, pp. 2586 – 2596, 2006.

[23] K. E. Perry, Jr. and J. McKelvie, "Reference phase shift determination in phase shifting interferometry," *Opt. Laser. Eng.*, vol. 22, no. 2, pp. 77 – 90, 1995.

[24] A. Poteomkin, N. Andreev, I. Ivanov, E. Khazanov, A. Shaykin, and V. Zelenogorsky, "Use of scanning Hartmann sensor for measurement of thermal lensing in TGG crystal," *SPIE Int. Soc. Opt. Eng.*, vol. 4970, pp. 10–21, 2003.

[25] Wavefront Sciences, Inc., "CLAS-2D Wavefront Analysis Specifications." http://www.wavefrontsciences.com/Specifications.pdf, 2006.

[26] J. A. Koch, R. W. Presta, R. A. Sacks, R. A. Zacharias, E. S. Bliss, M. J. Dailey, M. Feldman, A. A. Grey, F. R. Holdener, J. T. Salmon, L. G. Seppala, J. S. Toeppen, L. V. Atta, B. M. V. Wonterghem, W. T. Whistler, S. E. Winters, and B. W. Woods, "Experimental comparison of a Shack-Hartmann sensor and a phase-shifting interferometer for large-optics metrology applications," *Appl. Optics*, vol. 39, no. 25, pp. 4540–4546, 2000.

[27] J. D. Mansell, J. Hennawi, E. K. Gustafson, M. M. Fejer, R. L. Byer, D. Clubley, S. Yoshida, and D. H. Reitze, "Evaluating the effect of transmissive optic thermal lensing on laser beam quality with a Shack-Hartmann wave-front sensor," *Appl. Optics*, vol. 40, no. 3, pp. 366–374, 2001.

[28] D. Reitze, "Test mass substrate material selection for Advanced LIGO: An update from the optics working group." Doc. #:G040321-00-R, http://www.ligo.caltech.edu/docs/G/G040321-00/G040321-00.pdf.

[29] M. A. Arain, P. Willems, D. H. Reitze, D. B. Tanner, and G. Mueller, "Adaptive heating for thermal compensation in Advanced LIGO." Doc. #:G070234-00-E, http://www.ligo.caltech.edu/docs/G/G070234-00.pdf.

[30] S. Glas, *Optical Filters: Glass Filters.* http://www.schott.com/.

[31] D. R. Lide, ed., *CRC Handbook of Chemistry and Physics.* CRC Press, Inc., 79th ed., 1998-1999.

[32] Schott, "Material Safety Data Sheet: BG-20 inorganic glass." 2001.

[33] "Optical Glass Catalog - Data Table EXCEL May 1st, 2007." Web, 2007. http://www.schott.com/optics_devices/english/ download/opticalglassdatasheetsv010507c.xls.

[34] F.-T. Lentes, *The Properties of Optical Glass*, ch. 2. Springer-Verlag Berlin Heidelberg, 1995.

[35] R. C. Weast and M. J. Astle, eds., *CRC Handbook of Chemistry and Physics*. CRC Press, Inc, 59th ed., 1978-1979.

[36] Innolight, "Mephisto product line, ultrastable, cw, single-frequency lasers." http://www.innolight.de/pdfs/mephisto.pdf.

[37] D. Malacara, M. Servin, and Z. Malacara, *Interferogram Analysis for Optical Testing*. New York: Marcel Dekker, Inc., 1998.

[38] J. Hartmann, "Bemerkungen uber den bau und die justirung von spektrographen," *Zt. Instrumentenkd.*, vol. 20, p. 47, 1900.

[39] K. Suzuki, I. Ogura, and T. Ose, "Measurement of spherical aberrations using a solid-state image sensor," *Appl. Opt.*, vol. 18, no. 22, pp. 3866 – 3871, 1979.

[40] I. Ghozeil, *Optical Shop Testing*, ch. 10. John Wiley & Sons, Inc., 2nd ed., 1992.

[41] H. Lehmann, "Application of Hartmann's method of zonal testing to astronomical objectives. ii," *Zt. Instrumentenkd.*, vol. 22, pp. 325 – 330, 1902.

[42] J. A. Miller and R. W. Marriott, "Zone-tests of telescope objective," *J. Franklin I.*, vol. 178, pp. 465 – 481, 1914.

[43] A. Couder, "Construction of a telescope mirror of 1.20 m. diameter," *Bulletin Astronomique*, vol. 7, no. 10, pp. 423 – 433, 1932.

[44] H. H. Plaskett, "The Oxford 35m solar telescope," *Mon. Not. R. Astron. Soc.*, vol. 115, no. 5, pp. 542 – 549, 1995.

[45] B. Szczodrowska, "Study of Clark's astronomical objective," *Acta Astronom.*, vol. 19, no. 2, pp. 181 – 186, 1969.

[46] C. R. Forest, C. R. Canizares, D. R. Neal, M. McGuirk, and M. L. Schattenburg, "Metrology of thin transparent optics using Shack-Hartmann wavefront sensing," *Opt. Eng.*, vol. 43, no. 3, pp. 742–753, 2004.

[47] T. L. Kelly, P. J. Veitch, A. F. Brooks, and J. Munch, "A differential Hartmann wavefront sensor for accurate and precise optical testing," *Appl. Opt.*, vol. 46, no. 6, pp. 861 – 866, 2007.

[48] J. S. Plaskett, "Optical parts of 72-inch telescope," *J. Roy. Astron. Soc. Can.*, vol. 14, pp. 177 – 199, 1920.

[49] B. Loibl, "Hartmann tests on large telescopes carried out with a small screen in a pupil image," *Astron. Astrophys.*, vol. 91, no. 3, pp. 265–268, 1980.

[50] R. K. Tyson, *Principles of Adaptive Optics.* Academic Press, San Diego, California, 2nd ed., 1991.

[51] F. Roddier, ed., *Adaptive Optics in Astronomy.* Cambridge University Press, Cambridge, England, 1st ed., 1999.

[52] S. C. West, "Interferometric Hartmann wave-front sensing for active optics at the 6.5-m conversion of the Multiple Mirror Telescope," *Appl. Optics*, vol. 41, no. 19, pp. 3781–3789, 2002.

[53] C. Castellini, F. Francini, and B. Tiribilli, "Hartmann test modification for measuring ophthalmic progressive lenses," *Appl. Opt.*, vol. 33, no. 19, pp. 4120 – 4124, 1994.

[54] Y. Mejía-Barbosa and D. M. Malacara-Hernández, "Object surface for applying a modified Hartmann test to measure corneal topography," *Appl. Opt.*, vol. 40, no. 31, pp. 5778 – 5786, 2001.

[55] R. Goranson, J. Blea, A. Chipps, G. Denton, and J. Houchard, "Mid-infrared laser beam diagnostic wavefront analyzer," *SPIE Int. Soc. Opt. Eng.*, vol. 888, pp. 23 – 27, 1988.

[56] B. Schäfer, M. Lübbecke, and K. Mann, "Hartmann-Shack wave front measurements for real time determination of laser beam propagation parameters," *Rev. Sci. Instrum.*, vol. 77, pp. 053103–1 – 053103–8, 2006.

[57] P. Mercère, M. Idir, T. Moreno, G. Cauchon, G. Dovillaire, X. Levecq, L. Couvet, S. Bucourt, and P. Zeitoun, "Automatic alignment of a Kirkpatrick-Baez active optic by use of a soft-x-ray Hartmann wavefront sensor," *Opt. Lett.*, vol. 31, no. 2, pp. 199 – 201, 2006.

[58] J. Ares, T. Mancebo, and S. Bara, "Position and displacement sensing with Shack-Hartmann wave-front sensors," *Appl. Optics*, vol. 39, no. 10, pp. 1511–1520, 2000.

[59] J. Hartmann, "Objektuvuntersuchungen," *Zt. Instrumentenkd.*, vol. 24, p. 1, 1904.

[60] F. Roddier, "Variations on a Hartmann theme," *Opt. Eng.*, vol. 29, no. 10, pp. 1239 – 1242, 1990.

[61] J. L. Rayces, "Exact relation between wave aberration and ray aberration," *Opt. Acta.*, vol. 11, no. 2, pp. 85–88, 1964.

[62] W. H. Southwell, "Wave-front estimation from wave-front slope measurements," *J. Opt. Soc. Am.*, vol. 70, no. 8, pp. 998 – 1006, 1980.

[63] R. V. Shack and B. C. Platt, "Production and use of a lenticular Hartmann screen (abstract only)," *J. Opt. Soc. Am*, vol. 61, p. 656, 1971.

[64] J. D. Mansell and E. K. Gustafson, "Focal plane detection with a diffractive optic for Shack-Hartmann wave-front sensor fabrication," *Appl. Opt.*, vol. 40, no. 7, pp. 1074 – 1079, 2001.

[65] G. Artzner, "Microlens arrays for Shack-Hartmann wavefront sensors," *Opt. Eng.*, vol. 31, no. 6, pp. 1311–1322, 1992.

[66] J. Pfund, N. Lindlein, and J. Schwider, "Misalignment effects of the Shack-Hartmann sensor," *Appl. Opt.*, vol. 37, no. 1, pp. 22 – 27, 1998.

[67] J. E. Greivenkamp, D. G. Smith, and E. Goodwin, "Calibration issues with Shack-Hartmann sensors for metrology applications," *SPIE Int. Soc. Opt. Eng.*, vol. 5252, no. 1, pp. 372–380, 2004.

[68] S. Thomas, T. Fusco, A. Tokovinin, M. Nicolle, V. Michau, and G. Rousset, "Comparison of centroid computation of algorithms in a Shack-Hartmann sensor," *Mon. Not. R. Astron. Soc.*, vol. 371, pp. 323–336, 2006.

[69] S. Olivier, V. Laude, and J.-P. Huignard, "Liquid-crystal Hartmann wave-front scanner," *Appl. Optics*, vol. 39, no. 22, pp. 3838–3846, 2000.

[70] V. Laude, S. Olivier, C. Dirson, and J.-P. Huignard, "Hartmann wave-front scanner," *Opt. Lett.*, vol. 24, no. 24, pp. 1796–1798, 1999.

[71] V. V. Zelenogorsky, A. A. Solovyov, I. E. Kozhevatov, E. E. Kamenetsky, E. A. Rudenchik, O. V. Palashov, D. E. Silin, and E. A. Khazanov, "High-precision methods and devices for in situ measurements of thermally induced aberrations in optical elements," *Appl. Optics*, vol. 45, no. 17, pp. 4092–4101, 2006.

[72] I. C. Gardner and A. H. Bennett, "A modified Hartmann test based on interference," *J. Opt. Soc. Am. Rev. Sci. Instrum.*, vol. 11, pp. 441 – 452, 1925.

[73] A. Chernyshov, U. Sterr, F. Riehle, J. Helmcke, and J. Pfund, "Calibration of a Shack-Hartmann sensor for absolute measurements of wavefronts," *Appl. Opt.*, vol. 44, no. 30, pp. 6419 – 6425, 2005.

[74] M. Smith and P. Willems, "Auxiliary optics support system design requirements document, vol. 1: Thermal compensation system," Technical Note T000092-02, LIGO, 2000. http://www.ligo.caltech.edu/docs/T/T000092-02/T000092-02.pdf.

[75] F. Roddier, "Wavefront sensing and the irradiance transport equation," *Appl. Opt.*, vol. 29, no. 10, pp. 1402 – 1403, 1990.

[76] A. A. Michelson, *Studies in Optics.* The Univeristy of Chicago Press, Chicago & London, 1927.

[77] *ZEMAX Optical Design Program User's Guide*, 2004.

[78] J. W. Goodman, *Introduction to Fourier Optics.* McGraw-Hill, New York, 1968.

[79] D. Baer, "Private communication from laser micromachining solutions." email, Sept. 2005.

[80] J. W. Goodman, *Introduction to Fourier Optics.* Roberts & Company Publishers, Greenwood Village, Colorado, 3rd ed., 2005.

[81] D. R. Lide, ed., *CRC Handbook of Chemistry and Physics.* CRC Press, Inc., 84th ed., 2003-2004.

[82] G. C. Holst, *CCD Arrays, Cameras and Displays.* JCD Publishing, Winter Park, FL, 2 ed., 1998.

[83] DALSA Inc., *Application Note: Vertical Antiblooming. Doc#:03-36-00150-00.*

[84] S. R. Kamasz, S. P. Singh, S. G. Ingram, M. J. Kiik, Q. Tang, and B. Benwell, "Enhanced full well for vertical antiblooming, high sensitivity time-delay and integration (TDI) CCD with GHz data rates," in *IEEE Workshop on Charge-Coupled Devices and Advanced Image Sensors, June 7-9, Lake Tahoe, Nevada, USA*, 2001.

[85] DALSA Inc., *Pantera TF 1M60 and 1M30, 1K × 1K Progressive Scan Monochrome Camera, User's Manual and Reference. Doc#:03-32-10033-05*, 2004.

[86] DALSA Inc., *Data Sheet, FTT1010M, 1M Frame Transfer CCD Image Sensor*, 2004.

[87] Z. Jiang, S. Gong, and Y. Dai, "Monte-Carlo analysis of centroid detected accuracy for wavefront sensor," *Opt. Laser Technol.*, vol. 37, pp. 541–546, 2005.

[88] M. Nicolle, T. Fusco, G. Rousset, and V. Michan, "Improvement of Shack-Hartmann wave-front sensor measurement for extreme adaptive optics," *Opt. Lett.*, vol. 29, no. 23, pp. 2743 – 2745, 2004.

[89] S. A. Sallberg, B. M. Welsh, , and M. C. Roggemann, "Maximum *a posteriori* estimation of wave-front slopes using a Shack-Hartmann wave-front sensor," *J. Opt. Soc. Am. A*, vol. 14, no. 6, pp. 1347–1354, 1997.

[90] D. M. Topa, "Optimized methods for focal spot location using center of mass algorithms," *SPIE Int. Soc. Opt. Eng.*, vol. 4769, pp. 116 – 129, 2002.

[91] A. F. Brooks, T.-L. Kelly, P. J. Veitch, and J. Munch, "Ultra-sensitive wavefront measurement using a Hartmann sensor," *Opt. Express*, vol. 15, no. 16, 2007.

[92] N. Takato, M. Iye, , and I. Yamaguchi, "Wavefront reconstruction error of Shack-Hartmann wavefront sensors," *Publ. Astron. Soc. Pac.*, vol. 106, no. 696, pp. 182–188, 1994.

[93] M. E. Kasper, D. P. Looze, S. Hippler, M. Feldt, A. R. Weiß, A. Glindemann, and R. Davies, "A practical approach to modal basis selection and wavefront estimation," *SPIE Int. Soc. Opt. Eng.*, vol. 4007, pp. 592–599, 2000.

[94] S. I. Panagopoulou and D. R. Neal, "Zernike vs. zonal matrix iterative wavefront reconstructor." available from Wavefront Sciences website. http://www.wavefrontsciences.com/Zernike%20vs%20Zonal.pdf.

[95] D. M. Topa, "Wavefront reconstruction for the Shack-Hartmann wavefront sensor," *SPIE Int. Soc. Opt. Eng.*, vol. 4769, pp. 101–115, 2002.

[96] E. Kreyszig, *Advanced Engineering Mathematics.* John Wiley & Sons, Inc., 7th ed., 1993.

[97] C. Zhao, D. Blair, P. Barrigo, J. Degallaix, J.-C. Dumas, Y. Fan, S. Gras, L. Ju, B. Lee, S. Schediwy, Z. Yan, D. McClelland, S. Scott, M. Gray, A. Searle, S. Gossler, B. Slagmolen, J. Dickson, K. McKenzie, C. Mow-Lowry, A. Moylan, D. Rabeling, J. Cumpston, K. Wette, J. Munch, P. Veitch, D. Mudge, A. Brooks, and D. Hosken, "Gingin High Optical Power Test Facility," *J. Phys.: Conf. Ser.*, vol. 32, no. 1, pp. 368–373, 2006.

[98] J. Degallaix, *Compensation of strong thermal lensing in advanced interferometric gravitational waves detectors.* PhD thesis, The University of Western Australia, 2006.

[99] D. Hosken, D. Mudge, C. Hollitt, K. Takeno, P. Veitch, M. Hamilton, and J. Munch, "Development of power scalable lasers for gravitational wave interferometry," in *Tokyo-Adelaide Joint Workshop Quarks, Astrophysics and Space Physics Tokyo, Japan, 6-10 Jan. 2003*, no. 151 in Prog. Theor. Phys. Supp., pp. 216–220, 2003.

[100] QPhotonics, LLC, 1435 Crossways Blvd, Ste: 101, Chesapeake, VA 23320, USA, *QPhotonics QSDM-790-2 Fibre Coupled Superluminescent LED: Technical Specifications.* http://www.qphotonics.com.

[101] J. H. Romie, "Gingin ITM suspension assembly," tech. rep., LIGO, 2002. http://www.ligo.caltech.edu/docs/D/D020662-A.pdf.

[102] M. Arain, G. Mueller, D. Reitze, and D. Tanner, "A note on optimal spherical approximation to thermal lensing," Technical Note LIGO-T060080-00-Z, LIGO, 2006. http://www.ligo.caltech.edu/docs/T/T060080-00.pdf.

[103] A. E. Siegman, *Lasers.* University Science Books, 1986.

[104] M. C. Roggemann, B. M. Welsh, P. J. Garder, R. L. Johnson, and B. L. Pederson, "Sensing three-dimensional index-of-refraction variations by means of optical wavefront sensor measurements and tomographic reconstruction," *Opt. Eng.*, vol. 34, no. 5, pp. 1374–1384, 1995.

[105] E. de la Rosa Miranda, L. R. B. Valdos, and M. Funes-Gallanzi, "Optical tomography for smoothly-changing refractive index distributions," *SPIE Int. Soc. Opt. Eng.*, vol. 4778, pp. 325–332, 2002.

[106] P. R. Bevington and D. K. Robinson, *Data reduction and error analysis for the physical sciences.* The McGraw-Hill Companies, Inc, 2nd ed., 1992.

[107] C. L. Epstein, *Introduction to mathematics of medical imaging.* Prentice Hall, Upper Saddle River, NJ, 2003.